Developing carbon-based electrocatalysts for zinc-air batteries

Beatriz Janeiro Ferraz

A thesis presented for the degree of

Doctor of Philosophy

Supervised by

Professor Christopher Blackman

Department of Chemistry

Mathematical and Physical Sciences Faculty

University College London

March 2022

Declaration

I, Beatriz Janeiro Ferraz confirm that the work presented in this thesis is my own. Where information has been derived from other sources, I confirm that this has been indicated in the thesis.

Abstract

Zinc-air batteries (ZABs) are promising energy systems due to their safe and environmentally friendly nature, high theoretical energy density and low cost. However, the slow oxygen reduction (ORR) and oxygen evolution reactions (OER) that drive these batteries, impose a challenge for their use and upscaling. Hence, an electrocatalyst is necessary to help promoting these reactions. Additionally, the benchmark noble metal-based catalysts, not only are costly and rare but also suffer from stability issues. Therefore, this thesis was focused on the development of alternative electrocatalysts for efficient Zn-air batteries, including their synthesis, characterization, and larger scale cell application. Some key findings include123:

- The development of a metal-free and carbon-based ORR electrocatalyst by a facile strategy that allowed the introduction of N functionalities onto a carbon framework. This catalyst (CNDA900) was obtained due to the interaction of polydopamine with C_3N_4 while avoiding the use of templates, catalysts, or harsh chemicals. The battery containing the prepared catalyst presented a comparable performance to that of the ORR benchmark Pt-based catalyst.
- The synthesis of an efficient bifunctional electrocatalyst (ZIFCNDA) prepared by the introduction of Co ions during the polymerisation of dopamine, which lead to the direct doping of a carbon framework and the localized growth of Co-based MOFs polyhedrons, generating Co-based NPs upon pyrolysis. The C_3N_4-controlled polydopamine growth formed thin graphitized carbon nanosheets which can facilitate the transfer of electrons to the catalytically active sites. The ZAB containing the developed catalyst presented a long-term discharge of 600 h (at 5 mA cm^{-2}) and a high specific capacity of 686 mAh g^{-1}. The cell was even able to cycle at a high current density of 15 mA cm^{-2} for 65h.
- The development of polydopamine-coated electrospun fibers as a bifunctional ORR and OER catalyst. The polydopamine coating was crucial to provide a graphitic carbon coating and control the structural integrity of the catalyst composite during battery cycling. This strategy formed a composite with a large BET surface area, porosity and abundant

catalytically active sites. Additionally, the ZAB containing prepared air cathode catalyst exhibited excellent rechargeable performance for 100h, a steady and long-term discharge performance for about 230h and a high specific capacity of 530 mAh g^{-1} at a high current density of 10 mA cm^{-2}.

Impact Statement

Rechargeable zinc-air batteries (ZABs) are a promising alternative to replace the commercially used lithium-ion batteries (LIBs). Despite their high specific energy and power density, LIBs suffer from insufficient energy density, high cost and safety issues. Therefore, improvements are still necessary to achieve their full use. ZABs are driven by two electrochemical reactions: the oxygen reduction reaction (ORR) during discharge and the oxygen evolution reaction (OER) during the reverse charging reaction, but their slow kinetics still limits their efficiency and stability. Therefore, electrocatalysts on the air cathode may help to lower the ORR activation energy barrier and increase the conversion rate. This thesis describes the development of an efficient electrode catalyst. Firstly, by focusing on the development of an efficient and stable metal-free and carbon-based ORR catalyst; secondly by expanding the catalyst's activity by also promoting the reversible OER reaction and forming a bifunctional catalyst; and finally, by further improving the bifunctional catalyst's activity, stability and structural integrity due to the formation of a nanofibers-based catalyst composite.

Carbon-based composites are promising ORR electrocatalysts, especially when doped with heteroatoms such as N, forming catalytically active sites. due to their low cost, environmental friendliness, good electron conductivity and easy tailoring. However, the most commonly reported method for the preparation of such catalysts is the post-doping method, involving the incorporation of N functionalities into the stable carbon framework using harsh synthesis conditions and chemicals. Although in situ direct doping methods are less severe, the N content achieved is typically low, (under 9 at.%) or hidden in the bulk of the sample. Hence, the development of a facile and safe procedure for the preparation of a nitrogen-rich carbon composite was successfully achieved. This first study highlights the use of carbon nitride (C_3N_4) as a nitrogen-rich precursor material, which itself has low electrical conductivity. The addition of the self-polymerizing biopolymer, polydopamine (PDA), combined with the C_3N_4 was essential to allow the doping of extra nitrogen features from species originated from its high temperature decomposition while forming stable carbon layers, creating several active sites and stable carbon layers with greater electron conductivity ability than C_3N_4 itself. The ORR performance of the final catalyst presented a half-wave potential ($E_{1/2}$) of 0.78 V vs. RHE and a diffusion-limited current density of 4.60 mA cm^{-2}, comparable to the benchmark Pt/C catalyst. The developed catalyst was able to retain 87.94 % of its initial current after

4 h of continuous testing. The composite catalyst also presented promising OER results; a ZAB containing the aforementioned catalyst presented good cyclability for 75 h and a maximum voltage gap of 1.32 V, when cycling at 2.5 mA cm^{-2} for 30 min during charging, and at 5 mA cm^{-2} for 15 min during discharging. This study opens up an avenue for the development of nitrogen-rich and carbon-based catalysts.

Following the development of an efficient C- and N-based ORR electrocatalyst, improving the catalyst's ability to promote the charging and discharging (OER and ORR) ZAB reactions was crucial to improve the cell's cyclability and stability. Cobalt- and N-doped carbon composites (Co-N-C) have been studied as efficient multifunctional catalysts for ZABs due to the strong coupling effect of Co with N which form catalytically active sites. Cobalt has also been reported to promote the graphitization of amorphous carbon, which may promote electron movement to the active sites. However, well-distributed cobalt ions on the graphitic carbon framework have been challenging to achieve. Zeolitic imidazolate frameworks (ZIFs) may be employed to aid the formation of Co-N-C catalysts due to their tunable structure and porous and large surface area, however, the structure may collapse due to high temperature pyrolysis. Therefore, a strategy to promote the formation of distributed cobalt sites was achieved by inserting Co-ions during the polymerization of dopamine (DA) to form polydopamine (PDA), chelating the Co-ions by the N-atoms on the DA precursor and subsequent formation of ZIF-67 nanoparticles. Additionally, the controlled growth of a carbon layered structure was as achieved due to the addition of C_3N_4 template during the PDA synthesis. Some outstanding features of this catalyst composite include a high specific capacity of 686 mAh g^{-1} and a long-term cyclability at high current density values of 10 mA cm^{-2} and 15 mA cm^{-2} for over 150 h and 65 h, respectively.

Controlling the catalyst's structure stability may improve the long-term performance of the ZABs and increase their lifetime. Here, electrospinning was used to prepare a composite with a well-controlled surface area and pore structure which helped decrease the catalyst's degradation rate. In detail, a structure composed of Co-N-based nanoparticles coated by porous N-rich graphitic carbon nanofibers was obtained from a mixture of ZIF-67 particles and polystyrene (PS) which were electrospun and coated by self-polymerized PDA. the graphitic carbon coating formed by high temperature pyrolysis, helped promote electron transport to the catalytically active sites while stabilizing the composite's structural integrity. Additionally, this layered coating incorporated N-doped C, providing further catalytically active sites. The increased BET

surface area, porosity, active sites and 3D network structure of the prepared composite, exhibited outstanding ORR and OER performance. The assembled ZAB containing the developed air electrode displayed excellent rechargeability at a high current density of 10 mA cm^{-2} for 100 h and an outstanding long-term discharge for a prolonged period of 230 h.

Acknowledgements

First and foremost, I would like to express my deepest gratitude to my supervisor, Professor Christopher Blackman, for all his guidance and support throughout my PhD, both during my time at UCL and in Singapore. I am also thankful to Professor Zhengxiao Guo for providing me with the opportunity to pursue this PhD project.

I would also like to extend my deepest gratitude to Dr. Li Bing and Dr. Junhua Kong from IMRE, who constantly guided and supported me, and without whom the completion of my research project would have not been possible. I wish to thank Dr. Liu Zhaolin, for his support during my exchange at IMRE A*STAR (Singapore) and Ms. Sheau Wei, Ms. Siew Lang and Dr. Jisheng Pan for the meaningful discussions and for their support in equipment training and data collection.

I am very grateful to my colleagues and friends at IMRE, Ms. Silvia Fruncillo, Ms. Meltem Yilmaz, Mr. Alvaro Castillo-Bonillo, Mr. Norton West, Ms. Rachel Pooley, Mr. Matej Sebek, Mr. Daniil Bash who supported me during difficult times, especially the pandemic while being so far from home. I am also very grateful to my colleague and friend Dr Yijie Xue, for his constant help in the laboratories at IMRE, insightful discussions, and collaboration opportunities.

Finally, I am extremely grateful to my family, especially my mum, Custodia Janeiro, my sister, Carolina Ferraz and my boyfriend, Kenneth Chua, for their constant support, encouragement, understanding and love, without whom, the completion of this PhD thesis would have definitely not been possible.

Table of Contents

List of Figures

List of Tables

Abbreviations

2D	Two-dimensional
ADT	Accelerated Degradation Test
BE	Binding Energy
BET	Brunauer−Emmett−Teller
BJH	Barrett-Joyer-Halenda
C_{dl}	Electrochemical Double-Layer Capacitance
CNDA	Carbon Nitride and Dopamine-Derived Electrocatalyst
CNT	Carbon Nanotubes
Co-N-C	Cobalt-based N-doped Carbons
CPDA	Carbonized Polydopamine
CV	Cyclic Voltammetry
DA	Dopamine
E1/2	Half-wave Potential
ECSA	Electrochemical Surface Area
EDS	Energy Dispersive X-ray Spectroscopy
FE-SEM	Field Emission-Scanning Electron Microscope
GC	Glassy Carbon
GDE	Gas Diffusion Electrode
K-L	Koutecky-Levich
LSV	Linear Sweep Voltammetry
M-N-C	Metal N-doped Carbons
MOF	Molecular Organic Framework
NF	Nanofiber
NP	Nanoparticle
OER	Oxygen Evolution Reaction

ORR	Oxygen Reduction Reaction
PDA	Polydopamine
PTFE	Polytetrafluoroethylene
RDE	Rotating Disk Electrode
RHE	Reference Hydrogen Electrode
RPM	Rotations Per Minute
STA	Simultaneous Thermal Analysis
TEM	Transmission Electron Microscope
TM	Transition Metal
TMO	Transition Metal Oxides
XRD	X-ray Diffraction
XPS	X-ray Photoelectron Spectroscopy
ZAB	Zinc-Air Battery
ZIF	Zeolitic Imidazolate Framework
ZIFCNDA	Co-based Nanoparticles on N-doped Graphitic Carbon Layers

1. Background and Literature Review

1.1. Energy storage

The increased demand for energy generation by a modern industrialized society has been driving the transition from fossil fuels to renewable energy sources as a way to reduce environmental pollution.[1] The World Resources Institute reported that 61.4% of total greenhouse gas emissions originate from the energy sector.[2] Therefore, researchers across the world have focused on the development of advanced materials for sustainable and efficient energy harvesting, conversion, storage, and utilization. Alternative renewable energy sources such as solar, wind, biomass, geothermal or hydro-electric are already heavily used. However, these options are still constrained by climate conditions, high cost of large-scale sites and site-specific requirements and hence struggle to meet the worldwide energy demand. Consequently, the development of energy conversion systems based on safe, cost-effective, and reliable systems from sustainable sources is still required.

Batteries are a proven electrochemical conversion technology.[3,4] Since their creation in 1991, Li-ion batteries (LIBs) have been greatly employed in a variety of applications due to their high specific energy and power density (Figure 1.1).[5] Despite their commercial use, LIBs have not been able to meet the modern demands of electrified transportation and grid-scale stationary energy storage and they are reaching their performance limit.[6,7] Furthermore, current LIBs are affected by insufficient energy density (limited to be < 350 W h kg^{-1}) and high cost (~ \$150 $kW^{-1}h^{-1}$) which limits their large-scale applications.[7,8] Another challenge faced by LIBs is their change in volume during charge-discharge cycles and lithium's extreme reactivity which requires an inert production environment and extra circuit protection.[9,10]

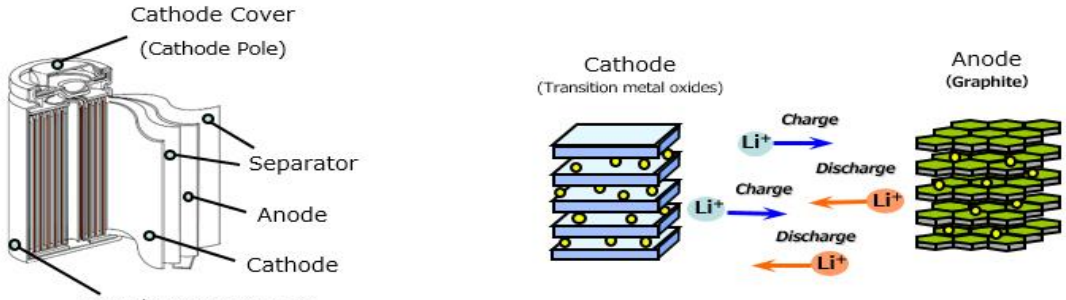

Figure 1.1: a) Configuration of a lithium-ion battery consisting of a cathode, anode, separator, and casing. b) During discharge, Li in the anode is oxidized to Li^+, and the ions migrate through the electrolyte to the cathode where they are incorporated into lithium cobalt oxide, reducing Co^{4+} to Co^{3+}. The reverse reaction recharges the cell. [11]

1.2. Metal-air batteries

In an attempt to find viable alternatives to LIBs, metal-air batteries have become the target of intensive research because of their high theoretical energy density (~ 1229-8076 W h kg^{-1}) and unlimited fuel supply (oxygen in the air). Since the O_2 is not retained within the battery structure, high energy densities are achieved (Figure 1.2).

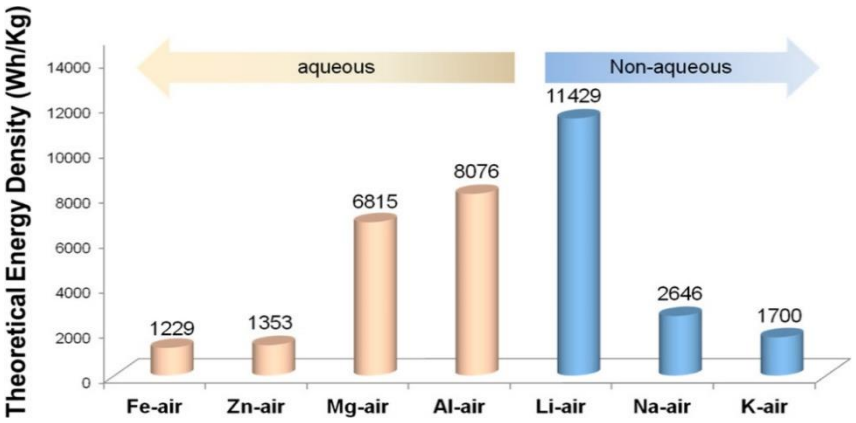

Figure 1.2: Different metal (Fe, Zn, Mg, Al, Li, Na and K)-air batteries and their respective theoretical energy densities.[6]

Metal-air batteries are open cell systems that produce electricity though a redox reaction between the metal anode and oxygen provided through an air-breathing cathode (Figure 1.3).[12] The anode metals can be alkali metals (eg. Na, K, Li), alkaline earth-metals (eg. Mg), first-row transition metals (eg. Fe, Zn) or post-transition metals (eg. Al).

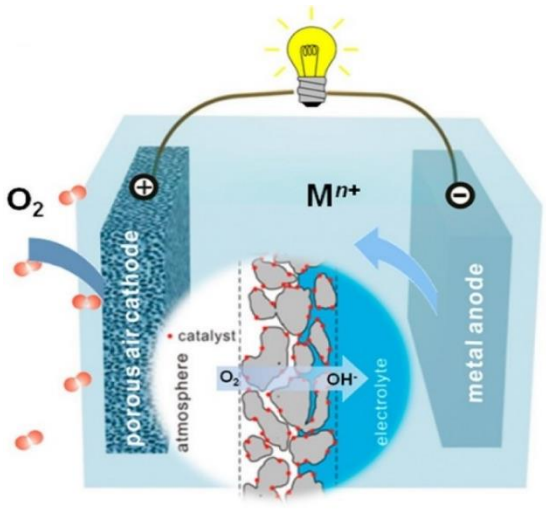

Figure 1.3: Schematic configuration of an aqueous metal-air battery.[6]

Metal-air battery systems may contain an aqueous electrolyte or otherwise feature an aprotic solvent-based electrolyte;[13] typically metal anodes such as Na, K and Li are too reactive under aqueous conditions and therefore require aprotic solvents. However, Na, K and Li anodes suffer from lower discharge capacities due to the accumulation of superoxide or peroxide reaction products on the air cathode, which eventually block the cathode active area and stop the battery from operating.[6] Mg, Fe, Zn and Al-based metal-air batteries are, to some extent, compatible with aqueous electrolytes since their surfaces can be passivated by the corresponding metal oxides and hydroxides. Despite being electrically rechargeable, Fe-air batteries present a very low practical energy density of about 60-80 Wh kg^{-1} and therefore cannot be considered for pure electrical vehicle applications. [14] Although Mg- and Al-air cells have a significant energy density, their metal anodes can be easily corroded in an aqueous solution. Additionally, they can only be mechanically recharged, implying that their discharged anodes and spent electrolyte must be replaced with fresh ones.[15,16]

1.3. Zinc-air batteries

Zinc-air batteries (ZABs) have been considered powerful, safe and environmentally friendly alternatives for future energy applications. Besides being an earth-abundant metal, zinc also has a low electrical resistivity (5.95 $\mu\Omega$ cm^{-1}).[4,17] Zinc-air batteries have a high theoretical energy density of 1353 Wh $kg^{-1,}$ which is about 5 times higher than that of LIBs.[6] Additionally, since Zn is one of the most abundant elements on Earth, when combined with an air-breathing cathode, the cost of ZABs is estimated to be less than 10 \$ $kW^{-1}h^{-1,}$ much lower than that of LIBs (~ \$150 $kW^{-1}h^{-1}$) .[5,7,18]

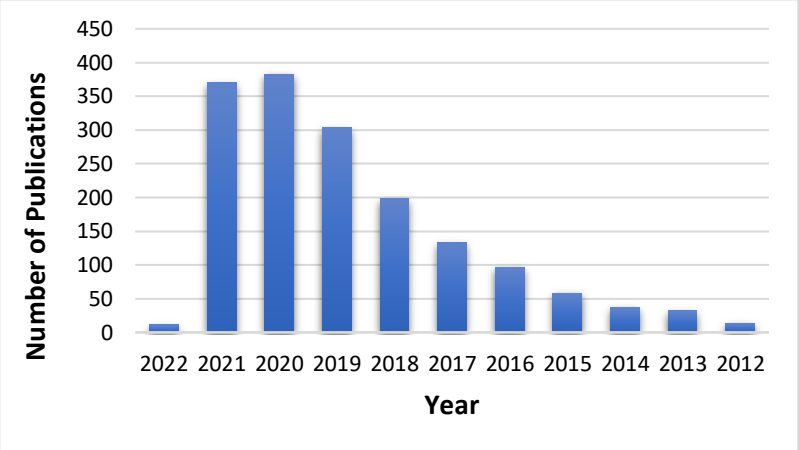

Figure 1.4: Number of publications per year from a Web of Science search on "zinc-air batteries".

Therefore, an increasing research interest in ZABs has been observed due to their promising large-scale applications (Figure 1.4).

Table 1.1: Commercialized zinc-air battery technologies. [4]

Company	Battery type	Features and performance
Fluidic energy[19]	Secondary	Ionic salts plus additives as the electrolyte, coupled with nanostructured Zn as the anode.
EOS[20]	Secondary	Neutral chloride electrolyte ($Zn/ZnCl_2$, NH_4Cl, H_2O/O_2); charge and discharge potentials at 2.1 V and 0.9 V; 2700 cycles with no degradation.
Revolt[21,22]	Mechanically rechargeable	Liquid Zn slurry which flows through tubes that function as air cathode; 200 cycles at 100 mA cm^{-2}.
EDF France[23]	Secondary	Faradaic efficiency is 96% at 30 mA cm^{-2}; energy efficiency is 70%; energy density is 100 W h kg^{-1}; cycle life is 90 cycles 15 min per cycle.

The first ZAB prototype was developed by Maiche in 1878 and it was first commercialized in the 1930s. Since then, they have been used in the hearing, medical, navigation and railway fields. Despite having been commercialized (Table 1.1), alike with other battery technologies, ZABs still suffer from some practical limitations.[1,5,7,24–26] On one hand, the anode suffers from severe passivation which may retard the electrolyte access and prevent the discharge of the remaining active material. Furthermore, the self-discharge and corrosion of the metal may degrade the anode coulombic efficiency, shortening the battery shelf-life. The main limitation of air cathodes lies in their slow reaction kinetics, high overpotentials and low reversibility of oxygen chemistry. The

cathode reactions are often complex and have not yet been fully understood, limiting the battery's full utilization.[12,27]

1.3.1. Zinc-air battery structure

As described above, zinc-air cells are composed of an electrolyte, a zinc metal anode and a bifunctional air cathode.[18] The air cathode is comprised of a catalytic active layer and a gas diffusion layer. ZABs can be classified as primary or secondary (mechanically or electrically rechargeable). Primary sealed ZABs will only experience 2% capacity decay after one year of storage and therefore have a long and stable storage life.[3,28] In mechanically recharged secondary ZABs, the consumed Zn anode is replaced with a fresh one and the used anode is separately processed to metallic Zn. These batteries suffer from short lifetime and irregular operation. Therefore, electrically rechargeable ZABs have been extensively studied as a possible alternative to the widely used LIBs.[4,20] The structure of a rechargeable ZAB is presented in Figure 1.5.

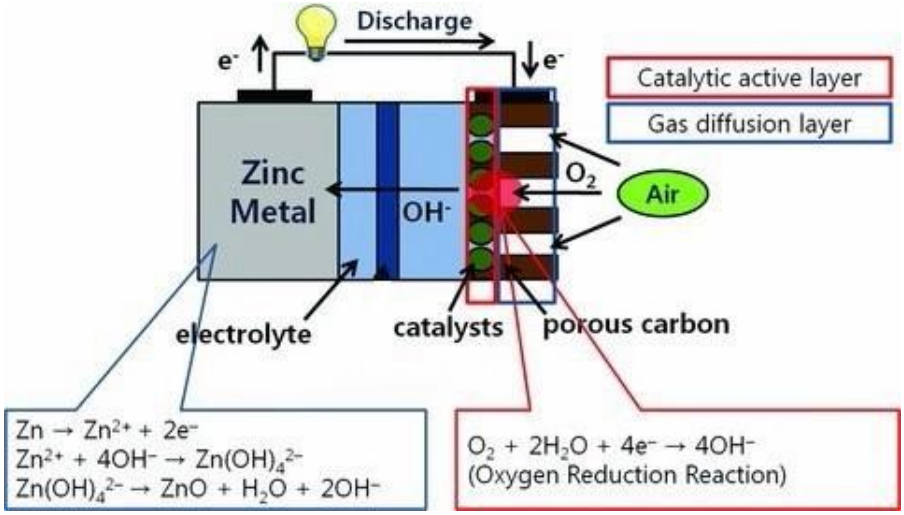

Figure 1.5: Structure and working principle of a zinc-air battery during discharge. The red circle indicates where the three-phase reaction takes place in the air cathode. [18]

Rechargeable zinc-air batteries yield and store electrical energy via electrochemical reactions, namely the oxygen reduction reaction (ORR) during discharge and the oxygen evolution reaction (OER) during the reverse charging reaction.

Generally, upon discharge of the battery the zinc metal is oxidized to form the $Zn(OH)_4^{2-}$ ion and release two electrons at the negative electrode. Driven by the difference in pressure on the outside and inside the cell, the oxygen from the atmosphere

diffuses through the porous carbon electrode into the electrolyte where it is then reduced to hydroxide ions at the cathode, assisted by the catalyst, by electrons obtained from the oxidation of the zinc metal in the anode. Due to the low solubility of oxygen in the electrolyte an electrocatalyst is necessary to facilitate the oxygen reduction, implying that the ORR takes place at a triple-phase boundary where, during discharge, the electrocatalyst at the air cathode (solid) accelerates the oxygen reduction (gas) in the electrolyte (liquid).[27] Finally, the hydroxide ions migrate from the cathode to the anode to combine with dissociated metal ions and form metal oxides. The reaction pathways described are reversed again upon recharge, which involves the reduction of zincate ions back into zinc and oxygen formation.[1,7]

Anode

$$Zn_{(s)} \rightarrow Zn^{2+}_{(aq)} + 2e^-$$

$$Zn^{2+}_{(aq)} + 4OH^-_{(aq)} \rightarrow Zn(OH)^{2-}_{4\,(aq)} \ (E_0 = -1.25 \text{ V vs. SHE})$$

$$Zn(OH)^{2-}_{4\,(aq)} \rightarrow ZnO_{(s)} + H_2O + 2OH^-_{(aq)}$$

Cathode

$$O_{2\,(g)} + 2H_2O_{(aq)} + 4e^- \rightarrow 4OH^-_{(aq)} \ (E_0 = +0.40 \text{ V vs. SHE})$$

Overall reaction

$$2Zn_{(s)} + O_{2\,(g)} \rightarrow 2ZnO_{(s)} \ (\text{Cell potential} = 1.65 \text{ V vs. SHE})$$

According to $E_{eq} = E_0(cathode) - E_0(anode)$, the reversible potential of the cell is 1.65 V, but practically, the working voltage can drop to 1.2 V, in order to obtain a considerable discharge current density.[5] This is mainly due to the high overpotential during the ORR and OER. This large charging and discharging voltage gap leads to a low cycling efficiency (55-65%) in rechargeable ZABs.[7] These are mainly caused by slow

reaction kinetics and resistance to the ion transport in the electrolyte and electrons in the cell hardware.

The anode is composed of zinc, which can be in the form of plates, fibres or powder. During charging, the parasitic hydrogen evolution reaction (HER) competes with the zinc deposition, generating reactive H_2 gas which can induce corrosion issues on the zinc anode, reducing the active material utilization and causing safety problems. The reaction proceeds as follows:

$$Zn + 2H_2O \rightarrow Zn(OH)_2 + H_2$$

In order to avoid the self-corrosion of Zn due to the generation of hydrogen gas during undesirable HER, a bigger particle size is preferred, despite lowering the anode surface area.[29–32] Another limiting factor of the use of Zn anodes is the formation of dendrites which can significantly reduce the overall performance of ZABs. Dendrites are formed due to the high solubility of zincate ions which oversaturate the electrolyte during extensive charge-discharge cycles and therefore impede the reactions at the zinc electrode and the electrolyte flow.[33]

The electrolyte allows the migration of ions, essential for the battery operation. Usually zinc-air batteries use an aqueous alkaline electrolyte since Zn violently reacts with hydrogen ions in acid solution, seriously corroding the anode.[1] Moreover, aqueous

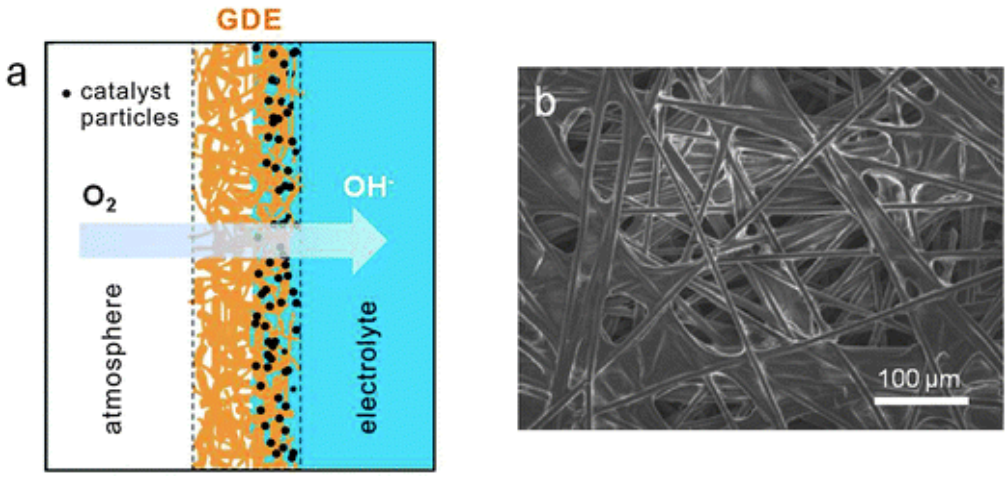

Figure 1.6: a) Schematic structure of a catalysts loaded onto the gas diffusion electrode (GDE) in contact with the oxygen from the atmosphere and the liquid electrolyte. b) SEM image of the commercial Toray carbon paper.

electrolytes have a relatively high boiling point which reduces the safety risks related to the volatile and flammable organic liquid electrolytes often used in LIBs.[34] A few examples of alkaline electrolytes utilized include KOH or NaOH. However, the most commonly used medium of ion migration is 26-30 wt% (6-7 M) potassium hydroxide (KOH) due to its superior conductivity (~0.6 S cm^{-1}) at room temperature.[6,35,36] The ionic resistance in the electrolyte is reduced at such concentration and so is the evolution of undesired hydrogen obtained from the HER. However, this concentration cannot be much further increased as it will lead to a higher electrolyte viscosity. A highly concentrated KOH electrolyte may promote the decomposition of zincate ions, fuelling the production of insoluble ZnO which can block the anode's active surface area and being less of an electrical conductor than metallic zinc, it may also prevent electrochemical reversibility and eventually cause the battery to fail.[37,38] Despite the advantages of the KOH electrolyte and the cell's open infrastructure, the cell capacity may also be reduced if the hydroxide ions present in the electrolyte react with atmospheric CO_2 to form carbonates. Carbonate poisoning not only reduces the availability of hydroxide ions in solution but also forms precipitates inside the pores of the air electrode, reducing the cell lifetime.[18,39]

The ORR takes place at the air cathode and therefore it requires a porous material which can facilitate oxygen diffusion. The porous gas diffusion layer, included in the air cathode, is required to provide adequate triple phase boundary and therefore deliver high and continuous ORR current density.[40] A gas diffusion electrode (GDE) is composed of a layered polytetrafluoroethylene (PTFE)-carbon structure containing distinct hydrophobic and hydrophilic sides (Figure 1.6a) and a current collector mesh or foam (eg. Ni or Cu). The hydrophobic side has a large pore size to facilitate the diffusion of oxygen to the catalytically active sites, while preventing the electrolyte infiltration. The opposite hydrophilic side contains a catalytic layer with a smaller pore structure, providing access to the electrolyte.[7,41–43] A ZAB is an open system due to its porous cathode structure that allows oxygen from the air to penetrate. Hence, in a low humidity environment, the electrolyte may evaporate and in a high humidity environment the air electrode may flood due to the accumulation of water, reducing the transport of oxygen to the active sites and the ionic conductivity in the diluted electrolyte.[35] On that account, a careful preparation and balance of the carbon and PTFE components ratio may control the appropriate wetting of the air electrode and maintenance of a stable three-phase boundary.[44,45] The commercially used Toray carbon paper is a porous and electrically

conductive GDE composed of carbon fibers attached by graphitized carbon layers and treated with PTFE to guarantee it is wet proof (Figure 1.6b).[1]

1.3.2. Reaction mechanism

The ORR mechanism involves the diffusion of oxygen through the porous electrode and consequent adsorption to the catalyst's surface.[18,46] There are different oxygen adsorption modes on the catalytic particles: bidentate and end-on (Figure 1.7). In a bidentate interaction, the O-O bond length is increased and weakened until it leads to the dissociative adsorption of the O-O bond. On an end-on interaction, only partial charge transfer takes place. The ORR process can take place either through a two (Scheme 1) or four electron pathway (Scheme 2). In Scheme 1, oxygen is indirectly reduced to OH^- via HO^{2-} after adsorption of only one oxygen atom which coordinates perpendicularly to the catalyst in an 'end-on' configuration. A subsequent two-electron reduction of the peroxide to hydroxide ions occurs, or the peroxide may disproportionate to form hydroxide. The formation of corrosive peroxide species reduces the energy efficiency and therefore makes promoting the four-electron pathway preferable.[47] In the four-electron pathway oxygen is directly reduced to OH^- through bidentate O_2 coordination to the catalyst (two O atoms coordinate to the catalyst). The relative stability of the O* and HOO* reaction intermediates generated after the O_2 adsorption on the catalysts determines whether the ORR can proceed either by a two- or four-electron pathway.[48] Therefore, scientific research has been focused on the development of catalysts that aid the ORR through a favourable 4-electron pathway with high energy efficiency. The two reactions (in an alkaline environment) are detailed below.

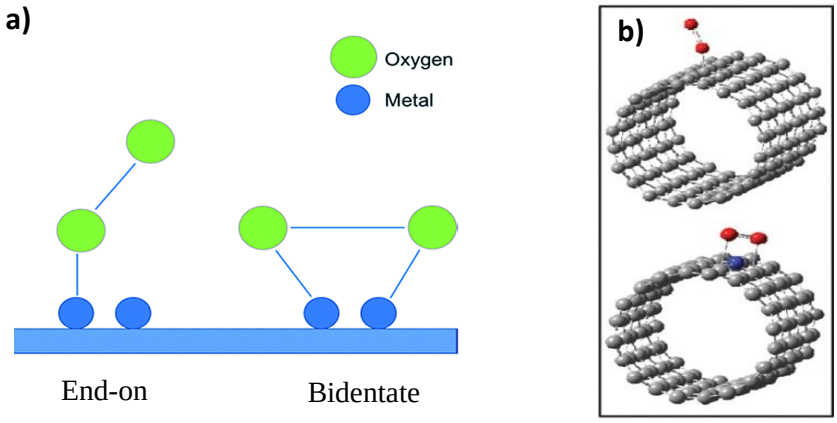

Figure 1.7: Oxygen adsorption mechanisms of an oxygen molecule with a a) metal and a b) CNTs-based catalyst. [4,232]

Two-electron pathway (Scheme 1):

$$O_{2(g)} + H_2O_{(l)} + 2e^- \rightarrow HO_{2\,(aq)}^- + OH_{(aq)}^-$$ (E_0 = - 0.07 V vs. SHE)

$$HO_{2\,(aq)}^- + H_2O_{(l)} + 2e^- \rightarrow 3OH_{(aq)}^-$$ (E_0 = 0.87 V vs. SHE)

$$2HO_{2\,(aq)}^- \rightarrow 2OH_{(aq)}^- + O_{2(g)}$$

Four-electron pathway (Scheme 2):

$$O_{2(g)} + 2H_2O_{(l)} + 4e^- \rightarrow 4OH_{(aq)}^-$$ (E_0 = 0.40 V vs. SHE)

The detailed four-electron pathway is given below (* indicates the adsorption sites):

$$* + O_{2(g)} + H_2O_{(l)} + e^- \rightarrow HOO^* + OH_{(aq)}^-$$

$$HOO^* + e^- \rightarrow O^* + OH_{(aq)}^-$$

$$O^* + H_2O_{(l)} + e^- \rightarrow HO^* + OH_{(aq)}^-$$

$$HO^* + e^- \rightarrow OH_{(aq)}^- + *$$

Overall: $O_{2(g)} + 2H_2O_{(l)} + 4e^- \rightarrow 4OH_{(aq)}^-$

Overall, the 4-electron ORR pathway involves oxygen diffusion through the porous gas diffusion layer and adsorption to the catalyst's surface, then electrons on the anode move to the oxygen molecules weakening and ultimately breaking the O-O bond forming hydroxide ions which are finally transferred through the electrolyte to the zinc anode.[1,18,46] However, the strong O=O bond (498 kJ mol^{-1}) is extremely difficult to electrochemically break. Additionally, since the ORR involves multiple electronic transfer steps, the kinetics are very sluggish. Hence, an electrocatalyst is necessary to

promote a more energetically favourable bond activation and cleavage by moderate adsorption of O_2 through various intermediates.[49,50] The catalytic activity is determined by the binding strength of the oxygenated species to the electrode's surface. On the one hand, if the adsorption is too weak, the activity is limited by the electron or proton transfer to the adsorbed oxygen (associative mechanism) or splitting of the O-O bond in O_2 (dissociative mechanism), depending on the applied potential. On the other hand, if the adsorption of oxygen is too strong, the activity will be limited by proton-electron transfer to O* or HO* and the desorption of H_2O will not be facilitated and the active site for further oxygen adsorption may be blocked.[13,51,52]

The reverse reaction of the ORR is the OER which involves four electron transfer steps in an alkaline electrolyte. Comparable to the ORR, the OER kinetics are mostly controlled by the oxygen adsorbates produced (designated by *) and their binding strength to the active sites surface. The reaction steps are detailed below:

$$* + OH^-_{(aq)} \rightarrow HO^* + e^-$$

$$HO^* + OH^-_{(aq)} \rightarrow O^* + H_2O_{(l)} + e^-$$

$$O^* + OH^-_{(aq)} \rightarrow HOO^* + e^-$$

$$HOO^* + OH^-_{(aq)} \rightarrow * + O_{2(g)} + H_2O_{(l)} + e^-$$

Overall: $4OH^-_{(aq)} \rightarrow O_{2(g)} + 2H_2O_{(l)} + 4e^-$

Following Sabatier's principle which states that, for an optimum catalysis, the binding energy between the catalyst and the reactant should be moderate, if the oxygen binding strength is too weak, the oxidation of HO* becomes the rate-determining step, but if the binding of oxygen is too strong, the formation of HOO* is then the rate-determining step.[5]

In nonstandard conditions, the equilibrium potential of oxygen electrode reactions is described by the Nernst equation:

$$E = E^o - \frac{RT}{nF} ln \frac{[Ox]}{[Red]}$$

This equation relates the potential of an electrochemical cell (E) to the standard potential of a species (E^0) and the concentration of the oxidized ([Ox]) and reduced ([Red]) species in the system at equilibrium. The other equation parameters include the universal gas constant (R), the temperature in Kelvin (T), the number of transferred electrons (n) and Faraday's constant (F).[53] Hence, it is possible to predict how a system will respond to a change in concentration of the species in solution or electrode potential using the Nernst equation.[54]

The equilibrium potential for the oxygen half-cell reaction is 1.23 V vs. RHE, indicating that the forward and reversed reactions are balanced and implying a zero net current at that point. The ORR is favoured below the half-cell potential and the OER is favoured above this potential.[55] Due to the poor ORR/OER kinetics, a significant deviation between the equilibrium potential and the experimentally applied potential (overpotential) is required to drive the reaction and yield appreciable current. Consequently, the cell efficiency is directly related to the overpotential, therefore, a high overpotential would lead to a decreased efficiency.[51]

1.3.3. Air cathode/oxygen electrocatalyst

The slow ORR and OER kinetics that drive the rechargeable ZABs remain one of the main challenges when designing efficient and stable batteries. The discharging process involves the ORR and takes place at the cathode, during which the O_2 molecules are reduced. Hence, an electrocatalyst is necessary to aid the bond activation and cleavage.[1] Electrocatalysts are added to the air cathode to help lower the activation energy barrier (defined by the overpotential) and increase the conversion rate. The varied adsorption/desorption reaction intermediates and reaction pathways also contribute to the slow kinetics. [47]

Platinum is the benchmark catalyst for ORR, but its cost, scarcity and low OER activity has triggered research of new catalysts for zinc-air batteries. Firstly, reversibility happens in a process taking place close to equilibrium and therefore if large overpotentials are necessary to drive the reaction in each direction, then the conditions to drive catalysis could be different. Additionally, Pt tends to undergo oxidation at the high positive

potentials required for OER, generating a different type of surface than that present under ORR conditions. Therefore, low OER performance of Pt/C is greatly related to the accumulation and surface coverage by oxygenated species which subsequently decrease the active surface area.[56] The ORR limiting steps are the reduction of OH* and O_2 and the OER limiting steps are the formation of OOH* and O*.[57,58] Therefore, the binding energies of the reaction intermediates with most active ORR and OER catalysts are not similar, so it is difficult to obtain one that can deliver both good ORR and OER performance. Accordingly, Ir or Ru-based electrocatalysts are efficient in catalysing the OER but are not as powerful in boosting the ORR. Therefore, the development of environmentally friendly and cost-effective alternatives with high ORR and/or OER activity is of great interest.

1.3.3.1. Noble metal-based electrocatalysts

Despite Pt and Ir-based catalysts being the benchmarks for ORR and OER, respectively, the use of these noble metals is not ideal due to their high cost and scarcity. Several alternative strategies such as alloying with other metals or metal oxides, using reduced cost options (eg. Ag,) or tuning the size and morphology of noble metals have been explored.[4]

Bimetallic catalysts such as $Pt_3Ni(111)$, Pt-Pd and Pt-Au have demonstrated improved catalytic activity and stability achieved by tuning the electronic structure and increasing and exposing active facets.[59–61]

Silver-based catalysts are cost effective precious metals which mainly include silver combined with MnO_2 or carbon supports, forming a bifunctional ORR/OER active catalyst.[62,63] Wang et al prepared a porous composite with catalytically active Ag NPs supported on conductive single-walled carbon nanotubes (SWNTs) which was effective at promoting O_2 reduction.[64] Additionally, this electrocatalyst presented reduced weight and thickness as well as improved OER activity in comparison to that of Pt/C. Varcoe et al and Guo et al analysed the effect of the metal loading on the catalytic activity of an Ag/C catalyst. They concluded that the performance of Ag/C catalysts with 60 wt% metal loading was comparable to that of the benchmark 20 wt% Pt/C.[65,66] In another example, a bifunctional catalyst including transition metal oxide nanorods ($LaMnO_3$ perovskite) embedded between reduced graphene oxide sheets and homogeneously overlaid Ag NPs was prepared by a simple hydrothermal method.[67] The catalyst with strong interaction

exhibited rapid charge transfer and reactant diffusion leading to an efficient 4-electron ORR pathway and high durability. The ZAB prepared with this catalyst showed high performance and cycle durability which was comparable to the Pt/C-based battery.

Another strategy involves precious metal- or metal oxide-coated carbon supports. A RuO_2-coated ordered mesoporous carbon nanofiber array composite was developed to be a bifunctional ORR/OER catalyst (Figure 1.9).[68] The uniform RuO_2 coating and the hierarchical mesoporous/macroporous structure of the composites promoted high electrical conductivity and provided efficient catalytic active sites.

This catalyst presented a high catalytic activity, especially the OER. The rechargeable ZAB containing the developed catalyst presented a long cycle life of 160 h at 4 mA cm^{-2}.

Different metals have varied catalytic activities depending on their adsorption energies to the intermediates, which is determined by the surface's electronic structure. This is regulated by the interaction between the adsorbate valence states and the metal *d*-states.[69] Accordingly, the higher in energy the *d*-states are comparative to the Fermi energy (highest occupied state) of the metal, the stronger the interaction to the absorbate states. If the *d*-states are close to the Fermi energy, antibonding states may be shifted above it and become empty or bonding states may be shifted below it and be occupied, increasing the bond strength.

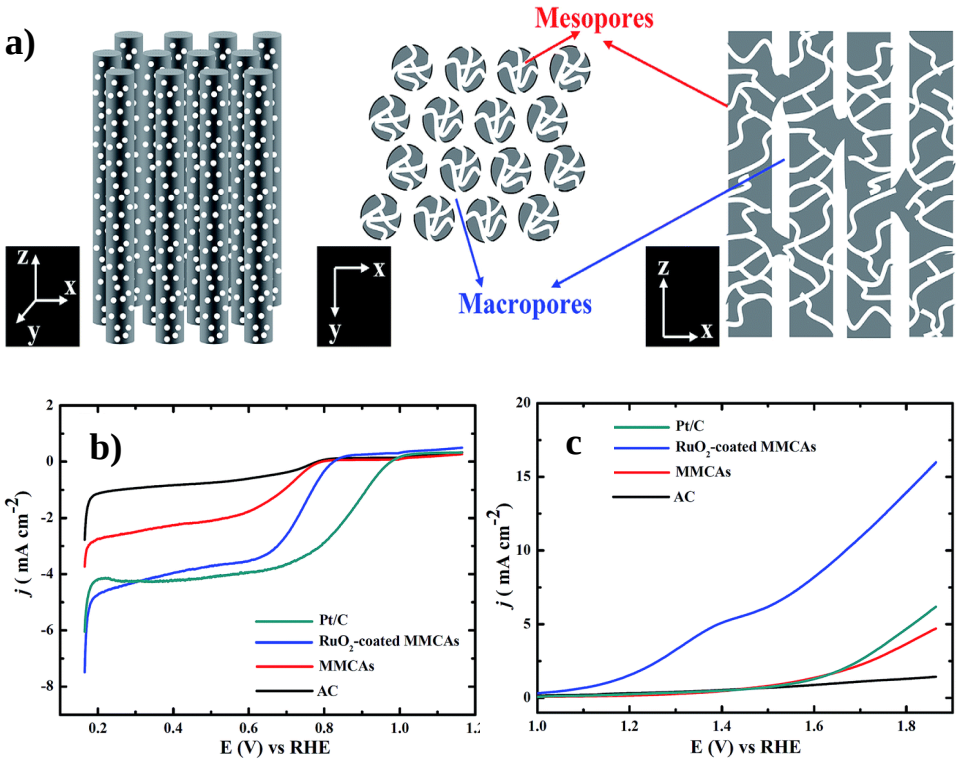

Figure 1.8: a) Structure of RuO_2-coated ordered mesoporous carbon nanofiber arrays (RuO_2-coated MCNAs). b) ORR LSV curves of AC (commercial activated carbon), MCNAs, RuO2-coated MCNAs and Pt/C at 1600 rpm in O_2 saturated 0.1 M KOH solution. c) OER LSV curves of AC, MCNAs, RuO_2-coated MCNAs and Pt/C. [68]

1.3.3.2. Non-noble metal-based electrocatalysts

Non-noble metals have attracted extensive attention as suitable electrocatalysts. Transition metals such as Ni, Fe and Co combined with carbon-rich materials have been considered as promising alternative electrocatalysts, due to their variable valences, great catalytic activity, stability, availability, and reduced cost in comparison to the benchmark Pt- and Ir-based catalysts. Metal N-doped carbons (M-N-C), especially Co/Fe-N_x-C have attracted attention due to their high catalytic activity and low cost. Their great bifunctional activity is originated due to the strong coupling effect between the metal and N in the carbon matrix which can regulate the local electronic structure to form active sites with suitable binding energies to the intermediate species. Taking into consideration the ability of metals to form complexes with N-ligands, metal particles can be formed on N-doped carbon substrates. Additionally, high annealing temperatures can stimulate de-coalescence of metal particles by migration and Ostwald ripening. Those metal particles subsequently react with the amorphous carbon, by acting as diffusion channels

transporting the carbon atoms and promoting the growth of a continuous graphitic-like carbon layer, which is known to improve electrical conductivity. [70,71]

Bao et al. synthesised Fe nanoparticles within N-doped carbon shells (Fe@N-C) by pyrolysis of dicyandiamide and ammonium ferric citrate precursors (Figure 1.10). The ORR and OER Fe@N-C electrocatalyst showed comparable performance to the state-of-the-art Pt and Ir-based catalysts and great performance and cycling durability when incorporated in the air cathode of a zinc-air battery.[72]

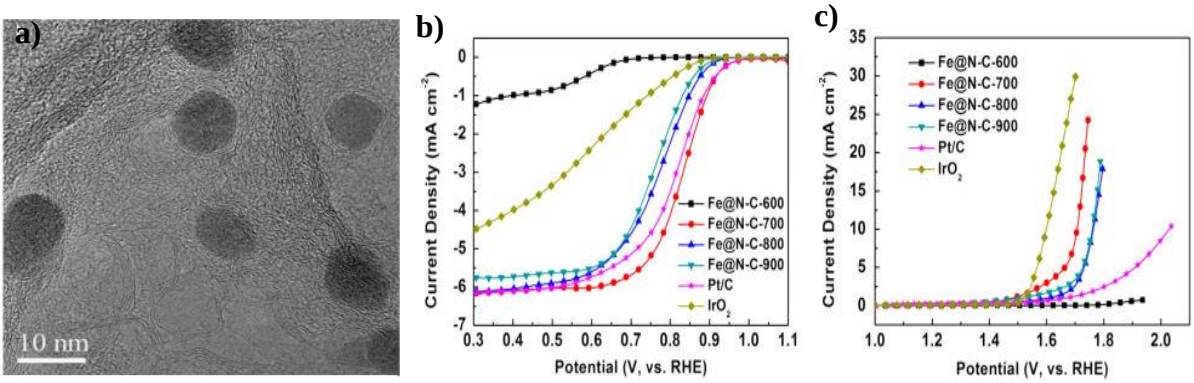

Figure 1.9: a) TEM image of the Fe@N-C-700 catalyst. b) ORR activity and c) OER activity of the Fe@N-C catalyst prepared at different pyrolysis temperatures, tested in O_2-saturated 0.1 M KOH solution.[72]

Another report by Zhang et al. demonstrated the synthesis of confined cobalt nanoparticles in carbon nanocages embedded on N-doped graphene-like nanosheets (Co-NCF).[73] This catalyst demonstrated excellent ORR performance confirmed by the high half-wave potential (0.83 V) recorded and high limiting current density (5.74 mA cm^{-2}) achieved, exceeding the commercial Pt/C catalyst. The Co-NCF-based ZAB also achieved a high power density of 134 mW cm^{-2} and a specific capacity of 766.6 mA $h.g^{-1}_{Zn}$. A bifunctional catalyst (Figure 1.11) consisting of dispersed Co-N-C moieties and carbon confined Co nanoparticles was derived from a dual nitrogen source (Co/Co-N-C) demonstrating a half-wave potential of 0.882 V (ORR) and a potential of 1.640 V at 10 mA cm^{-2} (OER).[74] The nanoparticles provide an enhanced specific surface area, increasing active sites exposure. The ZAB containing the Co/Co-N-C air cathode presented an excellent cycling stability for 167 h and a specific capacity of 700.6 mA $h.g^{-1}_{Zn}$.

Furthermore, a bifunctional ORR/OER electrocatalyst composed of FeCoNi alloy particles decorated on ultralarge N-doped graphene tubes has been reported by Wu et. al.[75] This one-step template-free and low cost synthesis used inexpensive DCDA as the carbon and nitrogen precursor and the ternary FeCoNi alloy as a catalyst. The in-situ formation of the FeCoNi alloy catalyst during the graphitization process led to the formation of a large tube size, forming electrochemically accessible surface areas, graphitized structures and high nitrogen content. These structures led to the high bifunctional ORR/OER activity and high electrochemical stability of the catalysts.

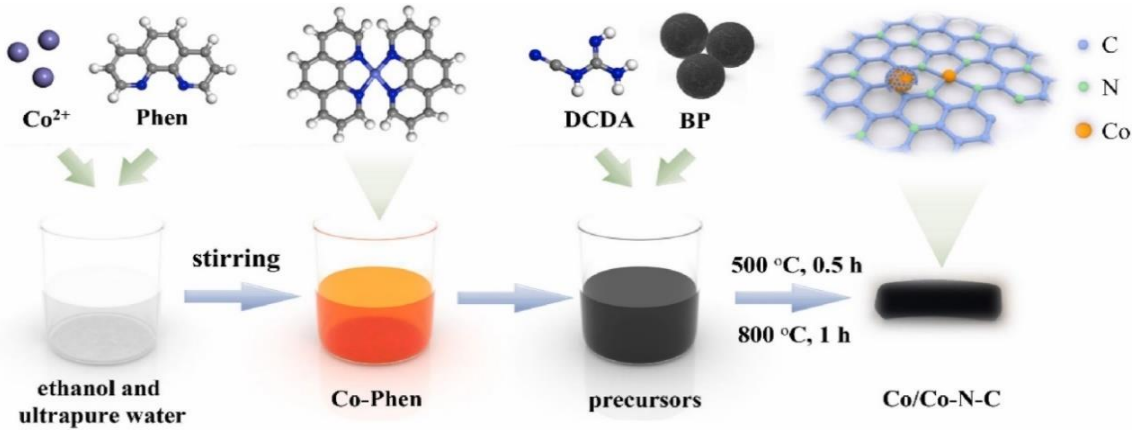

Figure 1.10: Synthetic procedure for the preparation of the Co/Co-N-C (Co- and C-based composite) catalyst.[74]

In order to find alternative options to replace the traditional and thoroughly studied N-doped carbons, a range of graphitic carbon nitride (g-C_3N_4)-coordinated metal structures were investigated as ORR and OER electrocatalysts in alkaline media. Theoretical predictions and experimental tests were performed on a Co-g-C_3N_4 complex, suggesting comparable activity with precious metals for the ORR and OER. The catalytic activity was originated from the Co-N_2 actives sites coordinated within the g-C_3N_4 matrix.[76] Transition metal and nitrogen co-doped carbon nanoparticles were successfully prepared by the introduction of selected metal salts into an aqueous solution of dopamine which then proceeded by a mussel-inspired polymerization reaction at room temperature followed by carbonization. From the metal-containing composites prepared (Co-PDA-C, Ni-PDA-C and Fe-PDA-C), Co-PDA-C presented a preferred structure composed of a porous matrix of coalesced carbon particles with small metallic Co NPs embedded. Co-

PDA-C presented a more positive half-wave potential (0.767 V) and higher current density (~ 3.5 mA cm^{-2}) in comparison to the other M-PDA-C hybrids. The ZAB containing the Co-PDA-C cathode electrocatalyst presented a good retention of the discharge voltage above 1 V for over 540 h at 5 mA cm^{-2} and a steady cycling behaviour for 500 h at 2 mA cm^{-2}.[77]

1.3.3.2.1. Metal Organic Frameworks

Metal organic frameworks (MOFs) are compounds composed of central metal ions or clusters connected by organic ligands. Zeolite imidazole frameworks (ZIFs) are a class of MOFs formed by tetrahedrally-coordinated transition metal ions coordinated by imidazolate linkers (Figure 1.12). ZIFs are topologically isomorphic with zeolites since the metal-imidazole-metal angle is 145˚, which is similar to the Si-O-Si angle of zeolites.[78]

ZIFs have attracted great attention in the catalysis field due to their highly ordered crystalline structure, tunable pore size and high specific surface area.

A few advantages of the use of MOFs as catalyst precursors include their controllable size, morphology and structure. The facilitated heteroatom doping of MOF-based composites (eg. metal atoms, N, S and P) can modify the local electronic structure of the catalysts and reduce the adsorption energy of the reaction intermediates, hence improving the catalytic performance. Using conductive ligands in the MOF structure may boost the

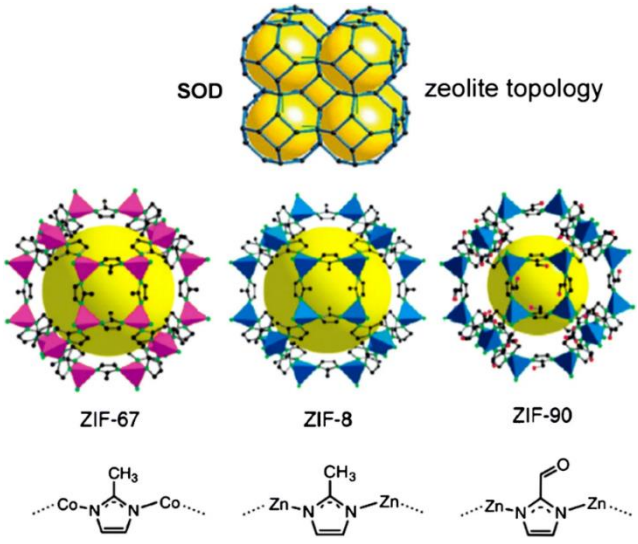

Figure 1.11: Crystal structures and topologies of different ZIFs.[233]

electrical conductivity, leading to improved electron transfer. Finally, MOFs' supermolecular structure may endow good electrochemical durability and stability.[5] Thus, the appropriate tunning of the metal ions, ligands and structure is key to obtain efficient MOF-based catalysts through simplified and cost-efficient processes.

MOF-based oxygen electrocatalysts are usually obtained from pristine MOFs or MOF composites. Pristine MOFs are two-dimensional (2D) conductive MOFs formed by the coordination between metal ions and ligands such as benzene or triphenylene with functional groups such as imine ($-NH_2$), phenol (-OH) or thiophenol (-SH). 2D MOFs' intrinsic structural porosity, chemical stability and excellent electrical conductivity derived from their in-plane π-conjugation structure, have attracted great attention as alternative ORR and OER electrocatalysts. A MOF structure composed of Ni ions coordinated by four amino groups from the 2,3,6,7,10,11-hexaiminotriphenylene (HITP) conductive ligands in a conjugate coplanar structure to form $Ni_3(HITP)_2$.[79] The large π

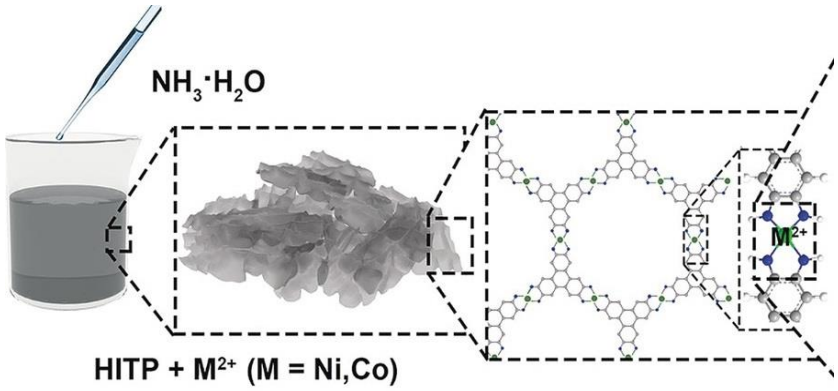

Figure 1.12: Synthesis procedure of M3HITP2.[81]

bond of the ligand provides good electron transfer and therefore the high conductivity. Dincă et al. reported that the binding and activation of O_2 in the pristine $Ni_3(HITP)_2$ electrocatalyst occurred on the ligand instead of the metal, promoting a high ORR activity.[80]

Peng et al. prepared and investigated the catalytic activity of another M_3HITP_2 MOF composed of Co^{2+} coordinated HITP ligands (Figure 1.13).[81] A distorted quadrilateral structure with lack of coplanarity originated due to the unpaired electron of $3dz^2$ was observed on the non-preferred Co_3HITP coordination structure with poor crystallinity and π-π stacking. The 3d electrons of the metal center can promote ORR activity, which was

confirmed by the $E_{1/2}$ of 0.80 V. The Co_3HITP-based ZABs were efficient and stable for over 80 h. Furthermore, Dou et al studied the combination of 2D MOF nanosheets with MOF nanoparticles as a successful ORR/OER catalyst alternative. A hybrid MOF prepared by deposition of inert Fe-MOF nanoparticles on active Ni-MOF nanosheets (Ni-MOF@Fe-MOF) presented enhanced catalytic performance originating from the 2D nanosheet morphology and synergistic effect between Ni and Fe species.[82] The optimized catalyst material presented a E_{10} (potential value at a current density of 10 mA cm^{-2}) of 1.495 V, which was lowered after hybridization. Additionally, it was observed that the hybrid MOFs were in situ converted to oxide nanoparticles during OER, behaving as active sites and building blocks for the porous nanosheets.

Several reports have shown successful application of pristine conductive MOFs as oxygen electrocatalysts. However, the use of costly conductive ligands and complicated synthesis procedures limits their application in large scale catalysis. Additionally, despite their outstanding OER performance, these catalysts still lack efficient ORR activity and their structural stability and electrical conductivity still require further improvements in order to guarantee their effective application in ZABs.

A new class of porous metal/metal compound carbon-based materials such as metal-nitrogen-carbon and carbon-based metal composites derived from MOFs have been studied as an efficient alternative strategy to synthesise bifunctional electrocatalysts. M-N-C composites include M-Nx species formed within a carbon framework. It has been shown that M-N_4 species are ORR active sites, facilitating O_2 adsorption and O=O bond breaking. MOF-derived M-N-C composites formed by carbonized ligands rich in N and transition metal sites exhibit both excellent ORR and OER.

Single-atom M-N-C catalysts composed of single metal atoms embedded into a ligand-derived porous carbon framework exhibit outstanding ORR and OER catalytic activity originating from the high atom utilization efficiency. Recent studies have shown that nitrogen-doped carbon supports obtained from MOFs lead to the development of Co-N_x active sites. A free-standing bifunctional catalyst composed of cobalt-single atom sites on N-doped porous carbon nanoflakes sustained by carbon nanofibers (Co SA@NCF/CNF) has been successfully developed by Guo et al (Figure 1.14).[83] The catalyst composite was synthesised using ZIF-67 and electrospun nanofiber precursors by an impregnation-carbonization-acidification method.

A porous structure with well distributed and accessible active sites delivered durable bifunctional catalytic activity with a reversible oxygen overpotential of 0.75 V. When incorporated as a flexible air cathode in a wearable ZAB, Co SA@NCF/CNF delivered satisfactory battery capacity of 540.17 ma h g_{Zn}^{-1} and displayed excellent shape stability when deformed. The atomically dispersed Co-N_x catalytic sites were formed by in situ reduction of ZIF-67 during pyrolysis delivering good conductivity and excellent stability.

Moreover, Fe-N-C containing Fe-N_x sites have been considered to be efficient in catalysing the ORR and OER in alkaline media. Ma et al. reported a composite composed of ZIF-8 polyhedrons embedded on both sides of polypyrrole-coated graphene and 2,2-bipyridine-coordinated iron ions dispersed on the ZIF-8 polyhedrons surface.[84] Pyrolysis at high temperature leads to the evaporation of Zn in ZIF-8 generating Fe-Nx active sites distributed on graphitic 2D porous nitrogen-doped carbon (FeNx-embedded PNC). The prepared catalyst exhibited high specific surface area, abundant Fe-Nx active sites and

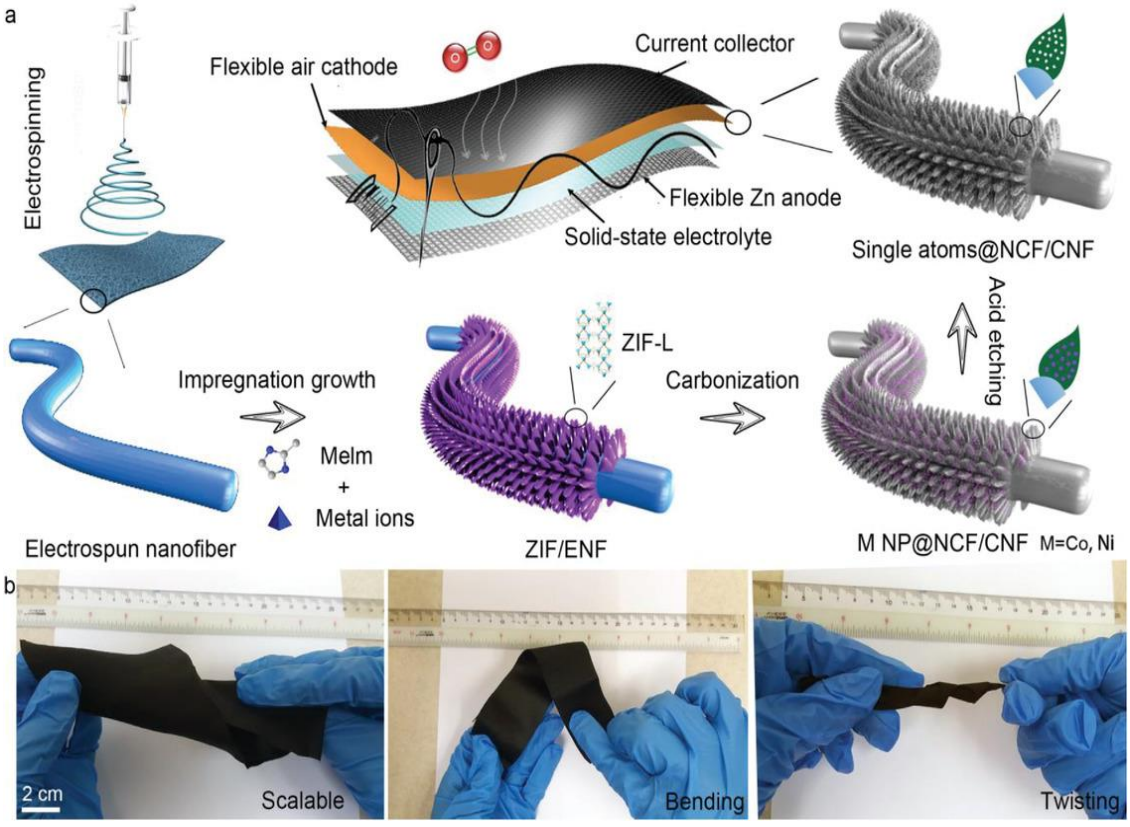

Figure 1.13: a) Schematic procedure for the scalable fabrication of M SA@NCF/CNF film through an "impregnation-carbonization-acidification" process for the preparation of a flexible air cathode in a wearable ZAB. b) Rolling, bending, and twisting of a flexible Co SA@NCF/CNF. [83]

superior conductivity. The FeNx-embedded PNC composited showed superior bifunctional catalytic activity with a half-wave potential of 0.86 V, more positive than the reported commercial Pt/C of 0.84 V, and a low E_{10} of 1.62 V for OER, leading to a reduced potential difference (ΔE) of 0.78 V. Additionally, a FeNx-embedded PNC-based solid-state zinc-air battery could be bent up to 90˚ and reach up to 54% compression strain without significant voltage degradation.

A different kind of MOF-derived M-N-C ORR/OER catalysts include Co-nanoparticles (CoNPs) distributed in an N-doped carbon framework.

A nanohybrid composed of N-doped carbon/cobalt nanoparticles/N-doped carbon multi-layered sandwich (NdC-CoNPs-NdC) was synthesised from pyrolysis of a new cobalt-based MOF (Figure 1.15).[85] The interlayer confined Co NPs with high stability and activity, the conductive multi-layer porous N-doped carbon matrix with extra active sites and the interconnection of these components lead to preparation of a durable bifunctional electrocatalyst with a $E_{1/2}$ of 0.80 V and a E_{10} of 1.63 V, obtaining a reduced ΔE of 0.83 V. An on-chip all-solid-sate flexible and rechargeable ZAB containing the NdC-CoNPs-NdC air cathode catalyst developed, exhibited large specific capacity (771 mA h g^{-1}), a maximum power density of 57 mW cm^{-2} and good rechargeability (150 cycles in 50 h).

ZIFs are MOFs with a regular dodecahedral shape, high surface area, porosity and easy to synthesise and hence can be the ideal precursor to prepare Co-N-C composites. ZIFs provide a highly tailorable platform considering pyrolyzed ZIFs can originate amorphous or graphitic carbon frameworks.[86]

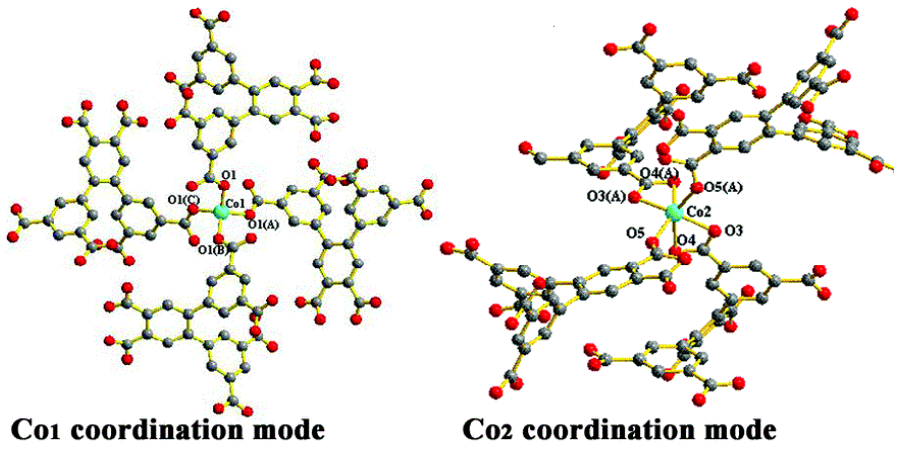

Figure 1.14: Single crystal structure of MOF synthesised through the reaction of H_6dpa ligands and cobalt nitrate (different coordination modes of the Co ions). This is the precursor for the synthesis of the NdC-CoNPs-NdC catalyst.[85]

Three-dimensional ZIF nanocrystals have been structurally transformed into metal-nitrogen co-doped carbon nanorod array (Co-N_x/C NRA) through pyrolysis.[87] The prepared Co-N_x/C NRA presented great catalytic activity, confirmed by the low ΔE of 0.65 V, obtained from the synergistic effect of the rich Co-N coupling centers and nanorod arrays with high specific surface area. The Co-N_x/C NRA-based rechargeable ZABs showed a high energy density of 853.12 W h kg_{Zn}^{-1} and a long cycling stability for up to 80 h at a high current density of 50 mA cm^{-2}.

Transition metal (eg. Fe, Co, Ni, Mn) compounds derived from MOFs integrated with porous carbon frameworks have also exhibited enhanced catalytic ability and durability for ZABs due to the synergistic effect between the two constituents.[88–91] Transition metal oxides (TMOs) are efficient electrocatalysts due to their variable valences and rich structures. The enhanced electrical conductivity and stability of TMOs-based catalyst originates from the high organic ligands-content in MOFs which leads to the uniform dispersion of TMOs in the porous carbon framework during carbonization.[5] An efficient catalyst composed of hollow Co_3O_4 nanospheres distributed within N-doped carbon nanowall arrays on carbon cloth (N-Co_3O_4/CC).[92] The composite was prepared through a facile carbonization-oxidation of a cobalt-based MOF precursor. During carbonization, a graphitic onion-like structure was coated on the cobalt nanoparticles which, during oxidation, facilitated the conversion of Co NPs into hollow Co_3O_4 nanospheres with a fine scale nanograin structure. A positive $E_{1/2}$ of 0.87 V for ORR confirmed the high activity of the catalyst, and when integrated as an air-cathode in a flexible solid-state ZAB, a high capacity of 387.2 mA h g^{-1}, stable cyclability and flexibility were reported. Furthermore, a hybrid composite of Co and Co_3O_4 nanoparticles stitched in porous graphitized carbon shells (Co/Co_3O_4@PGS) was successfully synthesised through an ionic exchange and redox reaction between Co^{2+} and 2D Zn MOF nanosheets (Figure 1.16).[93] The tri-phase structure containing atom trapping defect interfaces and porous graphitized carbon shells, facilitated charge transfer and improved active sites utilization. Hence a low ΔE of 0.69 V was observed, confirming the excellent catalytic activity. The Co/Co_3O_4@PGS air cathode-based ZAB exhibited enhance cycle stability with a reduced voltage decay for over 800 h at 10 mA cm^{-2}.

1.3.3.3. Metal-free carbon-based electrocatalysts

Carbon materials have attracted great attention as an alternative to Pt-based ORR catalysts for zinc-air batteries due to their facile preparation, adjustable morphology, large surface area, good conductivity and cost effectiveness. Different N-doped carbon structures have been extensively studied due to their ability to catalyse the ORR via a favourable four-electron pathway. Other heteroatoms (eg. N, P, S, B) can be included in the carbon framework, creating active sites on the carbons adjacent to those heteroatoms, which modulate the binding energy of oxygen and facilitate the breaking of the O=O bond.[94] Heteroatoms can be introduced into a carbon framework by in situ doping during the synthesis of those carbon materials or by post-treatment of a pre-synthesised carbon

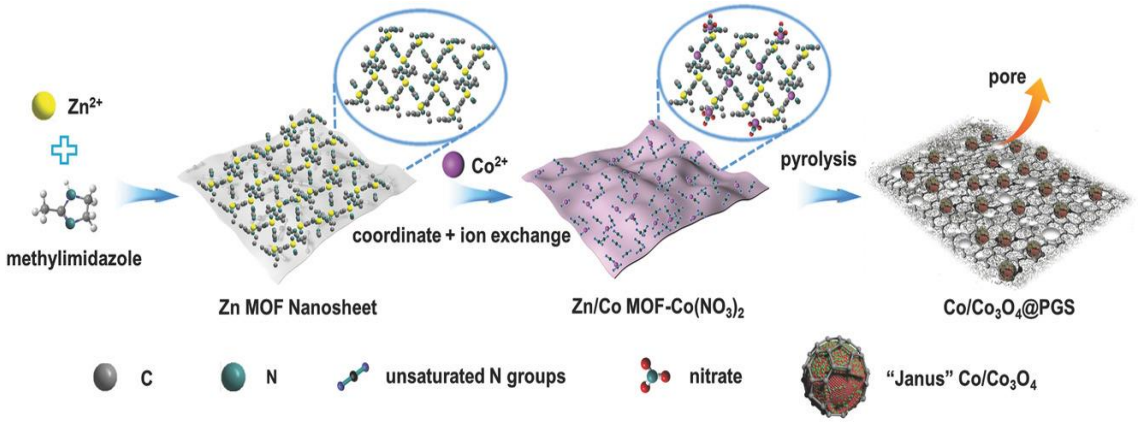

Figure 1.15: Synthesis procedure of a Co/Co_3O_4@PGS catalyst by interpenetration of Co and Co_3O_4 nanoparticles stitched in porous graphitized shells. The red areas represent metallic Co and the green areas represent Co_3O_4 in the "Janus" nanoparticles.[93]

structure.[95] Amongst the metal-free and heteroatom-doped carbon electrocatalysts, N-doped carbons are one of the most studied. A few examples, including carbon nanotubes (CNTs), nanofibers (CNFs), graphene, carbon nitride (C_3N_4), carbon black have presented ability to facilitate the catalytic process by promoting electron transfer and mass diffusion.[96–98]

The introduction of N atoms into the carbon framework perturbs the homogeneous π-electron cloud, changing the charge redistribution in the sp^2 conjugated carbon due to the large electronegativity difference between N and C atoms (X_N = 3.40 and X_C = 2.55 on the Pauling scale). Hence, the chemisorption mode of O_2 molecules is changed, enabling the attraction of electrons originated from the anode, subsequently improving the electrocatalytic activity.[99,100] Specifically, the electronic density of states near the Fermi level is increased, consequently helping the electronic transfer from the electronic bands of C to O σ*antibonding orbitals. In detail, electrons are donated from the catalyst surface to the empty or half-filled low-lying anti-bonding orbitals of O_2. This weakens or breaks the O-O bond to form either H_2O_2 or H_2O. Throughout this process, by applying a suitable potential, electrons with energy are supplied by the electrode to the level of $1\pi_g$ or $3\sigma_u$ orbital of O_2. But, if there is an electronic state around the Fermi level of the catalysts that matched the $1\pi_g$ or $3\sigma_u$ orbital of O_2 in energy, the electron transfer from the band to the orbital will be enabled. [101,102] Hence, the electrocatalytically active ORR center is not the N-doped site but the neighbouring C atoms.

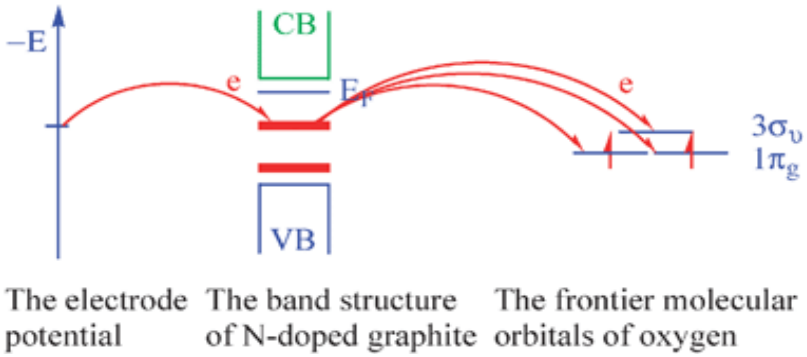

Figure 1.16: Representation of the electron transfer mechanism for the electrochemical ORR on N-doped graphite. CB refers to the conduction band and VB to the valence band. The bold lines in the gap indicate the electronic states. [101]

Once N is doped into carbon, different types of N sites can be formed (Figure 1.18). These include pyridinic N, pyrrolic N and quaternary N. The first indicates N atoms which are bonded to two other carbon atoms and are located at the edges of graphene planes, donating one p-electron to the aromatic π system. Pyrrolic N are those bonded to two carbon atoms included into five-membered heterocyclic rings, donate two p-electrons to the π system and are also located at the graphitic edge.[103] Quaternary N refers to those

replacing carbon atoms within the graphene layer and these can be located either at the edge or at the bulk of the carbon structure.[104] However, the overall contribution of the different N sites in the ORR and the optimum N concentration still remains unclear.

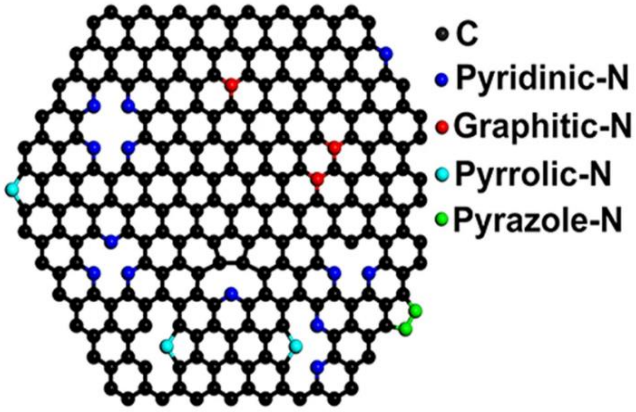

Figure 1.17: Different types of N-doping sites.[234]

An efficient method to prepare N-doped and ORR active carbons is through direct pyrolysis of N-rich carbon sources. A few examples include the nanoporous carbon fiber film catalytic electrode (denoted NCNFs) fabricated by Yao *et al.* by electrospinning of polyimide and further high-temperature pyrolysis. This flexible electrocatalyst exhibited large specific surface area and small charge-discharge voltage gap and outstanding stability when incorporated in the air cathode of a rechargeable ZAB.[105] Lot et al. also developed a metal-free mesoporous N-doped carbon electrocatalyst (denoted N/HPC) from the pyrolysis of enzymatic-treated wood with NH_4Cl (Figure 1.19)[106]. At 900˚C several N-doping sites (including both pyridinic and graphitic N) were created on the carbon framework leading to the formation of a highly ORR and OER active catalyst. Moreover, an N/HPC-based rechargeable ZAB exhibited an outstanding performance, including good charging and discharging behaviour and high stability.

Another outstanding metal-free and N-doped carbon electrocatalyst fabricated from the pyrolysis of ZIF-7 [$Zn(PhIM)_2.(H_2O)_3$; PhIM = benzimidazole] and glucose composites has been reported. This catalyst presented high porosity and surface area which endowed it with good ORR activity.[107]Additionally, defects in the basal plane and/or at the edges could "damage" the integrity of π conjugation and further contribute to the enhanced activity of carbon electrocatalysts. Defect regions in a sp^2-C matrix may induce a similar effect to that of heteroatom doping which induces charge polarization of carbon atoms, generating oxygen adsorption sites during the ORR.[108–110] Jeon et al

synthesised graphene nanoplatelets (GnPs) with selective edge defects from exfoliated pristine graphene through ball-milling.[111] The prepared edges with polar nature were found to primarily regulate the ORR performance of GnPs in alkaline electrolytes, despite the lack of heteroatom doping.

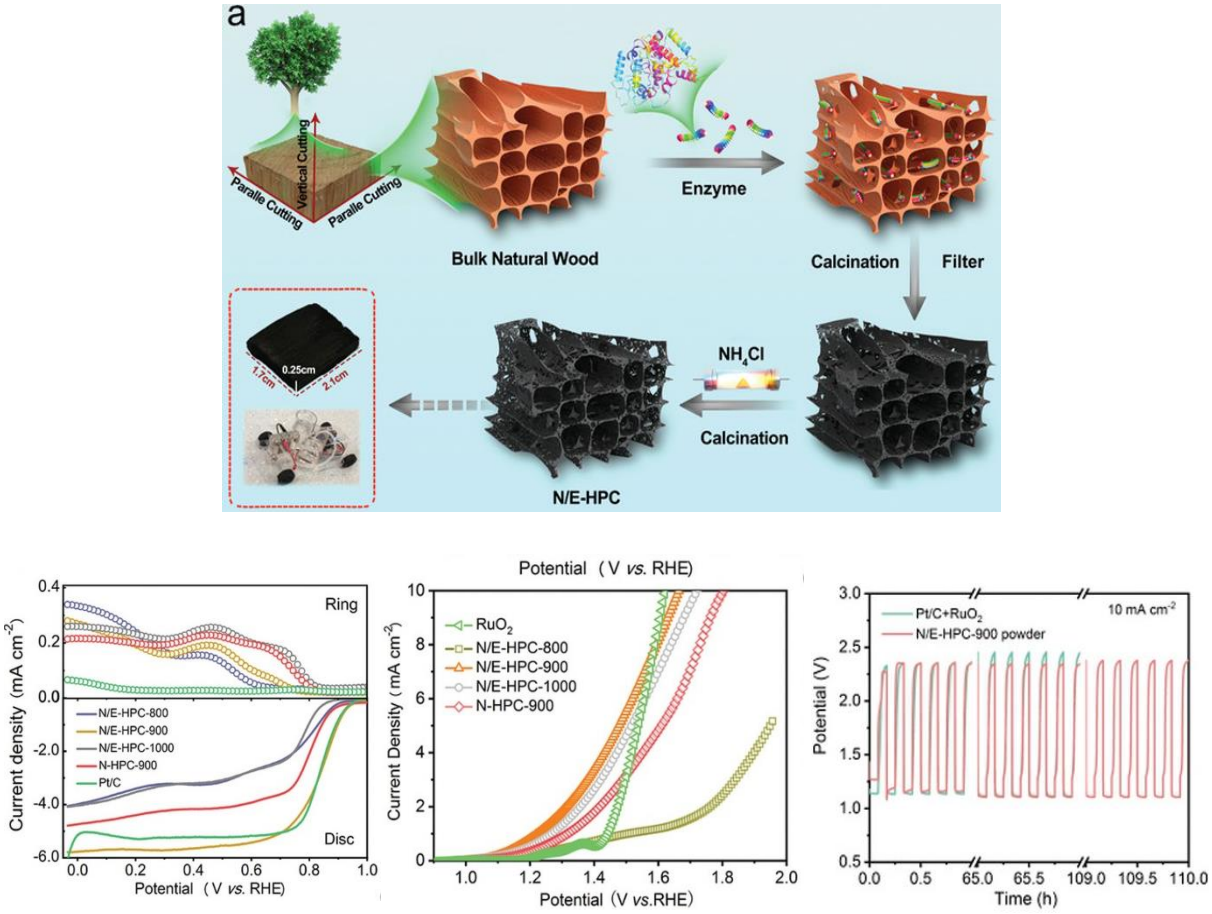

Figure 1.18: a) Schematic procedure depicting the transformation of raw wood into N-doped hierarchically porous catalysts through an enzyme-assisted method. b) RRDE results in O_2-saturated electrolyte at 1600 rpm. c) OER LSV curves of different catalysts at 1600 rpm in 0.1 M KOH.[106]

To evaluate the importance of edge and topological defects in the activity of nanocarbon oxygen electrocatalysts, Tang et al developed a defect-rich graphene mesh (GM) and a nitrogen-doped graphene mesh (NGM) through direct carbonization of sticky rice (carbon precursor), melamine (nitrogen source) and $Mg(OH)_2$ (template) (Figure 1.20).[112] The edges and topological defects were found to be more catalytically active than the N-doped sites. The adjacent carbon rings containing varied electron densities generate spatial curvature and form a permanent dipole moment. This dipole moment is weaker than the one between N and C atoms, thus a moderate adsorption and consequently a higher ORR activity is achieved. Zhao et al prepared a porous carbon

material composed of C and O atoms (PC-Zn-950) by carbonization of a Zn MOF.[113] The catalytic activity of PC-Zn-950 was attributed to the defect sites within the sp^2 carbon framework. The material presented comparable stability to the Pt/C benchmark catalyst.

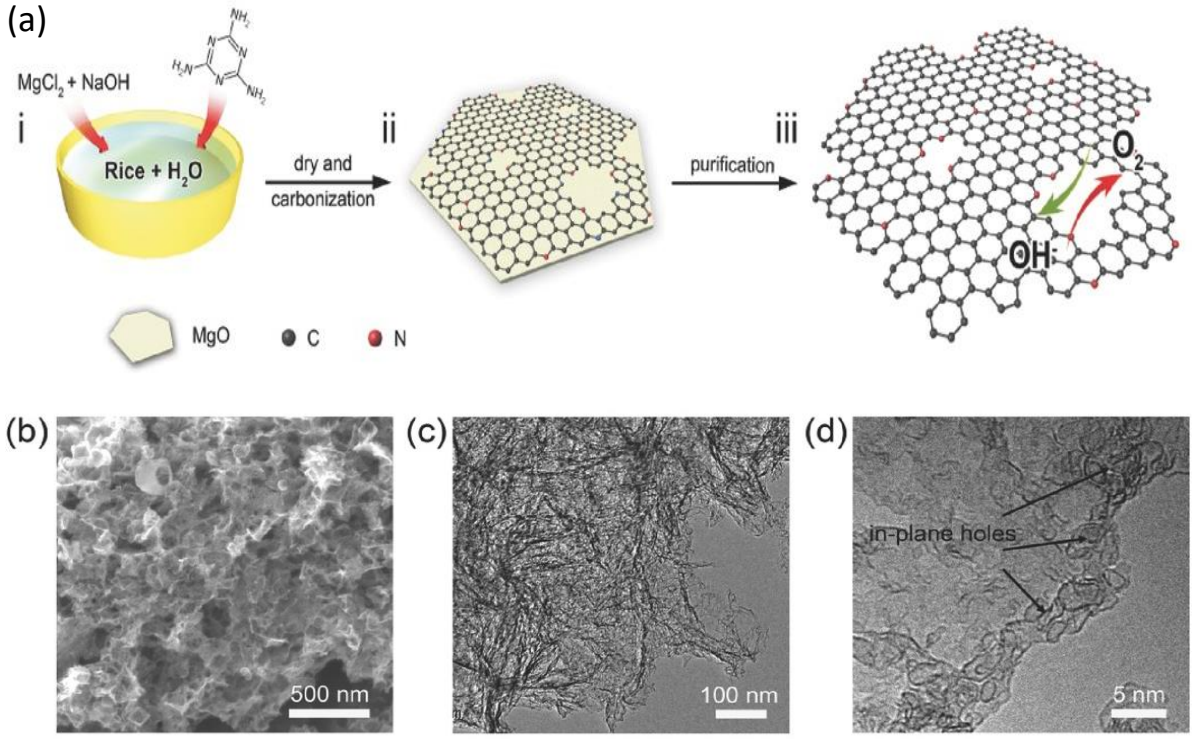

Figure 1.19: Synthesis procedure of NGM: i) in situ fabrication of ternary slurry from templates, a carbon and a nitrogen source. ii) NGM casting on MgO templates at 950˚C. iii) Removal of MgO templates and purification to obtain NGM. b) SEM image of the porous network. C) TEM image of the interconnected NGM nanoplates. D) High-resolution TEM image of the porous graphene nanosheets.[112]

1.4. Summary and Outlook

The sustainable development of energy conversion systems based on safe and cost-effective systems continues to be on the forefront of research efforts. Since LIBs have not been able to meet the modern demands of electrified transportation and grid-scale stationary energy storage, alternatives such as ZABs are being explored. However, a general concern involves the commercial use of precious metal-based ORR and OER electrocatalysts in ZABs, respectively Pt and Ir. Their scarcity, high cost and fast degradation, together with unsatisfactory long-term stability, limit the development and

commercialization of ZABs. As a consequence, great efforts have been focused on the development of alternative electrocatalysts with comparable performance to those of precious metals. Different studies on the ORR and OER and their electrocatalysts have been reported over the last decade, however, it remains a challenge to understand their reaction mechanisms and sluggish kinetics due to the complex protons/electron transfer process to the oxygen molecules, the O=O bond breaking and the active sites which are difficult to identify.[109]

In this thesis, the development of efficient ZAB air cathode catalysts is explored. Initially, focused on the optimization and investigation of a metal-free ORR electrocatalyst; then the bifunctional performance of a metal-containing catalyst; and finally, the improvement of the catalyst's stability and structural integrity during cell operation. The electrochemical behaviour and structure stability of the ZAB cathode electrocatalyst are both key parameters for the successful operation of the battery.

2. Characterization Techniques

Structural characterization techniques are essential to understand the structure of materials and correlate them with their properties, whilst electrochemical techniques help evaluate the performance of devices. A single technique is not enough to obtain a full analysis of the material under study and therefore a variety of characterization techniques are needed to analyse the electrode materials before and after they are incorporated into a device.

2.1. Structural characterization

Scanning electron microscopy (SEM) delivers information on the material's surface and its composition whereas transmission electron microscopy (TEM) provides information on the internal structure and morphology of the sample. The elemental composition of a material can be identified by energy-dispersive X-ray spectroscopy (EDS) where an EDS detector is incorporated to an electron microscope.

Furthermore, the chemical bonding and quantitative elemental information from a sample's surface can be obtained by X-ray Photoelectron Spectroscopy (XPS).

X-ray powder diffraction (XRD) is a technique that can provide detailed information about the crystal structure and chemical composition of the analysed sample. Diffraction occurs when the interaction between the X-rays and the sample satisfies Bragg's law: $n\lambda = 2d\sin\theta$. This law relates the wavelength of the beam (λ) to the diffraction angle (θ) and the lattice spacing (d) in a sample. The identification of plane spacings in a crystal lattice provides information on the sample's structure.

Raman spectroscopy provides information on the vibrational modes of molecules, revealing the structure of molecules. Specifically, Raman spectroscopy can help identifying hybridisation modes of carbon due to the observation of two bands, the D and G bands. The first one usually appears at around ~ 1350 cm^{-1} reflecting the defects and disorder from the out-of-plane sp^3 hybridised carbons and the second one appears at ~ 1580 cm^{-1} related to the in-plane sp^2 bonded graphitic carbon.

Another two important characteristics of electrode materials which can tune their electrocatalytic activity are the porosity and surface area. These may be measured based on the nitrogen sorption-desorption isotherms, Brunauer–Emmett–Teller (BET) theory

and the Barrett-Joyner-Halenda (BJH) method for surface area and pore size distribution, respectively.

The thermal stability of a material may be determined by thermogravimetric analysis (TGA) by monitoring the weight change occurring once a sample is heated at a certain constant rate. This method provides information on the physical and chemical properties of materials due to the different reactions taking place as the temperature is increased.

2.2. Electrochemical characterization

Cyclic voltammetry (CV) is an electrochemical technique commonly used to study the reduction and oxidation behaviour of molecular species.[54] In this thesis, CV was performed to study the behaviour of the developed ORR and OER catalyst electrodes. A cyclic voltammogram is obtained by cycling the potential of a working electrode and measuring the current that develops in the electrochemical cell. Typically, CV measurements are performed using a three-electrode setup (Figure 1.21) composed of a working electrode (WE), a counter electrode (CE) and a reference electrode (RE), all connected to a potentiostat. The current flows between the WE and CE while the RE accurately measures the potential applied relative to a stable reference reaction. This measurement is run at a set scan rate which determines how fast the applied potential is scanned, therefore, at a faster scan rate, the diffusion layer size is decreased and subsequently higher currents are observed.

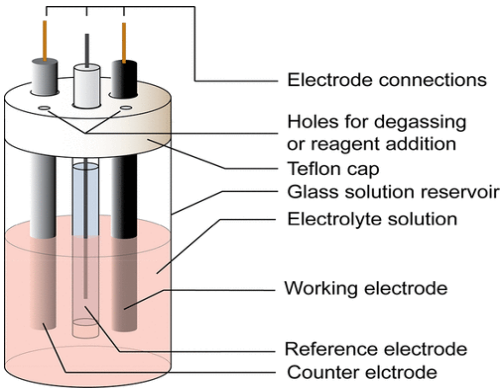

Figure 2.1: Schematic representation of a three-electrode electrochemical cell.

Similar to CV, linear sweep voltammetry (LSV) is another electrochemical technique, however, instead of linearly cycling over the potential range in both directions, LSV involves only a single linear sweep. This method is useful for irreversible systems.

Rotating-disk electrode (RDE) measurements are commonly used to practically assess the ORR and OER electrocatalytic performance. Certain activity parameters of the ORR reaction kinetics can be obtained from LSV curves by adhering the electrocatalysts to an RDE (Figure 1.22).[51] Typically, three different regions can be distinguished in the curve, depending on what drives the reaction. The first area is the kinetic-controlled area in which the reaction slowly proceeds as the current density slightly increases and the potential decreases. Then the reaction accelerates as the potential drops and the current density increases at the mixed kinetic- and diffusion-controlled area. Finally, in the diffusion-limited region, the diffusion rate of the reactants determines the current density, and the curve then reaches a platform at a certain rotation speed. The catalytic activity can be evaluated by some parameters such as the onset potential (E_{onset}), half-wave potential ($E_{1/2}$), overpotential (η_j), potential gap (ΔE), current density (J), and electron transfer number (n). The E_{onset} can be identified by the potential when the current deviates from the initial baseline and indicates the kinetic energy barrier that must be overcome for the reactions to proceed.[13] The $E_{1/2}$ is the potential at which the current density is equal to one half of the diffusion-limiting current. The more positive these potential values are, the more active is the catalyst. The η_j refers to the different between the theoretical and actual potential, it is the extra voltage required to carry out a non-spontaneous

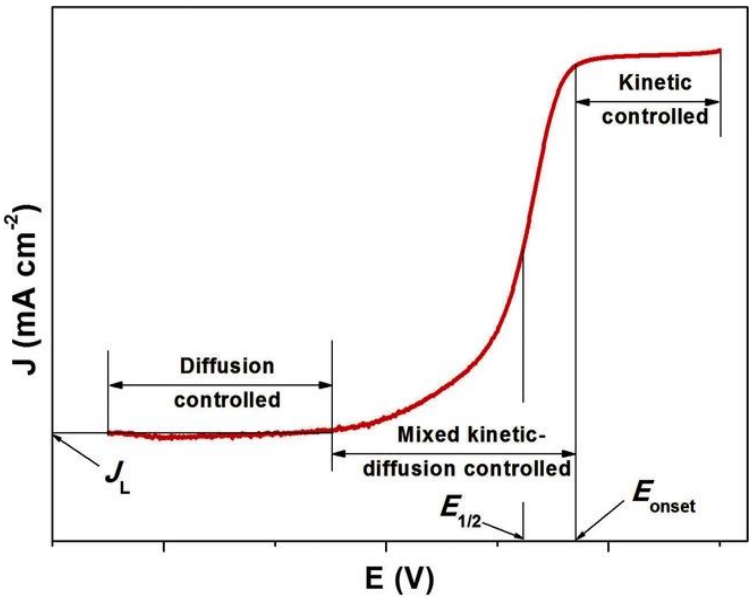

Figure 2.2: Typical LSV ORR polarization curve using a RDE.[51]

electrochemical reaction. The binding energies of the reaction intermediates deviate the catalytic activity from its ideal behaviour and therefore an overpotential is required.[48] The potential gap (ΔE) is measured between the ORR $E_{1/2}$ and the potential at a current density of 10 mA cm^{-2} for OER. Generally, a small potential gap is desired to obtain an improved bifunctional activity. Typically, the current density is normalized to the mass or surface area of the exposed catalysts, and it is a critical indicator of the practical performance of the catalyst.

The electron transfer number indicates whether the ORR mechanism occur through a direct four-electron pathway or a two-electron pathway involving the formation of peroxide. Following the LSV results measured by RDE, the number of electrons (n) transferred per O_2 molecule in ORR can be calculated from the Koutecky-Levich (K-L) equation as follows:

$$\frac{1}{J} = \frac{1}{J_L} + \frac{1}{J_K} = \frac{1}{B\omega^{1/2}} + \frac{1}{J_K} \quad (1)$$

$$B = 0.2nFC_0(D_0)^{2/3}\nu^{-1/6} \quad (2)$$

$$J_K = nFkC_0 \quad (3)$$

Where J is the measured current density, J_k and J_L are the kinetic limiting and diffusion limiting current densities, respectively, B is the Levich constant (determined by the inverse value of the slope of a straight linear fitting of the measured current densities, ω is the angular velocity of the electrode, F is the Faraday constant (96485 C mol^{-1}), C_0 is the concentration of dissolved O_2 in electrolyte solution (1.2×10^{-6} mol cm^{-3}), D_0 is the O_2 diffusion coefficient in KOH solution (1.9×10^{-5} cm^2 s^{-1}) and ν is the kinetic viscosity of the electrolyte solution (0.01 cm^2 s^{-1}).

The electrochemical surface area (ECSA) of a catalyst is proportional to the electrochemical double-layer capacitance (C_{dl}) at the catalyst-electrolyte interface and it can be determined from CV.[114] In a non-Faradaic potential region, charge transfer electrode reactions are considered negligible and therefore the measure current is assumed to be originated from the double layer charging. Considering this assumption, the charging current (i_c) can be calculated according to the following equation:

$$i_c = \nu C_{dl}$$

Where ν is the scan rate. The charging current can be plotted as a function of ν and the slope of the straight line originated is equal to the C_{dl}.

Furthermore, the performance of zinc-air batteries (battery structure described in Chapter 1.3.1.) containing the developed electrocatalyst cathode materials may be tested with a battery tester by galvanostatic cycling and then observing their charging and discharging behaviours or by evaluating the long-term discharging stability of the cell. A constant value of current density is set and a voltage versus time plot is obtained.

2.3. Experimental methods

2.3.1. Synthesis of carbon nitride (g-C_3N_4)

C_3N_4 was obtained by thermal polymerization of melamine. Typically, melamine (10 g) was placed in a porcelain crucible and heated to 550 °C at a ramping rate of 5 °C/min and kept at 550 °C for 4 h under Ar atmosphere. The sample was naturally cooled to room temperature and C_3N_4 was obtained with a yield of approximately 50%.

2.3.2. Synthesis of carbon nitride and dopamine-derived electrocatalysts (CNDA)

CNDA was synthesized by polymerization of dopamine in the presence of C_3N_4 followed by carbonization. The polydopamine was prepared according to a previously reported study.[77] In order to find the optimum catalyst based on its performance, different precursor combinations were prepared and electrochemically tested under the same conditions. Therefore, the concentration of dopamine hydrochloride was kept constant at 1 mg ml^{-1} while varying the concentration of C_3N_4 in solution between 0.2, 0.5, 1, 1.5 and 2 mg ml^{-1}. A certain concentration of the as-prepared C_3N_4 was dispersed in 500 mL of 10 mM Tris-buffer solution (pH = 8.5) and the mixture was left to stir for 30 min. Subsequently, 0.5 g of dopamine hydrochloride (1 mg ml^{-1}) was added to the mixture and left to stir for another 20 h. The product was collected by centrifugation, repeatedly washed with deionized water and dried in an oven at 70 °C overnight. Following this, different carbonization parameters were evaluated in order to obtain the ideal

electrocatalyst. The dried sample was carbonized in a furnace at varied temperatures of 850, 900 and 950 °C, heated at a ramping rate of 5 °C/min (parameter kept constant) and held at a certain temperature for 30 min, 1 h or 2 h under Ar atmosphere.

Initially, when optimizing the concentration ratios (0.2, 0.5, 1, 1.5 and 2 mg ml^{-1}), the samples were all tested at a temperature of 900 °C, heated at a ramping rate of 5 °C/min and then held for 2 h under Ar atmosphere. These samples were denoted 0.2CN-DA, 0.5CN-DA, 1 CN-DA, 1.5CN-DA and 2CN-DA. According to the electrochemical results, the optimum C_3N_4 ratio concentration was found to be 1 mg ml^{-1} (1CN-DA), so this was kept for further studies. Following the precursors concentration, the carbonization time was evaluated. While keeping the concentration at 1 mg ml^{-1} and the temperature at 900 °C, the heating time was varied between 30 min, 1 h and 2 h and the electrochemical performance dictated that the catalyst worked best when the heating time was kept at 1h. The samples were denoted 30min-CNDA, 1h-CNDA and 2h-CNDA. Finally, following the previous conclusions, the carbonization temperature was then varied between 850, 900 and 950 °C. The final products were denoted CNDA850, CNDA900 and CNDA950, respectively. CNDA900 refers to the N-rich carbon hybrid catalyst synthesized at 900 °C, for instance. For comparison, carbonized-PDA (CPDA) was synthesised following the same procedure described above but without the C_3N_4 addition.

2.3.3. Synthesis of a bifunctional electrocatalyst composed of Co/N nanoparticles obtained from ZIF-67 supported a C_3N_4/PDA framework (ZIFCNDA)

An aqueous solution containing the previously prepared C_3N_4 (0.45 mg cm^{-3}) was stirred for 30 min and then bath sonicated for 15 min. Subsequently, 75 mg of dopamine hydrochloride (0.3 mg cm^{-3} in the final solution) were added to the as-prepared C_3N_4 solution and stirred for 15 min. A solution containing $Co(NO_3)_2.6H_2O$ at a mole ratio of 2:1 ($Co(NO_3)_2.6H_2O$:Dopamine) was added to the previously prepared solution and stirred for 15 min. Then, 1.21 mg cm^{-3} of trizma base were added to the solution under vigorous stirring to trigger dopamine polymerisation. After 4 h of mild stirring, 100 ml of an aqueous solution of 2-methylimidazole (0.35 mg cm^{-3}) was added and the mixture stirred for 20 min. The product was finally collected by centrifugation (10 min at 8000 rpm) and repeatedly washed with deionized water and ethanol. After overnight oven

drying, the material was pyrolyzed at 900 °C for 2h, at a ramping rate of 5 °C min^{-1} in N_2 atmosphere (ZIFCNDA). For comparison, ZIFCNDA samples with different $Co(NO_3)_2.6H_2O$:Dopamine ratios of 0.5, 1 and 5 were prepared and the products denoted ZIFCNDA-0.5, ZIFCNDA-1 and ZIFCNDA-2. Accordingly, the intermediates, polydopamine (CPDA), carbon nitride/polydopamine (CNDA) and cobalt-doped carbon nitride/polydopamine (Co-CNDA) were synthesised following the procedure above. CPDA was prepared without the addition of C_3N_4, $Co(NO_3)_2.6H_2O$ and 2-methylimidazole; CNDA without the addition of $Co(NO_3)_2.6H_2O$ and 2-methylimidazole and Co-CNDA without the addition of 2-methylimidazole.

2.3.4. Preparation of ZIF-67 and C-ZIF-67

Following a typical synthesis procedure, two distinct solutions of $Co(NO_3)_2.6H_2O$ in (0.023 g ml^{-1}) and 2-methylimidazole (0.025 g ml^{-1}) in methanol were prepared.[115] Equal volumes of the two solutions were mixed under vigorous stirring and a blue-violet solution was instantly formed, indicating the formation of coordination bonds between the Co^{2+} centers and the N from the 2-MeIM ligands. The mixture solution was stirred for 20 min and then rested for 12 h. Finally, violet precipitate was collected by centrifugation and methanol washing, followed by vacuum drying at 80˚C for 2h. Finally, a bright purple powder of ZIF-67 was obtained. The pyrolysis of ZIF-67 was carried out in a tube furnace at a ramping rate of 5˚C min^{-1} and kept at 850˚C for 1h, under an argon atmosphere. The pyrolyzed ZIF-67 sample was denoted C-ZIF-67.

2.3.5. Synthesis of a porous bifunctional catalyst composed of pyrolyzed ZIF-67 particles encapsulated into polydopamine coated nanofibers (C-ZIF-67:PS-1-X)

2.3.5.1. Preparation of ZIF-67 and Polystyrene suspension for electrospinning

Polystyrene (Mw 350,000, Sigma-Aldrich) was added to dimethylformamide (DMF), vigorously stirred at 350 rpm for 5h at 60˚C to form a solution with a

concentration of 0.30 g ml^{-1} and then allowed to cool to room temperature. Separately, a suspension was prepared by adding previously prepared ZIF-67 powder to DMF, vigorously stirring for 30 min, followed by probe ultrasonication for 1h and further stirring for another 30 min. Afterwards, the ZIF-67 suspension was mixed with the polystyrene solution and stirred overnight. A final mixture containing a 1:1 ratio of ZIF-67:PS was obtained. For comparison, suspensions with 0.5:1 and 2:1 ratios of ZIF-67:PS were also prepared.

2.3.5.2. Preparation of electrospun PS and ZIF-67 composite fibers (C-ZIF-67:PS-X)

The previously prepared DMF suspension containing PS and ZIF-67 was loaded into a syringe and mounted with a 22-gauge blunt needle tip. The mixture was electrospun at a feeding rate of 0.6 ml h^{-1}, under a working voltage of 18 kV, and a spinneret width and speed of 30 mm and 10 mm sec^{-1}, respectively. The fibers were collected into an ethanol bath and a distance of 20 cm was kept between the needle tip and ethanol surface. The fibers prepared from a suspension containing a 1:1 ratio of ZIF-67:PS, were denoted ZIF-67:PS-1. The fibers obtained from suspensions with 0.5:1 and 2:1 ratios of ZIF-67:PS were named ZIF-67:PS-0.5 and ZIF-67:PS-2, respectively. The samples pyrolyzed in a tube furnace at a ramping rate of 5˚C min^{-1} and kept at 850˚C for 1h, under an argon atmosphere, were denoted C-ZIF-67:PS-0.5, C-ZIF-67:PS-1 and C-ZIF-67:PS-2 (C-ZIF-67:PS-X).

2.3.5.3. Preparation of carbonized PDA coated ZIF-67:PS-1 fibers (C-ZIF-67:PS-1-XDA)

The previously prepared ZIF-67:PS-1 fibers were transferred to a 0.5 mg ml^{-1} aqueous solution of dopamine, shook for 20 min and allowed to rest for another 40 min. The coating of the prepared fibers was triggered by in situ polymerization of DA by addition of 1.21 mg ml^{-1} of trizma base under continuous shaking for 20 min and subsequent rest for 2h40. This coating procedure was repeated for another 3 times using fresh solutions to achieve a series of coating layers. Thereafter, the fibers were washed with DI water and freeze dried for 48 h. Finally, the coated ZIF-67:PS-1 fibers were annealed under argon environment at a ramping rate of 5˚C min^{-1} and kept at 850˚C for

1h. The pyrolysis temperature is usually set in between 700 and 900˚C, since a low temperature may lead to an insufficient carbonization degree and therefore reduce the conductivity and a high temperature may lead to a loss of the precursor's structure, reducing the generation and exposure of catalytically active sites.[116] The annealed samples were denoted as C-ZIF-67:PS-1-1xDA, C-ZIF-67:PS-1-2xDA, C-ZIF-67:PS-1-3xDA and C-ZIF-67:PS-1-4xDA (C-ZIF-67:PS-1-XDA).

2.3.6. Structural characterization

Images of the morphologies and elemental mappings were obtained by a Field Emission-Scanning Electron Microscope (FE-SEM, JSM-7600F, 5-10 kV), an Energy Dispersive X-Ray (EDS equipped on the SEM, Oxford INCA), a Transmission Electron Microscope (TEM, Philips CM300, 300 kV), Jeol-2100 TEM (200 kV) or a FEI G2 F20 X-Twin Transmission Electron Microscope (200 kV), equipped with an Elite-T silicon drift detector (1.0sr solid angle, 70 mm2 SDD) for energy dispersive X-ray spectroscopic mapping (EDS). All samples were gold coated (10 µA for 30 seconds) before observation under the FE-SEM. Image J was used to view the images collected and obtain size measurements. The chemical compositions were investigated by X-ray Photoelectron Spectroscopy (XPS) using a Thermo Fisher Scientific Theta Probe electron spectrometer (VG ESCALAB200i-XL) with Al Kα X-ray source and a flood gun for charge compensation. The measured signals were evaluated using the CasaXPS software, using a Shirley background (70 % Gaussian/30 % Lorentzian). The binding energies were calibrated using C 1s peak at 284.4 eV. The crystallinity and phase composition of the samples were studied by X-ray Diffraction (XRD, Bruker D8 Discover GADDS with Cu K_α radiation, reflection mode or Stoe StadiP, Cu K_α) and Raman spectroscopy (WITec alpha300-R, 532 nm laser excitation). The Brunauer−Emmett−Teller (BET) surface area and pore size distribution were obtained from the nitrogen adsorption−desorption isotherms and the Barrett-Joyer-Halenda (BJH) method by using an Automatic High Resolution Physisorption Micropore/Mesopore Analyzer (ASAP2020MP MICROMERITICS).

2.3.7. Electrochemical characterization and calculations

The electrocatalytic activity of the synthesised catalysts was investigated by Cyclic Voltammetry (CV) and Linear Sweep Voltammetry (LSV) measurements acquired from a Metrohm Autolab potentiostat/galvanostat (PGSTAT302N) station using a three-electrode system consisting of a Ag/AgCl (in saturated KCl) reference electrode, a Pt-foil or a graphite rod counter electrode and a glassy carbon working electrode (GC, 5 mm diameter). 0.1 M KOH solution saturated with O_2 or N_2 was used as the electrolyte. The working electrode was prepared by adding 10 mg of catalyst to a solution containing 1.47 mL of deionised water, 0.73 mL of EtOH and 0.5 mL of Nafion (5 wt% in alcohol and water) and sonicating it for 30 min to obtain a homogenous ink. An aliquot (8.3 µL) of this ink was drop-cast onto the GC electrode surface to obtain a theoretical catalyst loading of 0.2 mg cm^{-2}, unless otherwise stated. Pt/C and Ir/C electrodes were also prepared following the same procedure. From the LSV results, the number of electrons (n) transferred per O_2 molecule in ORR was calculated from the Koutecky-Levich (K-L) equation as follows:[117]

$$\frac{1}{J} = \frac{1}{J_L} + \frac{1}{J_K} = \frac{1}{B\omega^{1/2}} + \frac{1}{J_K} \quad (1)$$

$$B = 0.2nFC_0(D_0)^{2/3}\nu^{-1/6} \quad (2)$$

$$J_K = nFkC_0 \quad (3)$$

Where J is the measured current density, J_k and J_L are the kinetic limiting and diffusion limiting current densities, respectively, B is the Levich constant (determined by the inverse value of the slope of a straight linear fitting of the measured current densities), ω is the angular velocity of the electrode, F is the Faraday constant (96485 C mol^{-1}), C_0 is the concentration of dissolved O_2 in electrolyte solution (1.2×10^{-6} mol cm^{-3}), D_0 is the O_2 diffusion coefficient in KOH solution (1.9×10^{-5} cm^2 s^{-1}) and ν is the kinetic viscosity of the electrolyte solution (0.01 cm^2 s^{-1}). Both CV and LSV measurements were recorded with reference to the Ag/AgCl electrode. The potentials recorded by Ag/AgCl reference electrode potentials were calibrated with respect to the RHE potential according to the Nernst equation:

$$E_{RHE} = E_{Ag/AgCl} + 0.059pH + E^o_{Ag/AgCl} \quad (4)$$

Where E_{RHE} is the potential converted, $E_{Ag/AgCl}$ is the experimentally measured potential against the Ag/AgCl reference, the measured pH was 13 and $E^{o}_{Ag/AgCl} = 0.1976$ at 25 ˚C.[118,119]

2.3.8. Zinc-air battery fabrication

The Zn-air cells were assembled using a polished zinc plate as the anode, an air cathode containing the developed catalysts or the benchmark Pt/C or Ir/C catalyst and a 6 M KOH aqueous solution containing 0.1 M $ZnCl_2$ as the electrolyte. For the preparation of the cathode ink, a solution containing 50 mg of active catalyst and 10 mL of an aqueous Nafion solution (1 wt.%) was sonicated for 30 min. Then, this solution with calculated amount was drop-casted onto a carbon paper (Sigracet 38BC) to obtain a catalyst loading of 0.5 mg cm^{-2}. The electrode was then dried overnight at room temperature. The discharge and discharge-charge performances of ZABs were evaluated by the galvanostatic method on a battery tester (NEWARE BTS-610).

3. Developing N-Rich and Metal-Free Carbon from C_3N_4-Polydopamine Composites for Efficient Oxygen Reduction Reaction

3.1. Introduction

In recent years several studies have focused on investigating alternative electrocatalysts with comparable performances to those of commercially available precious metals. Promising developments have been observed on carbonaceous materials enriched with heteroatoms such as N, S, P and B.[120–122] The low cost and more environmentally friendly nature of carbon-based composites together with their high surface area, easy tailoring and good electronic conductivity make these ideal alternatives for ORR electrocatalysts. Furthermore, the introduction of nitrogen (N) within carbon nanostructures can induce charge polarisation on the carbon atoms leading to narrowing of the band gap and enhanced electron mobility, and improvement of the ORR performance by promoting the adsorption and reduction of oxygen.[99,100]

The post-doping method is the main reported approach to prepare N-doped carbon catalysts by incorporating N-functionalities into the highly stable carbon framework.[123] These synthesis methods normally involve hydrothermal synthesis, acid exfoliation or surface functionalization with gas which often include the use of autoclaves, harsh chemicals and long and unsafe processes. In such processes only surface doping is normally achieved, limiting the scalable production of these materials.[121,124–127] *In situ* direct doping methods, on the other hand, involve less harsh synthesis procedures, but the nitrogen concentration achieved is typically low (below 9 at.%) or hidden in the bulk of the sample , limiting the number of redox active centres.[126,128] Additionally, templates such as silica, cellulose and polystyrene are commonly employed to control the surface morphology and increase the surface area, which have to then be removed, usually by immersion in organic solvents or by toxic solvents such as HF.[129–131] In this chapter, a synthesis procedure for the facile preparation of a catalytically active, metal-free and nitrogen-rich composite was developed, without the use of toxic chemicals and severe conditions, hence providing a more environmentally material process.

A carbon-based electrocatalyst with a high nitrogen concentration (12.5 at.%), was successfully prepared following a (desirable) template-free process. Carbon nitride (C_3N_4) and dopamine (DA) precursors originated non-metal containing nitrogen-rich carbon nanosheets and nanospheres, respectively (the electrocatalyst, CNDA). The formulation based on two benign and scalable C,N-based based precursors led to the formation of a highly active and durable ORR catalyst with exposed and stable active sites. The naturally nitrogen-rich content (47.75 at.%) of C_3N_4 promotes the formation of a highly N-doped carbon catalyst, which demonstrated successful interactions with the ORR intermediates. Additionally, C_3N_4 also served as a porogen and a surface template for the growth of dopamine (DA). C_3N_4 is synthesised by a facile, scalable, high yield and safe procedure, unlike other common N-doped carbons[132,133] and there is no requirement for post-doping or the removal of metal impurities. However, despite these advantages, the low electrical conductivity and subsequent slow charge transfer of C_3N_4 diminishes its electrocatalytic ability.[134] Polydopamine (PDA) is an N-containing biopolymer commonly found in mussels to facilitate their firm adhesion to surfaces. Therefore, its tendency for surface functionalization and electrophilicity is highly desirable. Dopamine instantly self-polymerizes, forming PDA at room temperature in a mild and alkaline medium. No severe conditions or the use of catalysts is required to perform this reaction, unlike in preparation of commonly used polymers of aniline,

pyrrole and o-phenylenediamine, to name but a few.[135] The formation of stable carbon layers by pyrolysis of the PDA coating may boost electrical conductivity and stability, promoted by the enhanced electron mobility of the active materials, naturally increasing the performance of oxygen electrocatalysts.[136] Additionally, when no PDA was added to the mixture, the C_3N_4 completely decomposed at the same pyrolysis conditions The introduction of PDA was found to promote the doping of extra nitrogen features from species originated from the decomposition of C_3N_4.[137–139] The high temperature pyrolysis (900 °C) of a C_3N_4/PDA mixture afforded the fusion of the two carbon-based precursors, resulting in an efficient nitrogen-doped nanocarbon ORR electrocatalyst.

3.2. Results and discussion

3.2.1. Preparation and structural characterization

Scheme 3.1 represents the synthesis procedure of the CNDA N-rich carbon catalyst (refer to Sections 2.3.1 and 2.3.2). Firstly, carbon nitride was obtained by thermal polymerization of melamine. Then, during the spontaneous oxidation polymerization reaction of DA to form PDA it can adhere to the surface of the previously prepared C_3N_4 layers originating the C_3N_4-PDA composite. The carbonization of the composite at a temperature of 900 °C under Ar-gas led to the fusion of the structures producing the CNDA900 composite.

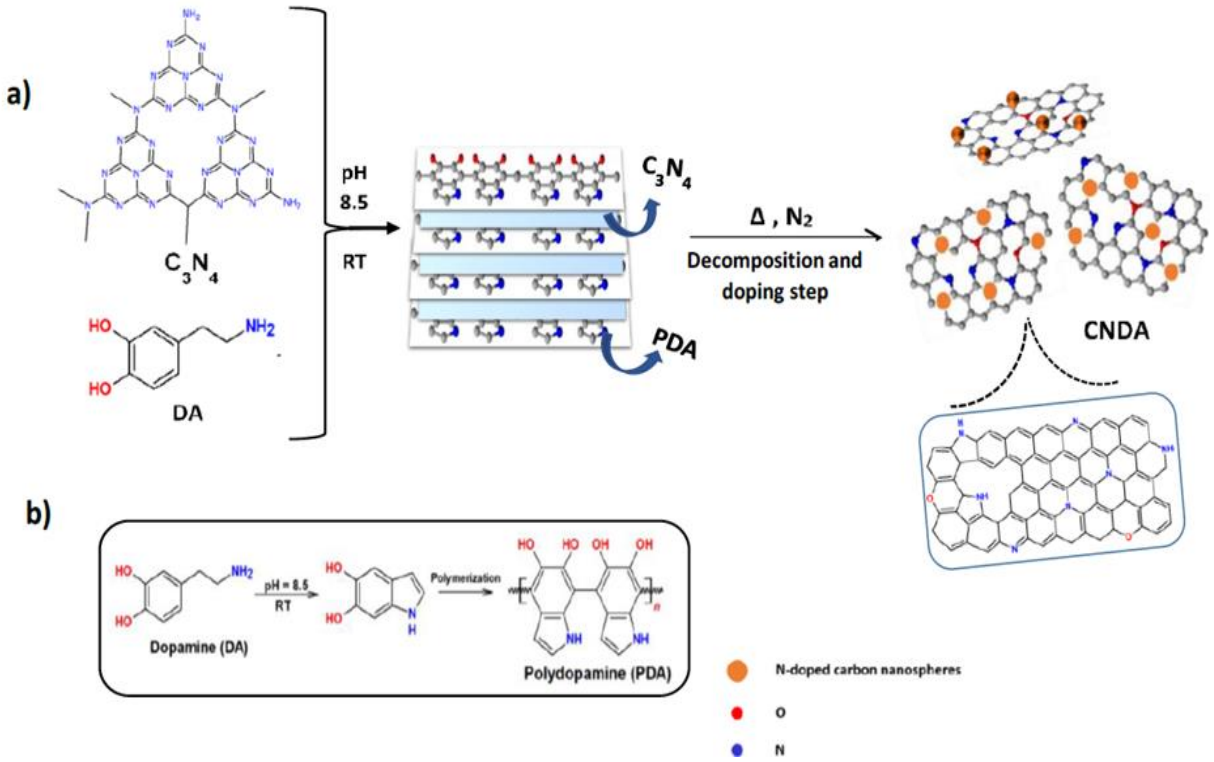

Scheme 3.1: Schematic representation of the fabrication of the CNDA catalysts and b) the polymerization of dopamine (DA) to form polydopamine (PDA).

Table 3.1: Experimental details for the synthesis of the different materials prepared.

Material	Synthesis conditions
C_3N_4	1) Thermal polymerization of melamine: 10 g of melamine was placed in a porcelain crucible and heated to 550 °C at a ramping rate of 5 °C/min and kept at 550 °C for 4 h under Ar atmosphere.
X-CNDA (X = 0.2, 0.5, 1, 1.5 or 2)	1) A certain concentration (0.2, 0.5, 1, 1.5 or 2 mg ml^{-1}) of the as-prepared C_3N_4 was dispersed in 500 mL of 10 mM Tris-buffer solution (pH = 8.5) and the mixture was left to stir for 30 min. 2) Then, 0.5 g of dopamine hydrochloride (1 mg ml^{-1}) was added to the mixture and left to stir for another 20 h. 3) Product collection by centrifugation, repeated washing with deionized water and drying in an oven at 70 °C overnight. 4) Sample pyrolysis at 900 °C: heating at a ramping rate of 5 °C/min and then held for 2 h under Ar atmosphere. The obtained samples were denoted 0.2CN-DA, 0.5CN-DA, 1 CN-DA, 1.5CN-DA and 2CN-DA. 5) Carbonization time optimization: using 1CN-DA and a carbonization temperature of 900 °C, the heating time was varied (30min-CNDA, 1h-CNDA and 2h-CNDA). The electrochemical performance dictated that the catalyst worked best when the heating time was kept at 1h. 6) Carbonization temperature optimization: variation between 850, 900 and 950 °C (CNDA850, CNDA900 and CNDA950) 7) Carbonized-PDA (CPDA) was synthesised following the same procedure (900 °C, 5 °C/min 2h) but without C_3N_4 addition.

SEM and TEM were used to observe the structures and morphologies of the bulk C_3N_4, carbonized-PDA (CPDA) and the CNDA catalysts and EDX revealed their elemental distribution through elemental mappings. As observed in **Figure 3.1a**, the bulk C_3N_4 demonstrated a typical aggregated morphology, but also included some stacked nanosheet structures indicating some level of exfoliation due to the high temperature

carbonization. In **Figure 3.1b**, the structure of the CPDA appears to contain a uniform distribution of spherical structures sized about 200 nm. The formation of uniformly distributed nanospheres across structured layers is revealed on the SEM image (**Figure 3.1d)** of the developed CNDA900 catalyst. Nonetheless, an annealing temperature of 950 °C created over-exfoliated nanosheets with observably large clusters (**Figure 3.2**). These may result from folded carbon layers that subsequently reduce the active sites' availability and limit the oxygen reduction reaction.[140,141] At an annealing temperature of 850 °C the SEM and TEM images of the CNDA850 catalyst (**Figures 3.3**) revealed incomplete carbonization, confirmed by the uneven distribution of nanoparticles with various sizes (~ 150-250 nm) on the surface of a dense structure. The pyrolysis temperature was found to play an essential role of on the surface structure formation of the composites, which controls their catalytic activity. The CNDA900 was composed of well-shaped and size controlled (~190 nm) nanospheres interconnected with thinner and well-defined nanolayers as observed in the TEM (**Figure 3.1c)**. The decreased number of nanospheres and improved nanosheet scattering indicated the successful conversion of the reaction intermediates into an N-doped carbon framework and the crucial role of C_3N_4 as a surface growth template. This catalytic surface configuration is expected to favour faster electron and mass transport.[142]

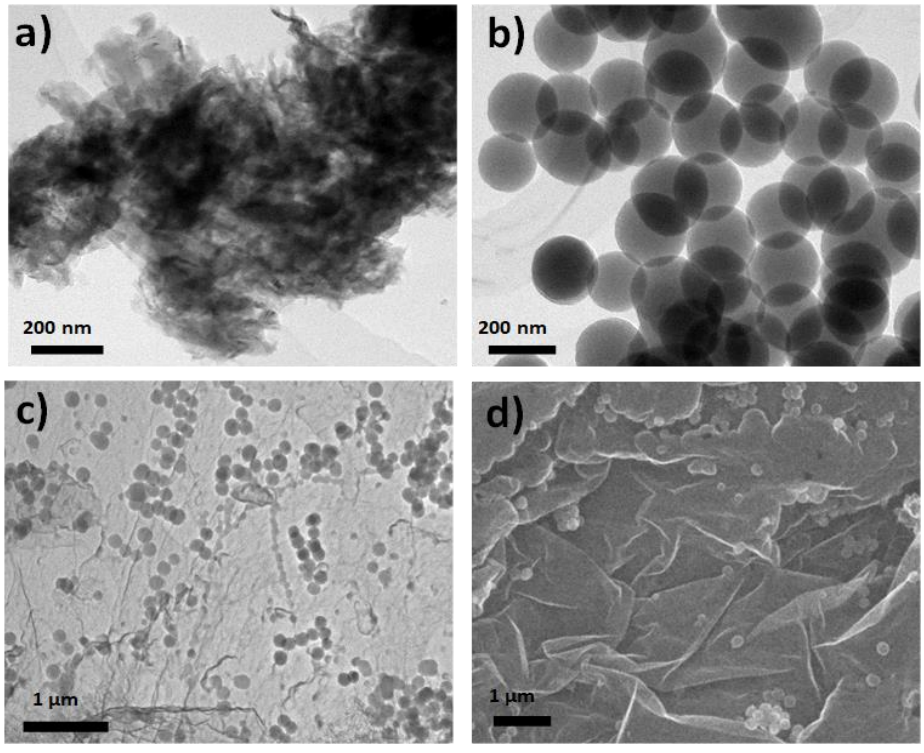

Figure 3.1: TEM images showing the morphologies of a) C_3N_4, b) CPDA and c) CNDA900. d) SEM image of CNDA900.

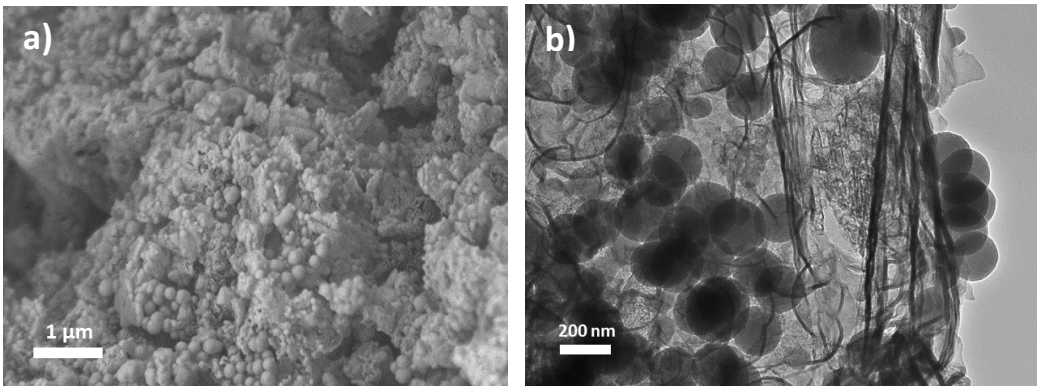

Figure 3.2: Morphologies of CNDA850: a) SEM image and b) TEM image.

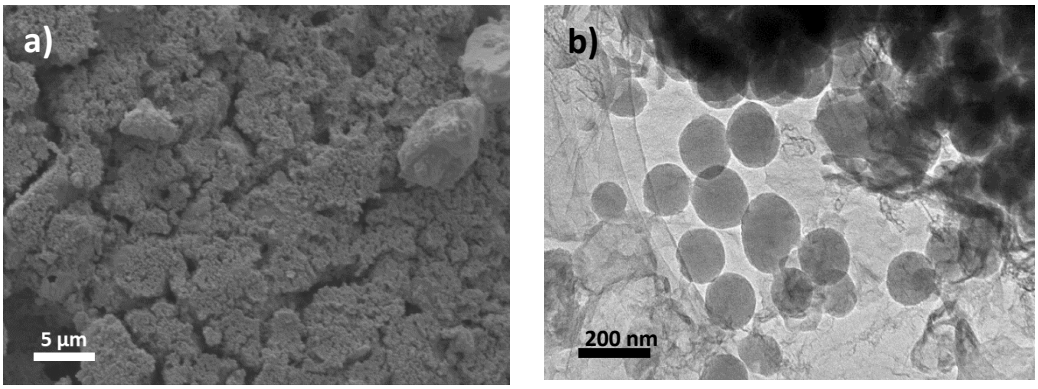

Figure 3.3: Morphologies of CNDA950: a) SEM and b) TEM.

A uniform distribution of C, N and O is observed on the elemental distribution maps of CNDA900 (Figure 3.4). A desirable synergistic effect induced by the doping of elements with distinctly different electronegativities (to carbon) has been reported to promote the activation of catalytic sites across the catalyst's surface.[143,144] C_3N_4 allowed the controlled surface growth of polymerized DA but it also clearly contributed as a nitrogen source for the synthesis of CNDA900. The fusion of the precursors led to the chemical rearrangement of the carbon and heteroatoms, producing an N-rich carbon composite. The PDA aided the stabilization of C_3N_4, avoiding its decomposition and therefore benefiting from its rich N content.

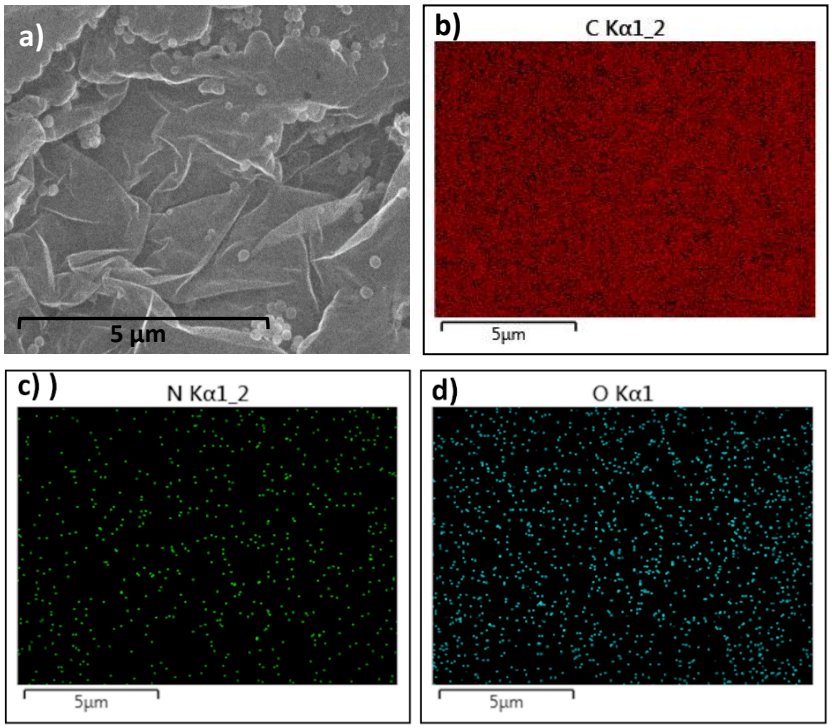

Figure 3.4: SEM image (a) of CNDA900 and the corresponding EDX elemental distribution of C (b), N (c) and O (d).

Sample	Elemental Composition (at. %)		
	C	N	O
C_3N_4	47.2	49.3	3.4
CPDA	93.1	5.3	1.5
CNDA850	82.7	12.1	5.2
CNDA900	83.4	12.5	4.1
CNDA950	91.3	6.3	2.4

Table 3.2: Elemental compositions obtained from the XPS C1 s, N 1s and O 1s high resolution spectra of CPDA, C_3N_4 and CNDA900.

XPS analysis was used to identify the elemental and chemical environment stoichiometries of C_3N_4, CPDA and the CNDA catalysts. The XPS survey spectra presented in Figure 3.5 and Table 3.2 suggest that both precursor materials, CPDA and C_3N_4, and the CNDA catalysts' surfaces are composed of C, N and O. As the annealing temperature was increased, the nitrogen content decreased. A high nitrogen content of 12.5 at.% was found on the surface composition of CNDA900. This is greatly improved in comparison to other reported nitrogen-doped carbon electrocatalysts.[145–147] These results reveal the adherence of CPDA to C_3N_4 as CPDA was only found to contain 5.3

at.% of N. An increased annealing temperature to 950 °C greatly reduced the N content to 6.3 at.%. Studies by Wiggins-Camacho et al. and others have shown that the increased N-doping level increases bulk electrical conductivity, density of states at the Fermi level and improves ORR activity.[148–150]

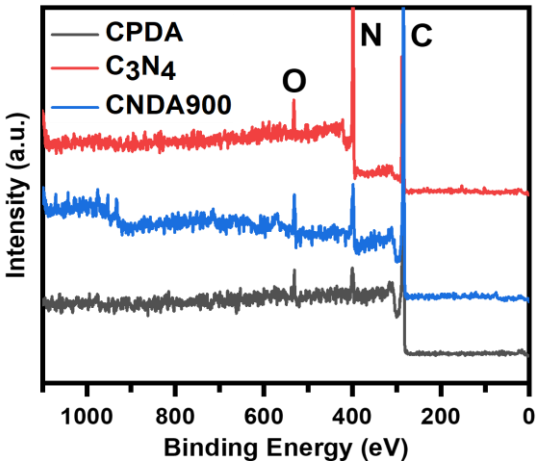

Figure 3.5: XPS survey spectrum of CPDA, C_3N_4 and CNDA900.

Figure 3.6a shows the C1s XPS spectra of CPDA, C_3N_4 and CNDA900. The C1s XPS spectrum of CPDA was deconvoluted into four peaks at 284.4 (sp^2 C), 285.6 (C-O and C=N), 287.1 (C-O-C) and 288.7 eV (C-N).[151,152] Two peaks at 284.3 and 287.8 eV were fitted on the XPS C1s spectrum of C_3N_4, related to sp^2 C and N-C-$(N)_2$ features.[153] The XPS spectrum for C1s of CNDA900 and CPDA present similar features, suggesting that CNDA900 is principally CPDA in character, which yielded the conductive carbon layers. The N1s XPS spectra of CPDA, C_3N_4 and CNDA900 is exhibited in **Figure 3.6b**. The two fitted N1s XPS peaks for CPDA centred at 399.7 and 402.3 eV refer to the pyrrolic and graphitic N, respectively. The XPS N1s spectrum of C_3N_4 can be deconvoluted into four peaks: 398.3, 399.4, 400.7 and 404.1 eV; corresponding to the sp^2-bonded aromatic N (C-N=C), tertiary N [N-$(C)_3$], terminal amino groups (C-N-H) and positive charge localization due to imperfect polymerization, respectively.[153–155] In the XPS N1s spectrum for CNDA900 four peaks were fitted: at 398.1 (46.3 at. %), 399.3 (15.4 at. %), 400.8 (31.8 at. %) and 402.6 eV (6.4 at. %). This spectrum presented a pattern close to that observed for C_3N_4, giving an indication of the origin of the principal N species of CNDA900. However, it appears that the overlap of the pyrrolic N binding energy from CPDA with the energy of the N-$(C)_3$ bonds from C_3N_4 contribute to the

increased intensity of the fitted peak at 399.3 eV of CNDA900. The peak at 402.6 eV confirms the presence of some graphitic-N environments on the structure of CNDA900. The N 1s spectra of CPDA is composed of two similar peaks with an area ratio of approximately 1:1, but the equivalent peaks in CNDA900 are observed with a ratio of about 3:1 (lower energy : higher energy) arising from the contribution of both PDA and C_3N_4 to the intensity of the lower energy peak. These results further indicate that PDA helps increasing the active sites' concentration by supressing the volatilization of C_3N_4 and subsequent loss of N species.

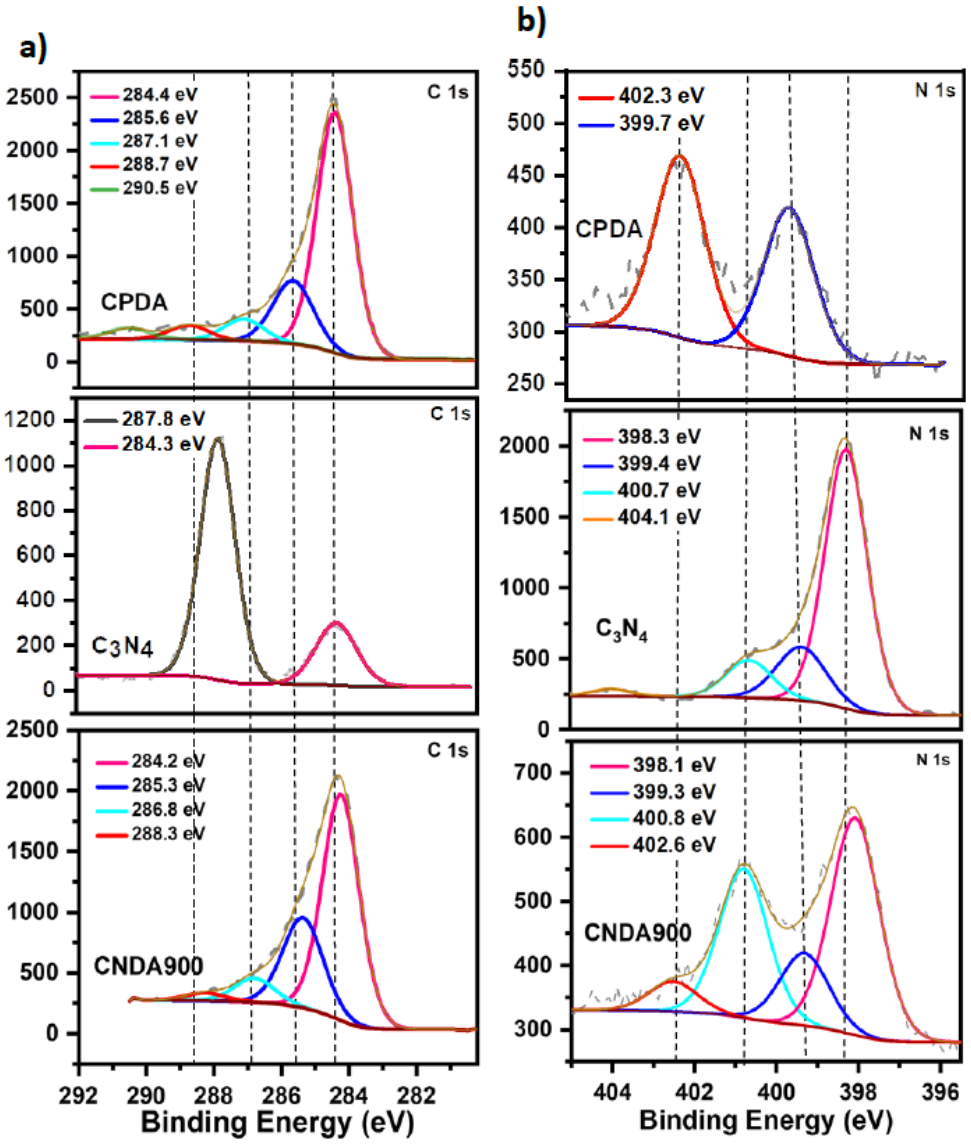

Figure 3.6: High-resolution XPS spectra of CPDA, C_3N_4 and CNDA900: a) C 1s and b) N 1s.

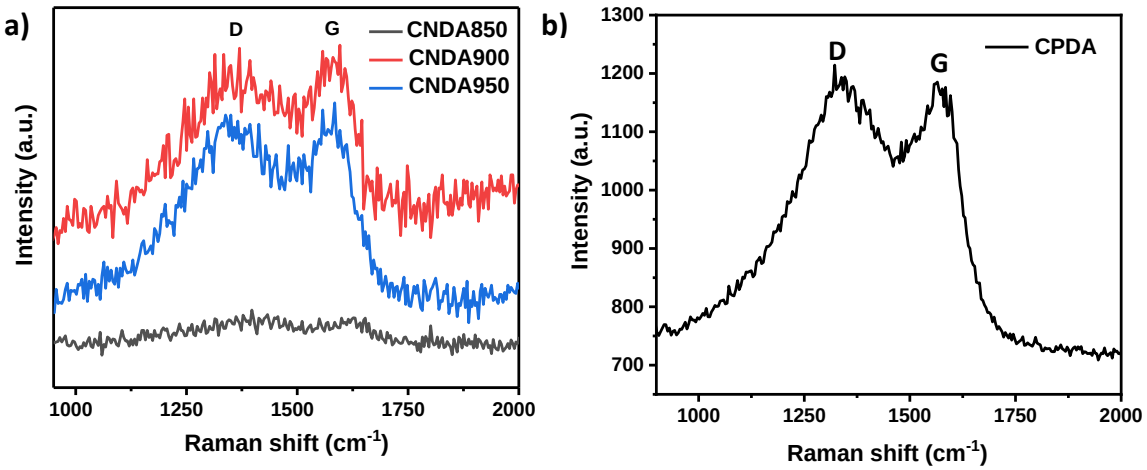

Figure 3.8: Raman spectra of a) CNDA850, CNDA900 and CNDA950 and b) CPDA in the region between 950-2000 cm^{-1}.

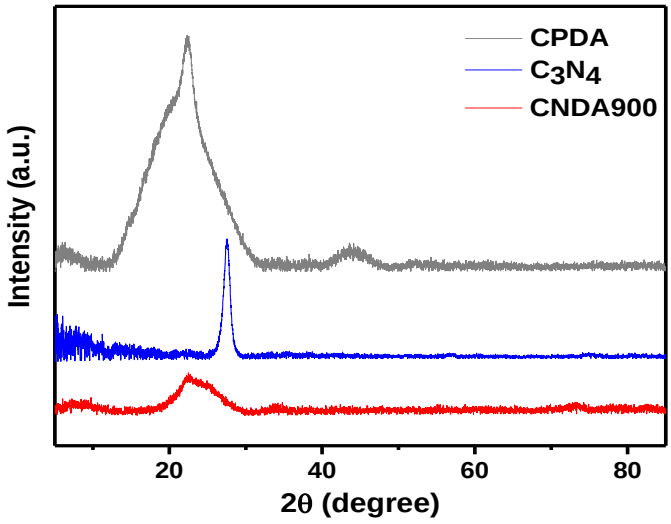

Figure 3.8: XRD patterns of CPDA, C_3N_4 and CNDA900.

Figure 3.7 shows the Raman spectra of CNDA850, CNDA900, CNDA950 and CPDA, revealing their degree of defective and graphitic character by comparison of the typical D and G bands at approximately 1350 and 1580 cm^{-1}, respectively.[156] The I_D/I_G band intensity ratios of CNDA900 and CNDA950 were 0.999 and 0.996, respectively, indicating a slightly higher level of graphitization with increasing carbonization temperature. The D band indicates the generation of defects which can be formed upon successful doping of nitrogen atoms and subsequent surface distortion.[152,156] In the case of CNDA850, both intensities for I_D and I_G were very low, implying a low content of graphite related structures formed at 850 °C. The addition of C_3N_4 to CPDA and further carbonization improved the graphitic character and reduced the number of defects on the

final product, which is confirmed by a lower I_D/I_G ratio in comparison to CPDA (I_D/I_G= 1.024). This graphitic character could promote the ORR by facilitating electron and mass transfers to the catalytically active sites.[157]

The XRD patterns of CPDA in **Figure 3.8** showed a broad diffraction peak at 22.3°, suggesting its amorphous nature.[158] As according to previous reports, the characteristic sharp XRD peak detected at 27.6° for C_3N_4 is originated by the interlayer stacking of C_3N_4.[153] A less broad peak and slightly positively shifted peak at around 23.8° was presented in the XRD pattern of the CNDA900 catalyst, suggesting some extent of enhancement of graphitic-like phases as compared to the CPDA, despite its overall amorphous nature. This was also previously suggested by the increased graphitic (G) band intensity observed in the Raman spectra of CNDA900 (**Figure 3.7**) in comparison to that of CPDA. The XPS, Raman and XRD results highlighted the essential contribution of each of the reaction precursors on the formation of the catalysts' structure.

3.2.2. Electrochemical characterization

As previously mentioned in section 2.3.2., in order to obtain a catalyst with an improved performance, the optimum composition and synthesis conditions were firstly studied based on their electrochemical behaviour. Linear sweep voltammetry curves (LSV) were collected for the different possible catalyst materials in 0.1 M KOH and the limiting current densities compared.

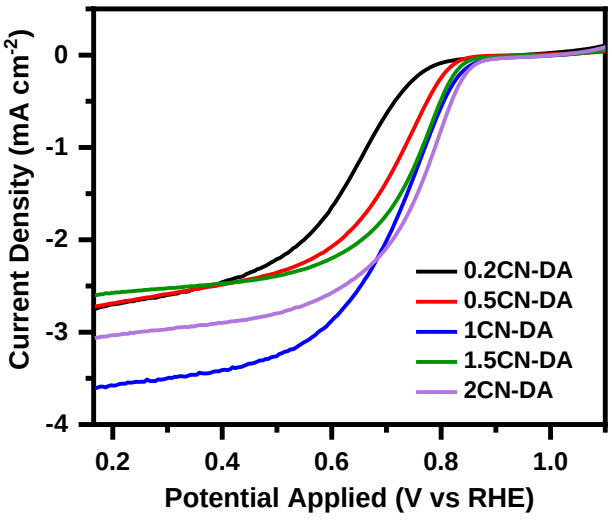

Figure 3.9: ORR LSV curves of different catalyst composites prepared by varying the C_3N_4:DA ratios, recorded at 1600 rpm, a scan rate of 5 mV s^{-1} in O_2-purged 0.1 M KOH electrolyte.

Initially, the C_3N_4:DA ratio was evaluated and it was concluded that 1CN-DA delivered the highest current density of 3.6 mA cm^{-2} (Figure 3.9). An equilibrium of 1:1 between the concentration of C_3N_4 and DA led to the right balance of nitrogen content and carbon layers originating an optimum content of exposed active sites. An excess amount of C_3N_4 would probably lead to a higher volatility rate and a reduced C_3N_4 content would mean lower N-content which greatly contributes to the formation of catalytically active sites. Furthermore, 1CN-DA was prepared at different carbonization times at 900 °C (30 min, 1 h and 2 h) and it was found that 1h-CNDA delivered the highest current density of 4.60 mA cm^{-2} (Figure 3.10). A long carbonization time (2 h) lead to the loss of N-dopants due to its volatility at high temperatures and a greater carbon content, whereas a shorter time (30 min) formed a composite with excess N content which may affect the electrical conductivity and reduce the ORR activity (Table 3.3). Once the catalyst's synthesis parameters were optimized leading to its best catalytic activity further studies were performed on the final composite materials.

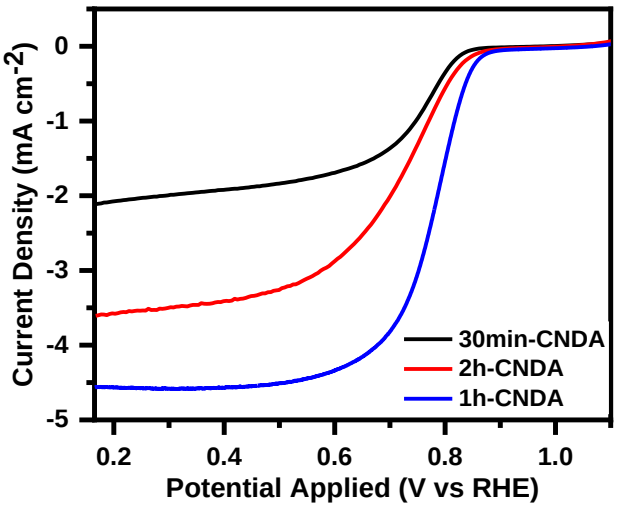

Figure 3.10: ORR LSV curves recorded at 1600 rpm, a scan rate of 5 mV s^{-1} in O_2-purged 0.1 M KOH electrolyte of the 1CN-DA catalyst prepared by varying the carbonization time (30min, 1 h or 2 h) while keeping the temperature at 900˚C.

Table 3.3: Elemental compositions obtained from the XPS C1 s, N 1s and O 1s high resolution spectra of 30min-CNDA, 1h-CNDA and 2h-CNDA.

Sample	Elemental Composition (at. %)		
	C	N	O
30min-CNDA	84.4	13.7	2
1h-CNDA	83.4	12.5	4.1
2h-CNDA	89.5	5.2	5.3

The electrocatalytic performance of the CNDA hybrid catalysts, CPDA and C_3N_4 were comparatively studied in 0.1 M KOH electrolyte. Cyclic voltammetry (CV) studies were performed to study the ORR catalytic activities of the prepared catalysts (Figure 3.11a and Figure 3.12a). Oxygen reduction peaks were observed in the O_2-saturated electrolyte solution, however no distinct features were observed in the N_2-saturated solution.

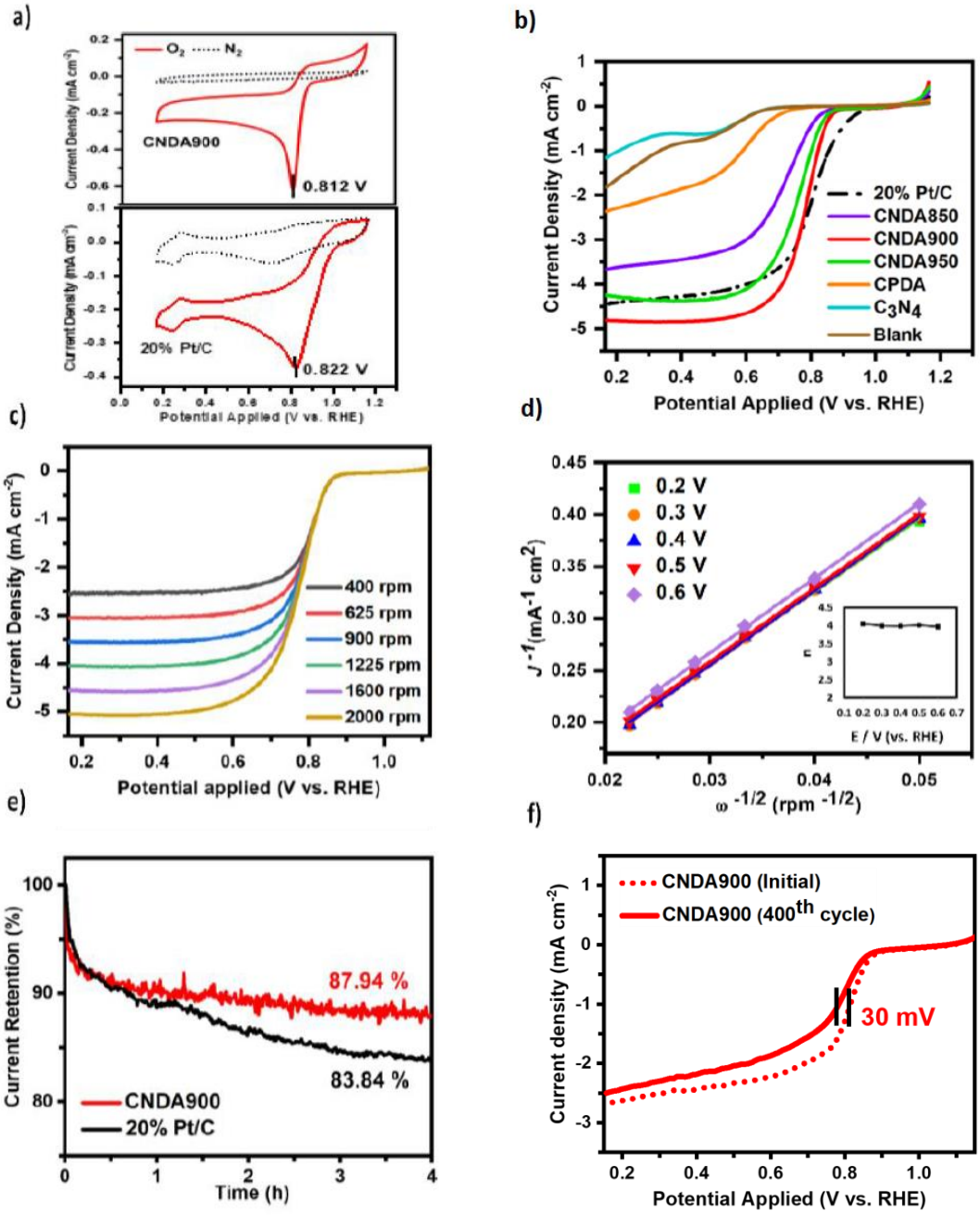

Figure 3.11: a) CV curves of the CNDA900 catalyst and Pt/C obtained in N_2/O_2-saturated 0.1 M KOH electrolyte. b) Combined LSV curves for ORR of all the CNDA catalysts, CPDA, C_3N_4 and Pt/C at 1600 rpm in O_2-purged 0.1 M KOH electrolyte. c) LSV curves of CNDA900 recorded at different rotation speeds (rpm) in O_2-purged 0.1 M KOH electrolyte. d) K-L plots of CNDA900 calculated from its RDE LSV curves at the potential range 0.2-0.6 V vs. RHE; the inset: plot of n (electron transfer number) per O_2 molecule at the different potentials. e) Chronoamperometric stability plots (i-t plots) of CNDA900 and Pt/C at 0.4 V and a fixed electrode rotation speed of 400 rpm in O_2-purged 0.1 M KOH electrolyte. f) ADT plots of CNDA900 and Pt/C before (dashed lines) and after (solid lines) 400 cycles for ORR at a fixed electrode rotation speed of 400 rpm in O_2-purged 0.1 M KOH electrolyte. The scan rate was kept at 5 mV s^{-1} for all the measurements.

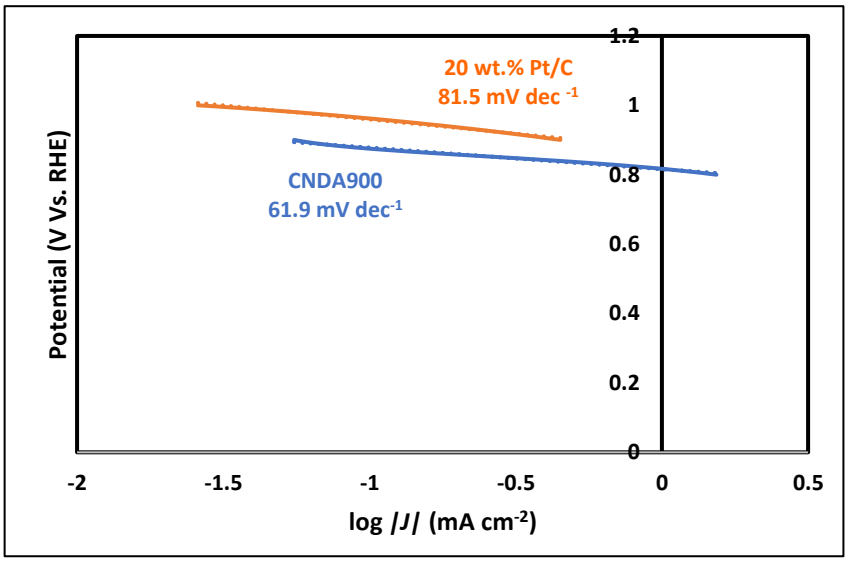

Figure 3.12) Tafel plots of CNDA900 and 20 wt% Pt/C obtained at 1600 rpm in O_2-saturated 0.1M KOH.

Furthermore, the Tafel plots of the CNDA900 catalyst, and the commercial Pt/C are drawn (Fig. 3.12). CNDA900 presented a lower Tafel slope of 61.9 mV dec^{-1} in comparison to the benchmark catalyst, indicating a faster cathodic reduction current enhancement as overpotential increased.

The reduction potential peak of Pt/C (20 wt.%) at 0.82 V versus reversible hydrogen electrode (RHE) was comparable to the peak of CNDA900 at 0.81 V and this was more positively shifted as compared to the CNDA950 sample (0.76 V, Figure 3.12a). The bare CPDA and C_3N_4 precursors were not as efficient at reducing oxygen, making them unsuitable catalysts for the ORR (Figure 3.12b). Figure 3.11b compares the LSV curves collected for the catalysts, and it can be clearly observed that all three CNDA catalysts showed improved ORR activity, suggesting the successful interaction between PDA and C_3N_4. A more efficient electron mobility and active sites formation may have led to the improved ORR activity, originated from the combination of these two π-conjugated polymers. Additionally, it has been reported that the introduction of extra N-species in the carbon framework may induce charge delocalisation on the adjacent C, creating these catalytically active sites.[138,159] Particularly, the CNDA900 presented the best performance amongst the CNDA catalysts, CPDA and C_3N_4, evidenced by the more positively shifted LSV curve and the highest diffusion-limited current density. The diffusion-limited current density for CNDA900 was 4.6 mA cm^{-2}, exceeding CNDA850 (3.7 mA cm^{-2}) and CNDA950 (4.3 mA cm^{-2}) and just 0.9 mA cm^{-2} lower than that of the

commercial Pt/C catalyst (5.50 mA cm^{-2}). The half-wave potential ($E_{1/2}$) of CNDA900 at 0.78 V was only 0.08 V more negative than that of the Pt/C benchmark (0.86 V), but 0.05 and 0.02 V positively shifted as compared to the CNDA850 and CNDA950, respectively. In addition, the $E_{1/2}$ demonstrated in the LSV curve of CNDA900 was comparable to that of other reported N-doped carbon catalysts and an improved diffusion-limited current density was recorded. Additionally, the CNDA900 catalyst delivered higher current density than some reported metal-based ORR electrocatalysts, despite being metal-free (Table 3.2).[88,160] The CNDA850 and CNDA950 catalysts presented an inferior performance, likely due to the reduced exposure, heterogeneous distribution of the active sites or decomposition of dopants due to overheating which leads to a higher charge-transfer resistance.

The electron transfer number per oxygen molecule (n) can be determined from the Koutecky-Levich (K-L) relations which were deduced from the measured current densities at different rotations (Figure 3.11c). The LSV of CNDA900 shows a wide and steady plateau which suggests a diffusion-controlled ORR process.[161] The steady, linear and parallel slopes of the CNDA900 K-L plots (Figure 3.11d) indicate first-order reaction kinetics with respect to the concentration of oxygen dissolved in the electrolyte.[77,162] The average n value of CNDA900 was calculated to be approximately 4.00 for the potential range of 0.2-0.6 V vs. RHE. This value is comparable to the benchmark ORR catalyst, Pt/C, which also follows a favourable 4-electron pathway.[45] The average n values deduced from the K-L plots for CNDA850 and CNDA950 observed in Figure 3.13 were 3.65 and 4.23, respectively, indicating a sluggish oxygen reduction reaction and possibly undesirable side reactions.

Chronoamperometric (*i-t*) measurements at a fixed potential of 0.40 V (vs. RHE) under the RDE rotating at 400 rpm were performed to evaluate the material's catalytic stability. Long-term catalytic stability is essential for practical zinc-air battery applications. On the one hand, the continuous rotation of the RDE attached catalyst at 400 rpm can result in the electrolyte solution to "flush" the catalyst at the electrode surface but on the other hand, it also increases the chance of catalyst detachment from the surface, reducing the catalytic performance. However, running the *i-t* test under such harsh conditions provides data related to the accelerated degradation of the catalyst which enables the development of durable catalysts for zinc-air batteries. The i-*t* test results (Figure 3.11e) show that after a 4 h continuous testing, the CNDA900 catalyst was able to retain about 87.94 % of its initial ORR current, evidently higher than that of the

benchmark Pt/C catalyst of 83.84 %, under the same testing conditions. These results unambiguously demonstrated the good ORR durability of CNDA900 as compared to the commercial Pt/C, although future studies including post-characterizations are recommended to precisely understand the reasons behind stability decay. Additional durability tests were performed to further clarify the performance of the CNDA900 catalyst. The accelerated degradation test (ADT) results presented in Figure 3.11f only showed a slight shift of 30 mV at a current density of 1 mA cm^{-2} on the LSV curve of CNDA900 after 400 continuous cycles. Continuous catalytic reactions may take place due to the presence of multiple electron transfer channels on CNDA900.

Catalysts	**Loading (mg cm^{-2})**	**$E_{1/2}$ (V vs. RHE)**	**Diffusion-limited current density (mA cm^{-2})**	**Ref.**
S-N-HPCS	0.41	0.84	4.24	
NGA900	0.28	0.83	4.60	

g-CN/C-2	Unknown	~0.80	4.10	
N,S-NC	0.20	0.76	~ 4.40	
Co_9S_8/CD@NSC	0.25	0.84	~ 4.20	
Co@Co_3O_4@NC-900	0.36	0.80	~ 4.72	
NC@NPC	0.10	~0.67	~ 3.75	
CNDA	0.20	0.78	4.80	This work

In addition to being efficient at promoting ORR with good stability, the CNDA900 catalyst was also found capable of promoting the reversible OER reaction. The LSV curve of CNDA900 (Figure 3.14) shows an increase in anodic current above 1.23 V, achieving a lower onset potential than that of Pt/C at 1.57 V and a higher current density. The CNDA900 catalyst also presents an enhanced OER performance as compared to the CNDA850 and CNDA950, but inferior to that of the benchmark OER catalyst, Ir/C.

Table 3.4: Comparison of the ORR performance of several reported metal and non-metal carbon-based electrocatalysts.

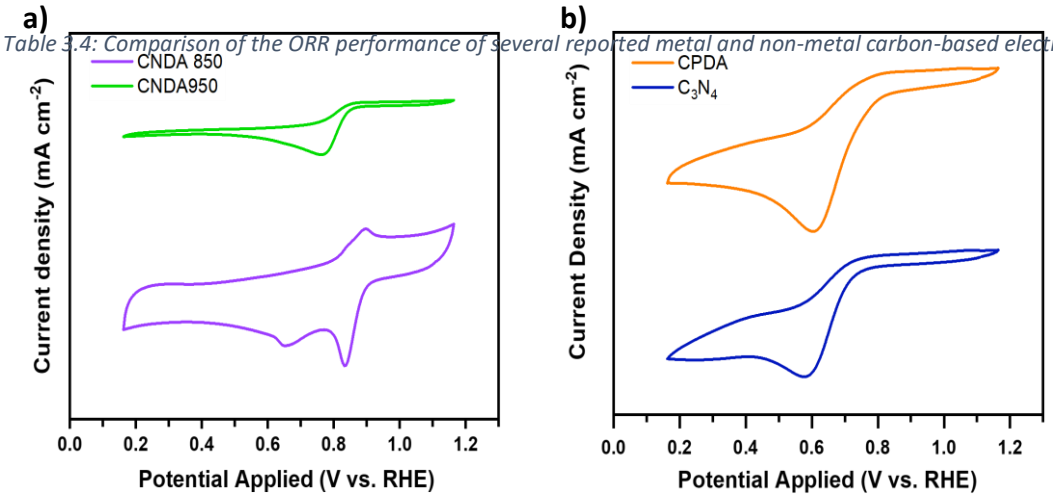

Figure 3.12: CV curves recorded at a scan rate of 5 mV s^{-1} of a) CNDA850 and CNDA950 and b) C_3N_4 and CPDA in O_2-saturated 0.1 M KOH electrolyte.

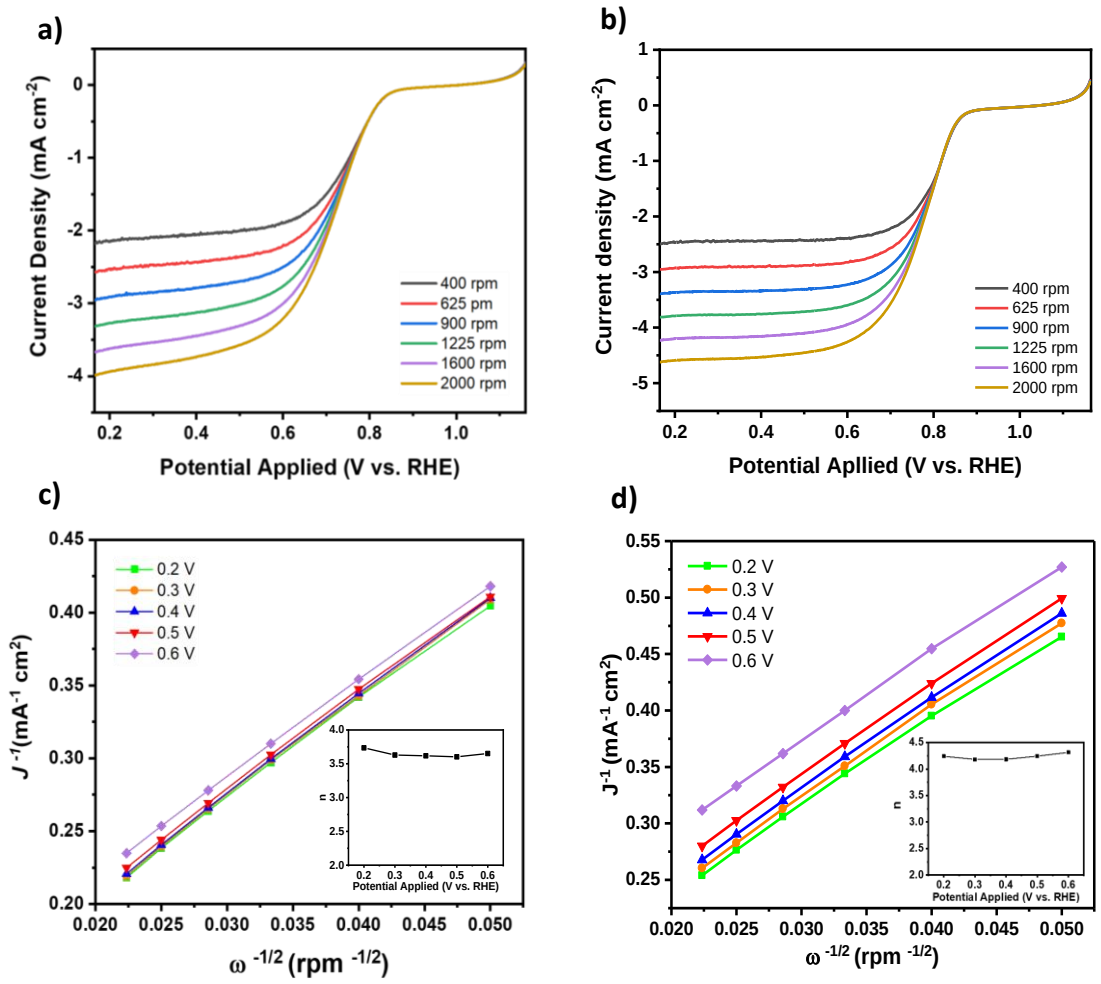

Figure 3.14: LSV curves of a) CNDA850 and b) CNDA950 recorded at different rotation speeds a scan rate of 5 mV s^{-1} in O_2-purged 0.1 M KOH electrolyte. K-L plots of c) CNDA850 and d) CNDA950 calculated from its RDE LSV curves at the potential range 0.2-0.6 V vs. RHE; the inset: plot of n (electron number) per O_2 molecule at different potentials.

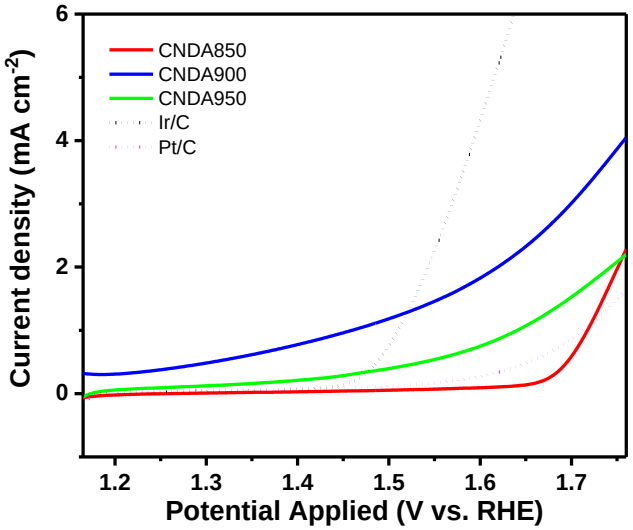

Figure 3.13: Combined OER LSV curves recorded at 1600 rpm and a scan rate of 5 mV s^{-1} of all the CNDA composites and Ir/C and Pt/C for comparison in 0.1 M KOH electrolyte.

3.2.3. Zinc-air battery performance

Following the previously reported electrochemical studies which suggested that the CNDA900 catalyst could efficiently promote stable ORR and also enhance the OER, its application in Zn-air batteries was evaluated. Prototype ZABs were assembled using the CNDA900 electrocatalyst as the air cathode and compared to a Pt/C-based ZAB. Figure 3.15a shows the polarization and power density curves. The cell with the CNDA900 catalyst showed an increase of current density with decreasing voltage. At 0.8 V, the CNDA900 catalyst achieved a current density of 65 mA cm^{-2} and a power density of 52 mW cm^{-2}, respectively, both higher than that delivered by the Pt/C catalyst, being 54 mA cm^{-2} and 43 mW cm^{-2} for current density and power density, respectively. Table 4 compares the power density of various previously reported zinc-air batteries.

Publication	Developed catalyst (mW cm^{-2})	Pt/C (mW cm^{-2})	Ref.
Zhang et al. [Nature Nanotech 2015, 10, 444.	55 (metal-free and carbon-based)	50	163
Li et al. Energy Storage Materials 2020, 25, 137	63 (Co-based)	49	164
Wu et al. Energy Technol. 2020, 8, 1901263	42 (Fe/P-based)	49	165
Pt/C	---	43	This work
CNDA900	52	---	

Table 3.5: Comparison of the power density of assembled zinc-air batteries with previous publications. In all the above-mentioned publications the batteries were prepared in a similar manner, with a similar or higher catalyst loading as that used in our work (0.5 mg cm^{-2}).

The galvanostatic discharge results of CNDA900 and Pt/C catalysts in ZABs obtained at different current densities (1, 5, 10, 15 and 30 mA cm^{-2}) are presented in Figure 3.15b. The CNDA900-based cell demonstrated a good rate performance with stable and flat discharge voltage plateaus at the various current densities. Particularly, even at a discharge current density as high as 30 mA cm^{-2} the battery achieved a high discharge voltage of 1.1 V, merely 10 mV lower than the ZAB with the Pt/C catalyst, confirming the superior ORR activity previously exhibited in the electrochemical studies.

Constant galvanostatic discharge-charge cycling tests were carried out at 2.5 mA cm^{-2} for 30 min during charging, followed by 5 mA cm^{-2} for 15 min during discharging

in each cycle. Figure 3.15c exhibits the cycling performances of the ZAB containing the CNDA900 based air-cathode. These show good rechargeability over a period of 75 h. In detail, the battery initially required a charge voltage of 2.47 V and delivered a discharge voltage of 1.12 V, corresponding to a voltage gap of 1.35 V, comparable to the 1.33 V voltage gap of the benchmark Pt/C catalyst-based ZAB (Figure 3.16a). After 50 h (Figure 3.16b), the difference between the charge and discharge cycles of CNDA900 decreased by 0.06 V to 1.29 V, originated from a charge voltage of 2.43 V and a discharge voltage of 1.14 V. The voltage gap of the Pt/C-based ZAB greatly increased to 1.45 V, which is 0.16 V higher than that of CNDA900. At this stage, the charging efficiency had greatly decreased, affecting the Pt/C-based ZAB's efficiency, which finally stopped cycling after 45 h (Figure 3.16c). In the end (Figure 3.14d), the battery maintained a reduced voltage gap of 1.32 V (increasing by 0.1 mV per cycle), obtained from a high discharging voltage of 1.04 V. At this stage the cell could not continue the charging process. The total discharge voltage had a mere drop of 0.15 V (from 1.12 to 1.04 V; 0.27 mV per cycle). These results highlight the favourable catalytic activity of CNDA900 in ZABs originated from the high electron transport and electrocatalytic active sites distribution.

3.3. Conclusion

In conclusion, a facile strategy to introduce high concentration of N functionalities onto a carbon framework without the use of templates, catalysts or harsh chemicals was successfully developed. We deduced that the two π-conjugated polymers interacted and allowed the rearrangement of the carbon framework and distribution of extra N features from species originated from the decomposition of C_3N_4 during high temperature pyrolysis. It was observed that without the presence of PDA, C_3N_4 completely decomposed at temperatures above 750˚C. An efficient ORR electrocatalyst was obtained due to the activation and exposure of active sites within the framework. The CNDA900 catalyst presented a comparable $E_{1/2}$ and a remarkably improved diffusion-limited current density compared with other reported N-doped carbon catalysts. The composite catalyst also presented promising results towards the OER. The battery test results of the ZABs containing CNDA900 confirmed their stability and practicality. The successful developments and noteworthy results reported in this work provide an avenue for the cost-effective fabrication of nitrogen-rich carbon-based catalysts for environmentally friendly ZABs.

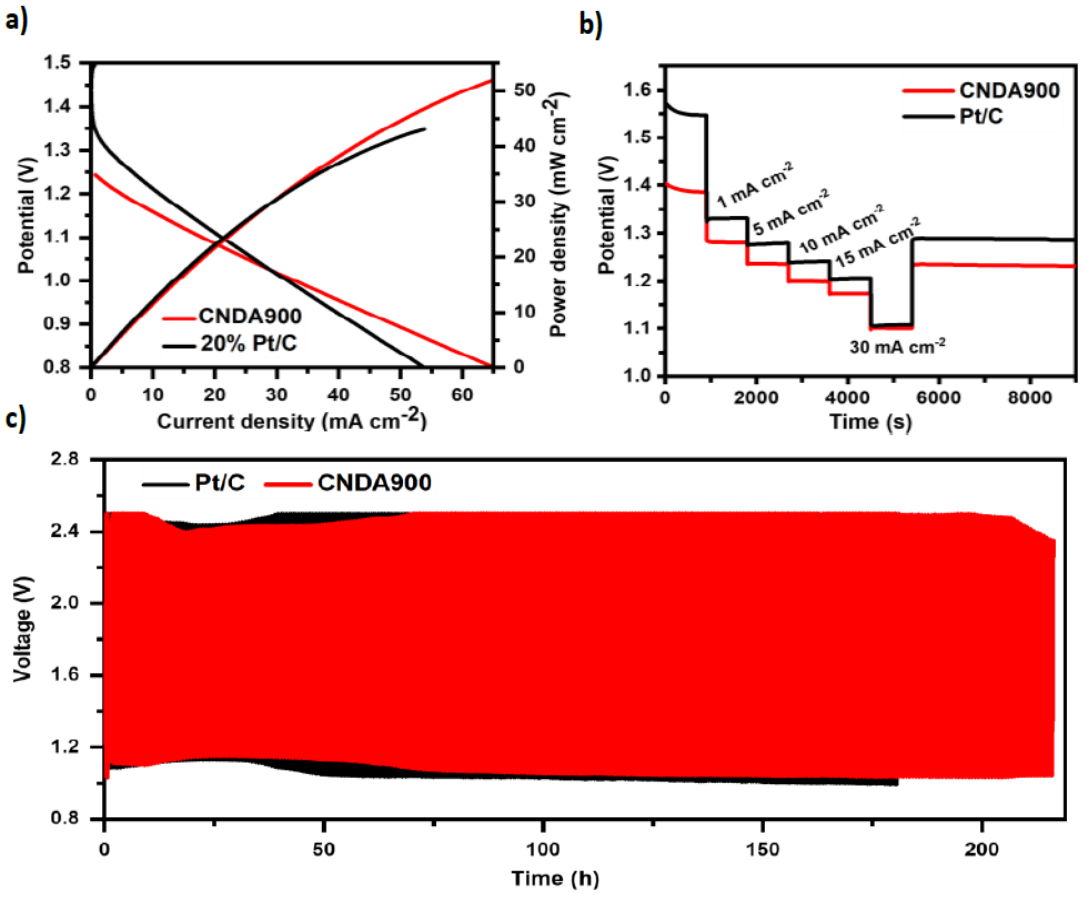

Figure 3.15: a) Polarization and power density curves of ZABs using CNDA900 and Pt/C as ORR catalyst with a mass loading of 0.5 mg cm^{-2} and 6 M KOH electrolyte at a scan rate of 5 mV s-1. b) Voltage profiles of CNDA900 and Pt/C-based ZABs with 6 M KOH electrolyte when discharged at different current densities: 1, 5, 10, 15 and 30 mA cm^{-2}. c) Galvanostatic discharge-charge cycling performances of ZABs with CNDA900 and Pt/C catalysts in 6 M KOH electrolyte carried out at 2.5 mA cm^{-2} for 30 min of charging, followed by 5 mA cm^{-2} for 15 min of discharging in each cycle.

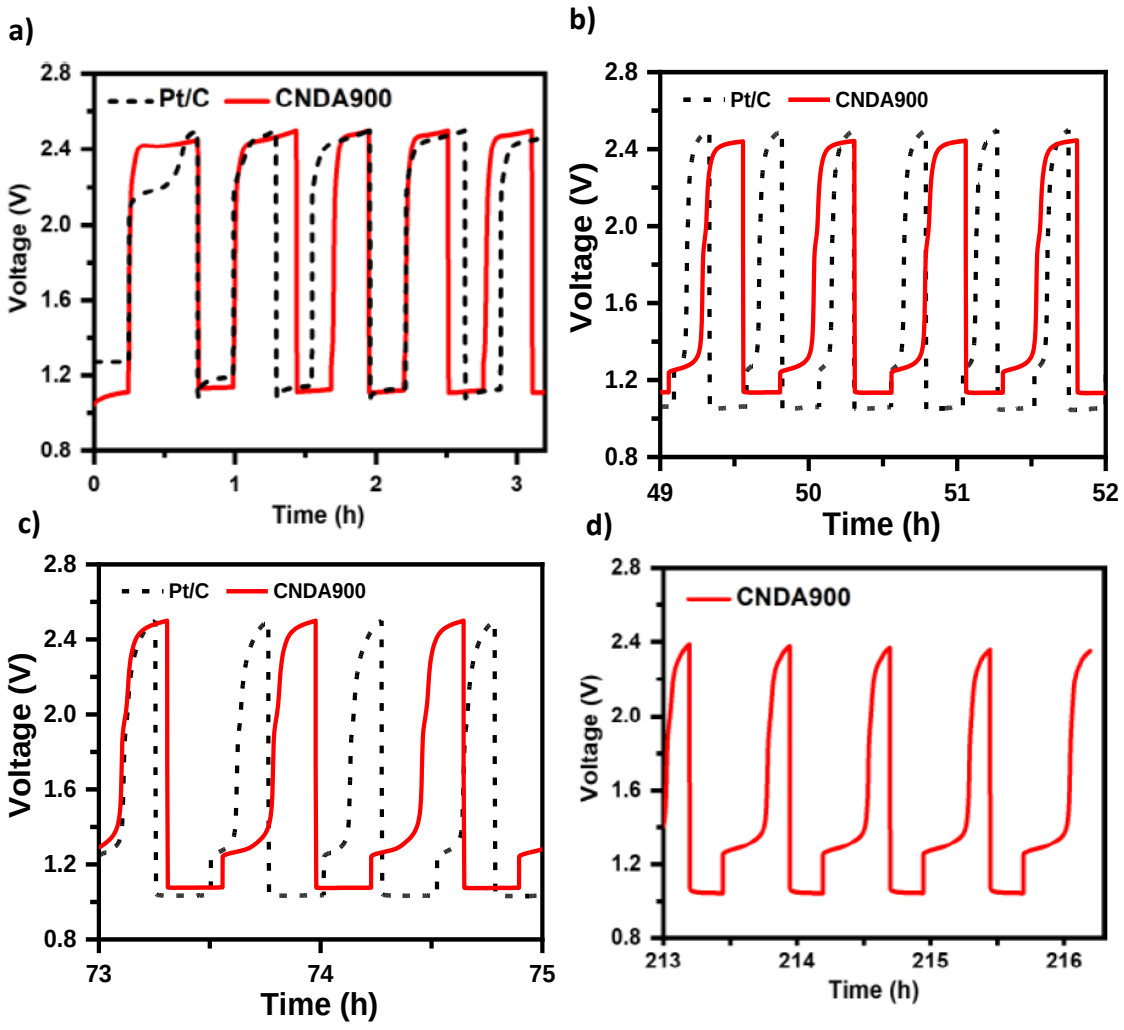

Figure 3.16: Selected sections of the discharge-charge cycling performances from Fig. 3.15 c) carried out at 2.5 mA cm^{-2} for 30 min of charging, followed by 5 mA cm^{-2} for 15 min of discharging in each cycle. Galvanostatic discharge-charge cycling performances of ZABs with CNDA900 and Pt/C catalysts at a) 0 to 3 h, b) 49 to 52 h, c) 73 to 75 h and d) 213 to 216 h.

4. Co/N nanoparticles obtained from ZIF-67 supported on a C_3N_4/Polydopamine framework as a bifunctional electrocatalyst for rechargeable zinc-air batteries

4.1. Introduction

Following the development of an efficient metal-free ORR electrocatalyst, a composite with both ORR and OER catalytic capabilities was further researched.

Heteroatom doped carbon-based materials have been found to be promising electrocatalysts due to their large surface area, tunable structure, appropriate pore size, excellent conductivity, long-term stability and availability of source materials.[144,166] As previously mentioned, nitrogen-doping can create abundant defects on the carbon framework, inducing a positive charge on the adjacent carbon atoms which can promote the ORR; this charge localization may promote the favourable side-on adsorption of O_2 on the catalyst surface, weakening the O-O bond and therefore facilitating the transfer of electrons between the surface and dioxygen.[167,168] Furthermore, metal N-doped carbons (M-N-C), specifically cobalt-based N-doped carbons (Co-N-C) have attracted extensive attention as suitable multifunctional catalysts.[34,53,76,169–171] Their high catalytic activity, originating from the strong coupling effect of Co with N, leads to the formation of active sites with suitable binding energies for promoting the discharging and charging reactions.[172] Cobalt may also promote the catalytic graphitization of amorphous carbon,[170,173,174] however it has been challenging to prepare catalysts with relatively well dispersed cobalt-based nanoparticles (Co NPs) on the graphitic carbon network, which is essential to promote even transport of electrons to the Co-based active sites and hence rate of reaction across the catalyst framework. Zeolitic imidazolate frameworks (ZIF), a type of metal organic frameworks (MOFs), are tetrahedral structures containing transition metal (TM) cations directly coordinated to N-rich sites via the imidazole linkers.[164,175] These structures have been studied as precursors for the formation of M-N-C catalysts due to their tunable and porous scaffold with a large surface area.[34,76,171,176,177] Nevertheless, upon pyrolysis, the porous nanostructure tends to collapse because of the aggregation of metal atoms into larger undesirable particles, volatility of N and the formation of random structures , which greatly reduces surface area, porosity and further reduces its catalytic activity.[34,143,172,178]

In this work, a strategy to promote the formation of well distributed cobalt active sites was developed, achieved due to the insertion of cobalt ions during the polymerization process of dopamine, instead of on a previously prepared framework (e.g. graphene, etc).[179] The Co ions were chelated by the N-atoms on the dopamine precursor, immobilizing them on the carbon support. Following this, the addition of the 2-methylimidazole ligand led to the formation of Co-based ZIF (i.e. ZIF-67) particles, which upon pyrolysis at 900˚C under N_2 atmosphere, originated well dispersed cobalt nanoparticles surrounded by a graphitized carbon shell on a layered graphitic carbon framework (ZIFCNDA). This strategy not only avoided the excessive growth and aggregation of metal nanoparticles but also led to the controlled formation of a thin layered structure due to the addition of a C_3N_4 template during polydopamine synthesis. The catalysts' stable network provides different catalysis paths for a more efficient performance. Furthermore, this avoided the undesired formation of random and irregular structures or bulky spheres, which can lead to the reduction of the catalytically active surface area. This work explores a novel and simplified synthesis process for the formation of well-dispersed Co NPs on a graphitized N-doped carbon framework.

4.2. Results and discussion

4.2.1. Preparation and structural characterization

Scheme 4.1 schematically details the synthetic procedure idea for the preparation of the ZIFCNDA catalyst (Table 4.1, refer to Sections 2.3.1 and 2.3.3). Firstly, different ratios (0.5, 1, 2 and 5) of cobalt nitrate, $Co(NO_3)_2.6H_2O$ and dopamine hydrochloride were added to a well-dispersed C_3N_4 solution yielding a light-pink coloured solution. Then, the addition of trizma base aimed to trigger the polymerization of dopamine along with the introduction of cobalt, forming a layered framework. Upon addition of the 2-MeIm ligand solution, the colour instantly changed to blue-violet, suggesting the formation of ZIF-67. The synthesis of ZIF-67 involves the quick Co-N coordination bond formation when cobalt salt and 2-MeIm solutions are mixed. The instant colour change is indicative of the coordination reaction. Finally, high-temperature pyrolysis at 900^{o}C yielded the formation of small particles scattered across the carbon sheets (ZIFCNDA).

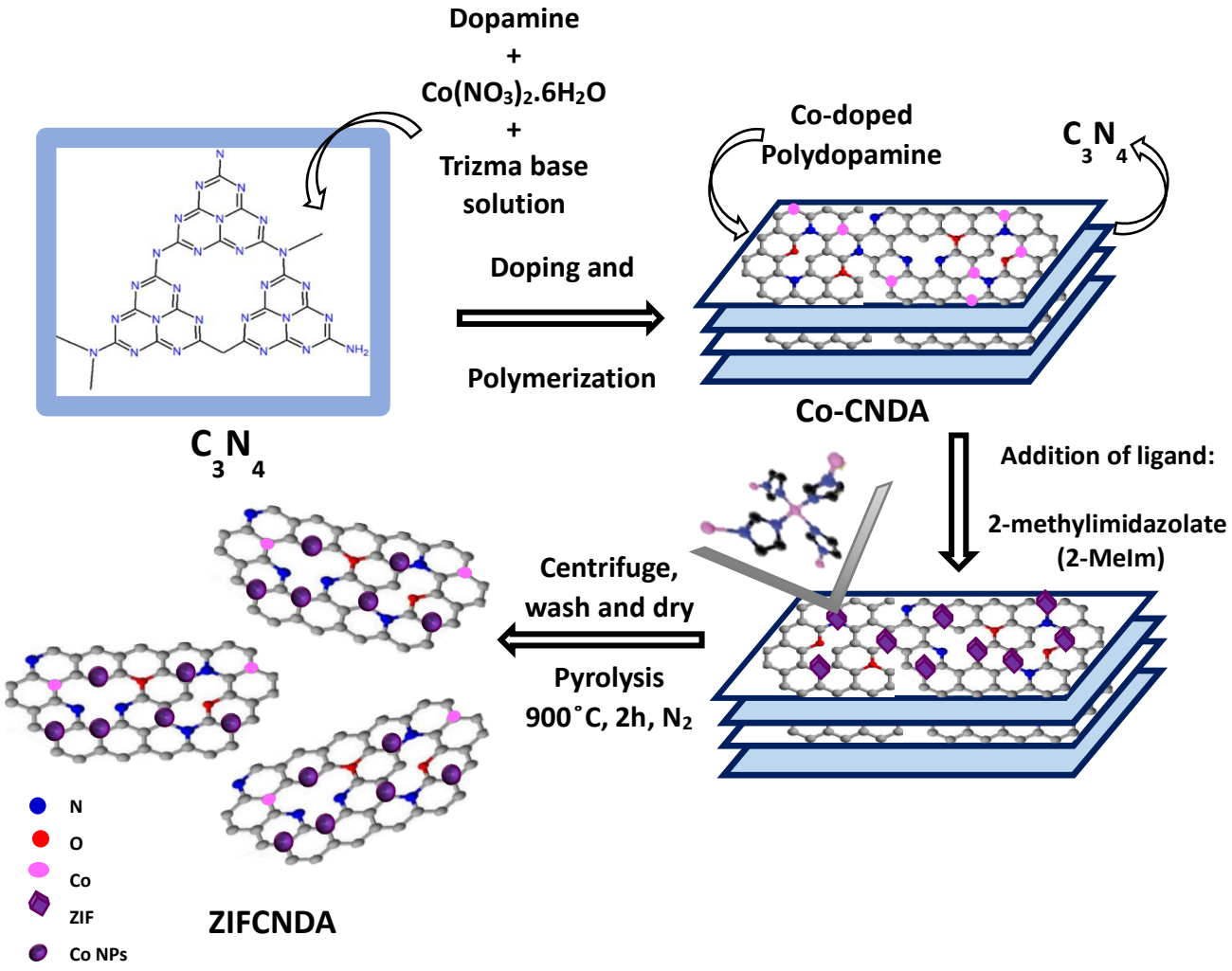

Scheme 4.1: Schematic illustration of the synthesis of the ZIFCNDA catalyst.

Table 4.1: Experimental details for the synthesis of the different materials prepared.

Material	Synthesis conditions
C_3N_4	1) Thermal polymerization of melamine: 10 g of melamine was placed in a porcelain crucible and heated to 550 °C at a ramping rate of 5 °C/min and kept at 550 °C for 4 h under Ar atmosphere.
ZIFCNDA-X (X = 0.5, 1 or 2)	2) Preparation of aqueous solution of C_3N_4 (0.45 mg cm^{-3}): 30 min stirring and then bath sonication for 15 min. 3) 75 mg of dopamine hydrochloride (0.3 mg cm^{-3} in the final solution) were added to the as-prepared C_3N_4 solution and stirred for 15 min. Then, a solution containing $Co(NO_3)_2.6H_2O$ at a mole ratios of 0.5:1, 1:1 or 2:1 ($Co(NO_3)_2.6H_2O$:Dopamine) were added to the previously prepared solution and stirred for 15 min. 4) 1.21 mg cm^{-3} of trizma base were added to the previous solution and vigorously stirred to trigger dopamine polymerisation. 5) After 4 h of mild stirring, 100 ml of an aqueous solution of 2-methylimidazole (0.35 mg cm^{-3}) was added and stirred for 20 min. 6) The product was collected by centrifugation (10 min at 8000 rpm) and repeatedly washed with deionized water and ethanol. 7) After overnight oven drying, the material was pyrolyzed at 900 °C for 2h, at a ramping rate of 5 °C min^{-1} in N_2 atmosphere.

Initially, the ZIFCNDA samples prepared with varied dopamine:cobalt nitrate ratios (ZIFCNDA-0.5, ZIFCNDA-1 and ZIFCNDA-2) were evaluated in an attempt to optimize the synthetic procedure conditions. XPS and BET analysis were used to differentiate the samples and find the optimum ratio. As the cobalt salt content increased in the reaction mixture, the C at.% in the final annealed composite followed the same trend up until the 2:1 ratio (Table 4.1). Specifically, the C=C content increased from 70.6 at.% to 74.0 at.%, indicating the formation of more graphitic C functionalities which can promote electron transport to the catalytically active sites. The greater addition of cobalt ions might have catalysed the formation of more graphitic C functionalities in ZIFCNDA-2. Additionally, an improved BET surface area was reported for the ZIFCNDA-2 as the mole ration of cobalt nitrate increased from 1 to 5 (Table 4.2). A greater surface area is beneficial to improve the accessibility to more active sites. The BET surface area of

ZIFCNDA-0.5 was found to be greater than the rest, which might have been due to the higher DA content, however, the conversion to graphitic C was not as efficient as on ZIFCNDA-2 due to the reduced Co ion content in the starting solution of ZIFCNDA-0.5.

Table 4.2: C at.% and C=C at.% obtained from the XPS survey spectra and high resolution C1s spectra of ZIFCNDA-0.5, ZIFCNDA-1, ZIFCNDA-2 and ZIFCNDA-5.

Sample	C at.% (from survey spectra)	C=C at.% (from high resolution C1s spectra)
ZIFCNDA-0.5	93.6	70.6
ZIFCNDA-1	93.9	70.6
ZIFCNDA-2	95.9	74.0
ZIFCNDA-5	95.0	70.3

Table 4.3: BET surface area results of ZIFCNDA-0.5, ZIFCNDA-1, ZIFCNDA-2 and ZIFCNDA-5.

Sample	BET Surface area ($m^2 g^{-1}$)
ZIFCNDA-0.5	416
ZIFCNDA-1	243
ZIFCNDA-2	268
ZIFCNDA-5	212

The morphologies of the composites at different stages of the process were examined by TEM in Figure 4.1 and Figure 4.2. The TEM image in Figure 4.1a shows the thin substrate layered structure (CNDA) formed by the growth-controlled polymerization of dopamine on a C_3N_4 template. During this polymerization process, cobalt ions were introduced to promote direct cobalt doping onto the carbon framework. Additionally, the 2-MeIM ligand was added to the solution to promote selective growth of Co-based MOF particles with a polyhedron-like structure (ZIF-67) and an average size of 900 nm, as observed in Figure 4.2a. The successful formation of ZIF-67 on the N-doped carbon-based scaffold was confirmed by the XRD pattern observed in Figure 4.3.[174]

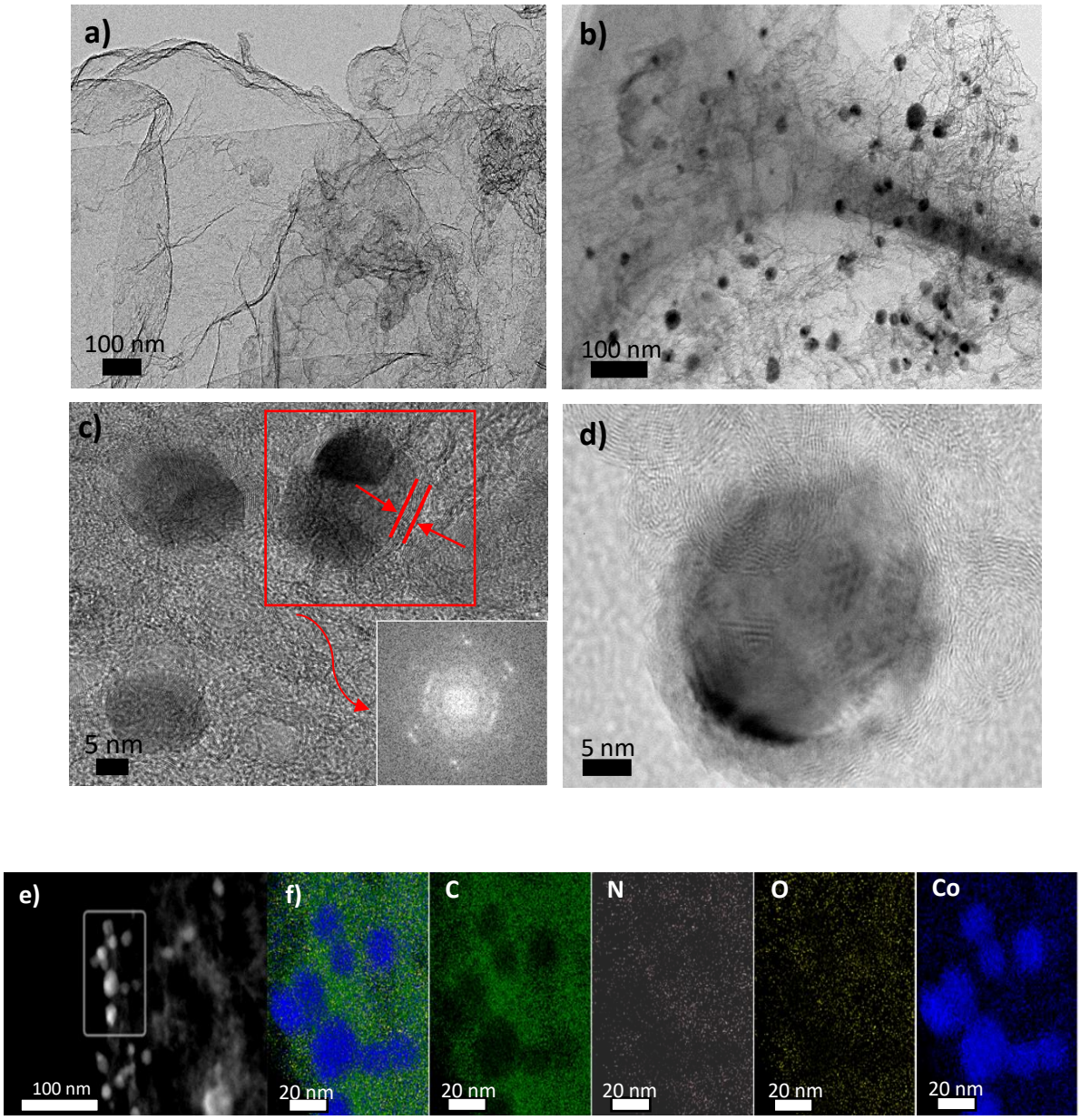

Figure 4.1: TEM images of a) CNDA and b) ZIFCNDA; c-e) HRTEM images of ZIFCNDA (inset: corresponding FFT) and f) corresponding elemental mapping images of e).

Following this, pyrolysis at 900˚C under an N_2 atmosphere yielded a structure composed of nanoparticles with diameters ranging from about 20-40 nm evenly distributed on thin carbon layers (ZIFCNDA), as revealed in Figures 4.1b and 4.2c. In order to confirm the elemental distribution on the nanoparticles and the supporting framework, TEM with EDS elemental mapping profile was used (Fig. 4.1e-f). The layered framework was found to contain evenly distributed C, N and O and mostly Co was localised in the nanoparticle regions, confirming the formation of Co nanoparticles on a carbon support. Figures 4.2d and 4.1c-d reveal the formation of graphene-like carbon nanosheets catalysed by the introduction of cobalt nanoparticles.[73] Additionally, the TEM image obtained at a higher

magnification (Figure 4.1c-d) showed that the Co NPs were supported by surrounding carbon shells. The FFT image (inset of Figure 4.1c) reveals the lattice fringes on the nanoparticles with d-spacings of about 0.20 nm and 0.18 nm correspondent to the (111) and (200) planes of face-centered cubic phase of metallic Co, respectively, whereas the lattice spacings of 0.34 nm were ascribed to the (002) plane of graphitized carbon surrounding the particles.

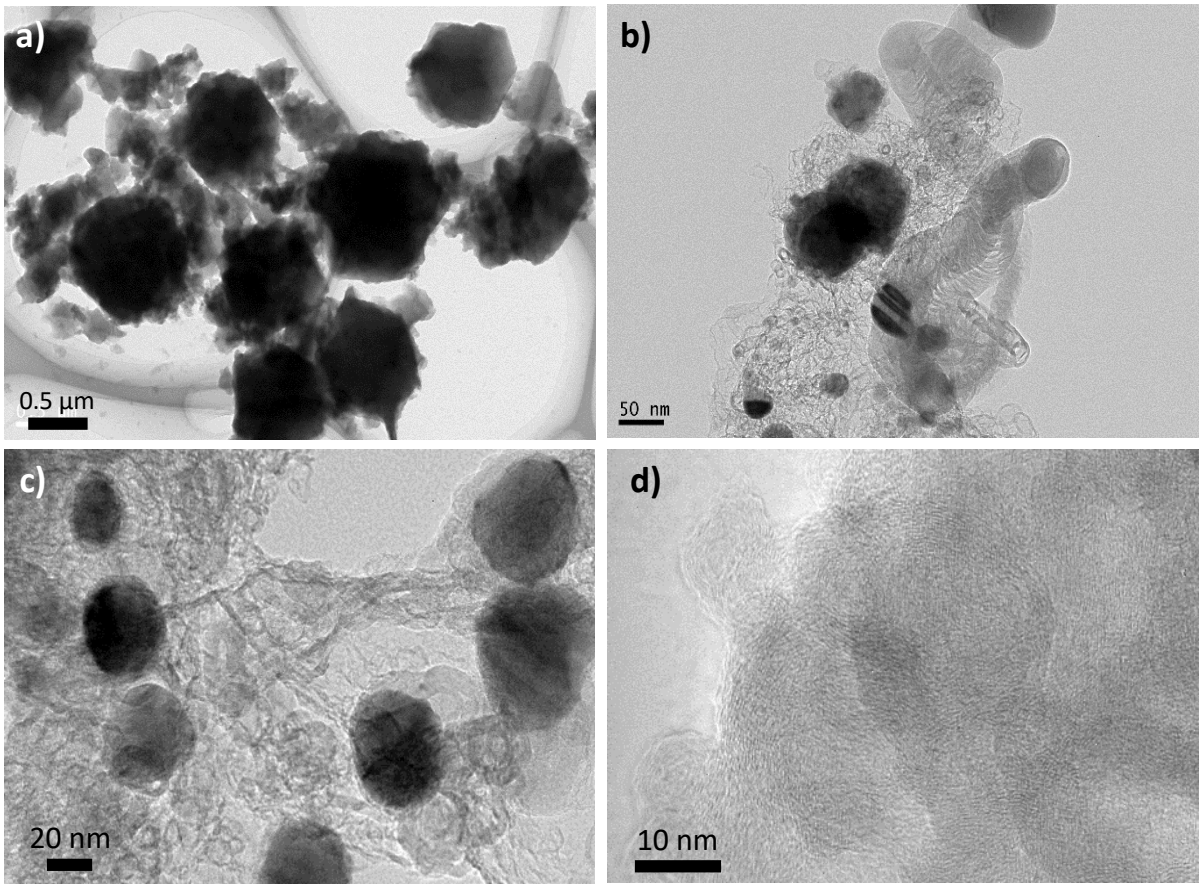

Figure 4.2: TEM images of a) ZIFCNDA catalyst before annealing at 900°C under N2 atmosphere, b) Co-CNDA (after annealing), c-d) final ZIFCNDA catalyst.

During thermal activation, the organic moieties are gradually converted to graphitic carbon, causing the loss of hydrogen and some carbon and nitrogen atoms, altering the structure of the framework, along with pore formation. After thermal activation, the original ZIF structure cannot be retained, however, it is important to aid the uniform distribution of Co and N-functional groups.[180] This strategy allowed the metal particles to be well dispersed on the carbon substrate, reducing the formation of unstable loose crystals and restraining their aggregation while avoiding the need for the addition of any nanoparticle growth-control agents.[34,74] It was observed that if the 2-methylimidazole

ligand is not added to promote the formation of Co-based MOFs, upon pyrolysis uneven nanoparticles and random aggregations are formed, encapsulating the nanoparticles, and therefore reducing the active sites exposure (Figure 4.2b).

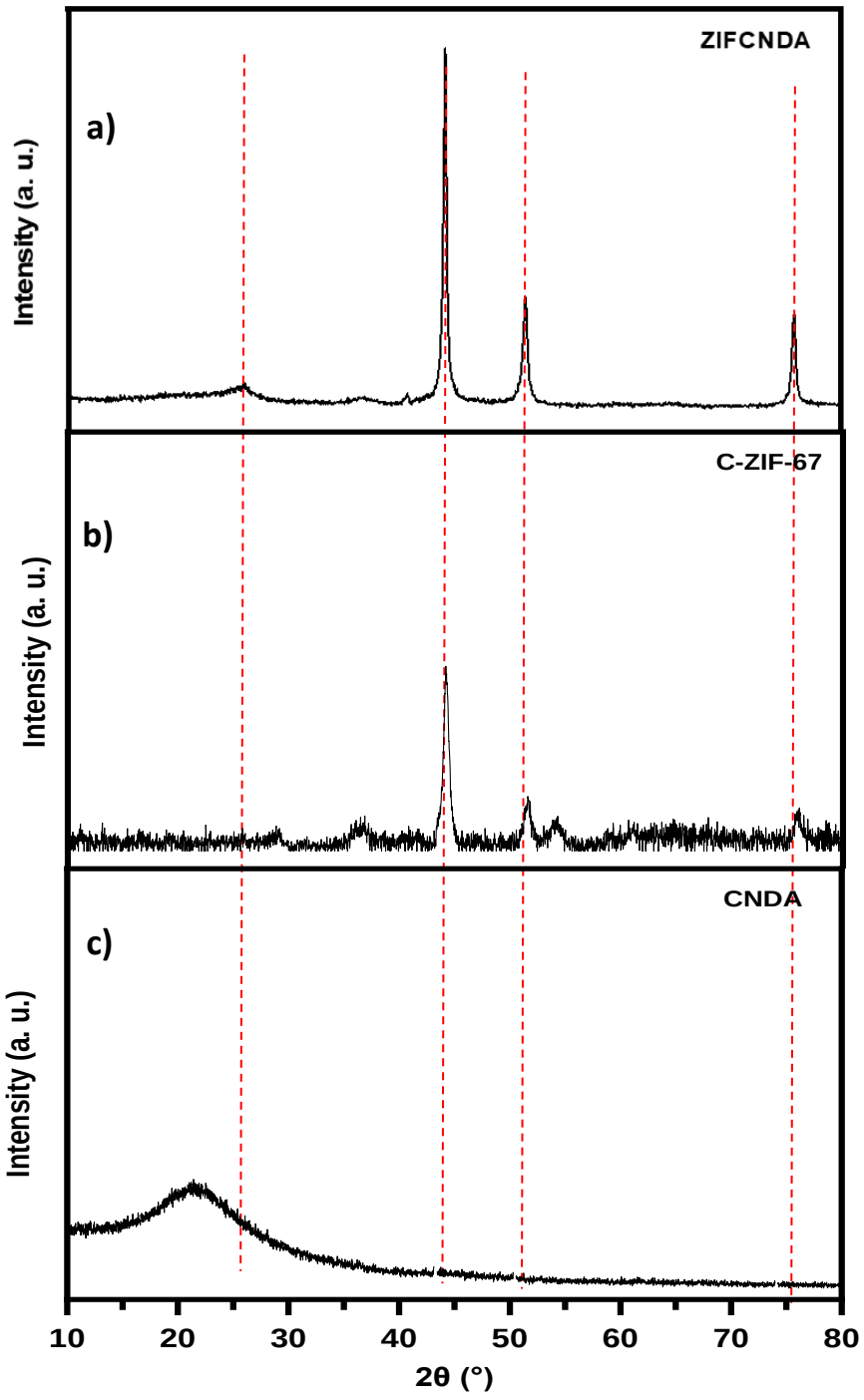

Figure 4.3: XRD patterns of a) ZIFCNDA, b) C-ZIF-67 and c) CNDA.

In accordance with the TEM results, the XRD pattern of ZIFCNDA show diffraction peaks at around 26°, 44.2°, 51.5° and 75.9°, that could be attributed to the (002) plane of graphitic carbon and the (111), (200) and (220) planes of metallic Co, respectively (JCPDS card 15-0806) (Figure 4.4a). [34,181] A shift towards higher angles of the C (002) peak at 21.5° of CNDA, assigned to amorphous carbon, indicates the formation of graphitized carbon in ZIFCNDA (Figure 4.3) and confirms the important role of Co in the formation of graphitic C.[174] The Co ions can catalytically promote the conversion of its coordinated organic linkers into graphitized carbon at high temperatures which may then enhance electrical conductivity.[174,182]

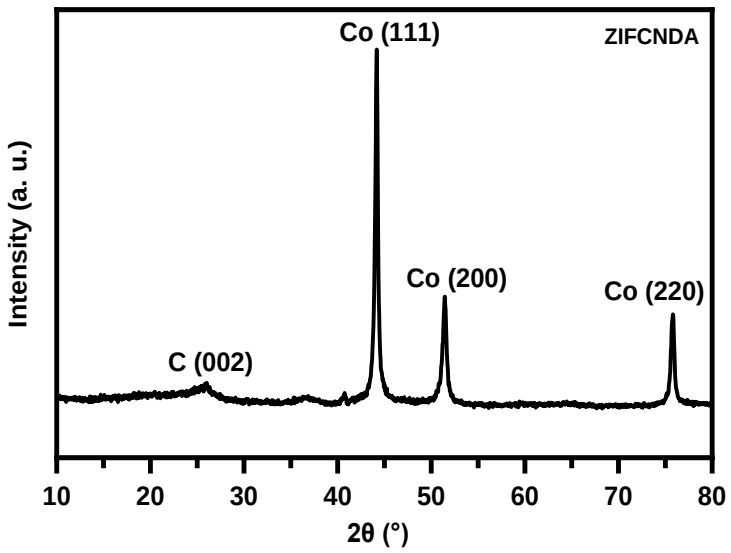

Figure 4.4: XRD pattern of ZIFCNDA.

Table 4.4: BET surface area, total pore volume and average pore radius of CPDA, CNDA and ZIFCNDA.

Sample	BET Surface area ($m^2 g^{-1}$)	Total pore volume ($cm^3 g^{-1}$)	Average pore radius (nm)
CPDA	64.1	0.20	10.6
CNDA	1590	5.08	6.20
ZIFCNDA	268	0.36	3.10

The surface area and pore structures were investigated by N_2 adsorption-desorption isotherms (Table 4.3). The ZIFCNDA catalyst shows a type IV isotherm with a hysteresis loop, suggesting the presence of mesopores (Figure 4.6a).[183,184] The ZIFCNDA catalyst presented a BET surface area of 268 $m^2 g^{-1}$ that is larger than that of CPDA (64.1 $m^2 g^{-1}$, Figure 4.6c), ascribed to the inclusion of C_3N_4 as a template for the controlled growth of the layered carbon framework, however the CNDA precursor presented a much larger BET surface area (1590 $m^2 g^{-1}$, Figure 4.6e) than that of the ZIFCNDA catalyst, possibly due to complete decomposition of C_3N_4 in these samples (Figure 4.5). Furthermore, the Co NPs formed on the ZIFCNDA catalyst structure may promote the conversion of some organic linkers into the carbon matrix while others can be decomposed as smaller molecules.[174] The rapid N_2 uptake observed at $P/P_0 > 0.8$ for CNDA indicates the existence of larger pores.[178] The BJH desorption average pore radius of the investigated composite was found to be 3.10 nm (6.20 nm diameter), which can facilitate the electrolyte access to the catalytically active sites (Figure 4.6b). The pore size reduction in comparison to those of CPDA and CNDA might be due to the coverage of some pores/defects by Co NPs (Figure 4.6d, 4.6f). Moreover, according to the BJH, the pore volume of ZIFCNDA was found to be about 0.36 $cm^3 g^{-1}$. As observed in previous studies the combination of ZIF-67-based nanoparticles and C_3N_4 originated bulky structures with random nanotubes, whereas the ZIF67-based catalyst originated well-defined nanoparticles on a carbon support due to the presence a C_3N_4 template to allow the controlled growth of polydopamine.[34,178]

The elemental compositions and chemical states of ZIFCNDA were determined by XPS. The survey spectra indicated the presence of C, N and O on CPDA and CNDA and the further incorporation of Co in the developed ZIFCNDA catalyst (Figure 4.7a). In the high resolution C1s spectra of ZIFCNDA, four peaks were fitted at about 285.1 eV, 286.3 eV, 288 eV and 290.5 eV, corresponding to sp^2 C, C-O and C=N, C-O-C and C-N,

respectively (Figure 4.7b).[151,152] These results were consistent with the C1s spectra of CPDA and CNDA observed in Figures 4.8a-b, confirming the essential presence of CPDA in the formation of a stable framework. The N1s XPS spectrum of ZIFCNDA (Figure 4.7c) was deconvoluted into a peak at 399.2 eV which includes contributions from the pyridinic N and N-Co binding energies (BE) and another one at 401.6 eV assigned to presence of graphitic N. The pyridinic N and N-Co peak binding energies are adjacent to one another and difficult to differentiate, the peak at 399.2 eV likely includes contributions from the both chemical environments.[185,186] Hence, a shift in the peak towards higher BE is observed in comparison to that of the pyridinic N peak of CPDA and CNDA due to the additional contribution of the N-Co (Figure 4.8c-d). The N on the graphitic carbon basal plane may attract Co ions to form the ZIF-67 structures.[178] The graphitic N peak did not suffer any shifts after incorporation of Co, confirmed by the comparison of the same peak of CPDA and CNDA with ZIFCNDA.

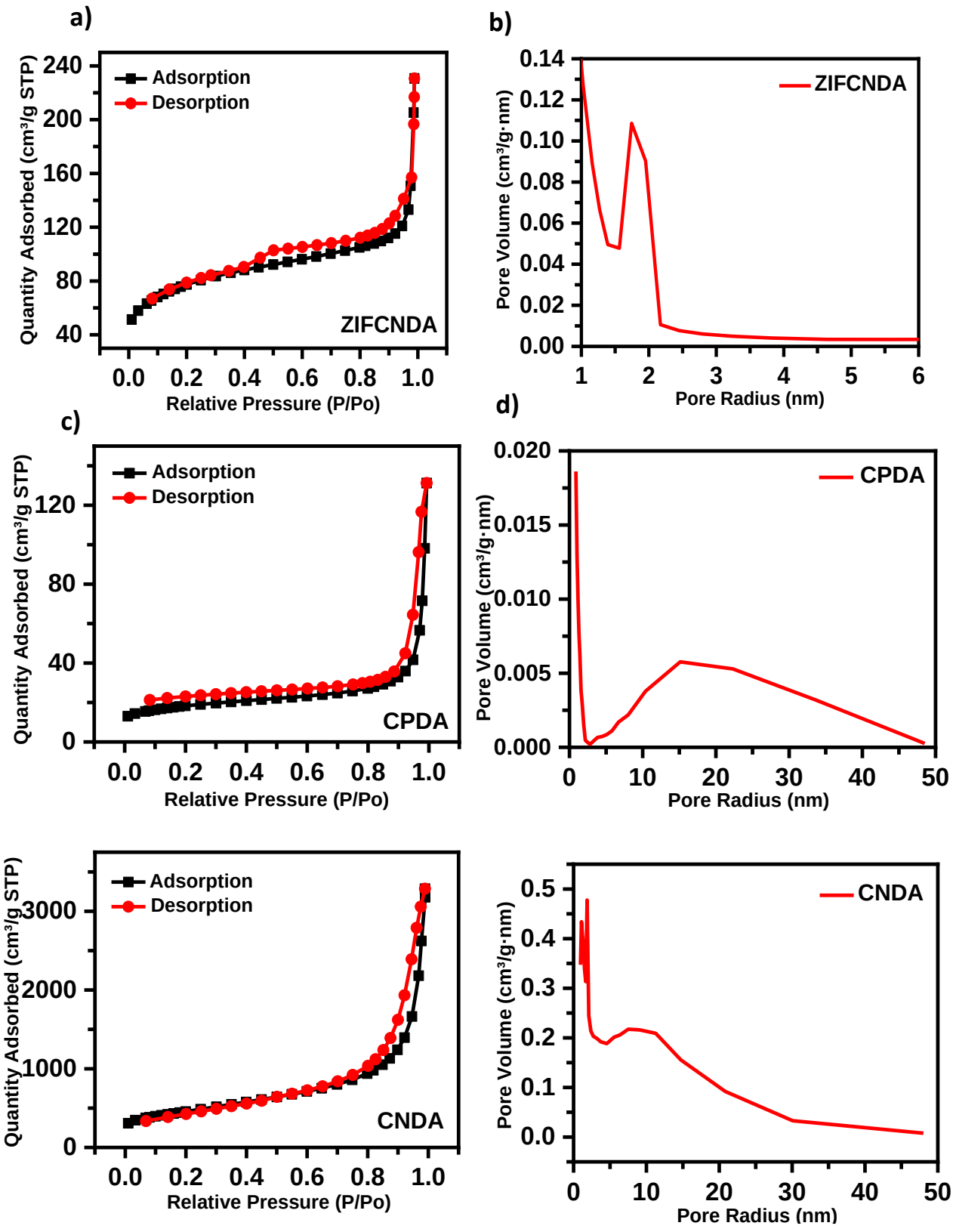

Figure 4.5: N_2 adsorption-desorption isotherms of a) ZIFCNDA, c) CPDA and e) CNDA and b, d, f) the corresponding BJH pore distributions.

Notably, the presence of pyridinic and graphitic N moieties are known to help improve the overall catalyst activity by promoting a favourable 4-electron pathway with a more positive onset potential and enhancing the limiting current density, respectively.[103,164,187] Figure 4.7d presents the Co 2p spectra of ZIFCNDA showing one main peak at 780.9 eV with a satellite peak at 786.2 eV and one main peak at 796.6 eV with a satellite peak at 803.3 eV, assignable to the Co $2p_{3/2}$ and Co $2p_{1/2}$ of Co^{2+}. The binding energy of the peaks at 780.9 eV 796.6 eV were close to those of Co-N reported for Co (II) porphyrin (cobalt ions and cross-linked N-based ligands) suggesting that the oxidized state of Co is coordinated with two adjacent atoms, indicating the formation of Co-N.[188–190] Since a higher stoichiometric ratio of C and N is required to form these sites than those available, some Co^{2+} may agglomerate as Co^0. Unreacted Co ions are reduced to Co metal which tend to agglomerate and created large particles.

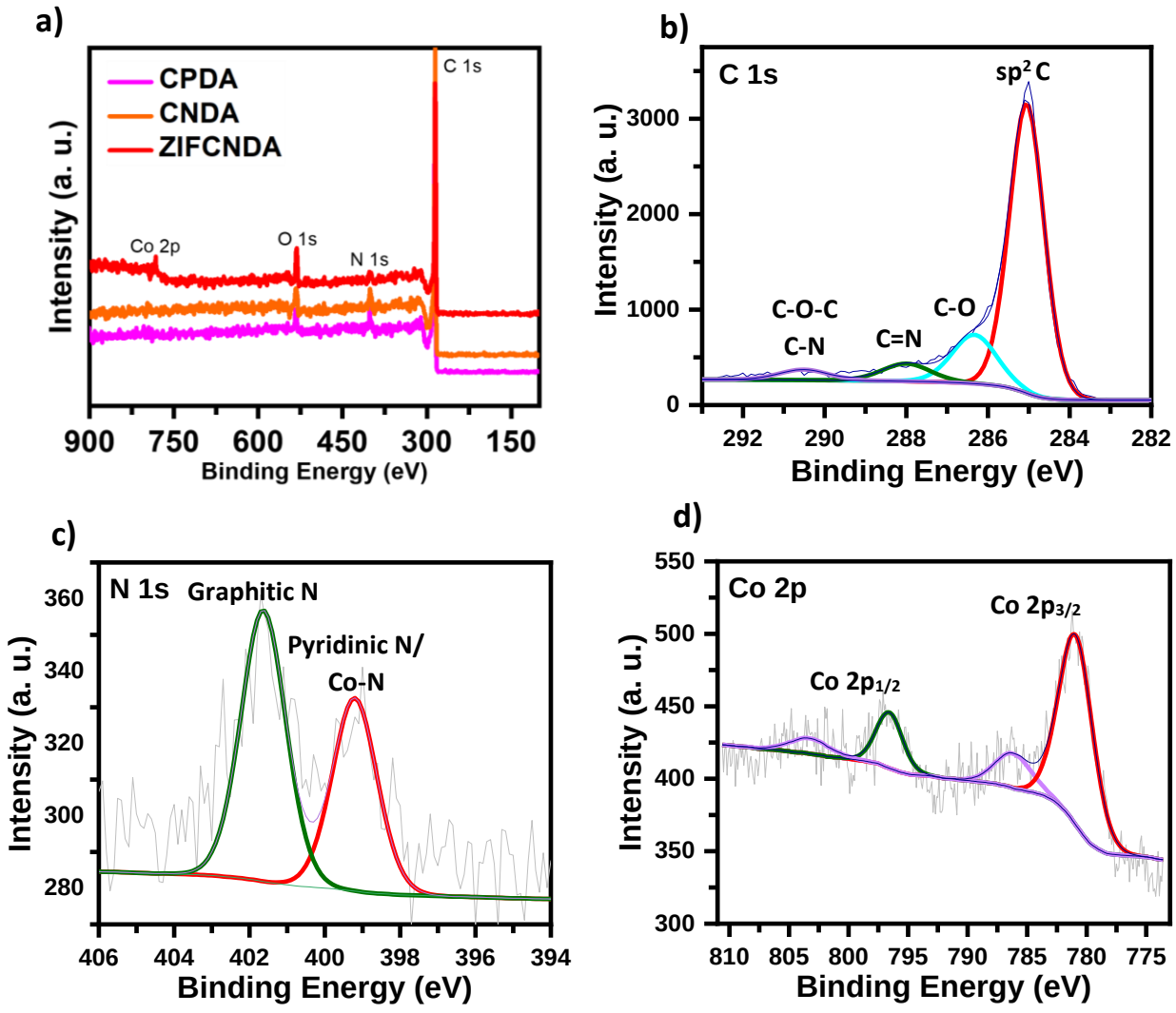

Figure 4.6: a) XPS survey spectra of CPDA, CNDA and ZIFCNDA; and the high-resolution spectrum for b) C 1s, c) N 1s and d) Co 2p of ZIFCNDA.

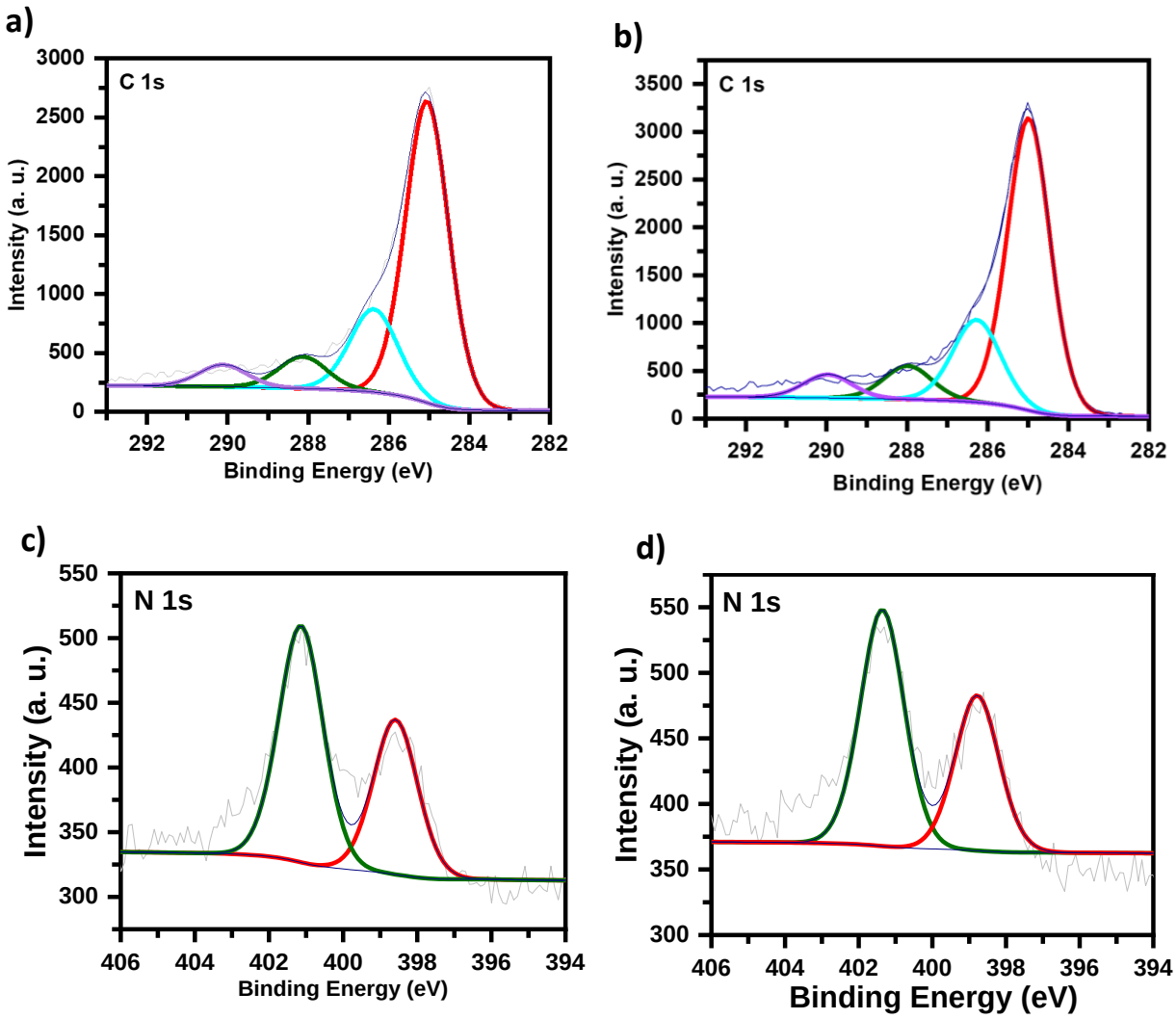

Figure 4.7: XPS high-resolution spectrum for C1s of a) CPDA and b) CNDA and N1s of a) CPDA and b) CNDA.

4.2.2. Electrochemical characterization

The electrocatalytic activity of the prepared catalysts towards ORR and OER was evaluated. Firstly, the performance of the ZIFCNDA samples prepared with different $Co(NO_3)_2.6H_2O$:Dopamine ratios (0.5, 1 and 5) was evaluated by LSV. The ORR LSV polarization curves (Figure 4.9a) reveal that ZIFCNDA-2 and ZIFCNDA-5 had the best ORR performance as observed by the lower overpotential and higher limiting current density achieved. However, ZIFCNDA-2 presented an improved overpotential as compared to ZIFCNDA-5, which is desirable for improved reaction kinetics. The OER LSV curves (Figure 4.9b) indicate that ZIFCNDA-2 delivered a higher current density with a reduced overpotential. Therefore, further electrochemical and battery tests were

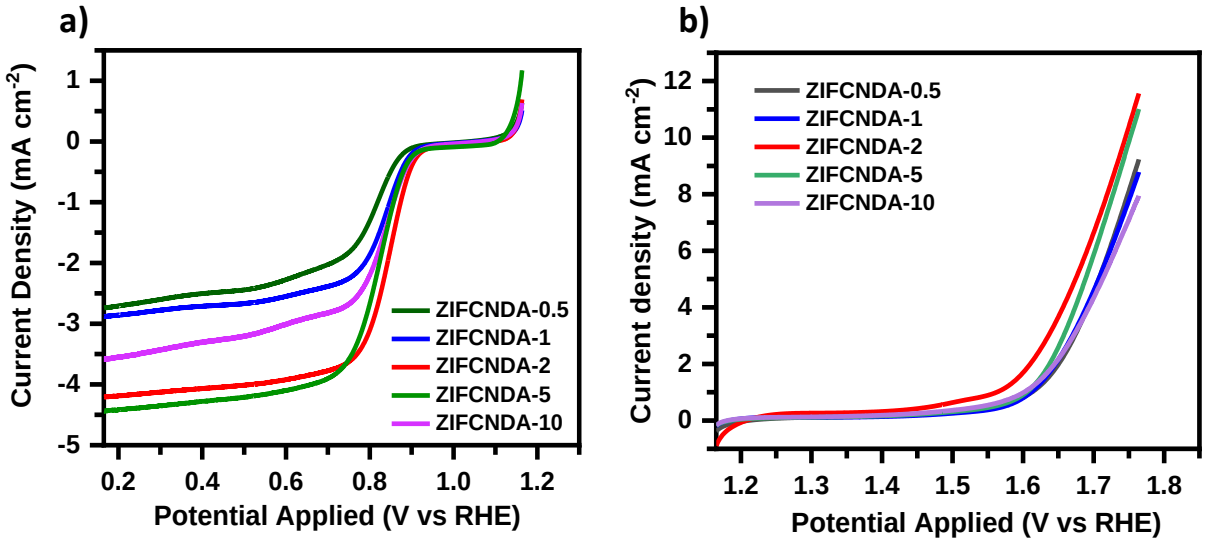

Figure 4.8: Combined LSV curves for a) ORR and b) OER of the ZIFCNDA catalyst, Co-CNDA, CNDA CPDA, C_3N_4 and Pt/C recorded at 1600 rpm and a scan rate of 5 mV s^{-1} in O_2-purged 0.1 M KOH electrolyte.

performed on the ZIFCNDA-2 catalyst, which is denoted ZIFCNDA from this point.

Initially, the ORR performance was studied in O_2-saturated alkaline electrolyte (0.1 M KOH) by CV as observed in Figure 4.10a. The final catalyst ZIFCNDA presented a positively shifted cathodic peak at 0.83 V vs. RHE, but no features were observed in the N_2-saturated electrolyte, confirming the oxygen reduction catalytic activity. The results were comparable to the peak of the benchmark Pt/C (20 wt.%) catalyst at 0.82 V vs. RHE, confirming the suitability of the electrocatalyst developed in this study. LSV

polarization curves of C_3N_4, CPDA, CNDA, Co-CNDA, ZIFCNDA and Pt/C tested by rotating disk electrode are observed in Figure 4.10b. Clearly, the ZIFCNDA catalyst showed improved ORR activity when compared to its precursors, C_3N_4, CPDA, CNDA, Co-CNDA, as observed by the greatly improved half-wave potential and limiting current density. The ZIFCNDA presented a positively shifted $E_{1/2}$ of 0.84 V and a limiting current density of 4.2 mA cm^{-2}, a comparable catalytic activity to the commercial Pt/C with a half-wave potential of 0.86 V and limiting current density of 4.4 mA cm^{-2}. These results imply an improved mass transport pathway and an increased concentration of active sites promoting O_2 adsorption and reduction. The synergistic effect between layered carbon shells and Co NPs may facilitate the electron transfer to the catalytically active sites and improve stability.[73,186]

The OER performance of the ZIFCNDA catalyst was evaluated following the ORR tests in the same 0.1 M KOH solution and the results compared to the commercial catalyst Ir/C. As presented in Figure 4.10c, the ZIFCNDA electrocatalyst achieved a current density as high as the benchmark OER catalyst, Ir/C, about 12 mA cm^{-2}, despite a higher anodic onset potential. Both CNDA and Co-CNDA precursors reached a much lower current density and a higher onset potential than the ZIFCNDA catalyst, confirming the essential contribution of the ZIF-67-based Co NPs for an improved OER performance and its promising use for rechargeable ZABs.

The electrochemically active surface area (ECSA) is proportional to the electrochemical double-layer capacitance (C_{dl}) at the catalyst-electrolyte interface and can be measured by cyclic voltammetry obtained at different scan rates at non-Faradaic potentials.[191] As observed in Figure 4.11 the notably higher C_{dl} value of ZIFCNDA of 75 mF cm^{-2} than of the benchmark Pt/C catalyst of 13 mF cm^{-2} are in good agreement with the ZIFCNDA catalyst's superior activity due to more exposed active sites. In order to further understand the ORR activity of the catalysts, ORR polarization curves were collected at different rotation speeds and the Koutecky-Levich (K-L) relations were deduced from the measured current densities and the number of electrons transferred per oxygen molecule (n) was determined (Figure 4.11). The LSV curves of ZIFCNDA

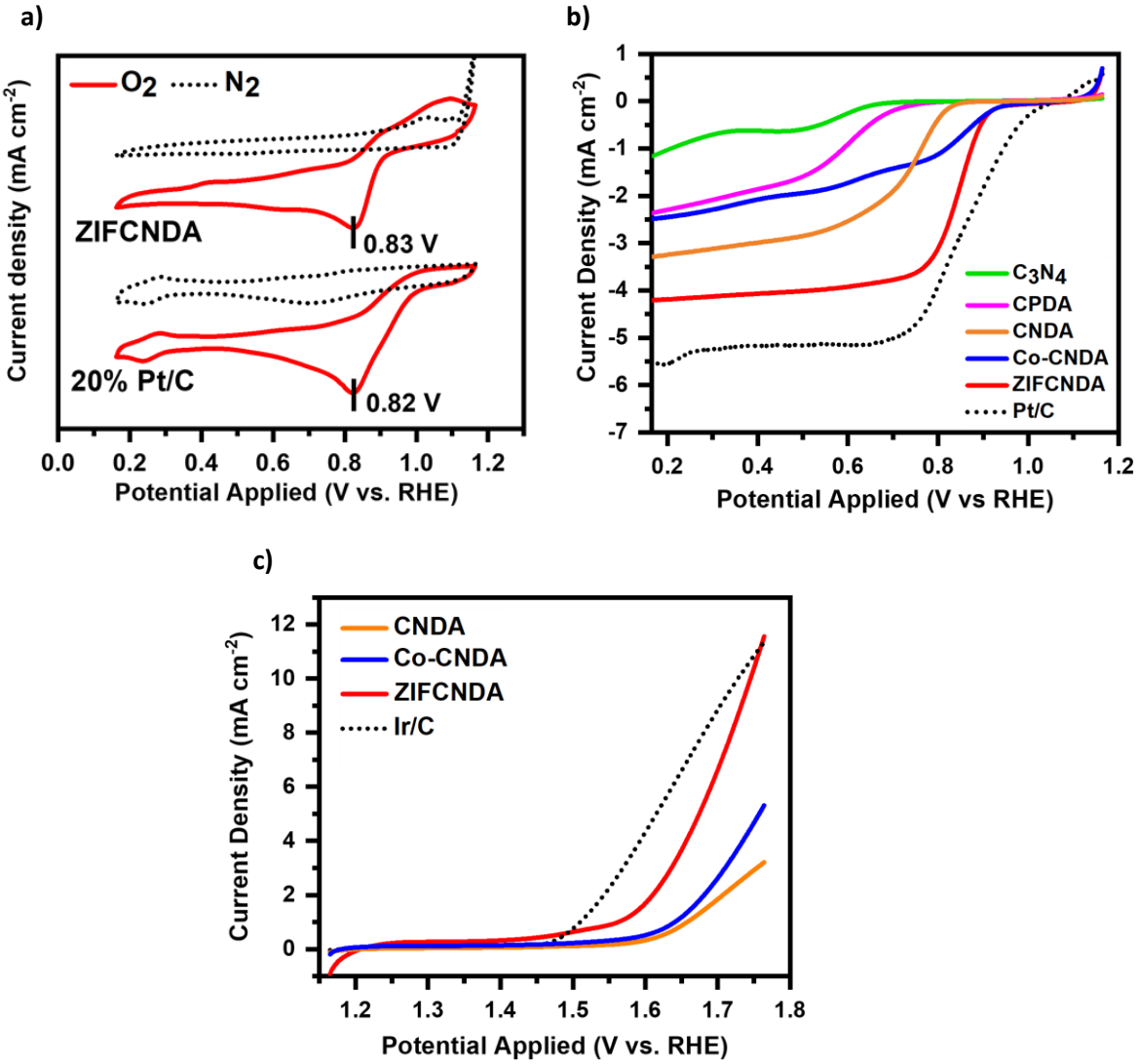

Figure 4.9: a) CV curves of the ZIFCNDA catalyst and Pt/C obtained in N_2/O_2-saturated 0.1 M KOH electrolyte. b) Combined LSV curves for ORR of the ZIFCNDA catalyst, Co-CNDA, CNDA CPDA, C_3N_4 and Pt/C at 1600 rpm in O_2-purged 0.1 M KOH electrolyte. c) Combined LSV curves for OER of ZIFCNDA, Co-CNDA and CNDA in 0.1 M KOH electrolyte. The scan rate was kept at 5 mV s^{-1} for all the measurements.

(Figure 4.11a) showed a wide and steady plateau suggesting a diffusion-controlled ORR and the correspondent linear and parallel K-L slopes (Figure 4.11b) suggested first-order reaction kinetics with respect to the concentration of O_2 dissolved in the electrolyte. The average n value for the potential range of 0.2-0.6 V vs. RHE was calculated to be of 3.9 for the ZIFCNDA catalyst, higher than an n value of 3.7, calculated for CNDA, suggesting an improved electron transport upon inclusion of the cobalt-based nanoparticles (Figure 4.11b and 4.11d). This was also comparable to the theoretical value of 4 for the Pt/C benchmark catalyst, suggesting a favourable 4-electron transfer pathway by avoiding the production of detrimental hydroperoxide.[164]

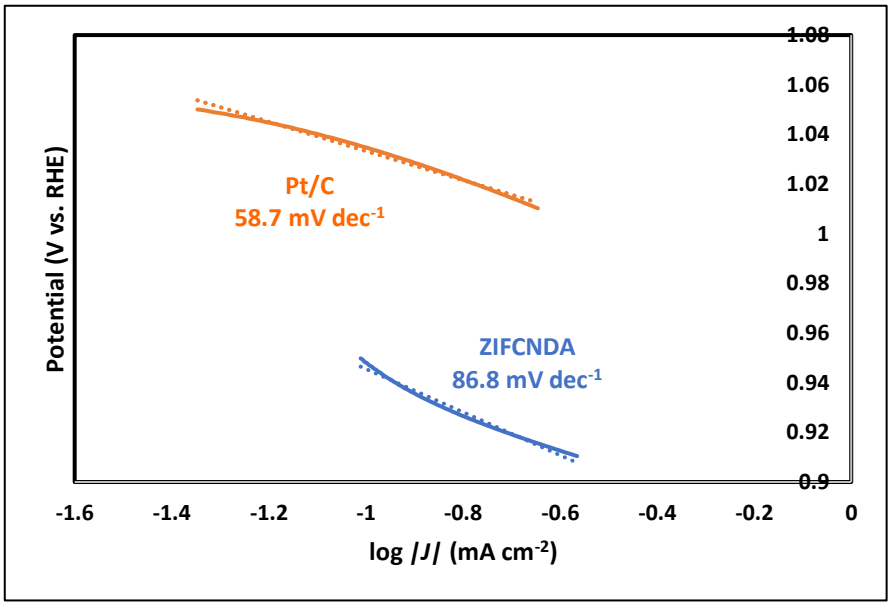

Figure 4.10) Tafel plots of ZIFCNDA and 20 wt% Pt/C obtained at 1600 rpm in O_2-saturated 0.1M KOH.

The Tafel plots of the ZIFCNDA catalyst, and the commercial Pt/C are presented in Figure 4.10. The developed ZIFCNDA catalyst presented a higher Tafel slope of 86.8 mV dec^{-1} corresponding to a slightly lower cathodic reduction current increase in comparison to the benchmark Pt/C catalyst.

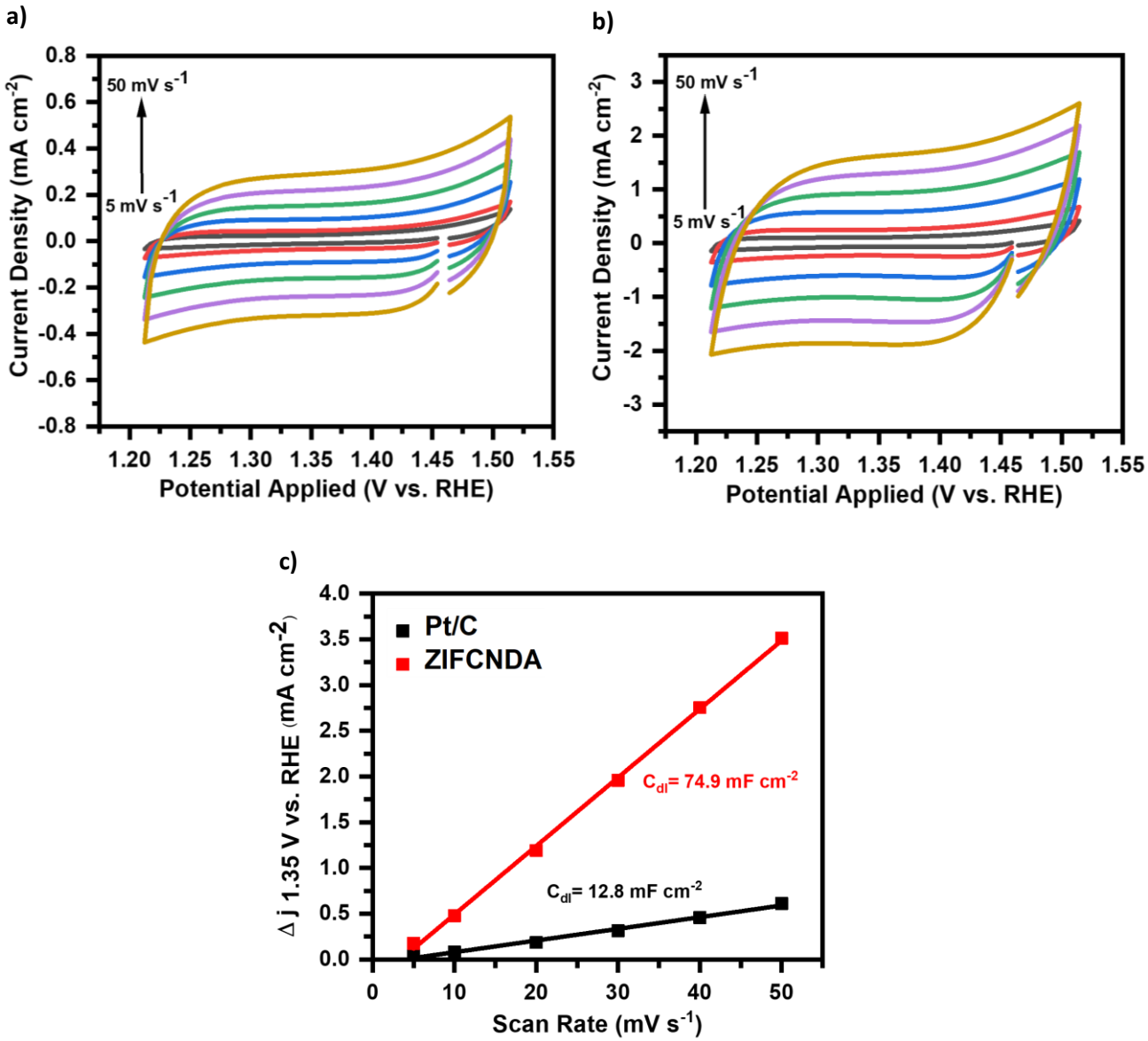

Figure 4.10: CV curves of a) Pt/C and b) ZIFCNDA at scan rates from 5 to 50 mVs^{-1} within 1.20 to 1.50 V vs. RHE. c) the corresponding linear fitting of the capacitive current densities at an overpotential of 1.35 V vs. RHE against the scan rates of Pt/C and ZIFCNDA electrodes.

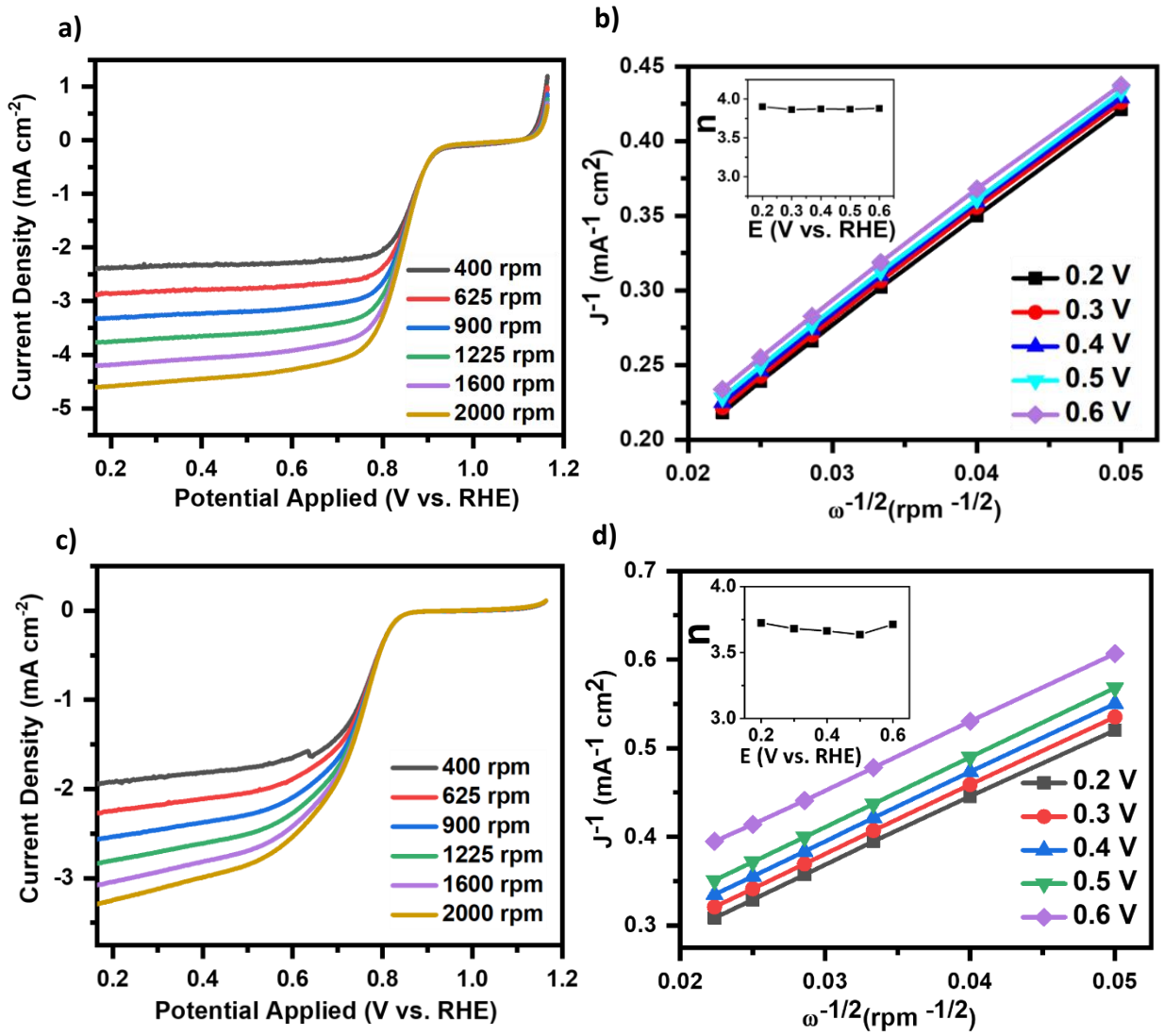

Figure 4.11: LSV curves of a) ZIFCNDA and c) CNDA recorded at different rotation speeds (rpm) and a scan rate of 5 mV s^{-1}. K-L plots of b) ZIFCNDA and d) CNDA calculated from its RDE LSV curves at the potential range 0.2-0.6 V vs. RHE; the inset: plot of n (electron transfer number) per O_2 molecule at the different potentials.

The long-term stability of the developed catalyst towards the ORR was analysed by chronoamperometric (current vs. time, *i-t*) experiments. The results presented in Figure 4.12a show that the ZIFCNDA catalyst was able to retain 96.8 % of its initial current after 15000 min at 0.4 V with a continuous O_2 flow. Despite being the benchmark catalyst for ORR, Pt/C was only able to conserve 83.8 % of its initial current after the same period of time. The methanol tolerance of the studied catalyst was also evaluated by chronoamperometric measurements. As presented in Figure 4.12b, upon addition of 5 mL of methanol to the O_2-saturated alkaline electrolyte only a slight reduction in the

current density was observed for the ZIFCNDA catalyst, whereas a sharp drop in current was detected for the Pt/C. These results further confirm the enhanced selectivity towards ORR of the developed catalyst and resistance to methanol crossover. Furthermore, the accelerated degradation tests (ADT) confirmed the durability of the ZIFCNDA catalyst since its LSV curve (Figure 4.12c) only shifted by 10 mV at a current density of – 1 mA cm^{-2} after 400 cycles.

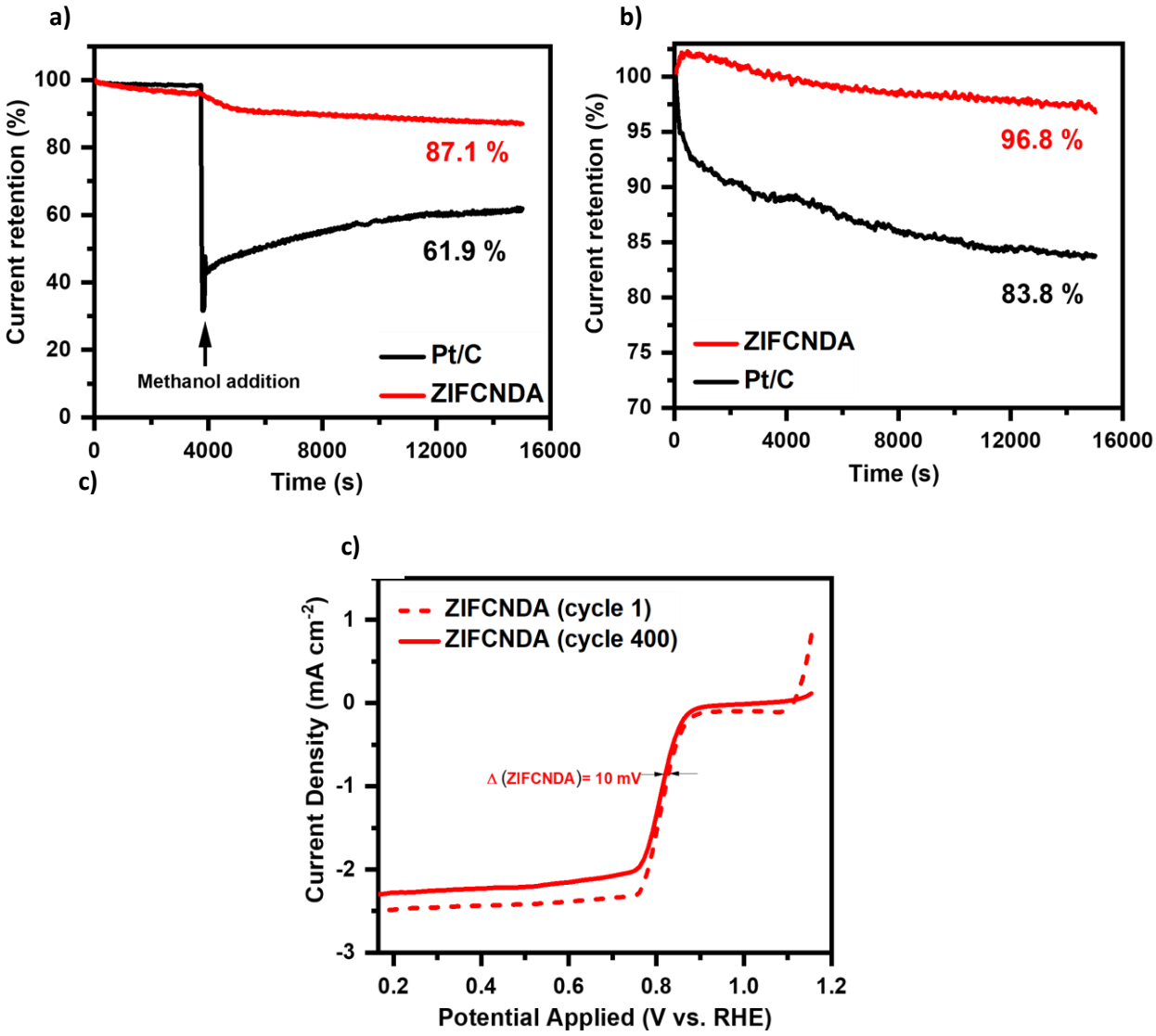

Figure 4.12: a) Chronoamperometric stability plots (i-t plots) of ZIFCNDA and Pt/C at 0.4 V and a fixed electrode rotation speed of 400 rpm in O_2-saturated 0.1 M KOH electrolyte. b) I-t plots of ZIFCNDA and Pt/C at 0.4 V and a fixed electrode rotation speed of 400 rpm in O_2-saturated 0.1 M KOH electrolyte with addition of 5 mL MeOH. c) ADT plots of ZIFCNDA before (dashed lines) and after (solid lines) 400 cycles for ORR at a fixed electrode rotation speed of 400 rpm. The scan rate was kept at 5 mVs^{-1} for all the measurements.

4.2.3. Zinc-air battery performance

Figure 4.13 shows the polarization and power density curves of the ZABs containing the ZIFCNDA and Pt/C electrocatalysts. The Pt/C-based cell achieved a maximum power density of 43 mW cm^{-2} at a current density 54 mA cm^{-2} but the addition of the ZIFCNDA electrocatalyst to the air cathode resulted in a cell activity improvement, which achieved a power density of 57 mW cm^{-2} at a current density 71 mA cm^{-2}.

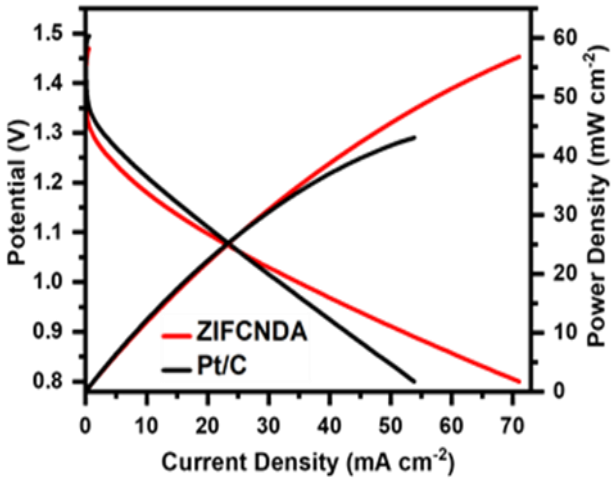

Figure 4.13: Polarization and power density curves of ZABs using ZIFCNDA and Pt/C as catalyst in 6 M KOH electrolyte.

Furthermore, the ZIFCNDA- and Pt/C-based ZABs were discharged at different current loads (5, 10 and 15 mA cm^{-2}) to evaluate their durability (Figure 4.14a-c). At all three current densities, the ZIFCNDA-based tested batteries presented similar flat discharge voltage plateaus to that of their Pt/C counterpart. In all long-term discharge plots the ZIFCNDA-based ZABs discharging time surpassed that of the Pt/C-based cells. Upon discharge at 5 mA cm^{-2} (Fig. 4.14a), the ZIFCNDA-based battery showed a similar initial discharge voltage to that of the Pt/C-based ZAB (1.2 V vs. 1.3 V) and achieved a maximum discharging time at nearly 600 h, 100 h longer than that observed for Pt/C. Additionally, the ZIFCNDA-based battery demonstrated a specific capacity of 686 mAh g^{-1} (normalized to the mass of consumed Zn), higher than that observed for the battery containing the commercial Pt/C 570 mAh g^{-1} (Figure 4.14d). The galvanostatic discharge plots of the ZIFCNDA-containing ZABs at increasing current densities (Figure 4.15) presented stable, flat and higher discharge voltage, particularly at 30 mA cm^{-2} when a high discharge voltage of 1.14 V was achieved, in comparison to 1.11 V of Pt/C.

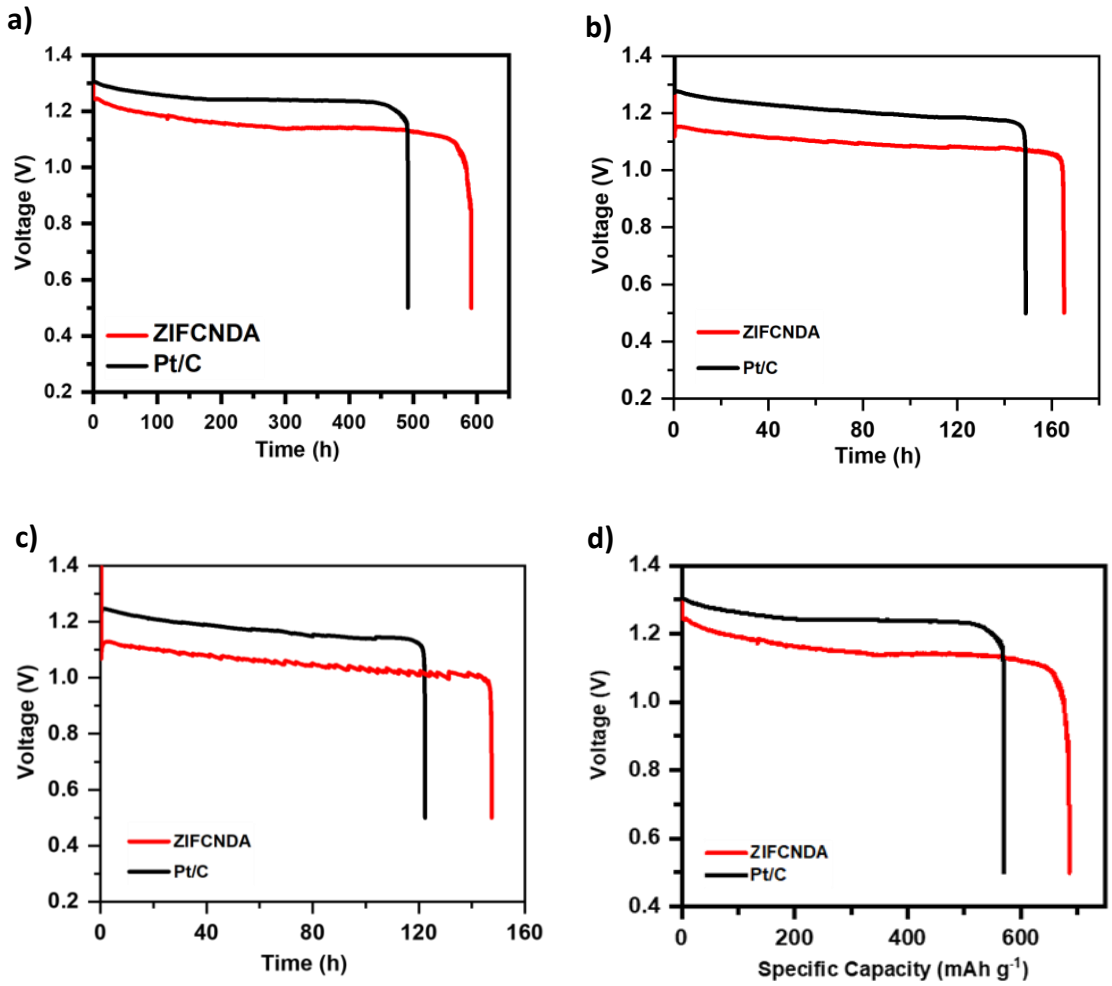

Figure 4.14: Long term discharge curves of ZABs with ZIFCNDA and Pt/C as the cathode catalyst in 6 M KOH electrolyte at a) 5 mA cm^{-2}, b) 10 mA cm^{-2} and c) 15 mA cm^{-2}. d) Specific capacity curves of ZABs with ZIFCNDA and Pt/C as the cathode catalyst, at 5 mA cm^{-2}.

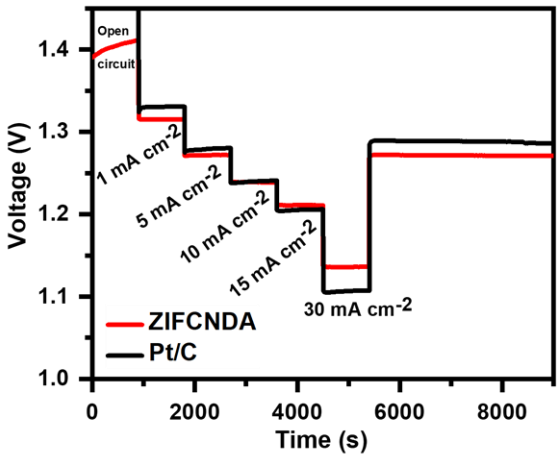

Figure 4.15: Voltage profiles of ZIFCNDA and Pt/C-based ZABs catalyst in 6 M KOH electrolyte when discharged at different current densities: 1, 5, 10, 15 and 30 mA cm^{-2}.

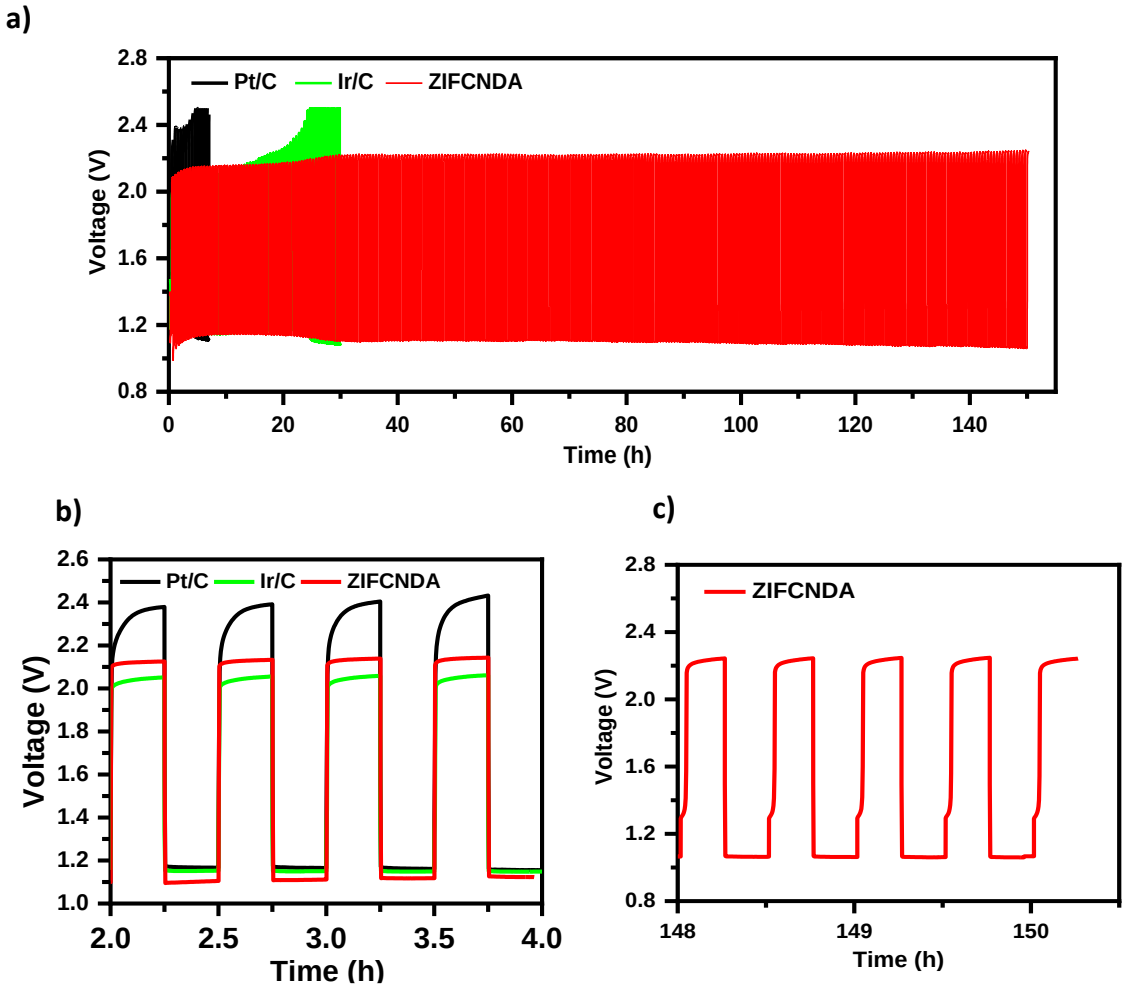

Figure 4.16: a) Discharge-charge cycling performances of ZABs with ZIFCNDA, Pt/C and Ir/C catalyst at 10 mA cm^{-2}. b and c) Selected sections of the cycling performances from c). All cells were tested in 6 M KOH electrolyte.

Zinc-air batteries containing the developed ZIFCNDA or the benchmark electrocatalysts (e.g. Pt/C or Ir/C) as the air-cathode were prepared and subjected to galvanostatic discharge-charge cycling at 10 mA cm^{-2} or 15 mA cm^{-2} (Figure 4.16a and 4.17). When a current density of 10 mA cm^{-2} is applied, the ZIFCNDA-based ZAB presented great stability and rechargeability for over 150 h, much longer than the life cycle of the Pt/C and Ir/C-based Zn-air batteries (7 h and 30 h). An initial voltage gap of 1.0 V was observed for the ZIFCNDA-driven ZAB, obtained from discharge and charge voltages of 1.1 V and 2.1 V respectively, comparable to the Ir/C containing battery and superior to the Pt/C-based battery, which presented a larger voltage gap of 1.2 V (Figure 4.16b). After 25 h, the battery containing the Ir/C electrocatalyst started degrading, increasing its voltage gap up to 1.4 V, while the ZIFCNDA-based ZAB suffered a slight voltage gap broadening of 30 mV, confirming its greater durability. Finally, after 300

cycles (approximately 150 h), the ZIFCNDA-based battery was able to continue to cycle with a voltage gap of 1.19 V, provided by a discharging voltage of 1.06 V and a charging voltage of 2.3 V (Figure 4.16c). The final discharge voltage suffered a mere drop of 50 mV while the charge voltage increased by 110 mV, leading to an overall increase in the voltage gap of only 164 mV than in the first cycle. Remarkably, even at a current of 15 mA cm^{-2} the ZIFCNDA-based ZAB was able to cycle at a reasonably constant voltage gap for 65 h, whereas the battery with the Ir/C catalyst quickly degraded after only 15 h, with the Pt/C-based cell struggling to charge throughout (Figure 4.17). The reduced overpotentials reflect the greater energy efficiency and bifunctional activity of the prepared catalyst, which reduce the degradation of the catalyst and consequently increase the battery-life.

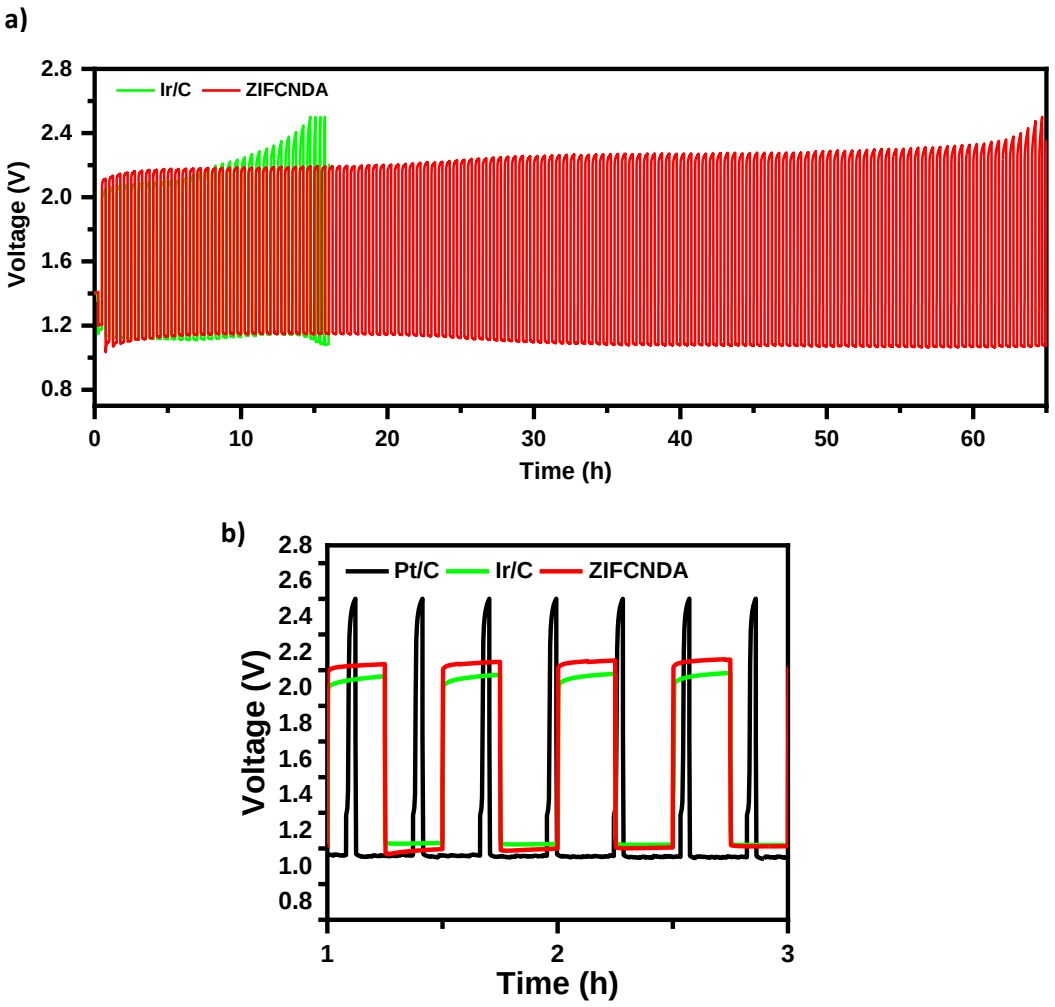

Figure 4.17: a) Discharge-charge cycling performances of ZABs with ZIFCNDA, Pt/C and Ir/C catalyst at 15 mA cm^{-2} in 6 M KOH electrolyte. b) Selected section of the cycling performance from a).

4.3. Conclusion

In summary, an efficient bifunctional electrocatalyst composed of naturally dispersed Co NPs surrounded by graphitic carbon shells on a N-doped carbon substrate was developed. This simplified strategy involved the introduction of Co ions along with the polymerisation of dopamine, leading to the direct doping of the carbon framework and further localized growth of Co-based MOFs polyhedrons which then generated Co-based NPs upon pyrolysis. Furthermore, the addition of C_3N_4 controlled the polydopamine growth to form thin carbon nanosheets which could then be graphitized during high temperature annealing, helping to facilitate the electron transfer to the catalytically active sites. This approach also restrained the formation of unstable loose particles while also preventing their aggregation and generating a porous structure. The ZIFCNDA catalyst presented an improved activity in comparison to the benchmark ORR and OER catalysts, Pt/C and Ir/C, respectively. The essential contribution of the Co NPs for a great bifunctional activity was demonstrated by the poor activity of the nanoparticles-free composite (CNDA) and Co-CNDA, which also confirmed the essential addition of the 2-MeIM ligand for the formation of stable Co NPs. The ZIFNCDA-containing ZABs presented an outstanding activity during the long-term discharge analysis at 5 mA cm^{-2}, reaching a 600 h maximum discharging time, 100 h longer than the Pt/C benchmark as well as a higher specific capacity of 686 mAh g^{-1}. The cell was able to cycle for 150 h at 10 mA cm^{-2} with a mere increase in the voltage gap of 164 mV and even at a higher current density of 15 mA cm^{-2}, the ZIFCNDA-based cell was able to cycle at a constate voltage for 65 h, surpassing both Pt/C and Ir/C-based cells.

5. Pyrolyzed ZIF-67 Particles Encapsulated into Polydopamine Coated Porous Nanofibers as an Electrocatalyst for Zinc-Air Batteries

5.1. Introduction

Following the successful preparation of a bifunctional ORR and OER catalyst composed of Co/N-C particles obtained from ZIF-67 supported on a C_3N_4/Polydopamine-derived graphitic carbon framework, an attempt to develop a bifunctional catalyst with an improved catalytic performance and more stable structure is reported in this chapter.

Accordingly, electrospinning of nanostructured precursors is an efficient and versatile technology to prepare structure- and composition-tailored nanofibers. The structure of elecrospun nanofibers can be tuned to obtain the desired pore structure, heteroatom doping and functional groups, which are significant parameters for the development of efficient catalysts.[192,193] Fibers with a mixed pore structure and a high surface area can enhance ion diffusion, electrolyte penetration, mass transportation, and aid the exposure of desirable active sites.[194] The interconnected fibrous framework may provide various electron conductive pathways while maintaining good stability and mechanical strength, favouring the catalytic reactions.[195]

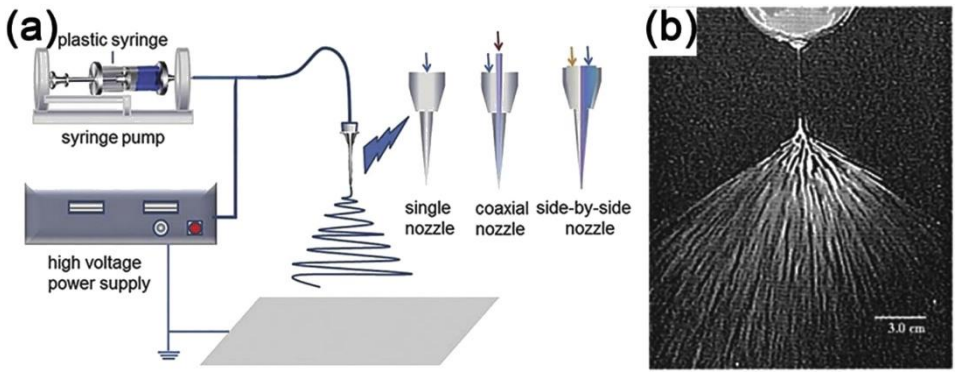

Figure 5.1: a) Schematic illustration of a laboratory electrospinning set up. b) Image of an electrospinning jet. [211]

As shown in Figure 5.1 an electrospinner is composed of a supply device such as an injector, a high-voltage power supply and a collector (usually a drum or a metal plate).[196] In this process, under the action of a high-voltage electrostatic field, a charged polymer solution or melt overcomes its own surface tension to form small jets which are

then accelerated and stretched in the electric field. The polymer jets then fall on the collector after solvent evaporation or melt cooling to finally form fibers.[197] A solution for electrospinning must include a polymer with a reasonably high molecular weight dissolved in a suitable solvent. The organic solvents found suitable for electrospinning can be divided into hydrophilic polymers such as polyvinyl alcohol (PVA)[198], polyethylene oxide (PEO)[199], and polyvinylpyrrolidone (PVP)[200]; and hydrophobic polymers such as polyacrylonitrile (PAN)[201], polylactic acid (PLA)[202], polystyrene (PS)[203], polyvinylidene fluoride (PVDF)[204], to name but a few. Different factors can affect the structure of the electrospun fibers. Firstly, the viscosity of the polymer solution must be suitable to be electrospun into fibers.[205] Secondly, operating parameters such as the feeding rate, spinning distance and spinning voltage may affect the spinning stability and fiber separation.[206] As an example, the spinning distance may affect the electric field strength and solvent volatility, altering the diameter and morphology of the fibers. If the voltage is either too high or too low, polymer beads may form. External factors such as ambient humidity and temperature may influence the solvent volatilization rate and alter the desired fiber structure.

Considering the advantages of electrospun nanomaterials, their application in ORR and OER catalysis has been recently investigated. Strategies including heteroatom doping and surface etching have been applied to improve the electrocatalytic activity of pure carbon nanofibers (CNFs). As previously mentioned, heteroatom doping may tune the surface polarity, change charge distribution and electronic properties and induce carbon defects. Carbon nanostructures are likely to be more catalytically active if they contain surface functional groups, edge dangling bonds and defective sites. A metal-free catalyst with high activity and good selectivity towards ORR composed of free-standing N-doped CNFs (NCNFs) obtained from electrospun PAN nanofibers was reported by Liu et al. The NCNFs were prepared by reusing the byproduct obtained from the thermal treatment of PAN, NH_3-containg gas, for nitrogen doping and surface etching.[207] Jiang et al. developed N-doped CNFs (N-PCNF) by electrospinning a mixture of PAN and PMMA, followed by pyrolysis. A sacrificial template method was used to effectively prepare high active site composites, with carbon defects, high porosity, surface roughness and N-doping. An excellent electrocatalytic activity and durability toward ORR was reported.[208] Park et al. fabricated N-doped carbon fibers (N-CFs-1100) with a churro-like arquitecture by electrospinning a mixture solution composed of PS and PAN. After pyrolysis of the electrospun fibers, nanofibers with very high surface area were collected

due to the gradual decomposition of PS. The ORR activity was reported to improve due to the formation of surface-exposed graphitic and pyridinic N.[209]

Transition metal (TM)/CNF composites have recently been considered for oxygen electrocatalysis. Gupta et al. proposed a model describing the adsorption of a transition metal (eg. Fe, Co) onto a modified carbon surface through interactions with residual nitrogen derived from heat-treated macrocycles. The study reported that the nitrile nitrogen of PAN was probably retained and converted to pyridyl nitrogen during the heat treatment, then this nitrogen provided binding sites for the TM ions, which then acted as catalytic sites.[210] The catalytic activity of TM coupled with N-doped carbons has been reported to be close to that of noble-metal based catalysts.[211] Accordingly, nanofiber precursors contain abundant N species which can combine with metal species and form uniformly distributed active sites. Zhu et al. reported that TM (Fe or Co) and N-doped electrospun nanofibers showed greater ORR activity than that of metal-free nanofibers doped only with N.[212] The TM-N_4 clusters embedded between two graphene edges and pyridinic N derived carbon atoms were proposed to be the active catalytic sites. Furthermore, Kim et al. proposed a free-standing N and Fe co-doped CNFs and graphene (N/Fe-CG) hybrid by electrospinning a mixture containing PAN, graphene oxide (GO) and $FeCl_3$, followed by heat treatment.[213] The electrocatalytic performance of CNFs was improved due to the introduction of a carbonaceous material, increasing the electrical conductivity and catalytic surface area. MOF-based electrocatalysts have been recently explored because of their ability to achieve a specific structure and tunable porosity at the molecular level by adjusting both metal species and organic ligands.[214] The coexistence of variable pore sizes can significantly enhance their adsorption capacity and electrical conductivity. Additionally, the nanofibers and active components cohesiveness increases the stability of the MOF-derived composite.[215] However, MOF particles may aggregate during pyrolysis, limiting the surface area and lead to pore collapse.[216] Electrospinning is a simple and efficient strategy that may be used to anchor MOF particles and form a porous and stable structure. Hierarchically porous N-doped CNFs embedded with Fe_3C nanoparticles (Fe_3C/NCNFs) were developed by electrospinning a mixture containing iron-based MOFs (Fe-MIL-88B-NH_2) and PAN precursors.[217] The electrocatalyst showed superior greater ORR activity compared with that of the benchmark Pt/C due to its unique morphology and highly dispersed Fe_3C NPs. Due to the different chemical properties of MOFs and polymer fibers, an uniform growth on the polymer fiber's surface is difficult to obtain. Therefore, an in-situ growth method to prepare 1D structure-

controllable ZIFs with a PAN core and shell fiber (PAN@ZIFs) was proposed.[218] Initially, the as-prepared PAN/PVP/$Co(acac)_2$ nanofiber precursor was immersed into a $Co(NO_3)_2$/MeOH solution to promote ZIF-67 in-situ growth while the PVP was completely dissolved in MeOH, providing very large pores for a uniform MOFs growth.

Considering the previously described challenges, a composite was prepared by electrospinning ZIF-67 particles with PS and further coating by self-polymerized PDA. Upon pyrolysis, a structure composed of Co-N-based nanoparticles coated by porous N-rich graphitic carbon nanofibers were obtained. The PS served as a porous template which decomposed at a high temperature and the polydopamine coating allowed the formation of a conductive graphitic carbon layer, promoting electron mobility towards the active sites.[209] Additionally, the porous carbon coating protects and stabilizes the active materials controlling the structural integrity of the electrode during change and discharge.[115] A rational adjustment of the electrospinning parameters, ZIF-67 and PS content and number of PDA layers led to the formation of an efficient bifunctional electrocatalyst for both ORR and OER.

5.2. Results and discussion

5.2.1. Preparation and structural characterization

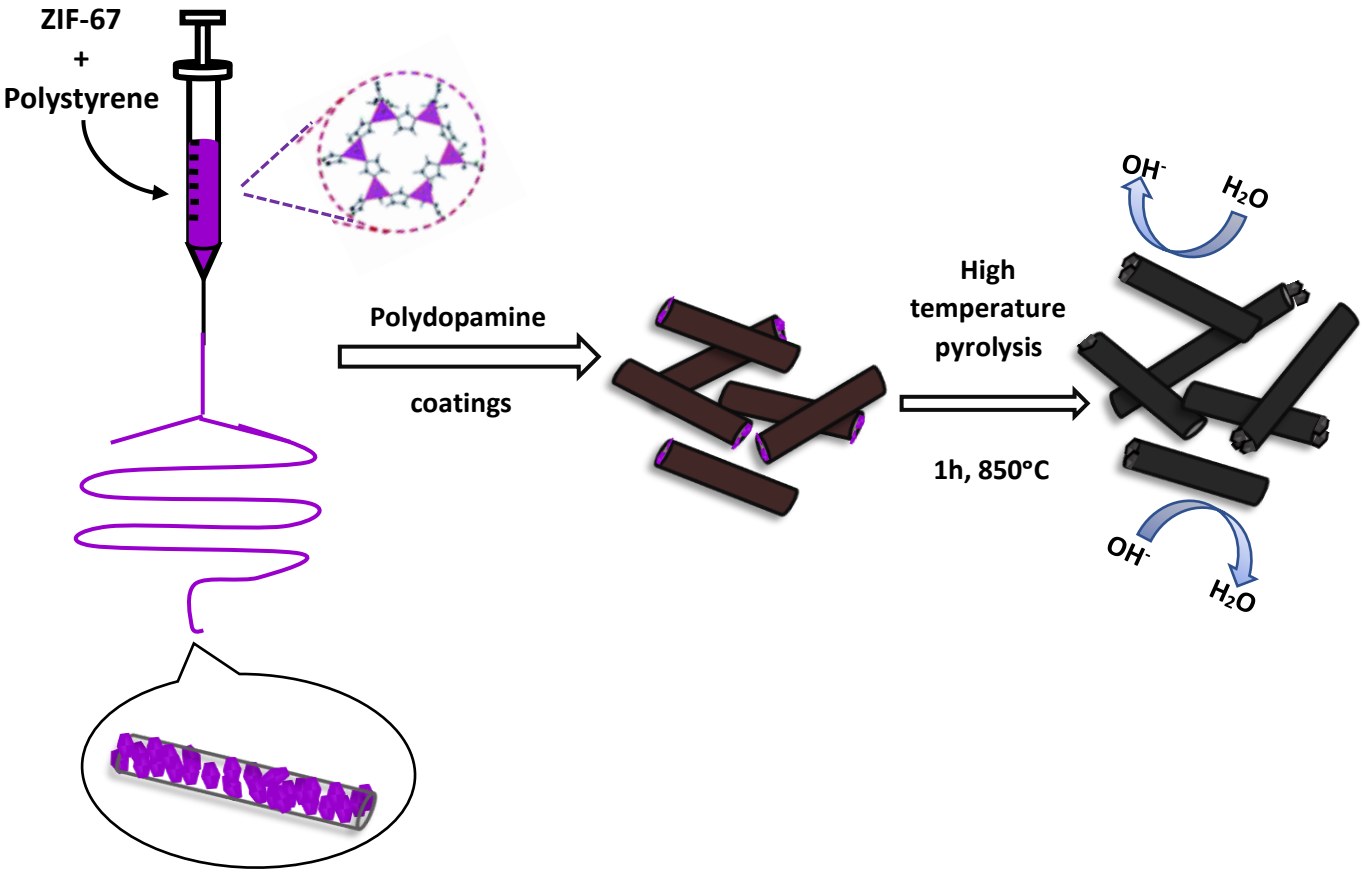

Scheme 5.1: Schematic illustration of the reaction procedure of C-ZIF-67:PS-1-XDA.

Table 5.1: Experimental details for the synthesis of the different materials prepared.

Material	Synthesis conditions
ZIF-67 and C-ZIF-67	1) Two distinct solutions of $Co(NO_3)_2.6H_2O$ in (0.023 g ml^{-1}) and 2-methylimidazole (0.025 g ml^{-1}) in methanol were prepared.[115] Equal volumes of the two solutions were mixed under vigorous stirring and a blue-violet solution was instantly formed. The mixture solution was stirred for 20 min and then left to rest for 12 h. 2) A violet precipitate was collected by centrifugation and methanol washing, followed by vacuum drying at 80˚C for 2h 3) The pyrolysis of ZIF-67 was carried out in a tube furnace at a ramping rate of 5˚C min^{-1} and kept at 850˚C for 1h, under an argon atmosphere (C-ZIF-67).
C-ZIF-67:PS-1-X (X = 1, 2, 3 or 4)	1) Preparation of ZIF-67 and PS suspension for electrospinning: PS was added to DMF (0.30 g ml^{-1}) and vigorously stirred (350 rpm, 5h, 60˚C) and then allowed to cool to room temperature. Separately, a suspension was prepared by adding ZIF-67 powder to DMF, vigorously stirring for 30 min, followed by 1h probe ultrasonication and further stirring for another 30 min. Then the ZIF-67 suspension was mixed with the polystyrene solution and stirred overnight to obtain a mixture with a 1:1 ZIF-67:PS ratio. Suspensions with 0.5:1 and 2:1 ratios of ZIF-67:PS were also prepared (ZIF-67:PS-X, X=0.5, 1 or 2). 2) Preparation of electrospun PS and ZIF-67 composite fibers (C-ZIF-67:PS-X): The previously prepared ZIF-67:PS suspension was loaded into a syringe and mounted with a 22-gauge blunt needle tip. The mixture was electrospun at a feeding rate of 0.6 ml h^{-1}, under a working voltage of 18 kV, and a spinneret width and speed of 30 mm and 10 mm sec^{-1}, respectively. The fibers were collected into an ethanol bath

	at a distance of 20 cm between the needle tip and ethanol surface. The samples were then pyrolyzed in a tube furnace (5˚C min^{-1}, 850˚C, 1h, Ar) and denoted C-ZIF-67:PS-X (X=0.5, 1 or 2). 3) Preparation of carbonized PDA coated ZIF-67:PS-1 fibers (C-ZIF-67:PS-1-XDA): The ZIF-67:PS-1 fibers were immersed in a 0.5 mg ml^{-1} aqueous solution of dopamine (20 min shaking and 40 min rest). The coating of the prepared fibers was triggered by in situ polymerization of DA by addition of 1.21 mg ml^{-1} of trizma base (20 min continuous shaking and 2h40 rest). This coating process was repeated for another 3 times using fresh solutions to achieve a series of coating layers. Thereafter, the fibers were washed with DI water and freeze dried for 48 h. Finally, the coated fibers were annealed (5˚C min^{-1}, 850˚C, 1h, Ar) (C-ZIF-67:PS-1-XDA).

Scheme 5.1 illustrates the synthetic process of C-ZIF-67:PS-1 and its coated versions (Table 5.1, refer to Sections 2.3.1, 2.3.4 and 2.3.5). Briefly, ZIF-67 is formed by bridging 2-methylimidazolate anions and cobalt cations in an instantaneous coordination reaction at room temperature.[219] The colour of the solution rapidly changes from light-pink to blue-violet when the Co-N coordination bond is formed.[220] The SEM and TEM images of C-ZIF-67 (Figures 5.2) revealed the formation of polyhedral structures with average sizes of 0.55 µm. The ZIF-67 precursor can provide both N-doped graphitic carbon and Co species, favourable for the promotion of the ORR and OER.[88,221]

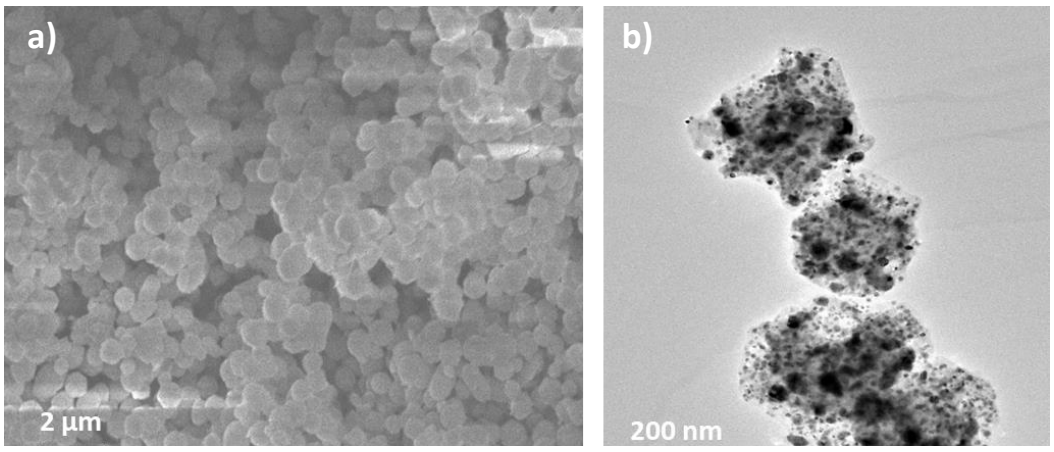

Figure 5.2: a) SEM and b) TEM figures of C-ZIF-67.

Polystyrene fibers densely packed with ZIF-67 particles were prepared by electrospinning of a suspension containing a mixture of these two precursors. To understand the effect of certain electrospinning parameters, such as the collection distance and the feeding rate in the fibers' physical structure, they were varied, and their structures observed under SEM. The collection distance is the distance measured between the tip of the needle and the surface of the ethanol bath, where fibers were collected. The feeding rate refers to the amount of suspension mixture forced through the needle, per hour. The SEM figures 5.3-5.5 show the different fibers obtained when varying elecrospinning operational parameters such as the feeding rate (0.4, 0.6 and 0.8 ml h^{-1}) and collection distance (18, 20 and 22 cm) generated microfibers with different physical structures.

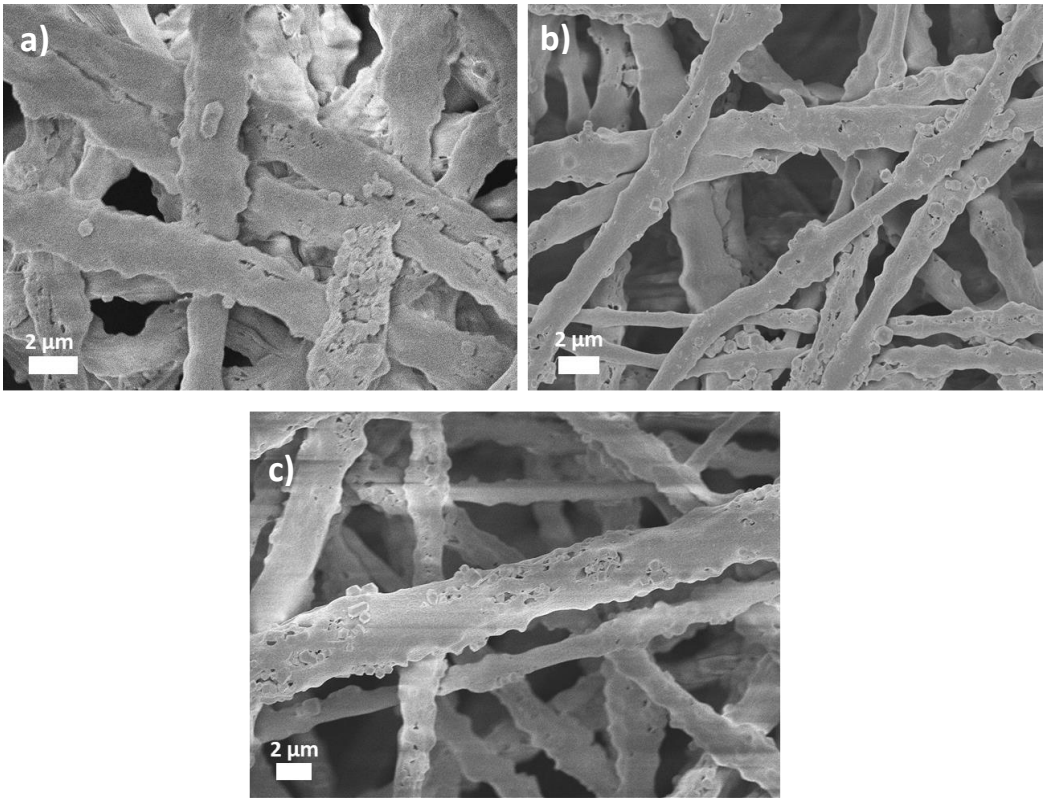

Figure 5.3: SEM figures of ZIF-67:PS-1 prepared with a feeding rate of 0.6 ml h^{-1} and a collection distance of a) 18 cm, b) 20 cm and c) 22 cm.

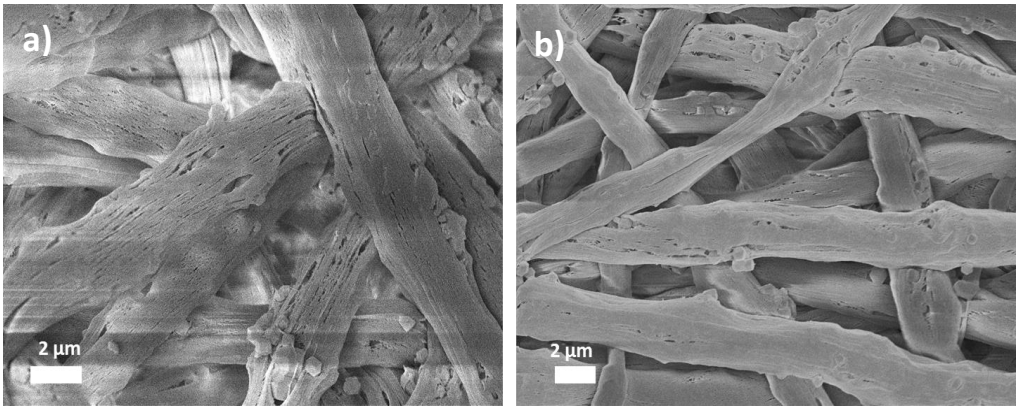

Figure 5.4: SEM figures of ZIF-67:PS-1 prepared with a feeding rate of 0.4 ml h^{-1} and a collection distance of a) 18 cm and b) 20 cm.

Naturally, a higher feeding rate led to the formation of thick fibers and a greater collection distance induced increased stretching allowing the formation of thinner fibers. Therefore, a balance between these two parameters was selected – 0.6 ml h^{-1} feeding rate and a collection distance of 20 cm.

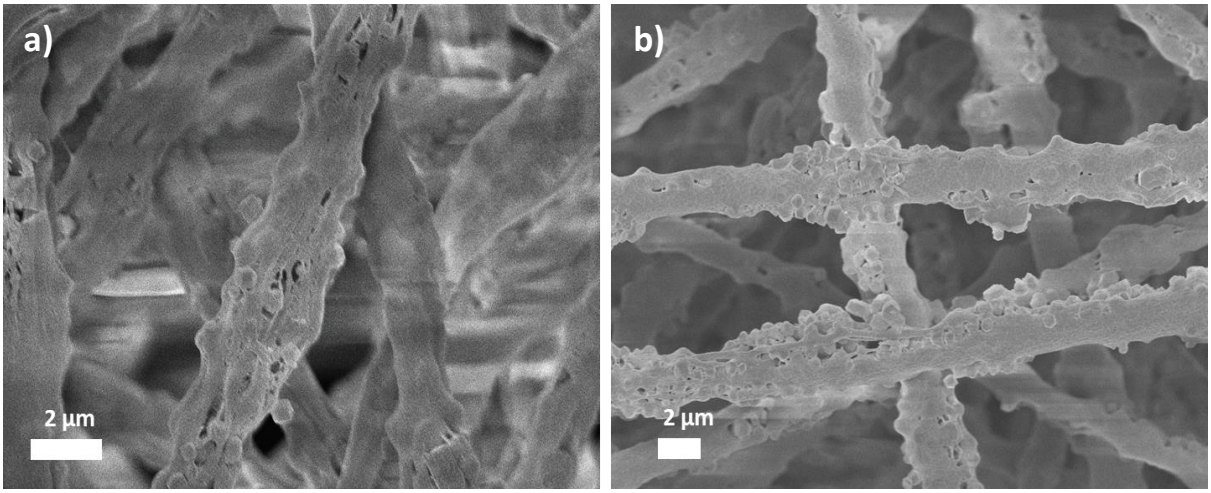

Figure 5.5: SEM figures of ZIF-67:PS-1 prepared with a feeding rate of 0.8 ml h-1 and a collection distance of a) 18 cm and b) 20 cm.

These fibers were collected in ethanol (Figure 5.6a) to allow their quick precipitation as a result of the good wetting of the fiber's surface by ethanol and the density difference between PS and ethanol. This method allows the formation of a loose lump of fibers with large inter-fiber spaces, guaranteeing a more even fiber coating.[222,223] Following this, the fibers were then transferred into a dopamine solution, to which a trizma solution was added to activate the polymerization process and formation of polydopamine during a 4h-process. Upon self-polymerization of dopamine, the colour of the fibers changed from purple to dark brown/black (Figure 5.6b).

This process was repeated for another three times to obtain a maximum of four coating layers. Lastly, the coated fibers were pyrolyzed at a ramping rate of 5˚C min^{-1} and kept at 850˚C for 1h under Ar atmosphere, to form carbon-coated fibers filled with Co-N/C hybrid particles.

The optimization of the synthesis procedure involved the variation of the ZIF-67:PS ratio (0.5, 1 and 2). The ZIF-67 filled fibers increased their thickness as the concentration of ZIF-67 particles was increased, as observed in Figure 5.7. The fibers containing a ZIF-67:PS ratio of 0.5 (ZIF-67:PS-0.5) (Figure 5.7b) presented an average thickness of 1.26 µm, which is just slightly higher than the thickness of bare polystyrene fibers (1.25 µm) (Figure 5.7a). As this ratio was increased to 1, well defined and slightly stretched fibers with visible pores were obtained (Figure 5.7c). Finally, at a ratio of 2, the PS fibers appeared considerably stretched, reaching a thickness of 14-15 µm, and torn, leaving the ZIF-67 particles noticeably exposed and prone to decomposition (Figure 5.7d). The BET surface area and pore structures of ZIF-67:PS-X were investigated by N_2

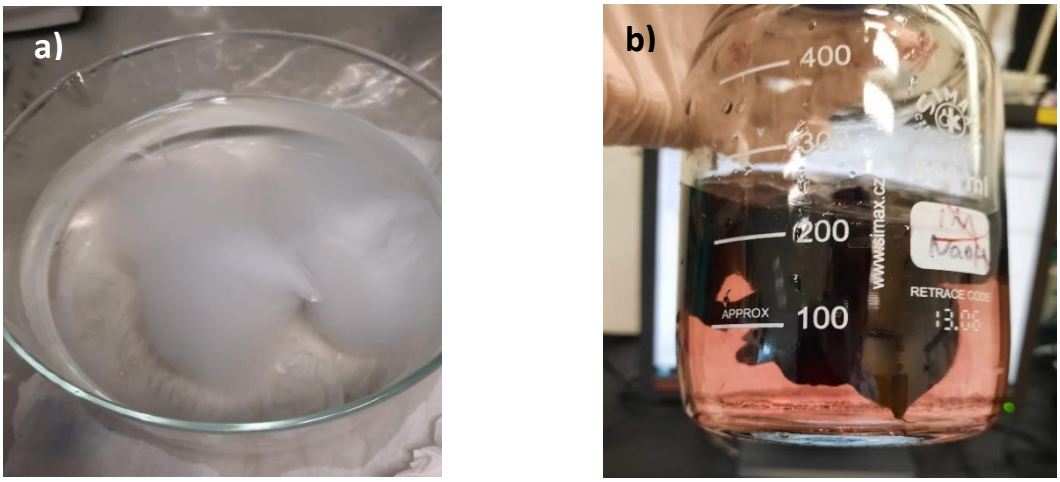

Figure 5.6: a) Example of the collection of bare PS electrospun fibers in ethanol. b) Polymerization of dopamine indicated by the change in colour to dark brown.

adsorption-desorption isotherms. Subsequently, the BET surface area of the fibers increased up to 892 $m^2 g^{-1}$ with the ZIF-67 concentration.

Upon further annealing of these structures (Figure 5.8), the fibers' configuration is destroyed since polystyrene is decomposed at high temperatures[209], leaving annealed ZIF-67 particles with an average size of 0.63 um.

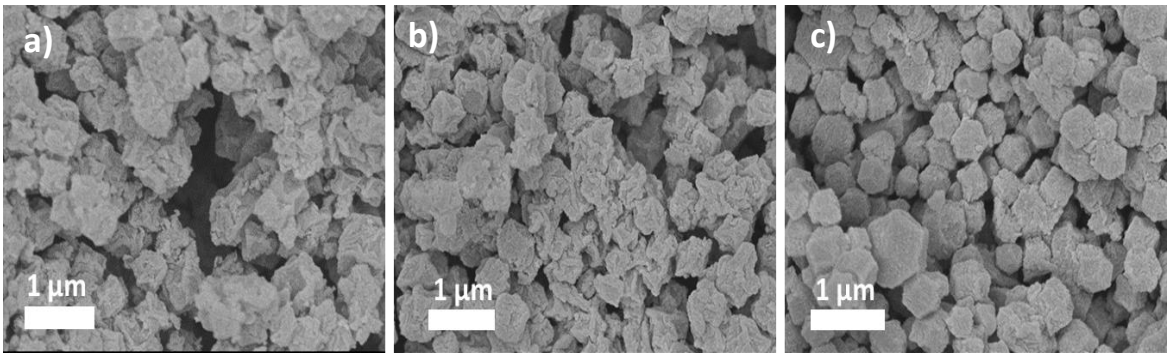

Figure 5.7: SEM figures of a) C-ZIF-67:PS-0.5, b) C-ZIF-67:PS-1 and c) C-ZIF-67:PS-2.

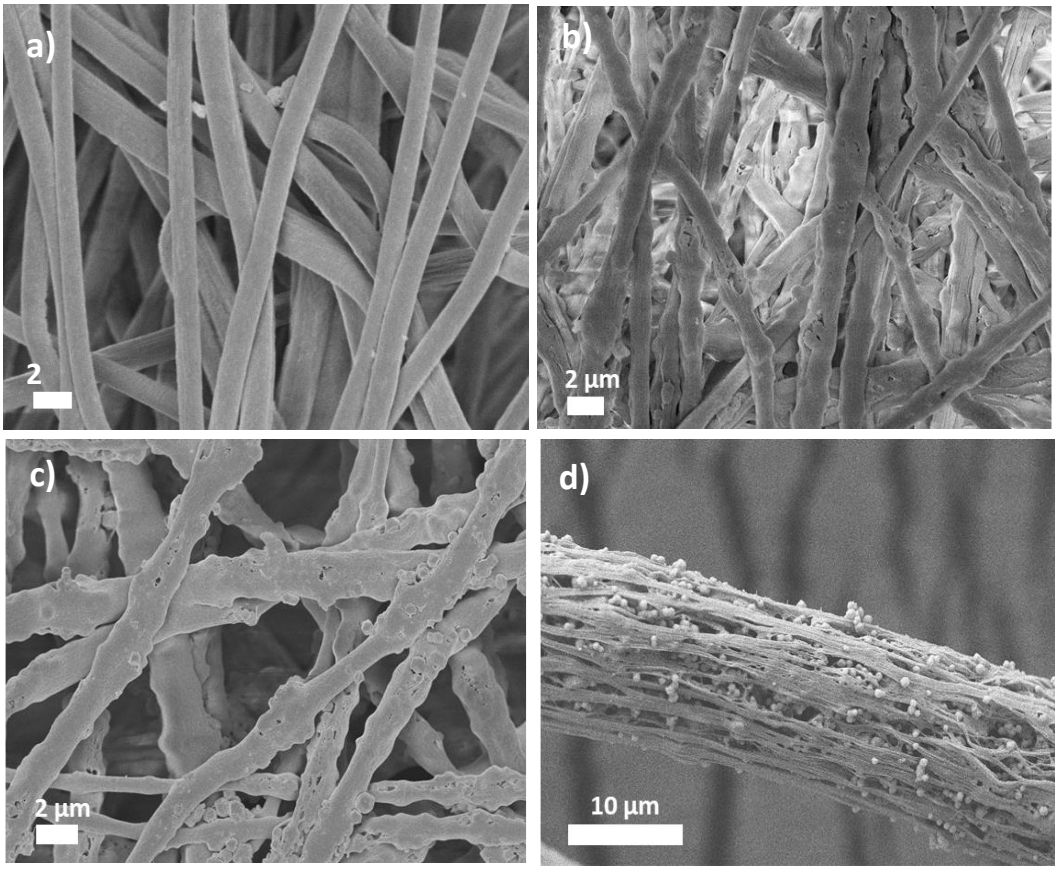

Figure 5.8: SEM figures of a) bare PS fibers, b) ZIF-67:PS-0.5, c) ZIF-67:PS-1 and d) ZIF-67:PS-2.

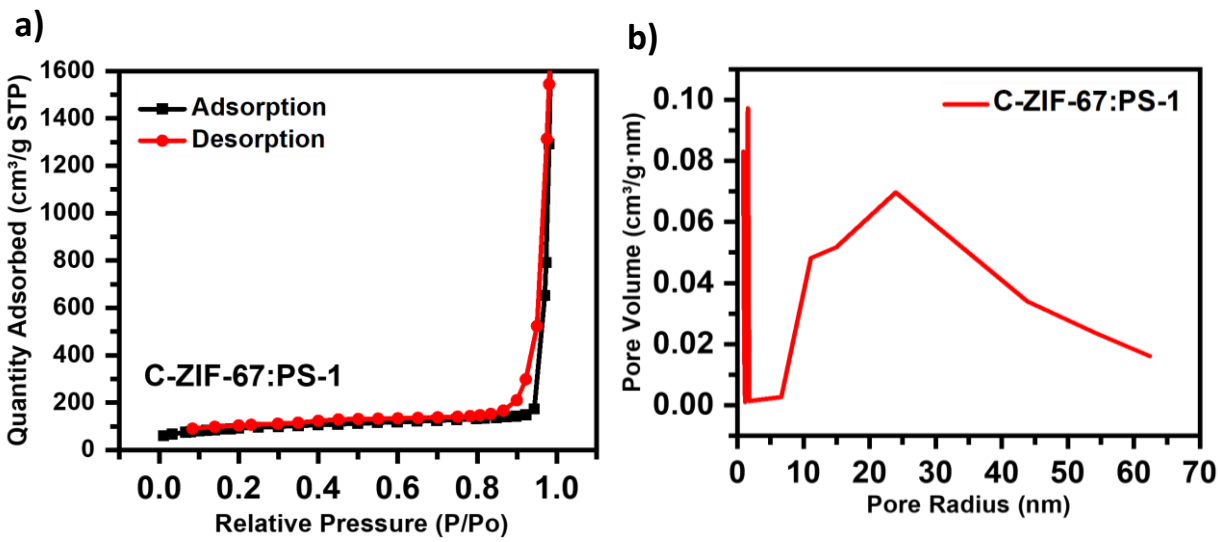

Figure 5.9: a) N_2 adsorption-desorption isotherms of C-ZIF-67:PS-1 and d) corresponding BJH pore distributions.

The BET surface area determined by the N_2 adsorption-desorption isotherms (Figure 5.9a) reveal a high value of 318 m^2 g^{-1} for C-ZIF-67:PS-1. Additionally, it also presented a greater BJH desorption (Figure 5.9b) average pore size of 18.4 nm.

The EDS images presented in Figures 5.10 and 5.11 exhibit the elemental distributions on C-ZIF-67:PS-1 and C-ZIF-67:PS-2, respectively. On both samples C, N, O and Co were identified, however these were distributed differently. On C-ZIF-67:PS-1 the formation of Co-N-C functional groups and some metallic Co particles is observed. However, on C-ZIF-67:PS-2 it is apparent that only Co particles are formed, and no Co-N are detected, likely due to severe Co particle aggregation as a result of an excessive ZIF-67 concentration.[224] The XPS survey spectra presented in Figure 5.12 indicate a higher level of carbonization as the ZIF-67:PS ratio is increased, from 91 at% to 94 at%, suggesting that a greater Co content may promote carbon graphitization.[225] Additionally, C-ZIF-67:PS-1 contains a higher N concentration, which has been reported to promote the ORR.

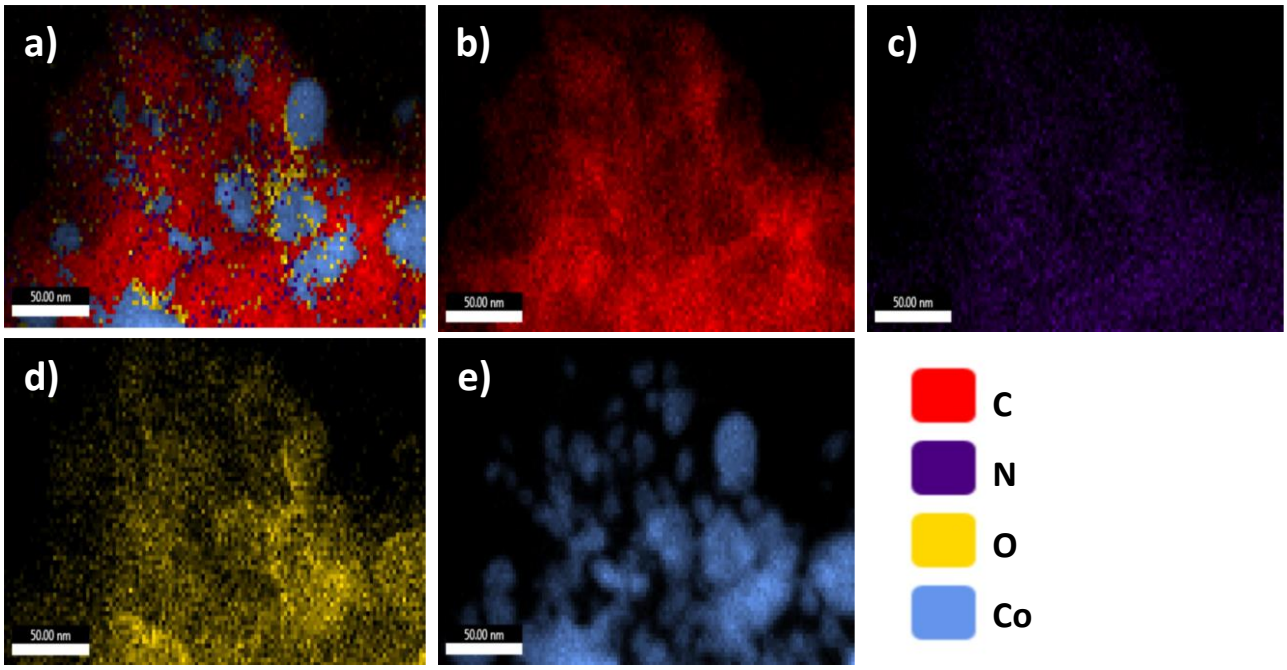

Figure 5.10: EDS elemental mapping of C-ZIF-67:PS-1.

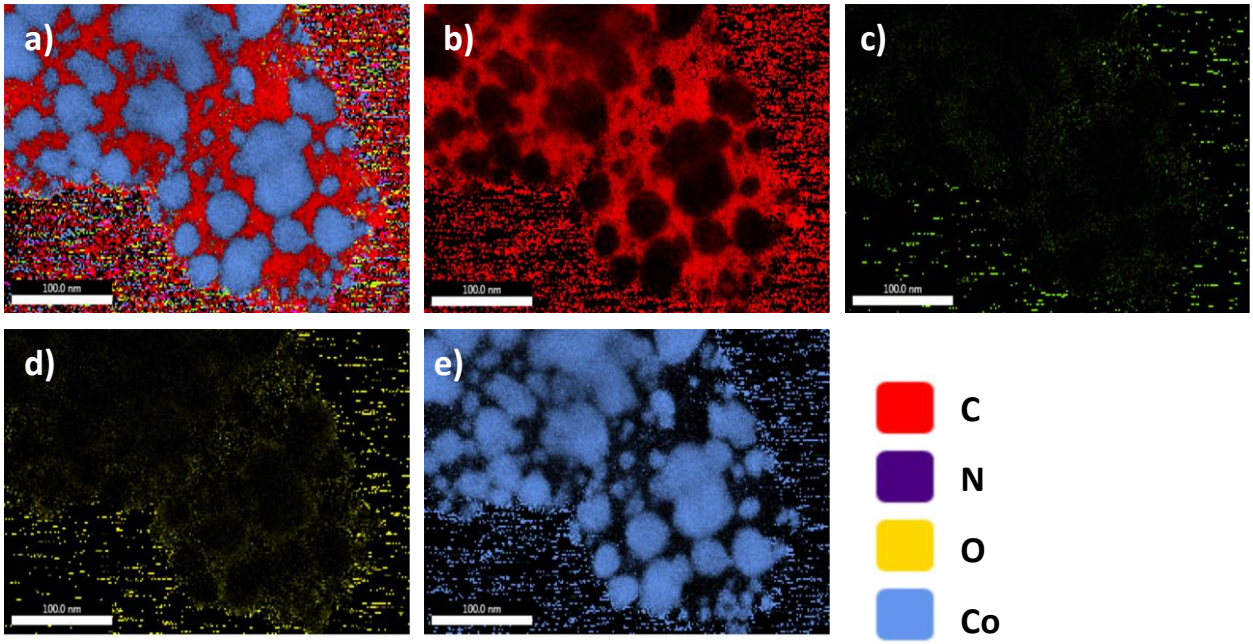

Figure 5.11: EDS elemental mapping of C-ZIF-67:PS-2.

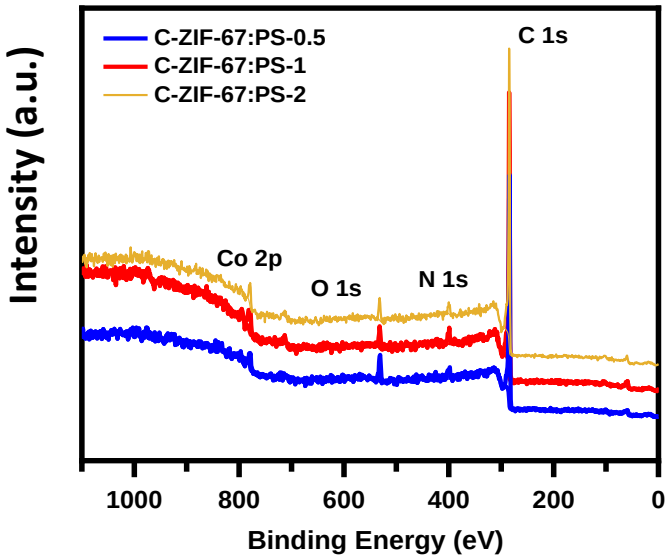

Figure 5.13: XPS survey spectra of C-ZIF-67:PS-0.5, C-ZIF-67:PS-1 and C-ZIF-67:PS-2.

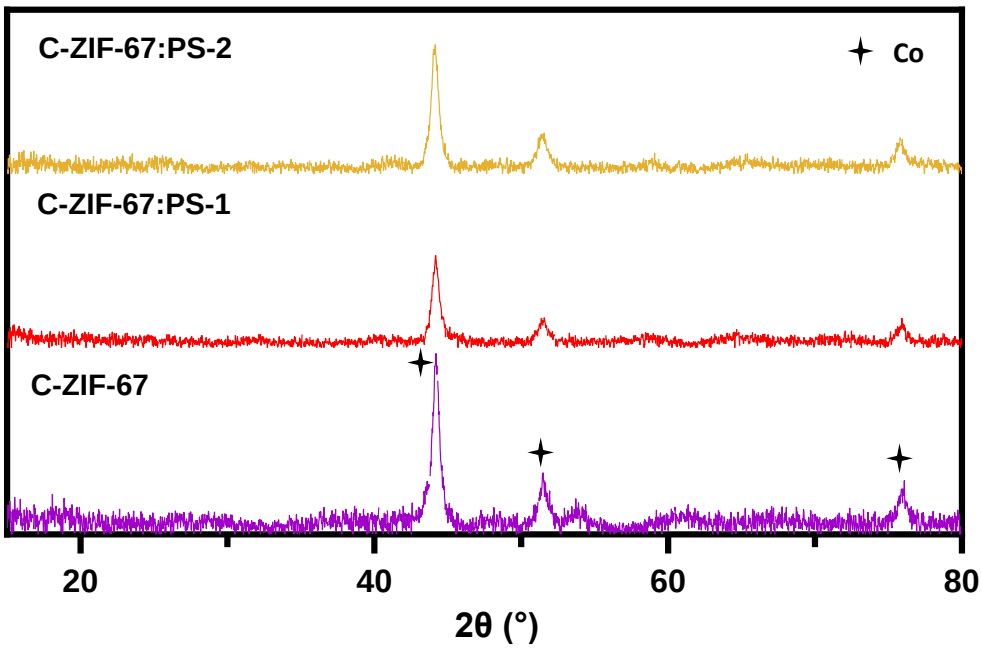

Figure 5.12: XRD patterns of C-ZIF-67, C-ZIF-67:PS-1 and C-ZIF-67:PS-2.

Figure 5.13 presents the XRD patterns corresponding to C-ZIF-67, C-ZIF-67:PS-1 and C-ZIF-67:PS-2. The three samples show similar patterns implying that the C-ZIF-67:PS-1 and C-ZIF-67:PS-2 structures are similar to that of C-ZIF-67, confirming the decomposition of polystyrene at high temperatures. The diffraction peaks at around 44°, 51.5° and 75.9°, could be attributed to the (111), (200) and (220) planes of metallic Co (JCPDS card 15-0806). The higher intensity of the diffraction peak at 44° on the XRD

pattern of C-ZIF-67:PS-2 suggest the preferred orientation plane and increased crystal size.[88,226]

As previously observed, the PS structure degrades at high temperatures[209] and the fiber structure is lost, therefore, the ZIF-67:PS-1 fibers were coated with a few layers (1-4 layers) of polydopamine in order to maintain the desired fiber structure (Figure 5.14). Additionally, the carbon coating generated upon annealing, may provide a path for electrons to reach the catalytic active sites as well as exposed carbon N-doped features on its surface. The formation of varied active site locations may improve its overall electrocatalytic performance. Accordingly, the thickness of the fibers increased as each PDA layer of about 0.15-0.20 um was added. The thickness of the C-ZIF-67:PS-1-1xPDA fibers (Figure 5.14a) was about 1.54 um and the fibers of the final C-ZIF-67:PS-1-4xPDA (Figure 5.14d) sample were about 2.08 um wide, clearly higher than that of the bare PS fibers which were about 1.25 um.

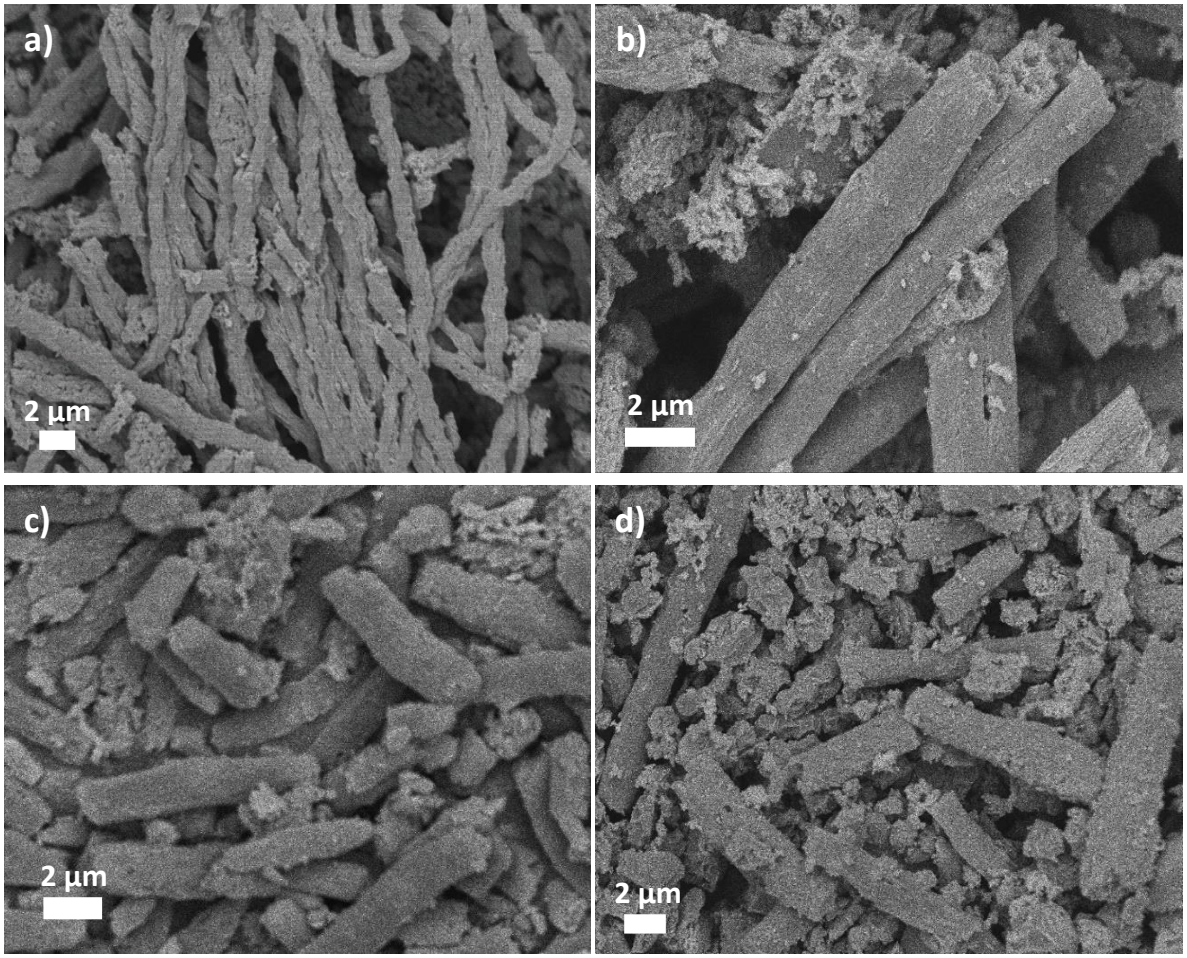

Figure 5.14: SEM figures of a) C-ZIF-67:PS-1-1xDA, b) C-ZIF-67:PS-1-2xDA, c) C-ZIF-67:PS-1-3xDA and d) C-ZIF-67:PS-1-4xDA.

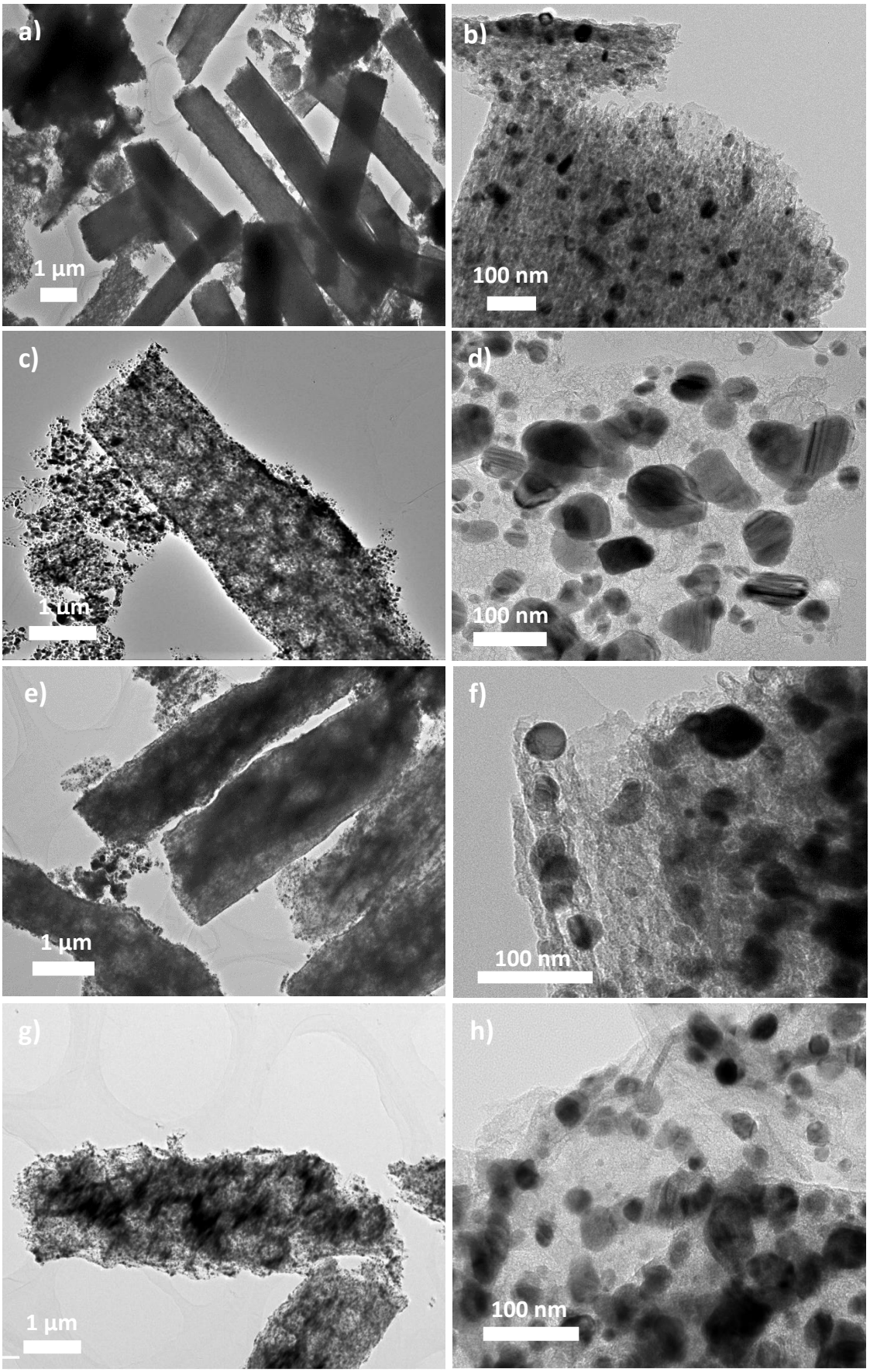

Figure 5.15: TEM figures of a-b) C-ZIF-67:PS-1-1xDA, c-d) C-ZIF-67:PS-1-2xDA, e-f) C-ZIF-67:PS-1-3xDA and g-h) C-ZIF-67:PS-1-4xDA.

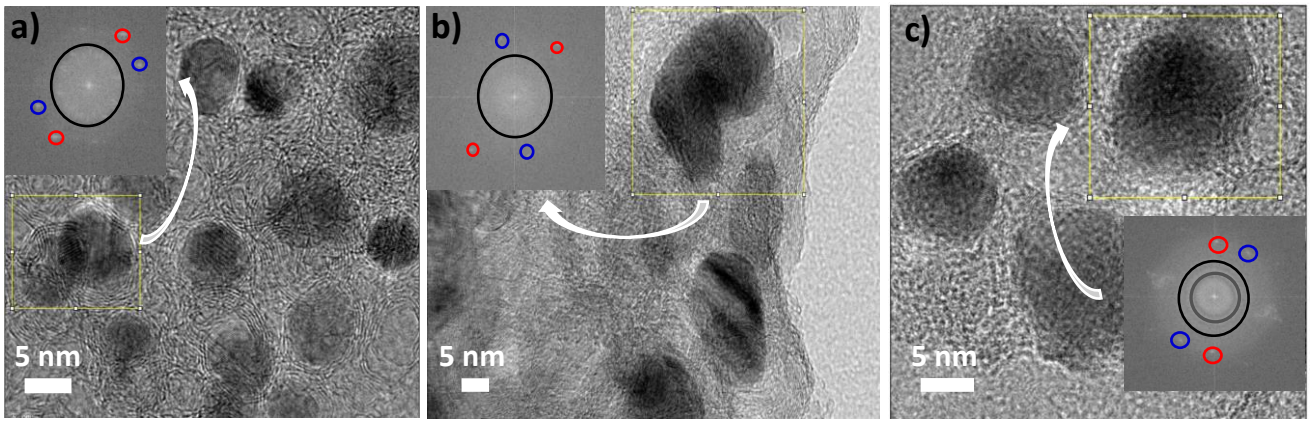

Figure 5.16: HRTEM images of a) C-ZIF-67:PS-1, b) C-ZIF-67:PS-1-1xDA and c) C-ZIF-67:PS-1-2xDA and the corresponding FFT.

Consistently, the TEM images (Figure 5.15) show uniform PDA coatings with increased thicknesses as the layers were added to the prepared fibers and the formation of dark nanoparticles. The FFT images (Figure 5.16) obtained for the nanoparticles' region reveal lattice fringes with d-spacings of 0.34 nm, which have been reported to correspond to the (002) plane of graphitized carbon, and d-spacings of 0.18 and 0.20 nm which were ascribed to the (200) and (111) planes of face-centered cubic (*fcc*) phase of metallic Co.[86] As two PDA coating layers were added, lattice fringes with d-spacings of 0.40 nm were observed, which may correspond to enlarged d-spacings of the (002) plane of graphitised carbon possibly due to some oxidation of the graphite layer, which may then reduce electric conductivity.[227,228]

Figure 5.18a presents the N_2 adsorption-desorption isotherm of C-ZIF-67:PS-1-1xPDA showing a type-IV isotherm with a distinct hysteresis loop, characteristic of the presence of abundant mesopores in the structure. The BJH desorption average pore size of C-ZIF-67:PS-1-1xPDA decreases in comparison to C-ZIF-67:PS-1 since C-ZIF-67 particles are compacted inside the fibers (Figures 5.9b and 5.18b). The BET surface area increases as the first layer of PDA is added (from 318 m^2 g^{-1} for C-ZIF-67:PS-1 to 515 m^2 g^{-1} for C-ZIF-67:PS-1-1xPDA), suggesting a successful coating process. The large specific surface area and abundant mesopores formation may favour the exposure of electrochemically active sites and electrolyte impregnation, reducing the ion diffusion pathways.[115] Finally, as the fourth layer was added, an average pore size increase is reported possibly due to a reduced adhesion efficiency of the subsequent layers (Figure 5.17). The EDS elemental mapping profiles of the coated C-ZIF-67:PS-1 fibers are

presented. In the lower magnification images of C-ZIF-67:PS-1-1xPDA (Figure 5.19) it is possible to identify the C and N coating on the fiber originated from the polymerization and high temperature annealing of DA. In the higher magnification images of C-ZIF-67:PS-1-2xPDA (Figure 5.20), particles composed of Co, N and C are clearly observed, suggesting the presence of Co-N-C domains which have been reported to favour the ORR and OER.[229,230]

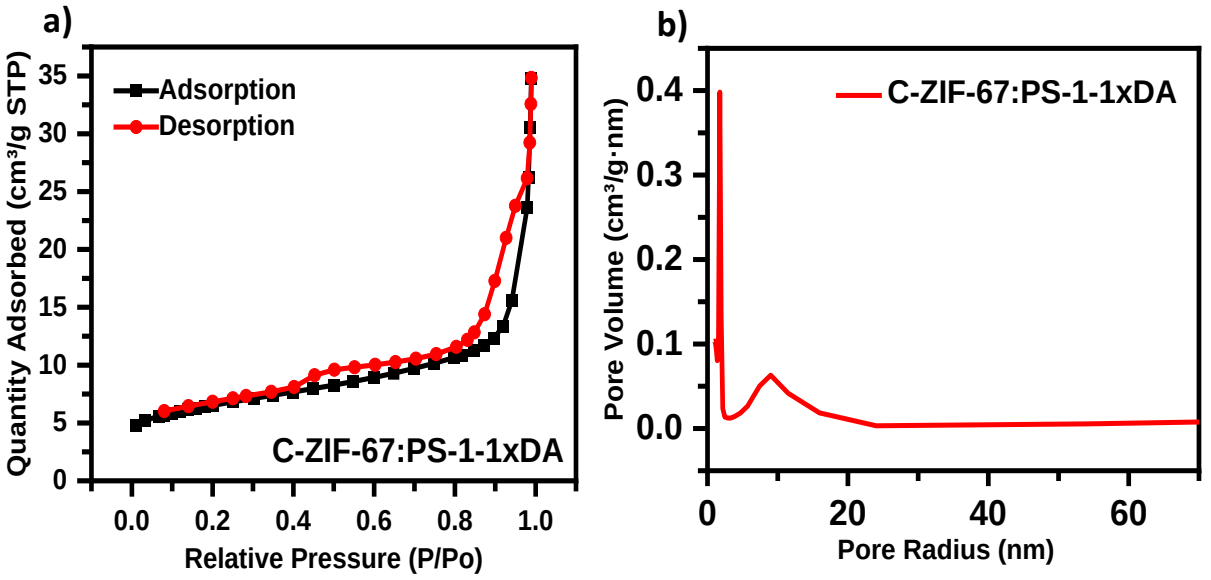

Figure 5.17: N_2 adsorption-desorption isotherms of C-ZIF-67:PS-1-1xDA and b) corresponding BJH pore distributions.

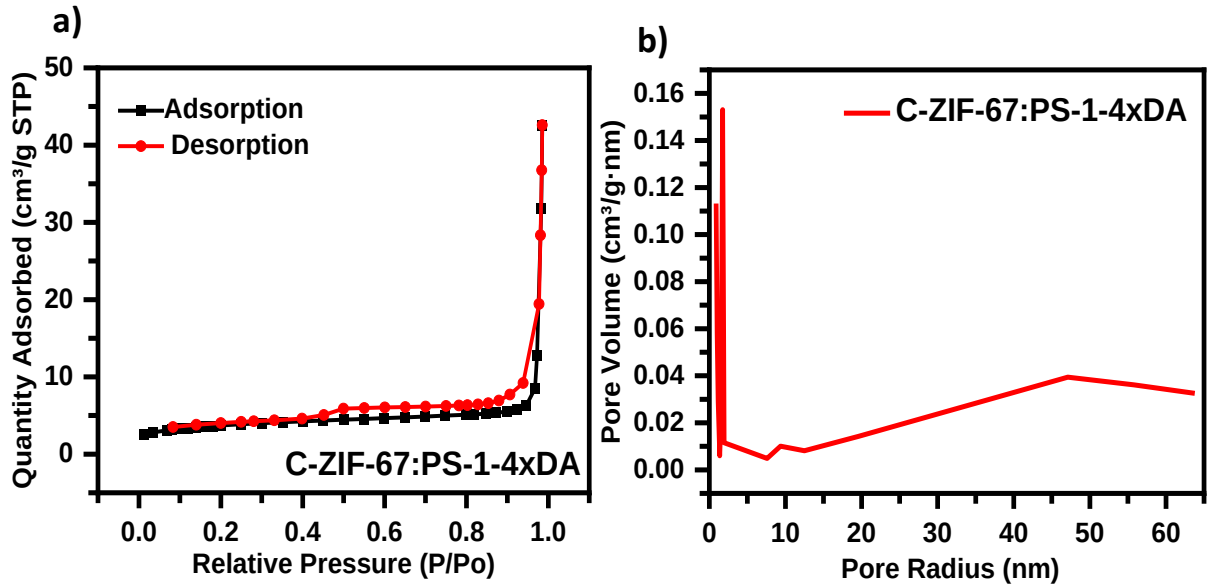

Figure 5.18: a) N_2 adsorption-desorption isotherms of C-ZIF-67:PS-1-4xDA and b) corresponding BJH pore distributions.

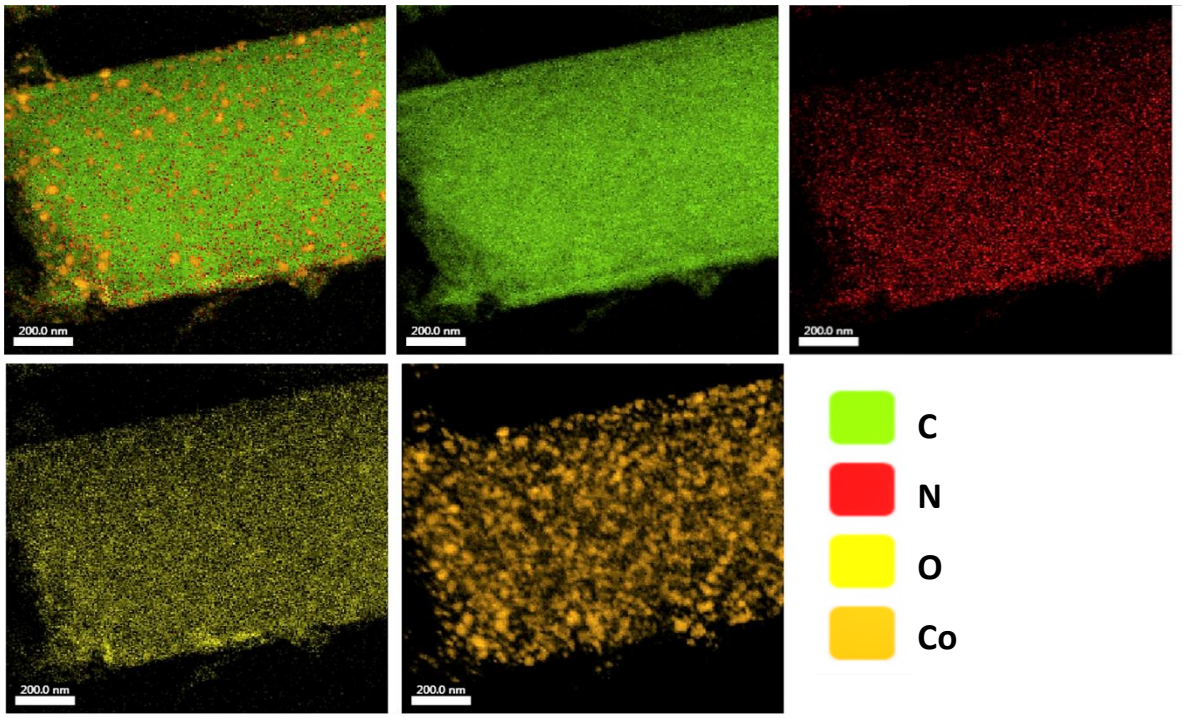

Figure 5.19: EDS elemental mapping of C-ZIF-67:PS-1-1xDA.

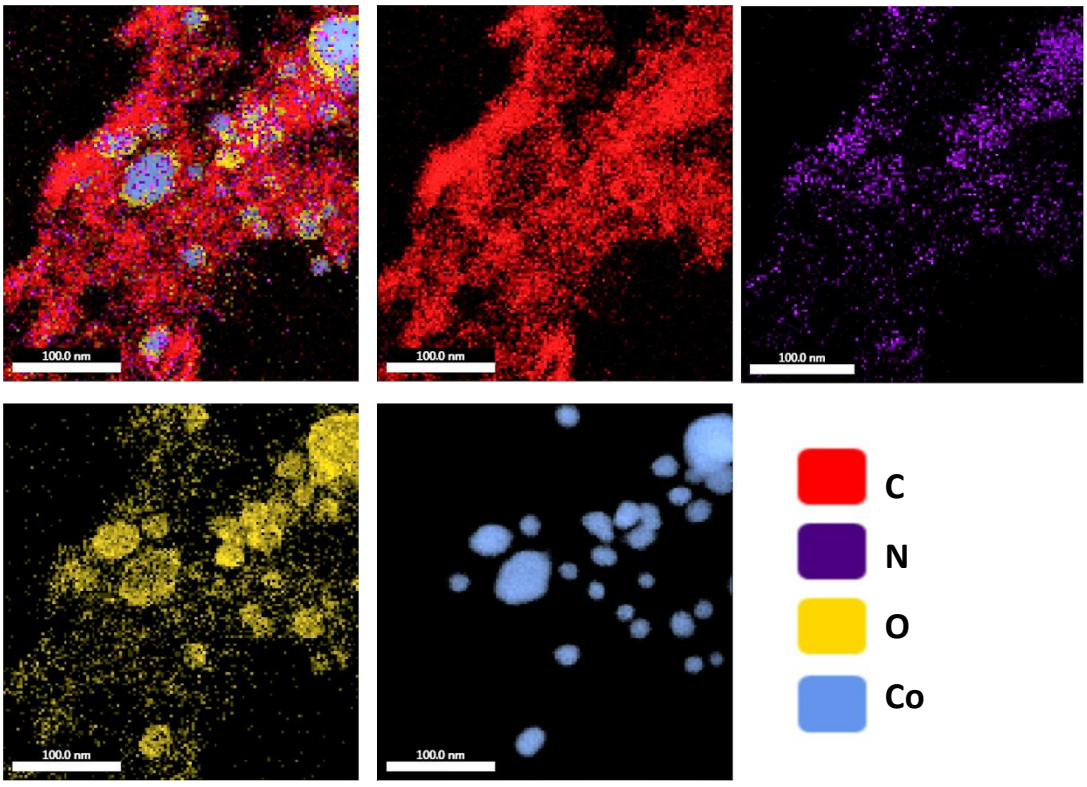

Figure 5.20: EDS elemental mapping of C-ZIF-67:PS-1-2xDA.

The XPS survey spectra of the coated ZIF-67:PS-1 fibers (C-ZIF-67:PS-1-XDA) presented in Figure 5.21a indicates that they are composed of C, N, O and Co. As extra PDA layers are added, the concentration of N increases, from 1.99 at% to 2.50 at%, demonstrating the successful coating. Simultaneously, the Co at% decreased from 0.72 at% to 0.36 at% indicating the coverage of the fibers by PDA and reduced exposure of Co-based particles found within the fibers. In the N1s high resolution XPS spectra of the coated fibers (Figure 5.21b-d), a peak at around 402 eV is observed, while this does not appear on the spectra of the uncoated sample, C-ZIF-67:PS-1. These results are likely to be due to the formation of graphitic N originated from the high temperature annealing of the PDA coating.[225,231] Pyridinic-N and graphitic-N have been reported to promote the ORR and more graphitic N could also improve electrical conductivity.[225]

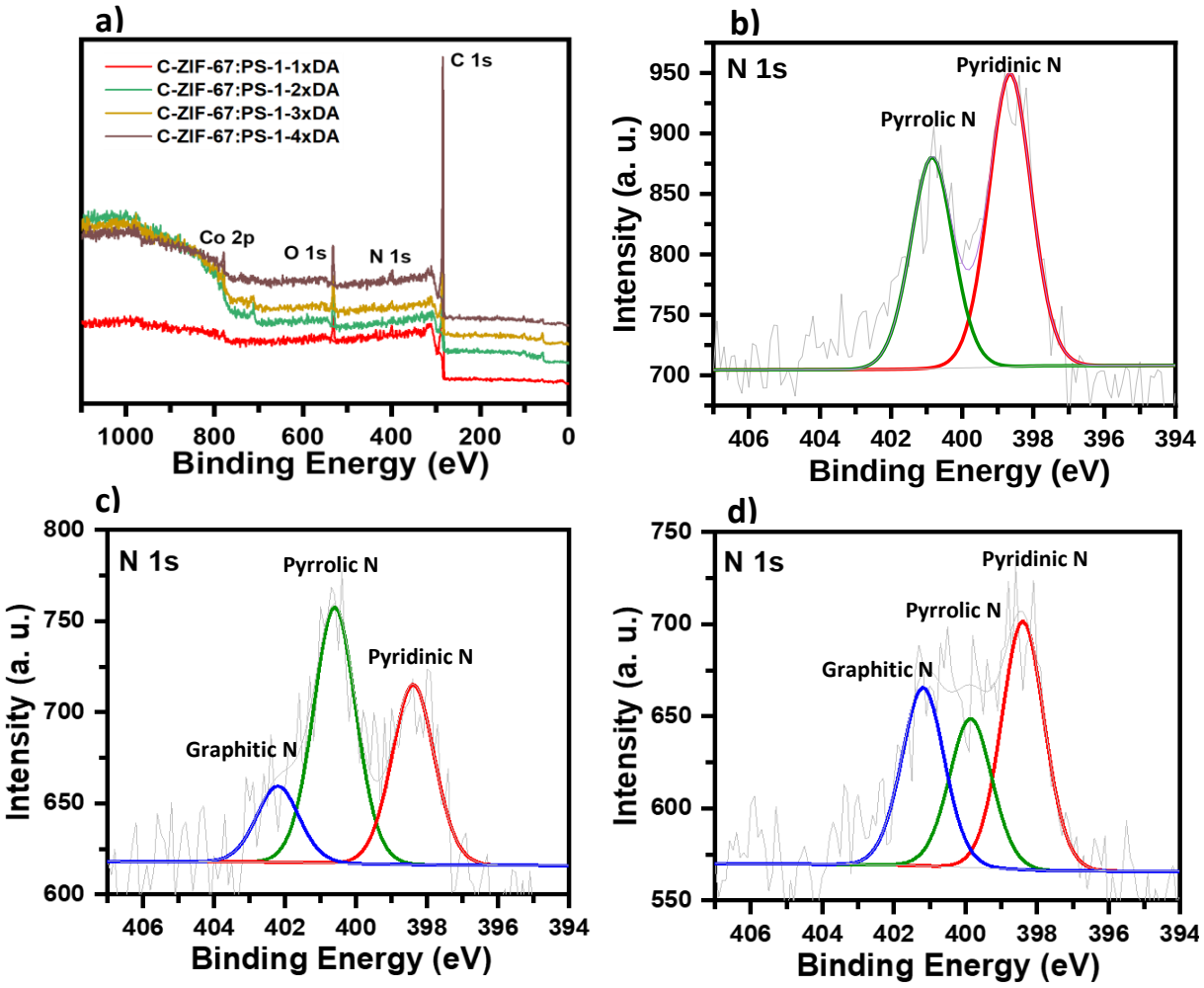

Figure 5.21: a) XPS Survey spectra of C-ZIF-67:PS-1-1xDA, C-ZIF-67:PS-1-2xDA, C-ZIF-67:PS-1-3xDA and C-ZIF-67:PS-1-4xDA. High resolution N1s spectrum of b) C-ZIF-67:PS-1, c) C-ZIF-67:PS-1-1xDA and d) C-ZIF-67:PS-1-4xDA.

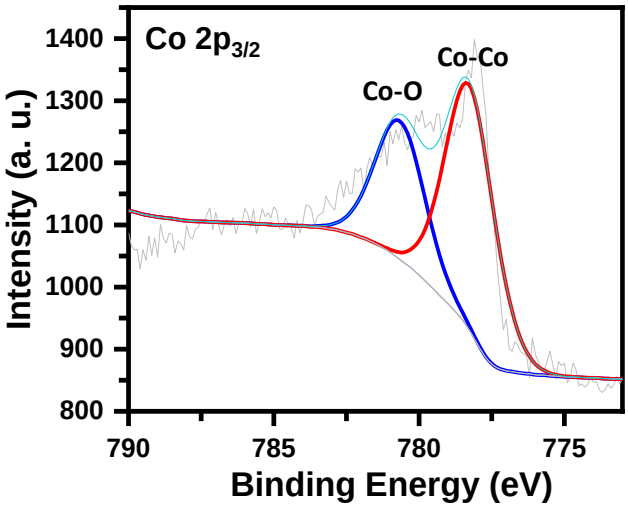

Figure 5.22: XPS high resolution Co $2p_{3/2}$ spectrum of C-ZIF-67:PS-1-1xDA.

The high-resolution Co $2p_{3/2}$ spectrum of C-ZIF-67:PS-1-1xDA can be deconvoluted into two peaks at 778.3 and 780.7 eV, attributed to metallic Co and O-coordinated Co, respectively (Figure 5.22).[226] Considering XPS is a surface-sensitive technique with a limited penetration depth (typically <10 nm), the detection of the Co NPs encapsulated by the PDA fibers may be limited.[77] The enclosed and stable metal particles and N-doped graphitic layer structure may synergistically enhance the electrocatalytic activity, however, the exact ORR and OER active sites still remain controversial.

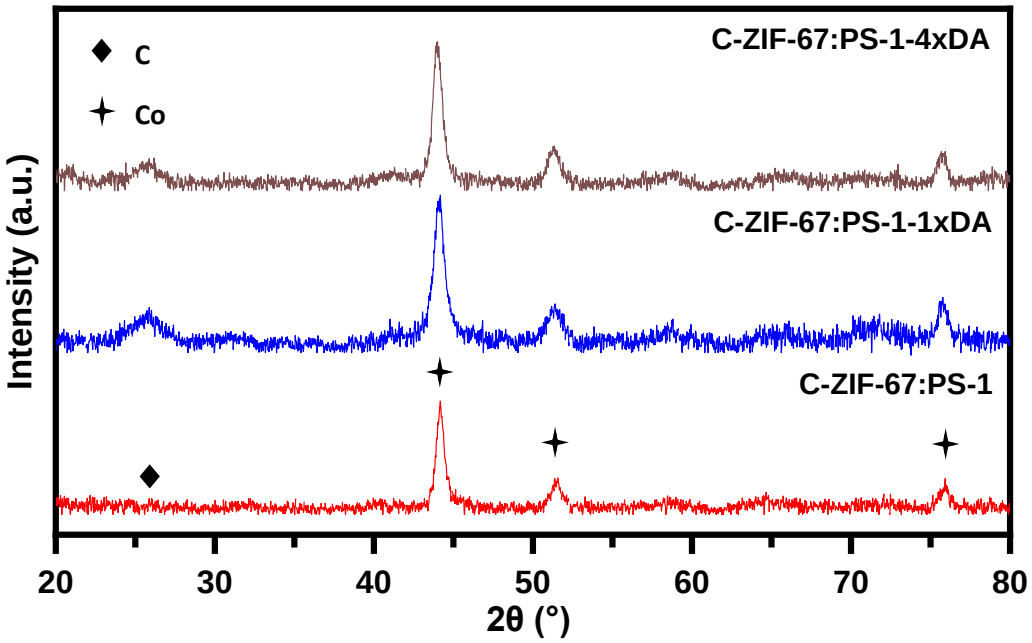

Figure 5.23: XRD patterns of C-ZIF-67:PS-1, C-ZIF-67:PS-1-1xDA and C-ZIF-67:PS-1-4xDA.

Additionally, the XRD patterns of the coated C-ZIF-67:PS-1 fibers present similar features to those of C-ZIF-67:PS-1 (Figure 5.23). However, as the PDA layers were added, a peak around 26˚ attributed to the (002) plane of graphitic carbon appeared, suggesting a high degree of carbon graphitization, which should be beneficial for electrical conductivity and catalytic activity.[226] These interpretations are in accordance with the TEM results previously reported.

5.2.2. Electrochemical characterization

The electrochemical behaviour of the catalysts developed in this study was comparatively evaluated to attempt to understand the influence of different formulations. Initially, the electrocatalytic activity of the catalysts was evaluated by CV in an O_2-saturated 1 M KOH aqueous electrolyte. As shown in Figure 5.24a, all of the ZIF-67-filled PS fibers catalysts (C-ZIF-67:PS-0.5, C-ZIF-67:PS-1 and C-ZIF-67:PS-2) presented strong cathodic peaks, close to that of the benchmark Pt/C, ~ 0.81 V and 0.91 V vs. RHE, respectively, confirming their active ORR performance. The CV curves of the coated C-ZIF-67:PS-1 catalysts (C-ZIF-67:PS-1-1xDA, C-ZIF-67:PS-1-2xDA, C-ZIF-67:PS-1-3xDA and C-ZIF-67:PS-1-4xDA) are demonstrated in Figure 5.24b and indicate that C-ZIF-67:PS-1-1xDA presented a slightly more positively shifted peak at 0.82 V vs. RHE, indicative of an improved ORR activity. The other catalysts exhibited peaks at slightly more negative potentials.

The ORR performance of the investigated catalysts was further studied by LSV. As presented in Figure 5.25a, C-ZIF-67:PS-1 presented the best ORR performance amongst the prepared catalysts, observed by a more positively shifted curve, reduced overpotential (0.92 V vs. RHE) and $E_{1/2}$ (0.82 V vs. RHE) and a higher current density (5.69 mA cm^{-2}). The excessive content of Co nanoparticles in C-ZIF-67:PS-2 may lead to their aggregation, blocking the electrochemically active sites. These results were also comparable to those of Pt/C which presented an overpotential of 0.96 V vs. RHE, a $E_{1/2}$ of 0.83 V vs. RHE. However, the current density reported by the Pt/C catalyst of 5.15 mA cm^{-2} was lower than that of C-ZIF-67:PS-1. Furthermore, the LSV results for the C-ZIF-67:PS-1-1xDA, 2xDA, 3xDA and 4xDA are presented in Figure 5.25b. It is possible to observe that C-ZIF-67:PS-1-1xDA presented an improved ORR activity in comparison to the other coated fiber samples as well as to the uncoated fibers, C-ZIF-67:PS-1,

confirming the advantages of the addition of one graphitic carbon coating layer. The C-ZIF-67:PS-1-1xDA catalyst achieved a high limiting current density of 6.72 mA cm^{-2} and an improved overpotential of 0.88 V vs. RHE.

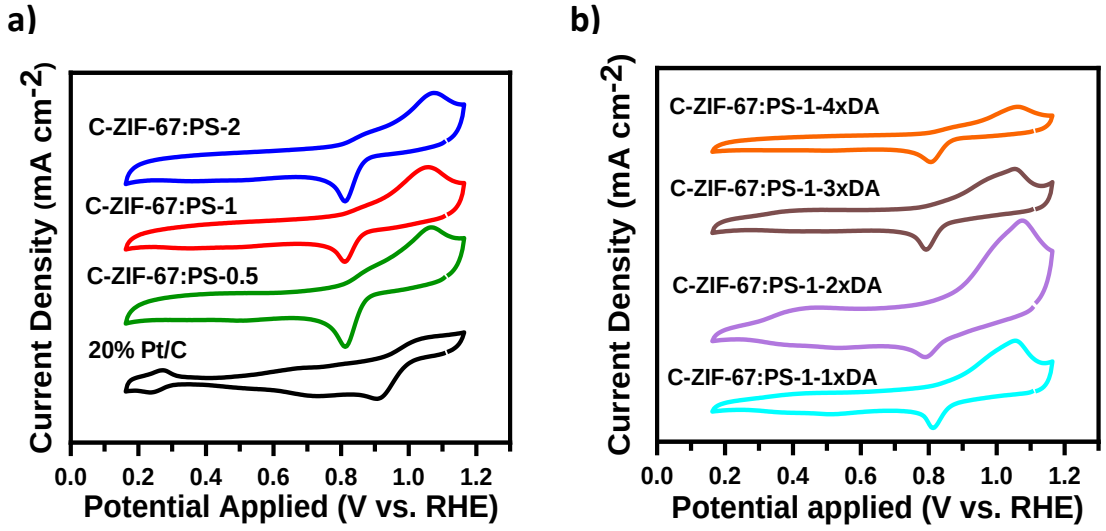

Figure 5.24: a) CV curves of a) the C-ZIF-67:PS-X catalysts and Pt/C and b) the C-ZIF-67:PS-1-XDA catalysts, obtained in O_2-saturated 0.1 M KOH electrolyte. The scan rate was kept at 5 mV s^1 for all measurements.

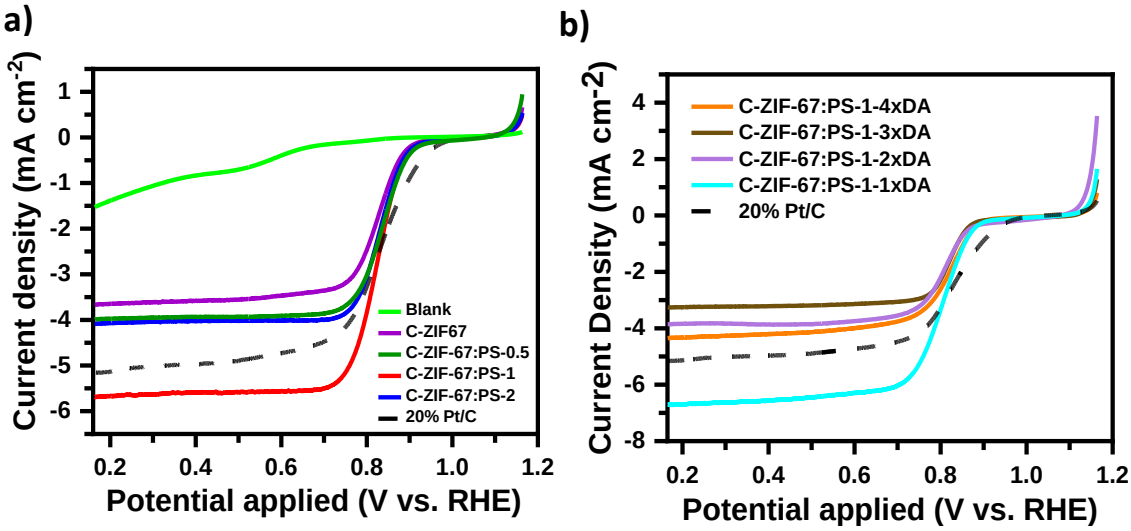

Figure 5.25: Combined LSV curves for ORR of a) C-ZIF-67, the C-ZIF-67:PS-X catalysts and 20% Pt/C and b) the C-ZIF-67:PS-XDA catalysts and 20% Pt/C at 1600 rpm in O_2-saturated 0.1 M KOH electrolyte. The scan rate was kept at 5 mV s^1 for all measurements.

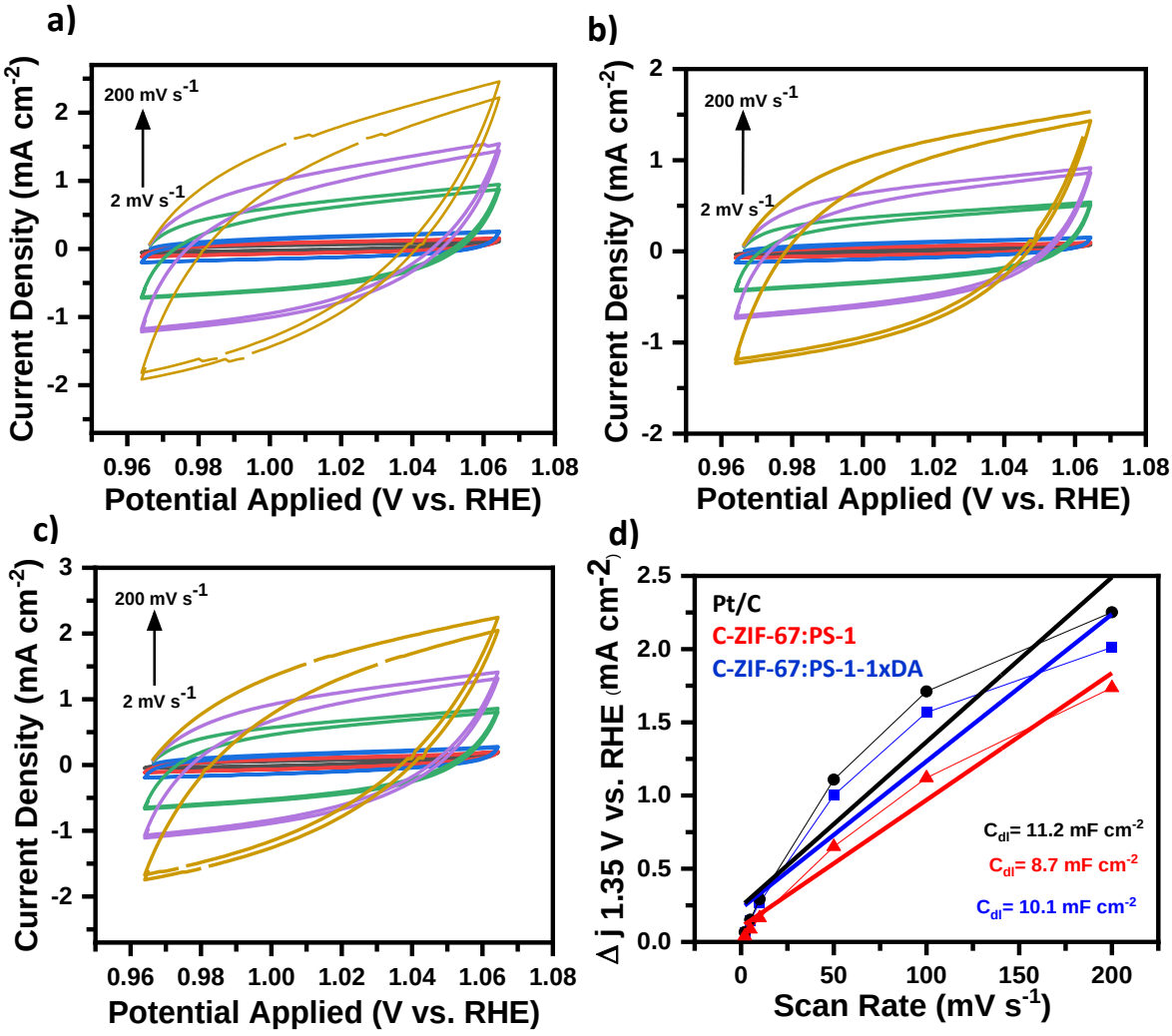

Figure 5.26: CV curves of a) Pt/C, b) C-ZIF-67:PS-1 and c) C-ZIF-67:PS-1-1xDA at scan rates from 2 to 200 mVs^{-1} within 0.96 to 1.06 V vs. RHE. d) the corresponding linear fitting of the capacitive current densities at an overpotential of 1.01 V vs. RHE against the scan rates of Pt/C and ZIFCNDA.

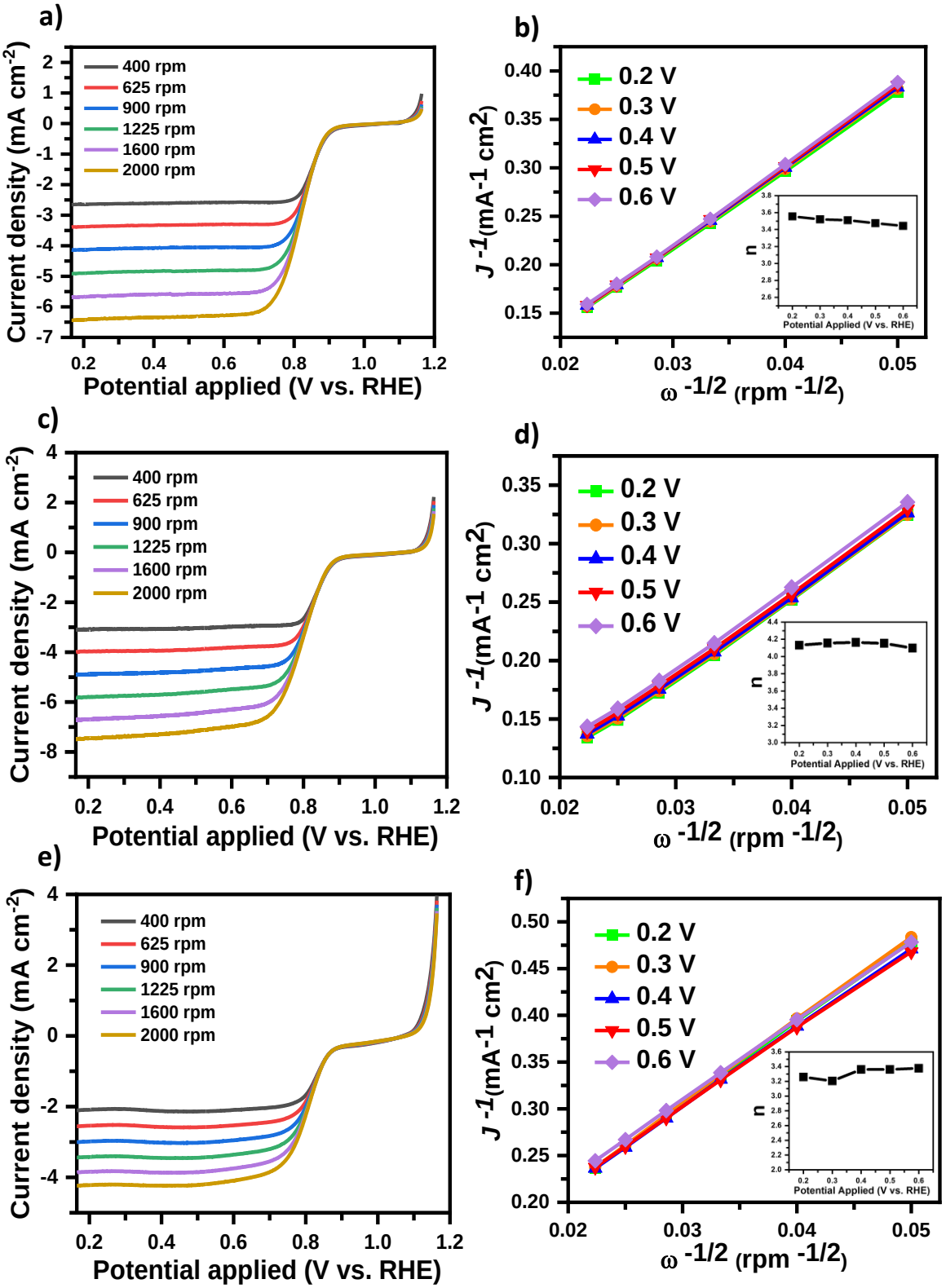

Figure 5.27: LSV curves of a) C-ZIF-67:PS-1, c) C-ZIF-67:PS-1-1xDA and e) C-ZIF-67:PS-1-2xDA, recorded at different rotation speeds (rpm) in O_2-purged 0.1 M KOH electrolyte. K-L plots of *b) C-ZIF-67:PS-1, d) C-ZIF-67:PS-1-1xDA and f) C-ZIF-67:PS-1-2xDA* calculated from their RDE LSV curves at the potential range 0.2-0.6 V vs. RHE; the inset: plot of n (electron transfer number) per O_2 molecule at the different potentials. The scan rate was kept at 5 mV s^{-1} for all measurements.

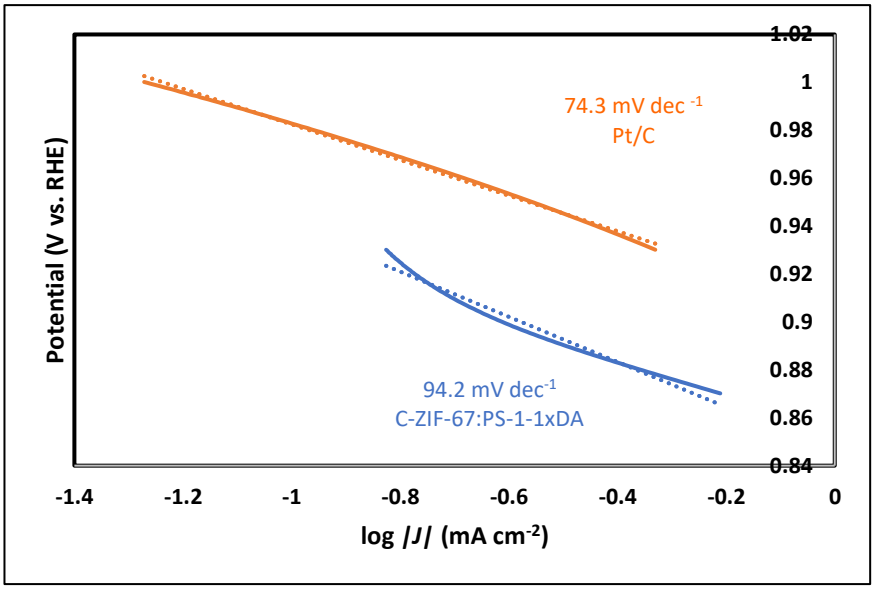

Figure 5.28) Tafel plots of CZIF-67:PS-1-1xDA and 20 wt% Pt/C obtained at 1600 rpm in O_2-saturated 0.1M KOH.

The Tafel plots of the C-ZIF-67:PS-1-1xDA catalyst, and the commercial Pt/C are presented in Figure 5.28. The C-ZIF-67:PS-1-1xDA catalyst presented a higher but comparable Tafel slope of 94.2 mV dec^{-1} to the benchmark Pt/C, indicating comparable performance with respect to the cathodic reduction current increase.

It is likely that the catalytic activity of the electrocatalyst is correlated to its electrochemical surface area (ECSA), proportional do the electrochemical double-layer capacitance (C_{dl}) at the interface between the electrolyte and the catalyst.[191] The C_{dl} was derived by the linear correlation obtained from the current density vs. scan rate plots obtained at a non-Faradaic potential range (Figure 5.26). It is clearly shown that the C-ZIF-67:PS-1 sample displayed a lower C_{dl} (8.7 mF cm^{-2}) while C-ZIF-67:PS-1-1xDA presented a higher value of 10.1 mF cm^{-2}, closer to that reported for Pt/C 11.2 mF cm^{-2}. The larger ECSA of the C-ZIF-67:PS-1-1xDA confirms the catalyst's improved performance and highlights the important role of the PDA coating in promoting electron transfer.

In order to better understand the ORR mechanism of some of the greater performed catalysts, LSV measurements at different rotating speeds were performed (Figures 5.27a, c, e). Flat ORR plateaus and improved limiting current densities are observed as the rotating speed increases, suggesting that the rate determining step is the diffusion of oxygen.[164] The K-L plots were then derived from the RDE curves and the number of electrons transferred per oxygen molecule (n) was calculated (Figures 5.27b, d, f). The n was calculated to be ~ 4 for C-ZIF-67:PS-1-1xDA, indicating a desirable 4-

electron transfer pathway, similar to that reported for Pt/C.[211] As the coating layers increased to 2, C-ZIF-67:PS-1-2xDA, the n number decreased to 3.3 indicating that the ORR reaction was found to be catalysed via a combination of 2-electron and 4-electron transfer reactions. A similar value (3.5) was observed for the C-ZIF-67:PS-1. These results highlight that one PDA coating layer may improve electron movement and conductivity, enhancing the ORR performance, and a greater coating thickness resulting from two PDA layers may start to hinder electron movement.

The stability and degradation of C-ZIF-PS-1, C-ZIF-PS-1-1xDA, C-ZIF-PS-1-2xDA and Pt/C were investigated by a chronoamperometric current-time (i-t) method in an O_2-saturated 0.1 M KOH aqueous electrolyte (Figure 5.28a). The C-ZIF-PS-1-2xDA presented the highest current retention of 82.8 %, for as long as 15,000 s of continuous operation, higher than that of the current retention by C-ZIF-PS-1-1xDA of 76.1 %, C-ZIF-PS-1 of 70.5 % and the benchmark Pt/C catalyst of 66.8 %. These results highlight the importance of an extra PDA coating layer on the catalyst's stability. The accelerated durability tests of C-ZIF-PS-1, C-ZIF-PS-1-1xDA, C-ZIF-PS-1-2xDA and Pt/C are presented in Figure 5.27b. After 400 cycles, the C-ZIF-PS-1 and C-ZIF-PS-1-1xDA catalysts present a reduced degradation behaviour in comparison to that of Pt/C, as suggested by the reduced half-wave potential variation, observed between cycles 1 and

400. The addition of an extra PDA coating layers (C-ZIF-PS-1-2xDA) reduces the catalyst degradation as observed by the reduced $E_{1/2}$ gap after 400 cycles.

The OER activities of the uncoated (C-ZIF-PS-X) and coated fibers (C-ZIF-PS-

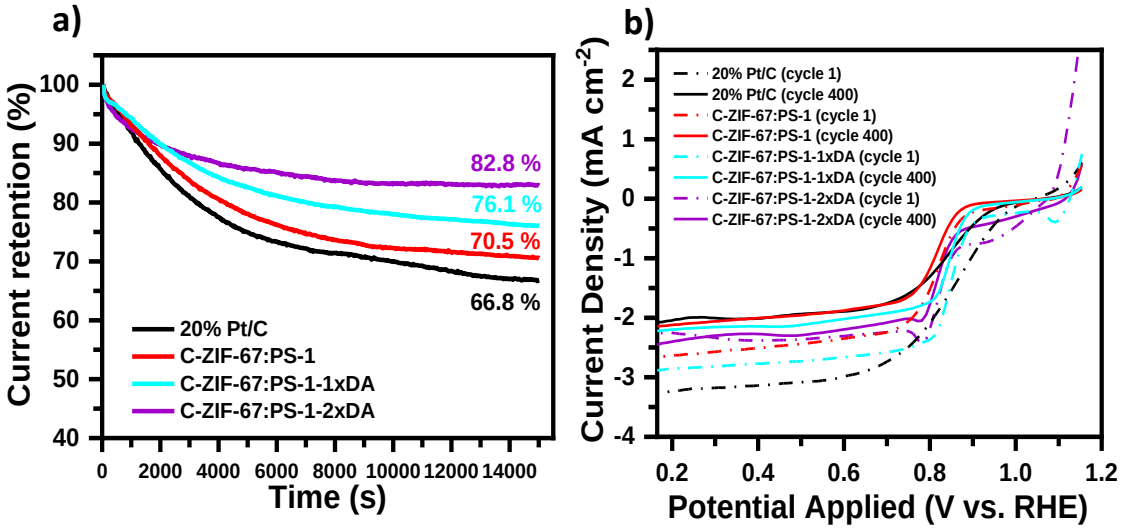

Figure 5.28: a) Chronoamperometric stability plots (i-t plots) of C-ZIF-67:PS-1, C-ZIF-67:PS-1-1xDA, C-ZIF-67:PS-1-2xDA and Pt/C at 0.4 V and a fixed electrode rotation speed of 400 rpm in O_2-saturated 0.1 M KOH electrolyte. b) ADT plots of *C-ZIF-67:PS-1, C-ZIF-67:PS-1-1xDA, C-ZIF-67:PS-1-2xDA and Pt/C before* (dashed lines) and after (solid lines) 400 cycles for ORR at a fixed electrode rotation speed of 400 rpm. The scan rate was kept at 5 mV s^{-1} for all measurements.

1-XDA) was also studied in 0.1 M KOH solution (Figures 5.29). As observed in Figure 5.28a, C-ZIF-67 and the three C-ZIF-PS-X catalysts achieve a current density of 10 mA cm^{-2} at similar potentials ($E_{j=10}$) of 1.75 V vs. RHE, comparable to that of the Ir-based benchmark OER catalyst of $E_{j=10}$=1.76 V vs. RHE. The onset potential of the C-ZIF-67 and C-ZIF-PS-X catalysts displays a similar value of ~ 1.52 V vs. RHE only 30 mV higher than that of Ir/C (1.49 V vs. RHE). As observed, the OER results of C-ZIF-67 and the C-ZIF-PS-X catalysts reveal similar trends. However, as the first two PDA coating layers were added, the OER performance of the catalysts improved (Figure 5.29b). The C-ZIF-PS-1-1xDA showed an onset potential of 1.44 V vs. RHE, $E_{j=10}$ of 1.73 V vs. RHE and achieved a maximum current density of 12.9 mA cm^{-2}, better than the Ir/C results. As the third and fourth coating layers were added, the performance decreased, displaying higher onset potentials and achieving lower energy densities due to reduced access of the electrons to the active sites.

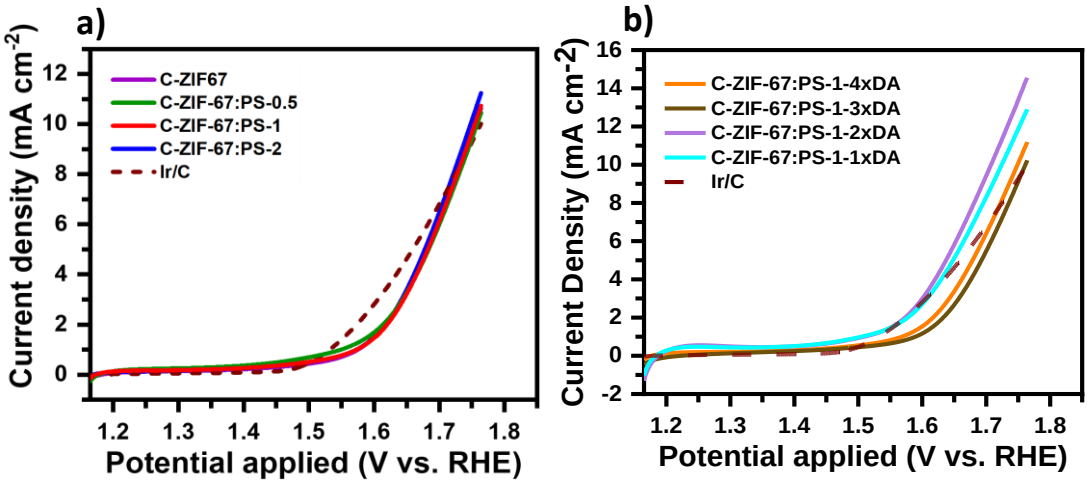

Figure 5.29: Combined LSV curves for OER of a) C-ZIF-67, the C-ZIF-67:PS-X catalysts and Ir/C and b) the C-ZIF-67:PS-XDA catalysts and Ir/C at 1600 rpm in 0.1 M KOH electrolyte. The scan rate was kept at 5 mV s^{-1} for all measurements.

5.2.3. Zinc-air battery performance

Considering the outstanding bifunctional ORR and OER catalytic activity of C-ZIF-PS-1-1xDA, a handmade Zn-air battery containing the developed catalyst on the air cathode was assembled to evaluate its performance under battery operation conditions. In Figure 5.30, the C-ZIF-PS-1-1xDA-based ZAB and the Pt/C-based ZAB show and open circuit voltage (OCV) of ~ 1.39 V and 1.54 V, respectively.

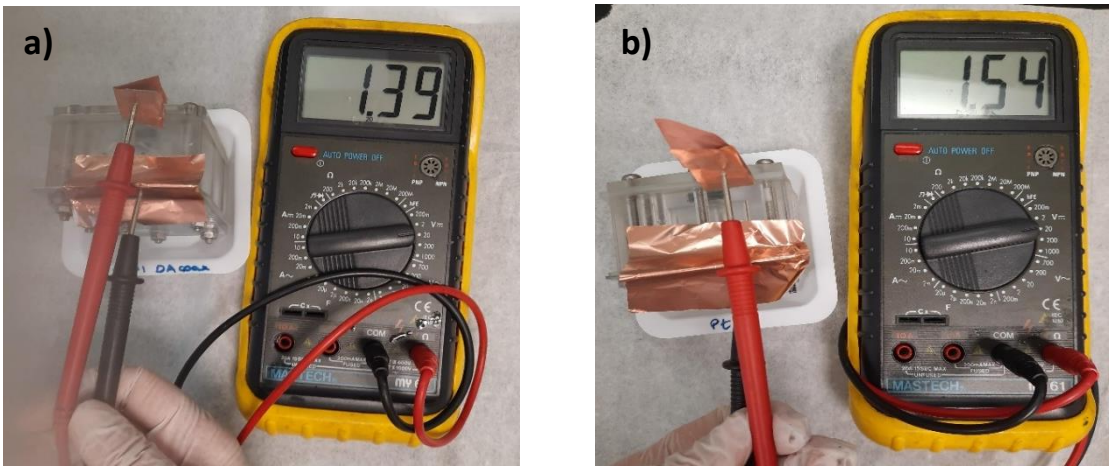

Figure 5.30: A photograph of a) a C-ZIF-PS-1-1xDA-based ZAB showing an OCV of ~ 1.39 V and b) a Pt/C-based ZAB showing an OCV of ~1.54 V.

Figure 5.31 presents the charge and discharge polarization curves of Pt/C, C-ZIF-67:PS-1 and C-ZIF-67:PS-1-1xDA. The C-ZIF-67:PS-1-1xDA electrode showed a slightly lower charge-discharge voltage gap and a higher discharge current in comparison to that of C-ZIF-67:PS-1 and Pt/C, indicating better rechargeability and activity.[172,226]

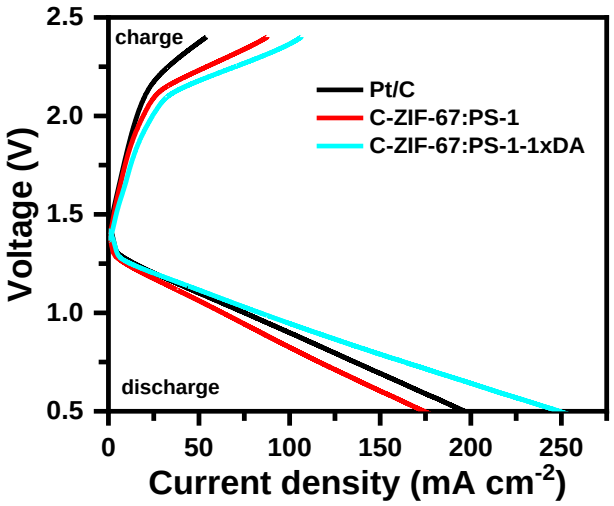

Figure 5.31: Charge and discharge polarization curves of C-ZIF-67:PS-1-1xDA and Pt/C-based ZABs in 6 M KOH electrolyte.

The prepared ZABs were discharged at different current densities of 1, 5, 10, 15 and 30 mA cm^{-2}, as observed in Figure 5.32. The ZAB containing the prepared C-ZIF-67:PS-1-1xDA presented stable discharge plateaus at a current density as high as 30 mA cm^{-2}, with comparable results to those of the ZAB containing the Pt/C catalyst. At such a high current density, the C-ZIF-PS-1-1xDA-based ZAB presented a discharge voltage of 1.1 V, which is only 81 mV lower than that of the Pt/C cell.

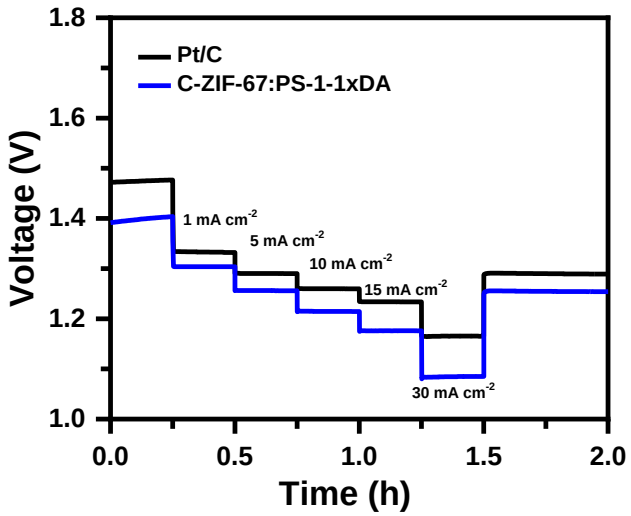

Figure 5.32: Voltage profiles of C-ZIF-67:PS-1-1xDA and Pt/C based ZABs in 6 M KOH electrolyte when discharged at different current densities: 1, 5, 10, 15 and 30 mA cm^{-2}.

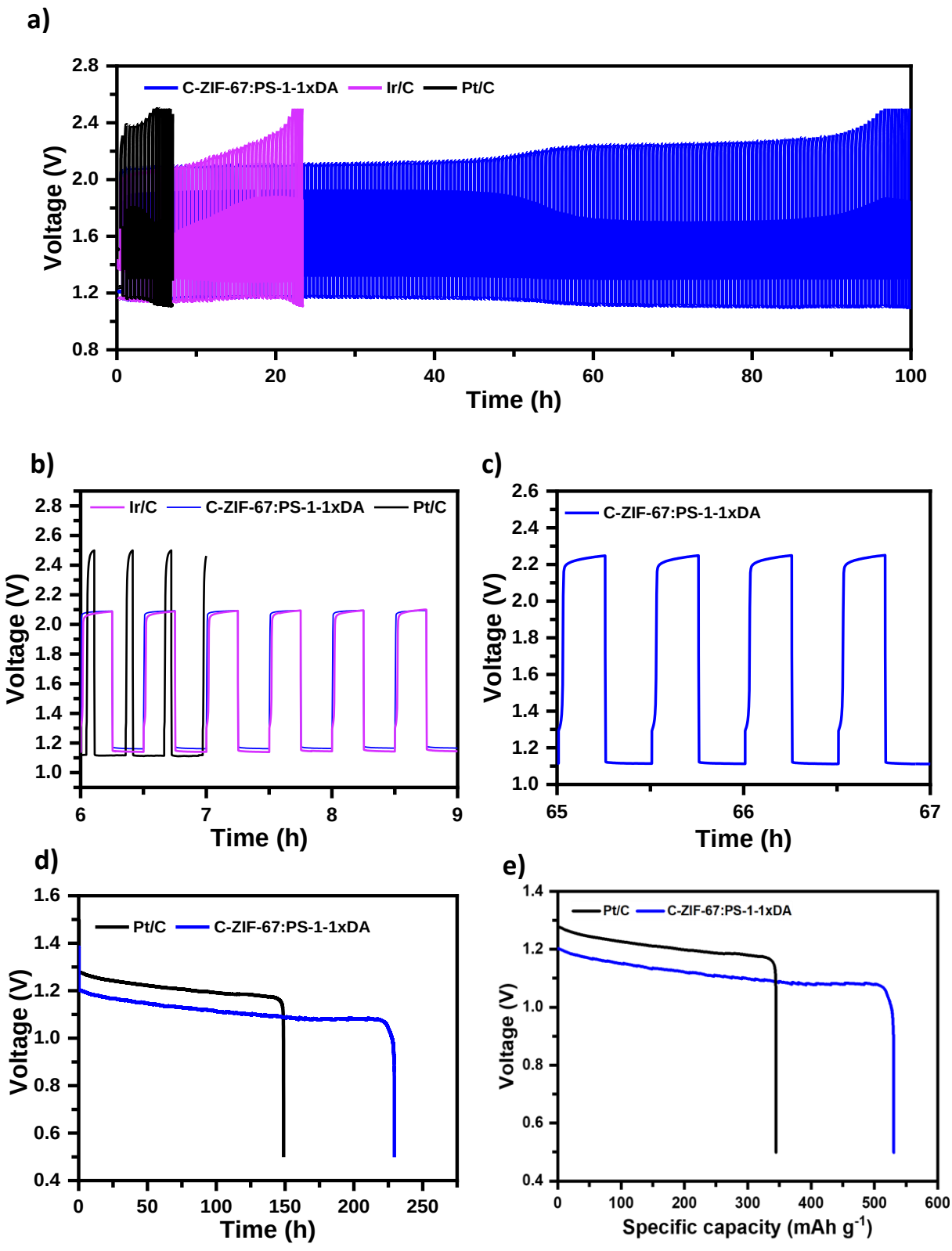

Figure 5.33: a) Discharge-charge cycling performances of ZABs with C-ZIF-67:PS-1-1xDA, Pt/C and Ir/C catalysts in 6 M KOH electrolyte at 10 mA cm^{-2}. b- c) Selected sections of the cycling performances from a). d) Long-term discharge curves of ZABs with C-ZIF-67:PS-1-1xDA, and Pt/C as the cathode catalyst in 6 M KOH electrolyte at 10 mA cm^{-2}. e) Specific capacity curves of ZABs with with C-ZIF-67:PS-1-1xDA, and Pt/C as the cathode catalyst, at 10 mA cm^{-2}.

The performance of the ZAB with the C-ZIF-PS-1-1xDA electrocatalyst was studied by galvanostatic cycling at a high current density of 10mA cm^{-2}, and compared to the Pt/C- and the Ir/C-containing ZABs, as exhibited on Figure 5.33a. The C-ZIF-PS-1-1xDA ZAB presented good rechargeability over a period of about 100 h, much higher than the Pt/C- and Ir/C-based cells which stopped cycling after 7h and 23 h, respectively. The initial voltage gap (Figure 5.33b) of the ZAB with the developed catalyst was about 0.89 V, due to a charging voltage of about 2.08 V and a discharging voltage of 1.2 V, comparable to the voltage gap of the ZAB containing the OER benchmark Ir/C catalyst of 0.88 V and much lower in comparison to the Pt/C-ZAB voltage gap of 1.2 V. After 65 h (Figure 5.33c) the voltage gap of the C-ZIF-PS-1-1xDA-based ZAB increased to about 1.1 V (from a discharge voltage of 1.1 V and a charge voltage of 2.2 V) while remaining stable. Finally, after about 100 h the cell started to degrade, presenting a voltage gap of 1.4 V, originated from a 1.1 V discharge voltage and a 2.5 V charge voltage, however, the cell never achieved the maximum discharge cut off voltage of 0.90 V. The results revealed a voltage gap increase of 0.51 V, obtained from a charging voltage increase of 0.42 V and a low discharge voltage change of only 0.080 V, confirming the catalyst' stability upon discharge. The C-ZIF-PS-1-1xDA- and Pt/C- based long-term discharge plots recorded at 10 mA cm^{-2} are presented in Figure 5.33d. The C-ZIF-PS-1-1xDA-containing ZAB showed a flat and steady discharge plateau for about 230 h, 81 h longer than that observed for the ZAB with the Pt/C catalyst, confirming the catalysts' stability and lower degradation rate, as previously presented in the electrochemical tests. Finally, the C-ZIF-PS-1-1xDA-based battery demonstrated a remarkably high specific capacity of 530 mAh g^{-1} (normalized to the mass of consumed Zn) at a high current density of 10 mA cm^{-2}, being higher than that observed for the battery containing the commercial Pt/C (345 mAh g^{-1}) (Figure 5.33e). This result confirms the outstanding stability and electrochemical performance of the developed C-ZIF-PS-1-1xDA electrocatalyst.

5.3. Conclusion

In Summary, an efficient bifunctional ORR and OER electrocatalyst was prepared by electrospinning ZIF-67 particles with PS and coating by self-polymerized PDA which upon pyrolysis, formed a structure composed of Co-N-based nanoparticles coated by a porous N-rich graphitic carbon nanofibers. The polydopamine coating was crucial to

control the structural integrity of the fiber structures and provide a graphitic carbon coating which has been found to promote electron conductivity.

The large BET surface area, porosity, active sites and 3D network structure of C-ZIF-PS-1-1xDA led to its excellent ORR and OER catalytic performance. Additionally, the ZAB containing the C-ZIF-PS-1-1xDA air cathode catalyst exhibited excellent rechargeable performance for 100h, a remarkably steady long term discharge performance for about 230h and high specific capacity of 530 mAh g^{-1} at a high current density of 10 mA cm^{-2}.

6. References

(1) Li, Y.; Dai, H. Recent Advances in Zinc–Air Batteries. *Chem. Soc. Rev.* **2014**, *43* (15), 5257–5275. https://doi.org/10.1039/C4CS00015C.

(2) Keho, Y. What Drives Energy Consumption in Developing Countries? The Experience of Selected African Countries. *Energy Policy* **2016**, *91* (December 2015), 233–246. https://doi.org/10.1016/j.enpol.2016.01.010.

(3) Caramia, V.; Bozzini, B. Materials Science Aspects of Zinc-Air Batteries: A Review. *Mater. Renew. Sustain. Energy* **2014**, *3* (2). https://doi.org/10.1007/s40243-014-0028-3.

(4) Davari, E.; Ivey, D. G. Bifunctional Electrocatalysts for Zn–Air Batteries. *Sustain. Energy Fuels* **2017**, *2* (1), 39–67. https://doi.org/10.1039/c7se00413c.

(5) Ren, S.; Duan, X.; Liang, S.; Zhang, M.; Zheng, H. Bifunctional Electrocatalysts for Zn-Air Batteries: Recent Developments and Future Perspectives. *J. Mater. Chem. A* **2020**, *8* (13), 6144–6182. https://doi.org/10.1039/c9ta14231b.

(6) Li, Y.; Lu, J. Metal-Air Batteries: Will They Be the Future Electrochemical Energy Storage Device of Choice? *ACS Energy Lett.* **2017**, *2* (6), 1370–1377. https://doi.org/10.1021/acsenergylett.7b00119.

(7) Gu, P.; Zheng, M.; Zhao, Q.; Xiao, X.; Xue, H.; Pang, H. Rechargeable Zinc-Air Batteries: A Promising Way to Green Energy. *J. Mater. Chem. A* **2017**, *5* (17), 7651–7666. https://doi.org/10.1039/c7ta01693j.

(8) Zhang, J.; Zhou, Q.; Tang, Y.; Zhang, L.; Li, Y. Zinc-Air Batteries: Are They Ready for Prime Time? *Chem. Sci.* **2019**, *10* (39), 8924–8929. https://doi.org/10.1039/c9sc04221k.

(9) Etacheri, V.; Marom, R.; Elazari, R.; Salitra, G.; Aurbach, D. Challenges in the Development of Advanced Li-Ion Batteries: A Review. *Energy Environ. Sci.* **2011**, *4* (9), 3243–3262. https://doi.org/10.1039/c1ee01598b.

(10) Prakoso, B.; Mahbub, M. A. A.; Yilmaz, M.; Khoiruddin; Wenten, I. G.; Handoko, A. D.; Sumboja, A. Recent Progress in Extending the Cycle-Life of Secondary Zn-Air Batteries. *ChemNanoMat* **2021**, *7* (4), 354–367. https://doi.org/10.1002/cnma.202000672.

(11) Panasonic. Lithium Ion Batteries. **2007**.

(12) Mezei, F. *Basics Concepts*; 2011. https://doi.org/10.1002/9780470933886.ch1.

(13) Huang, Z. F.; Wang, J.; Peng, Y.; Jung, C. Y.; Fisher, A.; Wang, X. Design of Efficient Bifunctional Oxygen Reduction/Evolution Electrocatalyst: Recent Advances and Perspectives. *Adv. Energy Mater.* **2017**, *7* (23), 1–21. https://doi.org/10.1002/aenm.201700544.

(14) Narayanan, S. R.; Prakash, G. K. S.; Manohar, A.; Yang, B.; Malkhandi, S.; Kindler, A. Materials Challenges and Technical Approaches for Realizing Inexpensive and Robust Iron-Air Batteries for Large-Scale Energy Storage. *Solid State Ionics* **2012**, *216*, 105–109. https://doi.org/10.1016/j.ssi.2011.12.002.

(15) Egan, D. R.; Ponce De León, C.; Wood, R. J. K.; Jones, R. L.; Stokes, K. R.; Walsh, F. C. Developments in Electrode Materials and Electrolytes for Aluminiumeair Batteries. *J. Power Sources* **2013**, *236*, 293–310. https://doi.org/10.1016/j.jpowsour.2013.01.141.

(16) Zhang, T.; Tao, Z.; Chen, J. Magnesium-Air Batteries: From Principle to Application. *Mater. Horizons* **2014**, *1* (2), 196–206. https://doi.org/10.1039/c3mh00059a.

(17) Hilder, M.; Winther-Jensen, B.; Clark, N. B. The Effect of Binder and Electrolyte on the Performance of Thin Zinc-Air Battery. *Electrochim. Acta* **2012**, *69*, 308–314. https://doi.org/10.1016/j.electacta.2012.03.004.

(18) Lee, J. S.; Kim, S. T.; Cao, R.; Choi, N. S.; Liu, M.; Lee, K. T.; Cho, J. Metal-Air Batteries with High Energy Density: Li-Air versus Zn-Air. *Adv. Energy Mater.* **2011**, *1* (1), 34–50. https://doi.org/10.1002/aenm.201000010.

(19) Yang, Z.; Zhang, J.; Kintner-Meyer, M. C. W.; Lu, X.; Choi, D.; Lemmon, J. P.; Liu, J. Electrochemical Energy Storage for Green Grid. *Chem. Rev.* **2011**, *111* (5), 3577–3613. https://doi.org/10.1021/cr100290v.

(20) Amendola, S. ELECTRICALLY RECHARGEABLE, METAL-AR BATTERY SYSTEMS AND METHODS, 2012.

(21) T. Burchardt and M. Lanfranconi. METAL-AIR BATTERY WITH IMPROVED ENVIRONMENTAL STABILITY. **2011**, *US Pat.* (0027664 A1).

(22) Burchardt, T.; Lanfranconi, M. METAL-AR BATTERY WITH ON EXCHANGE MATERALS, 2011.

(23) Toussaint, G.; Stevens, P.; Akrour, L.; Rouget, R.; Fourgeot, F. Development of a Rechargeable Zinc-Air Battery. *ECS Trans.* **2019**, *28* (32), 25–34. https://doi.org/10.1149/1.3507924.

(24) Pei, P.; Wang, K.; Ma, Z. Technologies for Extending Zinc-Air Battery's Cyclelife: A Review. *Appl. Energy* **2014**, *128*, 315–324. https://doi.org/10.1016/j.apenergy.2014.04.095.

(25) Heilig, M. L. United States Patent Office. *ACM SIGGRAPH Comput. Graph.* **1994**, *28* (2), 131–134. https://doi.org/10.1145/178951.178972.

(26) Hese, G. W. Air Depolarized Primary Battery. *U.S. Pat.* **1933**, *1,899,615*.

(27) Cheng, F.; Chen, J. Metal–Air Batteries: From Oxygen Reduction Electrochemistry to Cathode Catalysts. *Chem. Soc. Rev.* **2012**, *41* (6), 2172–2192. https://doi.org/10.1039/c1cs15228a.

(28) Dondelinger. Batteries: From Alkaline to Zinc-Air. *Biomed. Instrum. Technol. /* **2004**, *38* (2), 100.

(29) Parker, J. F.; Nelson, E. S.; Wattendorf, M. D.; Chervin, C. N.; Long, J. W.; Rolison, D.

R. Retaining the 3D Framework of Zinc Sponge Anodes upon Deep Discharge in Zn-Air Cells. *ACS Appl. Mater. Interfaces* **2014**, *6* (22), 19471–19476. https://doi.org/10.1021/am505266c.

(30) Parker, J. F.; Chervin, C. N.; Nelson, E. S.; Rolison, D. R.; Long, J. W. Wiring Zinc in Three Dimensions Re-Writes Battery Performance - Dendrite-Free Cycling. *Energy Environ. Sci.* **2014**, *7* (3), 1117–1124. https://doi.org/10.1039/c3ee43754j.

(31) Masri, M. N.; Mohamad, A. A. Effect of Adding Carbon Black to a Porous Zinc Anode in a Zinc-Air Battery. *J. Electrochem. Soc.* **2013**, *160* (4), A715–A721. https://doi.org/10.1149/2.007306jes.

(32) Zhang, X. G. Fibrous Zinc Anodes for High Power Batteries. *J. Power Sources* **2006**, *163* (1 SPEC. ISS.), 591–597. https://doi.org/10.1016/j.jpowsour.2006.09.034.

(33) Haas, O.; Holzer, F.; M, K.; M, S. Metal / Air Batteries : The Zinc / Air Case. **2010**, 1–27.

(34) Wu, J.; Hu, L.; Wang, N.; Li, Y.; Zhao, D.; Li, L.; Peng, X.; Cui, Z.; Ma, L. J.; Tian, Y.; Wang, X. Surface Confinement Assisted Synthesis of Nitrogen-Rich Hollow Carbon Cages with Co Nanoparticles as Breathable Electrodes for Zn-Air Batteries. *Appl. Catal. B Environ.* **2019**, *254* (March), 55–65. https://doi.org/10.1016/j.apcatb.2019.04.064.

(35) Mainar, A. R.; Iruin, E.; Colmenares, L. C.; Kvasha, A.; de Meatza, I.; Bengoechea, M.; Leonet, O.; Boyano, I.; Zhang, Z.; Blazquez, J. A. An Overview of Progress in Electrolytes for Secondary Zinc-Air Batteries and Other Storage Systems Based on Zinc. *J. Energy Storage* **2018**, *15*, 304–328. https://doi.org/10.1016/j.est.2017.12.004.

(36) McLarnon, F. R.; Cairns, E. J. The Secondary Alkaline Zinc Electrode. *J. Electrochem. Soc.* **1991**, *138* (2), 645–656. https://doi.org/10.1149/1.2085653.

(37) Sapkota, P.; Kim, H. Zinc-Air Fuel Cell, a Potential Candidate for Alternative Energy. *J. Ind. Eng. Chem.* **2009**, *15* (4), 445–450. https://doi.org/10.1016/j.jiec.2009.01.002.

(38) Mainar, A. R.; Colmenares, L. C.; Blázquez, J. A.; Urdampilleta, I. A Brief Overview of Secondary Zinc Anode Development: The Key of Improving Zinc-Based Energy Storage Systems. *Int. J. Energy Res.* **2018**, *42* (3), 903–918. https://doi.org/10.1002/er.3822.

(39) Drillet, J. F.; Holzer, F.; Kallis, T.; Müller, S.; Schmidt, V. M. Influence of CO2 on the Stability of Bifunctional Oxygen Electrodes for Rechargeable Zinc/Air Batteries and Study of Different CO2 Filter Materials. *Phys. Chem. Chem. Phys.* **2001**, *3* (3), 368–371. https://doi.org/10.1039/b005523i.

(40) Takeshita, Y.; Fujimoto, S.; Sudoh, M. Design of Rechargeable Air Diffusion Cathode for Metal-Air Battery Using Alkaline Solution. *ECS Trans.* **2013**, *50* (19), 3–12. https://doi.org/10.1149/05019.0003ecst.

(41) Bidault, F.; Brett, D. J. L.; Middleton, P. H.; Brandon, N. P. Review of Gas Diffusion Cathodes for Alkaline Fuel Cells. *J. Power Sources* **2009**, *187* (1), 39–48. https://doi.org/10.1016/j.jpowsour.2008.10.106.

(42) Zhu, W. H.; Poole, B. A.; Cahela, D. R.; Tatarchuk, B. J. New Structures of Thin Air Cathodes for Zinc-Air Batteries. *J. Appl. Electrochem.* **2003**, *33* (1), 29–36. https://doi.org/10.1023/A:1022986707273.

(43) Cheng, F.; Shen, J.; Peng, B.; Pan, Y.; Tao, Z.; Chen, J. Rapid Room-Temperature Synthesis of Nanocrystalline Spinels as Oxygen Reduction and Evolution Electrocatalysts. *Nat. Chem.* **2011**, *3* (1), 79–84. https://doi.org/10.1038/nchem.931.

(44) Maja, M.; Orecchia, C.; Strano, M.; Tosco, P.; Vanni, M. Effect of Structure of the

Electrical Performance of Gas Diffusion Electrodes for Metal Air Batteries. *Electrochim. Acta* **2000**, *46* (2–3), 423–432. https://doi.org/10.1016/S0013-4686(00)00601-0.

(45) Kordesch, K.; Jahangir, S.; Schautz, M. Engineering Concepts and Technical Performance of Oxygen-Reducing Electrodes for Batteries and Electrochemical Processes. *Electrochim. Acta* **1984**, *29* (11), 1589–1596. https://doi.org/10.1016/0013-4686(84)85013-6.

(46) Jörissen, L. Bifunctional Oxygen/Air Electrodes. *J. Power Sources* **2006**, *155* (1), 23–32. https://doi.org/10.1016/j.jpowsour.2005.07.038.

(47) Wang, Z. L.; Xu, D.; Xu, J. J.; Zhang, X. B. Oxygen Electrocatalysts in Metal-Air Batteries: From Aqueous to Nonaqueous Electrolytes. *Chem. Soc. Rev.* **2014**, *43* (22), 7746–7786. https://doi.org/10.1039/c3cs60248f.

(48) Lee, C. H.; Jun, B.; Lee, S. U. Metal-Free Oxygen Evolution and Oxygen Reduction Reaction Bifunctional Electrocatalyst in Alkaline Media: From Mechanisms to Structure-Catalytic Activity Relationship. *ACS Sustain. Chem. Eng.* **2018**, *6* (4), 4973–4980. https://doi.org/10.1021/acssuschemeng.7b04608.

(49) Ge, X.; Sumboja, A.; Wuu, D.; An, T.; Li, B.; Goh, F. W. T.; Hor, T. S. A.; Zong, Y.; Liu, Z. Oxygen Reduction in Alkaline Media: From Mechanisms to Recent Advances of Catalysts. *ACS Catal.* **2015**, *5* (8), 4643–4667. https://doi.org/10.1021/acscatal.5b00524.

(50) Blizanac, B. B.; Ross, P. N.; Markovic, N. M. Oxygen Electroreduction on Ag(1 1 1): The PH Effect. *Electrochim. Acta* **2007**, *52* (6), 2264–2271. https://doi.org/10.1016/j.electacta.2006.06.047.

(51) Xia, W.; Mahmood, A.; Liang, Z.; Zou, R.; Guo, S. Earth-Abundant Nanomaterials for Oxygen Reduction. *Angew. Chemie - Int. Ed.* **2016**, *55* (8), 2650–2676. https://doi.org/10.1002/anie.201504830.

(52) She, Z. W.; Kibsgaard, J.; Dickens, C. F.; Chorkendorff, I.; Nørskov, J. K.; Jaramillo, T. F. Combining Theory and Experiment in Electrocatalysis: Insights into Materials Design. *Science (80-.).* **2017**, *355* (6321). https://doi.org/10.1126/science.aad4998.

(53) Jiao, Y.; Zheng, Y.; Jaroniec, M.; Qiao, S. Z. Design of Electrocatalysts for Oxygen- and Hydrogen-Involving Energy Conversion Reactions. *Chem. Soc. Rev.* **2015**, *44* (8), 2060–2086. https://doi.org/10.1039/c4cs00470a.

(54) Elgrishi, N.; Rountree, K. J.; McCarthy, B. D.; Rountree, E. S.; Eisenhart, T. T.; Dempsey, J. L. A Practical Beginner's Guide to Cyclic Voltammetry. *J. Chem. Educ.* **2018**, *95* (2), 197–206. https://doi.org/10.1021/acs.jchemed.7b00361.

(55) Hong, W. T.; Risch, M.; Stoerzinger, K. A.; Grimaud, A.; Suntivich, J.; Shao-Horn, Y. Toward the Rational Design of Non-Precious Transition Metal Oxides for Oxygen Electrocatalysis. *Energy Environ. Sci.* **2015**, *8* (5), 1404–1427. https://doi.org/10.1039/c4ee03869j.

(56) Chatenet, M.; Genies-Bultel, L.; Aurousseau, M.; Durand, R.; Andolfatto, F. Oxygen Reduction on Silver Catalysts in Solutions Containing Various Concentrations of Sodium Hydroxide - Comparison with Platinum. *J. Appl. Electrochem.* **2002**, *32* (10), 1131–1140. https://doi.org/10.1023/A:1021231503922.

(57) Rossmeisl, J.; Qu, Z. W.; Zhu, H.; Kroes, G. J.; Nørskov, J. K. Electrolysis of Water on Oxide Surfaces. *J. Electroanal. Chem.* **2007**, *607* (1–2), 83–89. https://doi.org/10.1016/j.jelechem.2006.11.008.

(58) Dau, H.; Limberg, C.; Reier, T.; Risch, M.; Roggan, S.; Strasser, P. The Mechanism of Water Oxidation: From Electrolysis via Homogeneous to Biological Catalysis.

ChemCatChem **2010**, *2* (7), 724–761. https://doi.org/10.1002/cctc.201000126.

(59) Fang, P. P.; Duan, S.; Lin, X. D.; Anema, J. R.; Li, J. F.; Buriez, O.; Ding, Y.; Fan, F. R.; Wu, D. Y.; Ren, B.; Wang, Z. L.; Amatore, C.; Tian, Z. Q. Tailoring Au-Core Pd-Shell Pt-Cluster Nanoparticles for Enhanced Electrocatalytic Activity. *Chem. Sci.* **2011**, *2* (3), 531–539. https://doi.org/10.1039/c0sc00489h.

(60) Stamenkovic, V. R.; Fowler, B.; Mun, B. S.; Wang, G.; Ross, P. N.; Lucas, C. A.; Markovic, N. M. Improved Oxygen Reduction Activity on Pt3Ni(111) via Increased Surface Site Availability. *Science (80-.).* **2007**, *315* (5811), 493–497. https://doi.org/10.1126/science.1135941.

(61) Lim, B.; Jiang, M.; Camargo, P. H. C.; Cho, E. C.; Tao, J.; Lu, X.; Zhu, Y.; Xia, Y. Pd-Pt Bimetallic Nanodendrites with High Activity for Oxygen Reduction. *Science (80-.).* **2009**, *324* (5932), 1302–1305. https://doi.org/10.1126/science.1170377.

(62) Zhang, G. Q.; Zhang, X. G.; Wang, Y. G. A New Air Electrode Based on Carbon Nanotubes and Ag-MnO2 for Metal Air Electrochemical Cells. *Carbon N. Y.* **2004**, *42* (15), 3097–3102. https://doi.org/10.1016/j.carbon.2004.07.015.

(63) Hu, F. P.; Zhang, X. G.; Xiao, F.; Zhang, J. L. Oxygen Reduction on Ag-MnO2/SWNT and Ag-MnO2/AB Electrodes. *Carbon N. Y.* **2005**, *43* (14), 2931–2936. https://doi.org/10.1016/j.carbon.2005.06.010.

(64) Wang, T.; Kaempgen, M.; Nopphawan, P.; Wee, G.; Mhaisalkar, S.; Srinivasan, M. Silver Nanoparticle-Decorated Carbon Nanotubes as Bifunctional Gas-Diffusion Electrodes for Zinc-Air Batteries. *J. Power Sources* **2010**, *195* (13), 4350–4355. https://doi.org/10.1016/j.jpowsour.2009.12.137.

(65) Varcoe, J. R.; Slade, R. C. T.; Wright, G. L.; Chen, Y. Steady-State Dc and Impedance Investigations of H2/O2 Alkaline Membrane Fuel Cells with Commercial Pt/C, Ag/C, and Au/C Cathodes. *J. Phys. Chem. B* **2006**, *110* (42), 21041–21049. https://doi.org/10.1021/jp064898b.

(66) Guo, J.; Hsu, A.; Chu, D.; Chen, R. Improving Oxygen Reduction Reaction Activities on Carbon-Supported Ag Nanoparticles in Alkaline Solutions. *J. Phys. Chem. C* **2010**, *114* (10), 4324–4330. https://doi.org/10.1021/jp910790u.

(67) Hu, J.; Liu, Q.; Shi, L.; Shi, Z.; Huang, H. Silver Decorated LaMnO 3 Nanorod/Graphene Composite Electrocatalysts as Reversible Metal-Air Battery Electrodes. *Appl. Surf. Sci.* **2017**, *402*, 61–69. https://doi.org/10.1016/j.apsusc.2017.01.060.

(68) Guo, Z.; Li, C.; Li, W.; Guo, H.; Su, X.; He, P.; Wang, Y.; Xia, Y. Ruthenium Oxide Coated Ordered Mesoporous Carbon Nanofiber Arrays: A Highly Bifunctional Oxygen Electrocatalyst for Rechargeable Zn-Air Batteries. *J. Mater. Chem. A* **2016**, *4* (17), 6282–6289. https://doi.org/10.1039/c6ta02030e.

(69) Nørskov, J. K.; Bligaard, T.; Rossmeisl, J.; Christensen, C. H. Towards the Computational Design of Solid Catalysts. *Nat. Chem.* **2009**, *1* (1), 37–46. https://doi.org/10.1038/nchem.121.

(70) Loh, G. C.; Baillargeat, D. Graphitization of Amorphous Carbon and Its Transformation Pathways. *J. Appl. Phys.* **2013**, *114* (3). https://doi.org/10.1063/1.4816313.

(71) Rodríguez-Manzo, J. A.; Pham-Huu, C.; Banhart, F. Graphene Growth by a Metal-Catalyzed Solid-State Transformation of Amorphous Carbon. *ACS Nano* **2011**, *5* (2), 1529–1534. https://doi.org/10.1021/nn103456z.

(72) Wang, J.; Wu, H.; Gao, D.; Miao, S.; Wang, G.; Bao, X. High-Density Iron

Nanoparticles Encapsulated within Nitrogen-Doped Carbon Nanoshell as Efficient Oxygen Electrocatalyst for Zinc-Air Battery. *Nano Energy* **2015**, *13*, 387–396. https://doi.org/10.1016/j.nanoen.2015.02.025.

(73) Gao, L.; Zhang, M.; Zhang, H.; Zhang, Z. Cobalt-Carbon Nanocage Modified Carbon Foam as the Efficient Catalyst towards Oxygen Reduction Reaction and High-Performance Zinc-Air Battery. *J. Power Sources* **2020**, *450* (June 2019), 227577. https://doi.org/10.1016/j.jpowsour.2019.227577.

(74) Wang, D.; Yang, P.; Xu, H.; Ma, J.; Du, L.; Zhang, G. X.; Li, R.; Jiang, Z.; Li, Y.; Zhang, J.; An, M. The Dual-Nitrogen-Source Strategy to Modulate a Bifunctional Hybrid Co/Co–N–C Catalyst in the Reversible Air Cathode for Zn-Air Batteries. *J. Power Sources* **2021**, *485* (November 2020), 229339. https://doi.org/10.1016/j.jpowsour.2020.229339.

(75) Gupta, S.; Qiao, L.; Zhao, S.; Xu, H.; Lin, Y.; Devaguptapu, S. V.; Wang, X.; Swihart, M. T.; Wu, G. Highly Active and Stable Graphene Tubes Decorated with FeCoNi Alloy Nanoparticles via a Template-Free Graphitization for Bifunctional Oxygen Reduction and Evolution. *Adv. Energy Mater.* **2016**, *6* (22), 1–12. https://doi.org/10.1002/aenm.201601198.

(76) Zheng, Y.; Jiao, Y.; Zhu, Y.; Cai, Q.; Vasileff, A.; Li, L. H.; Han, Y.; Chen, Y.; Qiao, S. Z. Molecule-Level g-C3N4 Coordinated Transition Metals as a New Class of Electrocatalysts for Oxygen Electrode Reactions. *J. Am. Chem. Soc.* **2017**, *139* (9), 3336–3339. https://doi.org/10.1021/jacs.6b13100.

(77) Li, B.; Chen, Y.; Ge, X.; Chai, J.; Zhang, X.; Hor, T. S. A.; Du, G.; Liu, Z.; Zhang, H.; Zong, Y. Mussel-Inspired One-Pot Synthesis of Transition Metal and Nitrogen Co-Doped Carbon (M/N-C) as Efficient Oxygen Catalysts for Zn-Air Batteries. *Nanoscale* **2016**, *8* (9), 5067–5075. https://doi.org/10.1039/c5nr06538k.

(78) Park, K. S.; Ni, Z.; Côté, A. P.; Choi, J. Y.; Huang, R.; Uribe-Romo, F. J.; Chae, H. K.; O'Keeffe, M.; Yaghi, O. M. Exceptional Chemical and Thermal Stability of Zeolitic Imidazolate Frameworks. *Proc. Natl. Acad. Sci. U. S. A.* **2006**, *103* (27), 10186–10191. https://doi.org/10.1073/pnas.0602439103.

(79) Sheberla, D.; Sun, L.; Blood-forsythe, M. A.; Er, S.; Wade, C. R.; Brozek, C. K. High Electrical Conductivity in Ni3(2,3,6,7,10,11-Hexaiminotriphenylene)2, a Semiconducting Metal–Organic Graphene Analogue. *J. Am. Chem. Soc.* **2014**, *25* (136), 8859–8862.

(80) Miner, E. M.; Fukushima, T.; Sheberla, D.; Sun, L.; Surendranath, Y.; Dincə, M. Electrochemical Oxygen Reduction Catalysed by Ni3 (Hexaiminotriphenylene)2. *Nat. Commun.* **2016**, *7*, 10942. https://doi.org/10.1038/ncomms10942.

(81) Lian, Y.; Yang, W.; Zhang, C.; Sun, H.; Deng, Z.; Xu, W.; Song, L.; Ouyang, Z.; Wang, Z.; Guo, J.; Peng, Y. Unpaired 3d Electrons on Atomically Dispersed Cobalt Centres in Coordination Polymers Regulate Both Oxygen Reduction Reaction (ORR) Activity and Selectivity for Use in Zinc–Air Batteries. *Angew. Chemie - Int. Ed.* **2020**, *59* (1), 286–294. https://doi.org/10.1002/anie.201910879.

(82) Rui, K.; Zhao, G.; Chen, Y.; Lin, Y.; Zhou, Q.; Chen, J.; Zhu, J.; Sun, W.; Huang, W.; Dou, S. X. Hybrid 2D Dual-Metal–Organic Frameworks for Enhanced Water Oxidation Catalysis. *Adv. Funct. Mater.* **2018**, *28* (26), 1–9. https://doi.org/10.1002/adfm.201801554.

(83) Ji, D.; Fan, L.; Li, L.; Peng, S.; Yu, D.; Song, J.; Ramakrishna, S.; Guo, S. Atomically Transition Metals on Self-Supported Porous Carbon Flake Arrays as Binder-Free Air Cathode for Wearable Zinc−Air Batteries. *Adv. Mater.* **2019**, *31* (1808267), 1–8.

https://doi.org/10.1002/adma.201808267.

(84) Ma, L.; Chen, S.; Pei, Z.; Huang, Y.; Liang, G.; Mo, F.; Yang, Q.; Su, J.; Gao, Y.; Zapien, J. A.; Zhi, C. Single-Site Active Iron-Based Bifunctional Oxygen Catalyst for a Compressible and Rechargeable Zinc-Air Battery. *ACS Nano* **2018**, *12* (2), 1949–1958. https://doi.org/10.1021/acsnano.7b09064.

(85) Zhao, J.; Hu, H.; Wu, M. N-Doped-Carbon/Cobalt-Nanoparticle/N-Doped-Carbon Multi-Layer Sandwich Nanohybrids Derived from Cobalt MOFs Having 3D Molecular Structures as Bifunctional Electrocatalysts for on-Chip Solid-State Zn-Air Batteries. *Nanoscale* **2020**, *12* (6), 3750–3762. https://doi.org/10.1039/c9nr09779a.

(86) Tang, J.; Salunkhe, R. R.; Liu, J.; Torad, N. L.; Imura, M.; Furukawa, S.; Yamauchi, Y. Thermal Conversion of Core-Shell Metal-Organic Frameworks: A New Method for Selectively Functionalized Nanoporous Hybrid Carbon. *J. Am. Chem. Soc.* **2015**, *137* (4), 1572–1580. https://doi.org/10.1021/ja511539a.

(87) Amiinu, I. S.; Liu, X.; Pu, Z.; Li, W.; Li, Q.; Zhang, J.; Tang, H.; Zhang, H.; Mu, S. From 3D ZIF Nanocrystals to Co–Nx/C Nanorod Array Electrocatalysts for ORR, OER, and Zn–Air Batteries. *Adv. Funct. Mater.* **2018**, *28* (5), 1–9. https://doi.org/10.1002/adfm.201704638.

(88) Guo, Z.; Wang, F.; Xia, Y.; Li, J.; Tamirat, A. G.; Liu, Y.; Wang, L.; Wang, Y.; Xia, Y. In Situ Encapsulation of Core-Shell-Structured Co@Co3O4 into Nitrogen-Doped Carbon Polyhedra as a Bifunctional Catalyst for Rechargeable Zn-Air Batteries. *J. Mater. Chem. A* **2018**, *6* (4), 1443–1453. https://doi.org/10.1039/c7ta09958d.

(89) Wang, Q.; Shang, L.; Shi, R.; Zhang, X.; Waterhouse, G. I. N.; Wu, L. Z.; Tung, C. H.; Zhang, T. 3D Carbon Nanoframe Scaffold-Immobilized Ni3FeN Nanoparticle Electrocatalysts for Rechargeable Zinc-Air Batteries' Cathodes. *Nano Energy* **2017**, *40* (July), 382–389. https://doi.org/10.1016/j.nanoen.2017.08.040.

(90) Zhang, H.; Wang, T.; Sumboja, A.; Zang, W.; Xie, J.; Gao, D.; Pennycook, S. J.; Liu, Z.; Guan, C.; Wang, J. Integrated Hierarchical Carbon Flake Arrays with Hollow P-Doped CoSe2 Nanoclusters as an Advanced Bifunctional Catalyst for Zn–Air Batteries. *Adv. Funct. Mater.* **2018**, *28* (40), 1–9. https://doi.org/10.1002/adfm.201804846.

(91) Zhong, Y.; Pan, Z.; Wang, X.; Yang, J.; Qiu, Y.; Xu, S.; Lu, Y.; Huang, Q.; Li, W. Hierarchical Co3O4 Nano-Micro Arrays Featuring Superior Activity as Cathode in a Flexible and Rechargeable Zinc–Air Battery. *Adv. Sci.* **2019**, *6* (11). https://doi.org/10.1002/advs.201802243.

(92) Cheng, C.; Zhang, H.; Ren, W.; Liu, Z.; Wang, J.; Guan, C.; Liu, X.; Sumboja, A.; Pennycook, S. J.; Wu, H. Hollow Co 3 O 4 Nanosphere Embedded in Carbon Arrays for Stable and Flexible Solid-State Zinc-Air Batteries . *Adv. Mater.* **2017**, *29* (44), 1704117. https://doi.org/10.1002/adma.201704117.

(93) Jiang, Y.; Deng, Y. P.; Fu, J.; Lee, D. U.; Liang, R.; Cano, Z. P.; Liu, Y.; Bai, Z.; Hwang, S.; Yang, L.; Su, D.; Chu, W.; Chen, Z. Interpenetrating Triphase Cobalt-Based Nanocomposites as Efficient Bifunctional Oxygen Electrocatalysts for Long-Lasting Rechargeable Zn–Air Batteries. *Adv. Energy Mater.* **2018**, *8* (15), 1–11. https://doi.org/10.1002/aenm.201702900.

(94) Ikeda, T.; Boero, M.; Huang, S. F.; Terakura, K.; Oshima, M.; Ozaki, J. I. Carbon Alloy Catalysts: Active Sites for Oxygen Reduction Reaction. *J. Phys. Chem. C* **2008**, *112* (38), 14706–14709. https://doi.org/10.1021/jp806084d.

(95) Ma, R.; Lin, G.; Zhou, Y.; Liu, Q.; Zhang, T.; Shan, G.; Yang, M.; Wang, J. A Review of Oxygen Reduction Mechanisms for Metal-Free Carbon-Based Electrocatalysts. *npj*

Comput. Mater. **2019**, *5* (1). https://doi.org/10.1038/s41524-019-0210-3.

(96) Liang, H. W.; Wu, Z. Y.; Chen, L. F.; Li, C.; Yu, S. H. Bacterial Cellulose Derived Nitrogen-Doped Carbon Nanofiber Aerogel: An Efficient Metal-Free Oxygen Reduction Electrocatalyst for Zinc-Air Battery. *Nano Energy* **2015**, *11*, 366–376. https://doi.org/10.1016/j.nanoen.2014.11.008.

(97) Wen, L.; Li, F.; Cheng, H. M. Carbon Nanotubes and Graphene for Flexible Electrochemical Energy Storage: From Materials to Devices. *Adv. Mater.* **2016**, *28* (22), 4306–4337. https://doi.org/10.1002/adma.201504225.

(98) Li, J. C.; Hou, P. X.; Liu, C. Heteroatom-Doped Carbon Nanotube and Graphene-Based Electrocatalysts for Oxygen Reduction Reaction. *Small* **2017**, *13* (45), 1–13. https://doi.org/10.1002/smll.201702002.

(99) Strelko, V. V.; Kuts, V. S.; Thrower, P. A. On the Mechanism of Possible Influence of Heteroatoms of Nitrogen, Boron and Phosphorus in a Carbon Matrix on the Catalytic Activity of Carbons in Electron Transfer Reactions. *Carbon N. Y.* **2000**, *38* (10), 1499–1503. https://doi.org/10.1016/S0008-6223(00)00121-4.

(100) Hadidi, L.; Davari, E.; Iqbal, M.; Purkait, T. K.; Ivey, D. G.; Veinot, J. G. C. Spherical Nitrogen-Doped Hollow Mesoporous Carbon as an Efficient Bifunctional Electrocatalyst for Zn-Air Batteries. *Nanoscale* **2015**, *7* (48), 20547–20556. https://doi.org/10.1039/c5nr06028a.

(101) Wang, P.; Wang, Z.; Jia, L.; Xiao, Z. Origin of the Catalytic Activity of Graphite Nitride for the Electrochemical Reduction of Oxygen: Geometric Factors vs. Electronic Factors. *Phys. Chem. Chem. Phys.* **2009**, *11* (15), 2730–2740. https://doi.org/10.1039/b818408a.

(102) Luo, Z.; Lim, S.; Tian, Z.; Shang, J.; Lai, L.; MacDonald, B.; Fu, C.; Shen, Z.; Yu, T.; Lin, J. Pyridinic N Doped Graphene: Synthesis, Electronic Structure, and Electrocatalytic Property. *J. Mater. Chem.* **2011**, *21* (22), 8038–8044. https://doi.org/10.1039/c1jm10845j.

(103) Lai, L.; Potts, J. R.; Zhan, D.; Wang, L.; Poh, C. K.; Tang, C.; Gong, H.; Shen, Z.; Lin, J.; Ruoff, R. S. Exploration of the Active Center Structure of Nitrogen-Doped Graphene-Based Catalysts for Oxygen Reduction Reaction. *Energy Environ. Sci.* **2012**, *5* (7), 7936–7942. https://doi.org/10.1039/c2ee21802j.

(104) Biddinger, E. J.; Ozkan, U. S. Role of Graphitic Edge Plane Exposure in Carbon Nanostructures for Oxygen Reduction Reaction. *J. Phys. Chem. C* **2010**, *114* (36), 15306–15314. https://doi.org/10.1021/jp104074t.

(105) Liu, Q.; Wang, Y.; Dai, L.; Yao, J. Scalable Fabrication of Nanoporous Carbon Fiber Films as Bifunctional Catalytic Electrodes for Flexible Zn-Air Batteries. *Adv. Mater.* **2016**, *28* (15), 3000–3006. https://doi.org/10.1002/adma.201506112.

(106) Peng, X.; Zhang, L.; Chen, Z.; Zhong, L.; Zhao, D.; Chi, X.; Zhao, X.; Li, L.; Lu, X.; Leng, K.; Liu, C.; Liu, W.; Tang, W.; Loh, K. P. Hierarchically Porous Carbon Plates Derived from Wood as Bifunctional ORR/OER Electrodes. *Adv. Mater.* **2019**, *31* (16), 1–7. https://doi.org/10.1002/adma.201900341.

(107) Zhang, P.; Sun, F.; Xiang, Z.; Shen, Z.; Yun, J.; Cao, D. ZIF-Derived in Situ Nitrogen-Doped Porous Carbons as Efficient Metal-Free Electrocatalysts for Oxygen Reduction Reaction. *Energy Environ. Sci.* **2014**, *7* (1), 442–450. https://doi.org/10.1039/c3ee42799d.

(108) Jiang, Y.; Yang, L.; Sun, T.; Zhao, J.; Lyu, Z.; Zhuo, O.; Wang, X.; Wu, Q.; Ma, J.; Hu, Z. Significant Contribution of Intrinsic Carbon Defects to Oxygen Reduction Activity. *ACS Catal.* **2015**, *5* (11), 6707–6712. https://doi.org/10.1021/acscatal.5b01835.

(109) Jia, Y.; Jiang, K.; Wang, H.; Yao, X. The Role of Defect Sites in Nanomaterials for Electrocatalytic Energy Conversion. *Chem* **2019**, *5* (6), 1371–1397. https://doi.org/10.1016/j.chempr.2019.02.008.

(110) Jia, Y.; Zhang, L.; Du, A.; Gao, G.; Chen, J.; Yan, X.; Brown, C. L.; Yao, X. Defect Graphene as a Trifunctional Catalyst for Electrochemical Reactions. *Adv. Mater.* **2016**, *28* (43), 9532–9538. https://doi.org/10.1002/adma.201602912.

(111) Jeon, I. Y.; Choi, H. J.; Jung, S. M.; Seo, J. M.; Kim, M. J.; Dai, L.; Baek, J. B. Large-Scale Production of Edge-Selectively Functionalized Graphene Nanoplatelets via Ball Milling and Their Use as Metal-Free Electrocatalysts for Oxygen Reduction Reaction. *J. Am. Chem. Soc.* **2013**, *135* (4), 1386–1393. https://doi.org/10.1021/ja3091643.

(112) Tang, C.; Wang, H. F.; Chen, X.; Li, B. Q.; Hou, T. Z.; Zhang, B.; Zhang, Q.; Titirici, M. M.; Wei, F. Topological Defects in Metal-Free Nanocarbon for Oxygen Electrocatalysis. *Adv. Mater.* **2016**, *28* (32), 6845–6851. https://doi.org/10.1002/adma.201601406.

(113) Zhao, X.; Zou, X.; Yan, X.; Brown, C. L.; Chen, Z.; Zhu, G.; Yao, X. Defect-Driven Oxygen Reduction Reaction (ORR) of Carbon without Any Element Doping. *Inorg. Chem. Front.* **2016**, *3* (3), 417–421. https://doi.org/10.1039/c5qi00236b.

(114) McCrory, C. C. L.; Jung, S.; Ferrer, I. M.; Chatman, S. M.; Peters, J. C.; Jaramillo, T. F. Benchmarking Hydrogen Evolving Reaction and Oxygen Evolving Reaction Electrocatalysts for Solar Water Splitting Devices. *J. Am. Chem. Soc.* **2015**, *137* (13), 4347–4357. https://doi.org/10.1021/ja510442p.

(115) Yang, C.; Li, Y.; Zhang, B.; Lian, Y.; Ma, Y.; Zhao, X.; Zeng, X.; Li, J.; Deng, Z.; Ye, J.; Wu, W.; Peng, Y. Nitrogen-Doped Carbon Fibers Embedding CoO: X Nanoframes towards Wearable Energy Storage. *Nanoscale* **2020**, *12* (16), 8922–8933. https://doi.org/10.1039/d0nr00582g.

(116) Feng, L.; Ding, R.; Chen, Y.; Wang, J.; Xu, L. Zeolitic Imidazolate Framework-67 Derived Ultra-Small CoP Particles Incorporated into N-Doped Carbon Nanofiber as Efficient Bifunctional Catalysts for Oxygen Reaction. *J. Power Sources* **2020**, *452* (December 2019). https://doi.org/10.1016/j.jpowsour.2020.227837.

(117) Bard, A. J.; Faulkner, L. R. *Electrochemical Methods: Fundamentals and Applications*; 2001; Vol. 2nd ed. https://doi.org/10.1021/ed060pa25.1.

(118) Hoang, S.; Guo, S.; Hahn, N. T.; Bard, A. J.; Mullins, C. B. Visible Light Driven Photoelectrochemical Water Oxidation on Nitrogen-Modified TiO 2 Nanowires. *Nano Lett.* **2012**, *12* (1), 26–32. https://doi.org/10.1021/nl2028188.

(119) Nunes, M.; Rocha, I. M.; Fernandes, D. M.; Mestre, A. S.; Moura, C. N.; Carvalho, A. P.; Pereira, M. F. R.; Freire, C. Sucrose-Derived Activated Carbons: Electron Transfer Properties and Application as Oxygen Reduction Electrocatalysts. *RSC Adv.* **2015**, *5* (124), 102919–102931. https://doi.org/10.1039/c5ra20874b.

(120) Shin, J.; Guo, J.; Zhao, T.; Guo, Z. Functionalized Carbon Dots on Graphene as Outstanding Non-Metal Bifunctional Oxygen Electrocatalyst. *Small* **2019**, *15* (16). https://doi.org/10.1002/smll.201900296.

(121) Ma, T. Y.; Ran, J.; Dai, S.; Jaroniec, M.; Qiao, S. Z. Phosphorus-Doped Graphitic Carbon Nitrides Grown In Situ on Carbon-Fiber Paper: Flexible and Reversible Oxygen Electrodes. *Angew. Chemie - Int. Ed.* **2015**, *54* (15), 4646–4650. https://doi.org/10.1002/anie.201411125.

(122) Patil, I. M.; Lokanathan, M.; Kakade, B. Three Dimensional Nanocomposite of Reduced Graphene Oxide and Hexagonal Boron Nitride as an Efficient Metal-Free Catalyst for

Oxygen Electroreduction. *J. Mater. Chem. A* **2016**, *4* (12), 4506–4515. https://doi.org/10.1039/c6ta00525j.

(123) Florea, I.; Ersen, O.; Arenal, R.; Ihiawakrim, D.; Messaoudi, C.; Chizari, K.; Janowska, I.; Pham-Huu, C. 3D Analysis of the Morphology and Spatial Distribution of Nitrogen in Nitrogen-Doped Carbon Nanotubes by Energy-Filtered Transmission Electron Microscopy Tomography. *J. Am. Chem. Soc.* **2012**, *134* (23), 9672–9680. https://doi.org/10.1021/ja304079d.

(124) Qiao, M.; Tang, C.; He, G.; Qiu, K.; Binions, R.; Parkin, I. P.; Zhang, Q.; Guo, Z.; Titirici, M. M. Graphene/Nitrogen-Doped Porous Carbon Sandwiches for the Metal-Free Oxygen Reduction Reaction: Conductivity: Versus Active Sites. *J. Mater. Chem. A* **2016**, *4* (32), 12658–12666. https://doi.org/10.1039/c6ta04578b.

(125) Seredych, M.; László, K.; Rodríguez-Castellón, E.; Bandosz, T. J. S-Doped Carbon Aerogels/GO Composites as Oxygen Reduction Catalysts. *J. Energy Chem.* **2016**, *25* (2), 236–245. https://doi.org/10.1016/j.jechem.2016.01.005.

(126) Daems, N.; Sheng, X.; Vankelecom, I. F. J.; Pescarmona, P. P. Metal-Free Doped Carbon Materials as Electrocatalysts for the Oxygen Reduction Reaction. *J. Mater. Chem. A* **2014**, *2* (12), 4085–4110. https://doi.org/10.1039/c3ta14043a.

(127) Yu, H.; Shang, L.; Bian, T.; Shi, R.; Waterhouse, G. I. N.; Zhao, Y.; Zhou, C.; Wu, L. Z.; Tung, C. H.; Zhang, T. Nitrogen-Doped Porous Carbon Nanosheets Templated from g-C3N4as Metal-Free Electrocatalysts for Efficient Oxygen Reduction Reaction. *Adv. Mater.* **2016**, *28* (25), 5080–5086. https://doi.org/10.1002/adma.201600398.

(128) Qiu, K.; Chai, G.; Jiang, C.; Ling, M.; Tang, J.; Guo, Z. Highly Efficient Oxygen Reduction Catalysts by Rational Synthesis of Nanoconfined Maghemite in a Nitrogen-Doped Graphene Framework. *ACS Catal.* **2016**, *6* (6), 3558–3568. https://doi.org/10.1021/acscatal.6b00531.

(129) Wei, W.; Liang, H.; Parvez, K.; Zhuang, X.; Feng, X.; Müllen, K. Nitrogen-Doped Carbon Nanosheets with Size-Defined Mesopores as Highly Efficient Metal-Free Catalyst for the Oxygen Reduction Reaction. *Angew. Chemie - Int. Ed.* **2014**, *53* (6), 1570–1574. https://doi.org/10.1002/anie.201307319.

(130) He, W.; Jiang, C.; Wang, J.; Lu, L. High-Rate Oxygen Electroreduction over Graphitic-N Species Exposed on 3D Hierarchically Porous Nitrogen-Doped Carbons. *Angew. Chemie - Int. Ed.* **2014**, *53* (36), 9503–9507. https://doi.org/10.1002/anie.201404333.

(131) Liang, J.; Du, X.; Gibson, C.; Du, X. W.; Qiao, S. Z. N-Doped Graphene Natively Grown on Hierarchical Ordered Porous Carbon for Enhanced Oxygen Reduction. *Adv. Mater.* **2013**, *25* (43), 6226–6231. https://doi.org/10.1002/adma.201302569.

(132) Chen, S.; Duan, J.; Jaroniec, M.; Qiao, S. Z. Nitrogen and Oxygen Dual-Doped Carbon Hydrogel Film as a Substrate-Free Electrode for Highly Efficient Oxygen Evolution Reaction. *Adv. Mater.* **2014**, *26* (18), 2925–2930. https://doi.org/10.1002/adma.201305608.

(133) Zhang, J.; Sun, Y.; Zhu, J.; Gao, Z.; Li, S.; Mu, S.; Huang, Y. Ultranarrow Graphene Nanoribbons toward Oxygen Reduction and Evolution Reactions. *Adv. Sci.* **2018**, *5* (12), 1–7. https://doi.org/10.1002/advs.201801375.

(134) Xu, J.; Xu, F.; Qian, M.; Xu, F.; Hong, Z.; Huang, F. Conductive Carbon Nitride for Excellent Energy Storage. *Adv. Mater.* **2017**, *29* (31), 1–8. https://doi.org/10.1002/adma.201701674.

(135) Qu, K.; Wang, Y.; Zhang, X.; Chen, H.; Li, H.; Chen, B.; Zhou, H.; Li, D.; Zheng, Y.; Dai, S. Polydopamine-Derived, In Situ N-Doped 3D Mesoporous Carbons for Highly

Efficient Oxygen Reduction. *ChemNanoMat* **2018**, *4* (4), 417–422. https://doi.org/10.1002/cnma.201800032.

(136) Qu, K.; Wang, Y.; Vasileff, A.; Jiao, Y.; Chen, H.; Zheng, Y. Polydopamine-Inspired Nanomaterials for Energy Conversion and Storage. *J. Mater. Chem. A* **2018**, *6* (44), 21827–21846. https://doi.org/10.1039/C8TA05245J.

(137) Xia, P.; Liu, M.; Cheng, B.; Yu, J.; Zhang, L. Dopamine Modified G-C3N4 and Its Enhanced Visible-Light Photocatalytic H2-Production Activity. *ACS Sustain. Chem. Eng.* **2018**, *6* (7), 8945–8953. https://doi.org/10.1021/acssuschemeng.8b01300.

(138) Niu, W.; Marcus, K.; Zhou, L.; Li, Z.; Shi, L.; Liang, K.; Yang, Y. Enhancing Electron Transfer and Electrocatalytic Activity on Crystalline Carbon-Conjugated g-C3N4. *ACS Catal.* **2018**, *8* (3), 1926–1931. https://doi.org/10.1021/acscatal.8b00026.

(139) Tang, Y.; Chen, J.; Wang, X.; Wang, X.; Zhao, Y.; Mao, Z.; Wang, D. Fabrication of Highly N-Doped Graphene-like Carbon Templated from g-C3N4 Nanosheets as Promising Li-Ions Battery Anode. *Electrochim. Acta* **2019**, *324*, 134880. https://doi.org/10.1016/j.electacta.2019.134880.

(140) Liang, Z.; Zheng, H.; Cao, R. Importance of Electrocatalyst Morphology for the Oxygen Reduction Reaction. *ChemElectroChem* **2019**, *6* (10), 2600–2614. https://doi.org/10.1002/celc.201801859.

(141) Nguyen, D. N.; Sim, U.; Kim, J. K. Biopolymer-Inspired N-Doped Nanocarbon Using Carbonized Polydopamine: A High-Performance Electrocatalyst for Hydrogen-Evolution Reaction. *Polymers (Basel).* **2020**, *12* (4), 912. https://doi.org/10.3390/polym12040912.

(142) Shi, Q.; Ma, Y.; Qin, L.; Tang, B.; Yang, W.; Liu, Q. Metal-Free Hybrid of Nitrogen-Doped Nanocarbon@Carbon Networks for Highly Efficient Oxygen Reduction Electrocatalyst. *ChemElectroChem* **2019**, *6* (11), 2924–2930. https://doi.org/10.1002/celc.201900662.

(143) Zhu, Y. P.; Guo, C.; Zheng, Y.; Qiao, S. Z. Surface and Interface Engineering of Noble-Metal-Free Electrocatalysts for Efficient Energy Conversion Processes. *Acc. Chem. Res.* **2017**, *50* (4), 915–923. https://doi.org/10.1021/acs.accounts.6b00635.

(144) Zhu, Y. P.; Liu, Y.; Liu, Y. P.; Ren, T. Z.; Du, G. H.; Chen, T.; Yuan, Z. Y. Heteroatom-Doped Hierarchical Porous Carbons as High-Performance Metal-Free Oxygen Reduction Electrocatalysts. *J. Mater. Chem. A* **2015**, *3* (22), 11725–11729. https://doi.org/10.1039/c5ta01611h.

(145) Lin, Z.; Waller, G. H.; Liu, Y.; Liu, M.; Wong, C. P. Simple Preparation of Nanoporous Few-Layer Nitrogen-Doped Graphene for Use as an Efficient Electrocatalyst for Oxygen Reduction and Oxygen Evolution Reactions. *Carbon N. Y.* **2013**, *53*, 130–136. https://doi.org/10.1016/j.carbon.2012.10.039.

(146) Liu, X.; Kang, J.; Dai, Y.; Dong, C.; Guo, X.; Jia, X. Graphene-Like Nitrogen-Doped Carbon Nanosheet Prepared from Direct Calcination of Dopamine Confined by g-C3N4 for Oxygen Reduction. *Adv. Mater. Interfaces* **2018**, *5* (14). https://doi.org/10.1002/admi.201800303.

(147) Yang, W.; Hou, L.; Xu, X.; Li, Z.; Ma, X.; Yang, F.; Li, Y. Carbon Nitride Template-Directed Fabrication of Nitrogen-Rich Porous Graphene-like Carbon for High Performance Supercapacitors. *Carbon N. Y.* **2018**, *130*, 325–332. https://doi.org/10.1016/j.carbon.2018.01.032.

(148) Kim, J.; Lim, S.; Kim, S. K.; Peck, D. H.; Lee, B.; Yoon, S. H.; Jung, D. Electrochemical Catalytic Activity for Oxygen Reduction Reaction of Nitrogen-Doped Carbon Nanofibers. *J. Nanosci. Nanotechnol.* **2011**, *11* (7), 6350–6358.

https://doi.org/10.1166/jnn.2011.4443.

(149) Chen, Z.; Higgins, D.; Tao, H.; Hsu, R. S.; Chen, Z. Highly Active Nitrogen-Doped Carbon Nanotubes for Oxygen Reduction Reaction in Fuel Cell Applications. *J. Phys. Chem. C* **2009**, *113* (49), 21008–21013. https://doi.org/10.1021/jp908067v.

(150) Wiggins-Camacho, J. D.; Stevenson, K. J. Effect of Nitrogen Concentration on Capacitance, Density of States, Electronic Conductivity, and Morphology of N-Doped Carbon Nanotube Electrodes. *J. Phys. Chem. C* **2009**, *113* (44), 19082–19090. https://doi.org/10.1021/jp907160v.

(151) Ai, K.; Liu, Y.; Ruan, C.; Lu, L.; Lu, G. Sp2 C-Dominant N-Doped Carbon Sub-Micrometer Spheres with a Tunable Size: A Versatile Platform for Highly Efficient Oxygen-Reduction Catalysts. *Adv. Mater.* **2013**, *25* (7), 998–1003. https://doi.org/10.1002/adma.201203923.

(152) Li, R.; Parvez, K.; Hinkel, F.; Feng, X.; Müllen, K. Bioinspired Wafer-Scale Production of Highly Stretchable Carbon Films for Transparent Conductive Electrodes. *Angew. Chemie - Int. Ed.* **2013**, *52* (21), 5535–5538. https://doi.org/10.1002/anie.201300312.

(153) Yu, Z.; Li, F.; Yang, Q.; Shi, H.; Chen, Q.; Xu, M. Nature-Mimic Method to Fabricate Polydopamine/Graphitic Carbon Nitride for Enhancing Photocatalytic Degradation Performance. *ACS Sustain. Chem. Eng.* **2017**, *5* (9), 7840–7850. https://doi.org/10.1021/acssuschemeng.7b01313.

(154) Gholipour, M. R.; Béland, F.; Do, T. O. Post-Calcined Carbon Nitride Nanosheets as an Efficient Photocatalyst for Hydrogen Production under Visible Light Irradiation. *ACS Sustain. Chem. Eng.* **2017**, *5* (1), 213–220. https://doi.org/10.1021/acssuschemeng.6b01282.

(155) Ong, W. J.; Tan, L. L.; Chai, S. P.; Yong, S. T.; Mohamed, A. R. Surface Charge Modification via Protonation of Graphitic Carbon Nitride (g-C3N4) for Electrostatic Self-Assembly Construction of 2D/2D Reduced Graphene Oxide (RGO)/g-C3N4 Nanostructures toward Enhanced Photocatalytic Reduction of Carbon Dioxide to Methane. *Nano Energy* **2015**, *13*, 757–770. https://doi.org/10.1016/j.nanoen.2015.03.014.

(156) Qu, K.; Zheng, Y.; Dai, S.; Qiao, S. Z. Graphene Oxide-Polydopamine Derived N, S-Codoped Carbon Nanosheets as Superior Bifunctional Electrocatalysts for Oxygen Reduction and Evolution. *Nano Energy* **2016**, *19*, 373–381. https://doi.org/10.1016/j.nanoen.2015.11.027.

(157) Zhong, K.; Wang, Y.; Wu, Q.; You, H.; Zhang, H.; Su, M.; Liang, R.; Zuo, J.; Yang, S.; Tang, J. Highly Conductive Skeleton Graphitic-C3N4 Assisted Fe-Based Metal-Organic Frameworks Derived Porous Bimetallic Carbon Nanofiber for Enhanced Oxygen-Reduction Performance in Microbial Fuel Cells. *J. Power Sources* **2020**, *467* (June), 228313. https://doi.org/10.1016/j.jpowsour.2020.228313.

(158) Luo, H.; Gu, C.; Zheng, W.; Dai, F.; Wang, X.; Zheng, Z. Facile Synthesis of Novel Size-Controlled Antibacterial Hybrid Spheres Using Silver Nanoparticles Loaded with Poly-Dopamine Spheres. *RSC Adv.* **2015**, *5* (18), 13470–13477. https://doi.org/10.1039/c4ra16469e.

(159) Shinde, S. S.; Lee, C. H.; Sami, A.; Kim, D. H.; Lee, S. U.; Lee, J. H. Scalable 3-D Carbon Nitride Sponge as an Efficient Metal-Free Bifunctional Oxygen Electrocatalyst for Rechargeable Zn-Air Batteries. *ACS Nano* **2017**, *11* (1), 347–357. https://doi.org/10.1021/acsnano.6b05914.

(160) Zhang, P.; Bin, D.; Wei, J. S.; Niu, X. Q.; Chen, X. B.; Xia, Y. Y.; Xiong, H. M.

Efficient Oxygen Electrocatalyst for Zn-Air Batteries: Carbon Dots and Co 9 S 8 Nanoparticles in a N,S-Codoped Carbon Matrix. *ACS Appl. Mater. Interfaces* **2019**, *11* (15), 14085–14094. https://doi.org/10.1021/acsami.8b22557.

(161) Zheng, Y.; Jiao, Y.; Ge, L.; Jaroniec, M.; Qiao, S. Z. Two-Step Boron and Nitrogen Doping in Graphene for Enhanced Synergistic Catalysis. *Angew. Chemie* **2013**, *125* (11), 3192–3198. https://doi.org/10.1002/ange.201209548.

(162) Liang, Y.; Li, Y.; Wang, H.; Zhou, J.; Wang, J.; Regier, T.; Dai, H. Co3O4 Nanocrystals on Graphene as a Synergistic Catalyst for Oxygen Reduction Reaction. *Nat. Mater.* **2011**, *10* (10), 780–786. https://doi.org/10.1038/nmat3087.

(163) Zhang, J.; Zhao, Z.; Xia, Z.; Dai, L. A Metal-Free Bifunctional Electrocatalyst for Oxygen Reduction and Oxygen Evolution Reactions. *Nat. Nanotechnol.* **2015**, *10* (5), 444–452. https://doi.org/10.1038/nnano.2015.48.

(164) Li, B.; Igawa, K.; Chai, J.; Chen, Y.; Wang, Y.; Fam, D. W.; Tham, N. N.; An, T.; Konno, T.; Sng, A.; Liu, Z.; Zhang, H.; Zong, Y. String of Pyrolyzed ZIF-67 Particles on Carbon Fibers for High-Performance Electrocatalysis. *Energy Storage Mater.* **2020**, *25* (April 2019), 137–144. https://doi.org/10.1016/j.ensm.2019.10.021.

(165) Wu, M.; Liu, R. Pearl Necklace Fibrous Carbon Sharing Fe–N/Fe–P Dual Active Sites as Efficient Oxygen Reduction Catalyst in Broad Media and for Liquid/Solid-State Rechargeable Zn–Air Battery. *Energy Technol.* **2020**, *8* (3), 1–8. https://doi.org/10.1002/ente.201901263.

(166) Li, F.; Shu, H.; Liu, X.; Shi, Z.; Liang, P.; Chen, X. Electrocatalytic Activity and Design Principles of Heteroatom-Doped Graphene Catalysts for Oxygen-Reduction Reaction. *J. Phys. Chem. C* **2017**, *121* (27), 14434–14442. https://doi.org/10.1021/acs.jpcc.7b03093.

(167) Tang, C.; Zhang, Q. Nanocarbon for Oxygen Reduction Electrocatalysis: Dopants, Edges, and Defects. *Adv. Mater.* **2017**, *29* (13). https://doi.org/10.1002/adma.201604103.

(168) Xue, W.; Zhou, Q.; Cui, X.; Jia, S.; Zhang, J.; Lin, Z. Metal–Organic Frameworks-Derived Heteroatom-Doped Carbon Electrocatalysts for Oxygen Reduction Reaction. *Nano Energy* **2021**, *86* (May), 106073. https://doi.org/10.1016/j.nanoen.2021.106073.

(169) Fu, T.; Li, G.; Xiang, Y.; Tang, Y.; Cai, D.; Jiang, S.; Xue, Y.; Xiong, Z.; Si, Y.; Guo, C. Hierarchical Cobalt-Nitrogen-Doped Carbon Composite as Efficiently Bifunctional Oxygen Electrocatalyst for Rechargeable Zn-Air Batteries. *J. Alloys Compd.* **2021**, *878*, 160349. https://doi.org/10.1016/j.jallcom.2021.160349.

(170) Bai, Y.; Yang, D.; Yang, M.; Chen, H.; Liu, Y.; Li, H. Nitrogen/Cobalt Co-Doped Mesoporous Carbon Microspheres Derived from Amorphous Metal-Organic Frameworks as a Catalyst for the Oxygen Reduction Reaction in Both Alkaline and Acidic Electrolytes. *ChemElectroChem* **2019**, *6* (9), 2546–2552. https://doi.org/10.1002/celc.201900343.

(171) Wu, Y.; Wu, X.; Tu, T.; Zhang, P.; Li, J.; Zhou, Y.; Huang, L.; Sun, S. Controlled Synthesis of FeNx-CoNx Dual Active Sites Interfaced with Metallic Co Nanoparticles as Bifunctional Oxygen Electrocatalysts for Rechargeable Zn-Air Batteries. *Appl. Catal. B Environ.* **2020**, *278* (June), 119259. https://doi.org/10.1016/j.apcatb.2020.119259.

(172) Li, J.; Kang, Y.; Liu, D.; Lei, Z.; Liu, P. Nitrogen-Doped Graphitic Carbon-Supported Ultrafine Co Nanoparticles as an Efficient Multifunctional Electrocatalyst for HER and Rechargeable Zn-Air Batteries. *ACS Appl. Mater. Interfaces* **2020**, *12* (5), 5717–5729. https://doi.org/10.1021/acsami.9b18101.

(173) Bai, Q.; Shen, F.; Li, S.; Liu, J.; Dong, L.; Wang, Z.; Lan, Y. Cobalt@Nitrogen-Doped Porous Carbon Fiber Derived from the Electrospun Fiber of Bimetal–Organic

Framework for Highly Active Oxygen Reduction. *Small Methods* **2018**, *2* (12), 1800049. https://doi.org/10.1002/smtd.201800049.

(174) Tang, J.; Salunkhe, R. R.; Zhang, H.; Malgras, V.; Ahamad, T.; Alshehri, S. M.; Kobayashi, N.; Tominaka, S.; Ide, Y.; Kim, J. H. Bimetallic Metal-Organic Frameworks for Controlled Catalytic Graphitization of Nanoporous Carbons. *Nat. Publ. Gr.* **2016**, No. April, 3–4. https://doi.org/10.1038/srep30295.

(175) Wagia, R.; Strashnov, I.; Anderson, M. W.; Attfield, M. P. Insight and Control of the Crystal Growth of Zeolitic Imidazolate Framework ZIF-67 by Atomic Force Microscopy and Mass Spectrometry. *Cryst. Growth Des.* **2018**, *18* (2), 695–700. https://doi.org/10.1021/acs.cgd.7b01058.

(176) Wang, G.; Deng, J.; Yan, T.; Zhang, J.; Shi, L.; Zhang, D. Turning on Electrocatalytic Oxygen Reduction by Creating Robust Fe-N: X Species in Hollow Carbon Frameworks via in Situ Growth of Fe Doped ZIFs on g-C3N4. *Nanoscale* **2020**, *12* (9), 5601–5611. https://doi.org/10.1039/d0nr00138d.

(177) Zheng, L.; Yu, S.; Lu, X.; Fan, W.; Chi, B.; Ye, Y.; Shi, X.; Zeng, J.; Li, X.; Liao, S. Two-Dimensional Bimetallic Zn/Fe-Metal-Organic Framework (MOF)-Derived Porous Carbon Nanosheets with a High Density of Single/Paired Fe Atoms as High-Performance Oxygen Reduction Catalysts. *ACS Appl. Mater. Interfaces* **2020**, *12* (12), 13878–13887. https://doi.org/10.1021/acsami.9b22577.

(178) Wang, R.; Yan, T.; Han, L.; Chen, G.; Li, H.; Zhang, J.; Shi, L.; Zhang, D. Tuning the Dimensions and Structures of Nitrogen-Doped Carbon Nanomaterials Derived from Sacrificial g-C3N4/Metal-Organic Frameworks for Enhanced Electrocatalytic Oxygen Reduction. *J. Mater. Chem. A* **2018**, *6* (14), 5752–5761. https://doi.org/10.1039/c8ta00439k.

(179) Hao, Y.; Xu, Y.; Liu, J.; Sun, X. Nickel-Cobalt Oxides Supported on Co/N Decorated Graphene as an Excellent Bifunctional Oxygen Catalyst. *J. Mater. Chem. A* **2017**, *5* (11), 5594–5600. https://doi.org/10.1039/c7ta00299h.

(180) Ma, S.; Goenaga, G. A.; Call, A. V.; Liu, D. J. Cobalt Imidazolate Framework as Precursor for Oxygen Reduction Reaction Electrocatalysts. *Chem. - A Eur. J.* **2011**, *17* (7), 2063–2067. https://doi.org/10.1002/chem.201003080.

(181) Ma, L.; Wang, R.; Li, Y. H.; Liu, X. F.; Zhang, Q. Q.; Dong, X. Y.; Zang, S. Q. Apically Co-Nanoparticles-Wrapped Nitrogen-Doped Carbon Nanotubes from a Single-Source MOF for Efficient Oxygen Reduction. *J. Mater. Chem. A* **2018**, *6* (47), 24071–24077. https://doi.org/10.1039/c8ta08668k.

(182) Chen, Y. Z.; Wang, C.; Wu, Z. Y.; Xiong, Y.; Xu, Q.; Yu, S. H.; Jiang, H. L. From Bimetallic Metal-Organic Framework to Porous Carbon: High Surface Area and Multicomponent Active Dopants for Excellent Electrocatalysis. *Adv. Mater.* **2015**, *27* (34), 5010–5016. https://doi.org/10.1002/adma.201502315.

(183) Wang, Y.; Zhong, K.; Huang, Z.; Chen, L.; Dai, Y.; Zhang, H.; Su, M.; Yan, J.; Yang, S.; Li, M.; Xu, T.; Tang, J. Novel G-C3N4 Assisted Metal Organic Frameworks Derived High Efficiency Oxygen Reduction Catalyst in Microbial Fuel Cells. *J. Power Sources* **2020**, *450* (January), 227681. https://doi.org/10.1016/j.jpowsour.2019.227681.

(184) Graphene, N.; Xu, L.; Tian, Y.; Deng, D.; Li, H.; Zhang, D. Cu Nanoclusters / FeN4 Amorphous Composites with Dual Active Cu Nanoclusters / FeN 4 Amorphous Composites with Dual Active Sites in N-Doped Graphene for High-Performance Zn-Air Batteries. **2020**. https://doi.org/10.1021/acsami.0c03823.

(185) Zang, W.; Sumboja, A.; Ma, Y.; Zhang, H.; Wu, Y.; Wu, S.; Wu, H.; Liu, Z.; Guan, C.;

Wang, J.; Pennycook, S. J. Single Co Atoms Anchored in Porous N-Doped Carbon for Efficient Zinc-Air Battery Cathodes. *ACS Catal.* **2018**, *8* (10), 8961–8969. https://doi.org/10.1021/acscatal.8b02556.

(186) Yang, F.; Chen, Y.; Cheng, G.; Chen, S.; Luo, W. Ultrathin Nitrogen-Doped Carbon Coated with CoP for Efficient Hydrogen Evolution. *ACS Catal.* **2017**, *7* (6), 3824–3831. https://doi.org/10.1021/acscatal.7b00587.

(187) Yasuda, S.; Yu, L.; Kim, J.; Murakoshi, K. Selective Nitrogen Doping in Graphene for Oxygen Reduction Reactions. *Chem. Commun.* **2013**, *49* (83), 9627–9629. https://doi.org/10.1039/c3cc45641b.

(188) Wang, L.; Guo, X.; Chen, Y.; Ai, S.; Ding, H. Cobalt-Doped g-C 3 N 4 as a Heterogeneous Catalyst for Photo-Assisted Activation of Peroxymonosulfate for the Degradation of Organic Contaminants. *Appl. Surf. Sci.* **2019**, *467–468* (August 2018), 954–962. https://doi.org/10.1016/j.apsusc.2018.10.262.

(189) Song, Q.; Li, J.; Wang, L.; Pang, L.; Liu, H. Controlling the Chemical Bonding of Highly Dispersed Co Atoms Anchored on an Ultrathin G-C3N4@Carbon Sphere for Enhanced Electrocatalytic Activity of the Oxygen Evolution Reaction. *Inorg. Chem.* **2019**, *58* (16), 10802–10811. https://doi.org/https://pubs.acs.org/doi/10.1021/acs.inorgchem.9b01089.

(190) Xie, M.; Tang, J.; Kong, L.; Lu, W.; Natarajan, V.; Zhu, F.; Zhan, J. Cobalt Doped G-C 3 N 4 Activation of Peroxymonosulfate for Monochlorophenols Degradation. *Chem. Eng. J.* **2019**, *360* (September 2018), 1213–1222. https://doi.org/10.1016/j.cej.2018.10.130.

(191) Ma, T. Y.; Dai, S.; Jaroniec, M.; Qiao, S. Z. Metal-Organic Framework Derived Hybrid Co3O4-Carbon Porous Nanowire Arrays as Reversible Oxygen Evolution Electrodes. *J. Am. Chem. Soc.* **2014**, *136* (39), 13925–13931. https://doi.org/10.1021/ja5082553.

(192) Babu, V. J.; Vempati, S.; Uyar, T.; Ramakrishna, S. Review of One-Dimensional and Two-Dimensional Nanostructured Materials for Hydrogen Generation. *Phys. Chem. Chem. Phys.* **2015**, *17* (5), 2960–2986. https://doi.org/10.1039/c4cp04245j.

(193) Lu, X.; Wang, C.; Wei, Y. One-Dimensional Composite Nanomaterials: Synthesis by Electrospinning and Their Applications. *Small* **2009**, *5* (21), 2349–2370. https://doi.org/10.1002/smll.200900445.

(194) Pan, Z.; Chen, H.; Yang, J.; Ma, Y.; Zhang, Q.; Kou, Z.; Ding, X.; Pang, Y.; Zhang, L.; Gu, Q.; Yan, C.; Wang, J. CuCo2S4 Nanosheets@N-Doped Carbon Nanofibers by Sulfurization at Room Temperature as Bifunctional Electrocatalysts in Flexible Quasi-Solid-State Zn–Air Batteries. *Adv. Sci.* **2019**, *6* (17). https://doi.org/10.1002/advs.201900628.

(195) Tomboc, G. M.; Kim, H. Derivation of Both EDLC and Pseudocapacitance Characteristics Based on Synergistic Mixture of NiCo2O4 and Hollow Carbon Nanofiber: An Efficient Electrode towards High Energy Density Supercapacitor. *Electrochim. Acta* **2019**, *318*, 392–404. https://doi.org/10.1016/j.electacta.2019.06.112.

(196) Lu, X.; Wang, C.; Favier, F.; Pinna, N. Electrospun Nanomaterials for Supercapacitor Electrodes: Designed Architectures and Electrochemical Performance. *Adv. Energy Mater.* **2017**, *7* (2), 1–43. https://doi.org/10.1002/aenm.201601301.

(197) Reneker, D. H.; Yarin, A. L.; Fong, H.; Koombhongse, S. Bending Instability of Electrically Charged Liquid Jets of Polymer Solutions in Electrospinning. *J. Appl. Phys.* **2000**, *87* (9 I), 4531–4547. https://doi.org/10.1063/1.373532.

(198) Ju, J.; Kang, W.; Deng, N.; Li, L.; Zhao, Y.; Ma, X.; Fan, L.; Cheng, B. Preparation and

Characterization of PVA-Based Carbon Nanofibers with Honeycomb-like Porous Structure via Electro-Blown Spinning Method. *Microporous Mesoporous Mater.* **2017**, *239*, 416–425. https://doi.org/10.1016/j.micromeso.2016.10.024.

(199) Zhang, L.; Hsieh, Y. Lo. Carbon Nanofibers with Nanoporosity and Hollow Channels from Binary Polyacrylonitrile Systems. *Eur. Polym. J.* **2009**, *45* (1), 47–56. https://doi.org/10.1016/j.eurpolymj.2008.09.035.

(200) Wang, H.; Yang, X.; Wu, Q.; Zhang, Q.; Chen, H.; Jing, H.; Wang, J.; Mi, S. B.; Rogach, A. L.; Niu, C. Encapsulating Silica/Antimony into Porous Electrospun Carbon Nanofibers with Robust Structure Stability for High-Efficiency Lithium Storage. *ACS Nano* **2018**, *12* (4), 3406–3416. https://doi.org/10.1021/acsnano.7b09092.

(201) Yang, C.; Yao, Y.; Lian, Y.; Chen, Y.; Shah, R.; Zhao, X.; Chen, M.; Peng, Y.; Deng, Z. A Double-Buffering Strategy to Boost the Lithium Storage of Botryoid MnO x /C Anodes. *Small* **2019**, *15* (16), 1–12. https://doi.org/10.1002/smll.201900015.

(202) Xu, T.; Yang, H.; Yang, D.; Yu, Z. Z. Polylactic Acid Nanofiber Scaffold Decorated with Chitosan Islandlike Topography for Bone Tissue Engineering. *ACS Appl. Mater. Interfaces* **2017**, *9* (25), 21094–21104. https://doi.org/10.1021/acsami.7b01176.

(203) Zhao, Y.; Lai, Q.; Wang, Y.; Zhu, J.; Liang, Y. Interconnected Hierarchically Porous Fe, N-Codoped Carbon Nanofibers as Efficient Oxygen Reduction Catalysts for Zn-Air Batteries. *ACS Appl. Mater. Interfaces* **2017**, *9* (19), 16178–16186. https://doi.org/10.1021/acsami.7b01712.

(204) Ren, G.; Lu, X.; Li, Y.; Zhu, Y.; Dai, L.; Jiang, L. Porous Core-Shell Fe3C Embedded N-Doped Carbon Nanofibers as an Effective Electrocatalysts for Oxygen Reduction Reaction. *ACS Appl. Mater. Interfaces* **2016**, *8* (6), 4118–4125. https://doi.org/10.1021/acsami.5b11786.

(205) Deitzel, J. M.; Kosik, W.; McKnight, S. H.; Beck Tan, N. C.; DeSimone, J. M.; Crette, S. Electrospinning of Polymer Nanofibers with Specific Surface Chemistry. *Polymer (Guildf).* **2001**, *43* (3), 1025–1029. https://doi.org/10.1016/S0032-3861(01)00594-8.

(206) Krishnappa, R. V. N.; Desai, K.; Sung, C. Morphological Study of Electrospun Polycarbonates as a Function of the Solvent and Processing Voltage. *J. Mater. Sci.* **2003**, *38* (11), 2357–2365. https://doi.org/10.1023/A:1023984514389.

(207) Liu, D.; Zhang, X.; Sun, Z.; You, T. Free-Standing Nitrogen-Doped Carbon Nanofiber Films as Highly Efficient Electrocatalysts for Oxygen Reduction. *Nanoscale* **2013**, *5* (20), 9528–9531. https://doi.org/10.1039/c3nr03229a.

(208) Wang, Y.; Jin, J.; Yang, S.; Li, G.; Jiang, J. Nitrogen-Doped Porous Carbon Nanofiber Based Oxygen Reduction Reaction Electrocatalysts with High Activity and Durability. *Int. J. Hydrogen Energy* **2016**, *41* (26), 11174–11184. https://doi.org/10.1016/j.ijhydene.2016.04.235.

(209) Park, G. S.; Lee, J. S.; Kim, S. T.; Park, S.; Cho, J. Porous Nitrogen Doped Carbon Fiber with Churros Morphology Derived from Electrospun Bicomponent Polymer as Highly Efficient Electrocatalyst for Zn-Air Batteries. *J. Power Sources* **2013**, *243*, 267–273. https://doi.org/10.1016/j.jpowsour.2013.06.025.

(210) Gupta, S.; Tryk, D.; Bae, I.; Aldred, W.; Yeager, E. Heat-Treated Polyacrylonitrile-Based Catalysts for Oxygen Electroreduction. *J. Appl. Electrochem.* **1989**, *19* (1), 19–27. https://doi.org/10.1007/BF01039385.

(211) Xu, Z.; Zhao, H.; Liang, J.; Wang, Y.; Li, T.; Luo, Y.; Shi, X.; Lu, S.; Feng, Z.; Wu, Q.; Sun, X. Noble-Metal-Free Electrospun Nanomaterials as Electrocatalysts for Oxygen Reduction Reaction. *Mater. Today Phys.* **2020**, *15*, 1–16.

https://doi.org/10.1016/j.mtphys.2020.100280.

(212) Yan, X.; Liu, K.; Wang, T.; You, Y.; Liu, J.; Wang, P.; Pan, X.; Wang, G.; Luo, J.; Zhu, J. Atomic Interpretation of High Activity on Transition Metal and Nitrogen-Doped Carbon Nanofibers for Catalyzing Oxygen Reduction. *J. Mater. Chem. A* **2017**, *5* (7), 3336–3345. https://doi.org/10.1039/c6ta09462g.

(213) Li, B.; Sasikala, S. P.; Kim, D. H.; Bak, J.; Kim, I. D.; Cho, E. A.; Kim, S. O. Fe-N4 Complex Embedded Free-Standing Carbon Fabric Catalysts for Higher Performance ORR Both in Alkaline & Acidic Media. *Nano Energy* **2019**, *56* (November 2018), 524–530. https://doi.org/10.1016/j.nanoen.2018.11.054.

(214) Liu, M.; Cai, N.; Chan, V.; Yu, F. Development and Applications of MOFs Derivative One-Dimensional Nanofibers via Electrospinning： a Mini-Review. *Nanomaterials* **2019**, *9* (9). https://doi.org/10.3390/nano9091306.

(215) Wang, C.; Zheng, T.; Luo, R.; Liu, C.; Zhang, M.; Li, J.; Sun, X.; Shen, J.; Han, W.; Wang, L. In Situ Growth of ZIF-8 on PAN Fibrous Filters for Highly Efficient U(VI) Removal. *ACS Appl. Mater. Interfaces* **2018**, *10* (28), 24164–24171. https://doi.org/10.1021/acsami.8b07826.

(216) Wang, X.; Li, Y.; Jin, T.; Meng, J.; Jiao, L.; Zhu, M.; Chen, J. Electrospun Thin-Walled CuCo2O4@C Nanotubes as Bifunctional Oxygen Electrocatalysts for Rechargeable Zn-Air Batteries. *Nano Lett.* **2017**, *17* (12), 7989–7994. https://doi.org/10.1021/acs.nanolett.7b04502.

(217) Zhong, R.; Wu, Y.; Liang, Z.; Guo, W.; Zhi, C.; Qu, C.; Gao, S.; Zhu, B.; Zhang, H.; Zou, R. Fabricating Hierarchically Porous and Fe3C-Embeded Nitrogen-Rich Carbon Nanofibers as Exceptional Electocatalysts for Oxygen Reduction. *Carbon N. Y.* **2019**, *142*, 115–122. https://doi.org/10.1016/j.carbon.2018.10.040.

(218) Zhao, Y.; Lai, Q.; Zhu, J.; Zhong, J.; Tang, Z.; Luo, Y.; Liang, Y. Controllable Construction of Core–Shell Polymer@Zeolitic Imidazolate Frameworks Fiber Derived Heteroatom-Doped Carbon Nanofiber Network for Efficient Oxygen Electrocatalysis. *Small* **2018**, *14* (19), 1–9. https://doi.org/10.1002/smll.201704207.

(219) Qian, J.; Sun, F.; Qin, L. Hydrothermal Synthesis of Zeolitic Imidazolate Framework-67 (ZIF-67) Nanocrystals. *Mater. Lett.* **2012**, *82* (2012), 220–223. https://doi.org/10.1016/j.matlet.2012.05.077.

(220) Zhou, Y. X.; Chen, Y. Z.; Cao, L.; Lu, J.; Jiang, H. L. Conversion of a Metal-Organic Framework to N-Doped Porous Carbon Incorporating Co and CoO Nanoparticles: Direct Oxidation of Alcohols to Esters. *Chem. Commun.* **2015**, *51* (39), 8292–8295. https://doi.org/10.1039/c5cc01588j.

(221) Xia, B. Y.; Yan, Y.; Li, N.; Wu, H. Bin; Lou, X. W. D.; Wang, X. A Metal-Organic Framework-Derived Bifunctional Oxygen Electrocatalyst. *Nat. Energy* **2016**, *1* (1), 1–8. https://doi.org/10.1038/nenergy.2015.6.

(222) Kong, J.; Zhao, C.; Wei, Y.; Phua, S. L.; Dong, Y.; Lu, X. Nanocups-on-Microtubes: A Unique Host towards High-Performance Lithium Ion Batteries. *J. Mater. Chem. A* **2014**, *2* (36), 15191–15199. https://doi.org/10.1039/c4ta02813a.

(223) Kong, J.; Yao, X.; Wei, Y.; Zhao, C.; Ang, J. M.; Lu, X. Polydopamine-Derived Porous Nanofibers as Host of ZnFe2O4 Nanoneedles: Towards High-Performance Anodes for Lithium-Ion Batteries. *RSC Adv.* **2015**, *5* (18), 13315–13323. https://doi.org/10.1039/c4ra16460a.

(224) Yan, J.; Lu, H.; Huang, Y.; Fu, J.; Mo, S.; Wei, C.; Miao, Y. E.; Liu, T. Polydopamine-

Derived Porous Carbon Fiber/Cobalt Composites for Efficient Oxygen Reduction Reactions. *J. Mater. Chem. A* **2015**, *3* (46), 23299–23306. https://doi.org/10.1039/c5ta06217a.

(225) Zhang, W.; Yao, X.; Zhou, S.; Li, X.; Li, L.; Yu, Z.; Gu, L. ZIF-8/ZIF-67-Derived Co-Nx-Embedded 1D Porous Carbon Nanofibers with Graphitic Carbon-Encased Co Nanoparticles as an Efficient Bifunctional Electrocatalyst. *Small* **2018**, *14* (24), 1–8. https://doi.org/10.1002/smll.201800423.

(226) Wang, S.; Qin, J.; Meng, T.; Cao, M. Metal–Organic Framework-Induced Construction of Actiniae-like Carbon Nanotube Assembly as Advanced Multifunctional Electrocatalysts for Overall Water Splitting and Zn-Air Batteries. *Nano Energy* **2017**, *39* (May), 626–638. https://doi.org/10.1016/j.nanoen.2017.07.043.

(227) Kim, T. H.; Jeon, E. K.; Ko, Y.; Jang, B. Y.; Kim, B. S.; Song, H. K. Enlarging the D-Spacing of Graphite and Polarizing Its Surface Charge for Driving Lithium Ions Fast. *J. Mater. Chem. A* **2014**, *2* (20), 7600–7605. https://doi.org/10.1039/c3ta15360f.

(228) Wu, F.; Liu, L.; Yuan, Y.; Li, Y.; Bai, Y.; Li, T.; Lu, J.; Wu, C. Expanding Interlayer Spacing of Hard Carbon by Natural K+ Doping to Boost Na-Ion Storage. *ACS Appl. Mater. Interfaces* **2018**, *10* (32), 27030–27038. https://doi.org/10.1021/acsami.8b08380.

(229) Meng, F.; Zhong, H.; Bao, D.; Yan, J.; Zhang, X. In Situ Coupling of Strung Co4N and Intertwined N-C Fibers toward Free-Standing Bifunctional Cathode for Robust, Efficient, and Flexible Zn-Air Batteries. *J. Am. Chem. Soc.* **2016**, *138* (32), 10226–10231. https://doi.org/10.1021/jacs.6b05046.

(230) Bai, Q.; Shen, F. C.; Li, S. L.; Liu, J.; Dong, L. Z.; Wang, Z. M.; Lan, Y. Q. Cobalt@Nitrogen-Doped Porous Carbon Fiber Derived from the Electrospun Fiber of Bimetal–Organic Framework for Highly Active Oxygen Reduction. *Small Methods* **2018**, *2* (12), 1–8. https://doi.org/10.1002/smtd.201800049.

(231) Li, X.; Niu, Z.; Jiang, J.; Ai, L. Cobalt Nanoparticles Embedded in Porous N-Rich Carbon as an Efficient Bifunctional Electrocatalyst for Water Splitting. *J. Mater. Chem. A* **2016**, *4* (9), 3204–3209. https://doi.org/10.1039/c6ta00223d.

(232) Paul, D. R.; Koros, W. J.; Liu, R. Y. F.; Hu, Y. S.; Baer, E.; Hiltner, A.; Keith, H. D.; Liu, R. Y. F.; Hiltner, A.; Baer, E.; Cohen, R. E.; Bellare, A.; Albalak, R. J.; Hu, W.; Reiter, G. Nitrogen-Doped Carbon Nanotube. **2009**, *323* (FEBRUARY).

(233) Zhang, J.; Tan, Y.; Song, W. J. Zeolitic Imidazolate Frameworks for Use in Electrochemical and Optical Chemical Sensing and Biosensing: A Review. *Microchim. Acta* **2020**, *187* (4). https://doi.org/10.1007/s00604-020-4173-3.

(234) Li, X. F.; Lian, K. Y.; Liu, L.; Wu, Y.; Qiu, Q.; Jiang, J.; Deng, M.; Luo, Y. Unraveling the Formation Mechanism of Graphitic Nitrogen-Doping in Thermally Treated Graphene with Ammonia. *Sci. Rep.* **2016**, *6* (March), 1–10. https://doi.org/10.1038/srep23495.

7. Conclusions and Further Work

It is well-known that zinc-air batteries are driven by the slow oxygen reduction and evolution reaction kinetics which require the aid of an electrocatalyst to convert the reactants and generate energy. Hence, this PhD thesis focused on the development of a series of electrocatalysts that could efficiently drive the discharging and charging reactions.

The three experimental chapters reported, show a continuous evolution towards practical applications of carbon-based catalysts for the ORR and OER in ZABs. Firstly, the inclusion of C_3N_4 in the preparation of an efficient metal-free C and N-based electrocatalyst for the ORR is investigated, overcoming the concerns related to its low electronic conductivity. A template-free strategy to dope high concentrations of N functional groups originated from the decomposition of C_3N_4 during high temperature pyrolysis was successfully developed. C_3N_4 would completely decompose at temperatures above 750˚C, without the presence of the PDA framework. As a consequence, the large surface area catalyst composite led to improved active sites exposure and consequently good battery cyclability performance at 5mA/cm^{-2}.

Following the strategy developed in the first chapter to prepare an N-doped carbon composite with exposed active sites, the focus was to then improve the catalyst's OER performance and consequently the battery's cycle life. The second chapter describes the development of a bifunctional ORR/OER catalyst with well distributed cobalt sites on an N-doped C framework was developed and studied. This efficient strategy promoted the formation of distributed cobalt sites, remarkably achieved by inserting Co ions during the polymerization of dopamine to form polydopamine, chelating the Co ions by the N-atoms on the dopamine precursor and subsequently allowing the localized growth of Co-based nanoparticles. The addition of a C_3N_4 template to control the PDA layered growth, avoided particle agglomeration, which would have greatly reduced the catalyst's surface area and access to active sites. These key developments contributed to the battery's improved performance. The cell discharged at 5 mA cm^{-2} for 600 h, 100 h longer than the Pt/C benchmark and even at a high current density of 15 mA cm^{-2}, the battery surpassed both Pt/C and Ir/C-based cells performances.

Finally, following the previously reported developments, the aim was to prepare a composite with variable ORR and OER response by tuning properties such as its BET surface area, pore structure and chemical structure. In this third chapter, electrospinning, a fast, safe and efficient method to prepare nanofibers, was incorporated in the development of high surface area catalysts with exposed active sites. A thin PDA coating was formed on the fibers originating a conductive graphitic carbon coating with encapsulated Co-N-based nanoparticles, upon pyrolysis, maintaining the catalyst's structural integrity and stability. The cell exhibited excellent rechargeable performance for 100h, a remarkably steady long-term discharge performance for about 230h and high specific capacity of 530 mAh g^{-1} at a high current density of 10 mA cm^{-2}.

The developed catalysts contributed, to different extents, to the overall battery performance, depending on their composition, surface area, porosity, active site exposure, electron pathways, interconnecting channels, and electrochemical stability. The addition of a cathode catalyst promotes the adsorption of reaction intermediates at the electrode interphase, facilitating the charge transfer process and subsequently enhancing the electronic conductivity. The reduced overpotential observed for all developed catalyst composites demonstrated the reduction of the activation energy barrier, which in turn increases the kinetics and lowers the resistance on the air electrode interphase and the liquid electrolyte. All catalysts were able to promote a favourable 4-electron pathway confirming the relative stability of the reaction intermediates generated after the O_2 adsorption. This led to the reduction of charge and mass transfer resistance at the cathode interface, improving the full battery impedance. These findings contribute to a better understanding of the synthesis and activity of C, N -based ORR and OER electrocatalysts, providing efficient alternatives which can help the future development of scaled up energy storage systems.

The practical use of ZABs with high specific capacity and cyclability is desired, but several challenges still remain unsolved. The sluggish ORR and OER reaction kinetics which control the ZABs are highly dependent on the presence of electrocatalysts, imposing a serious challenge holding back the development of these battery systems. The complex proton/electron transfer processes to the oxygen molecules, the O=O bond breaking, and the identification of the catalytically active sites are some of the reaction mechanisms that remain to be clarified. For N-doped carbon catalysts, the specific catalytic role of different nitrogen doping types is still not fully understood. Additionally, the determination of the exact location of N atoms in the carbon framework is a challenge,

as well as the chemical nature of the catalytic sites and electrochemical kinetics of the N-doped carbon-based electrodes. Hence, prior to scaling up the production of ZABs, in-depth theoretical and in-situ studies should be performed to better understand the electrocatalytic reactions and advance larger scale systems.

Despite the structural and catalytic developments reported here, the lack of suitable techniques for the larger-scale preparation of C and N-based electrocatalysts limits their potential. Most cells prepared using such catalysts have been limited to research laboratory methods, which are challenging to scale up. Techniques such as ultrasonication bath, freeze-drying and high temperature annealing in furnaces would not suit larger scale production and would greatly increase manufacturing costs. Such processing techniques may also lead to a product yield reduction, again not compatible with a cost-efficient production. Despite the cheaper precursor materials in comparison to the expensive commercially used noble metals. Hence, future studies should be focused on the development of upscaling production techniques of C and N-based electrocatalysts.

Generally, the prepared ZAB cathode catalysts are mixed with a polymer binder (eg. Nafion) and dispersed on a conductive substrate. However, polymeric binders are usually inactive and insulating, leading to a reduced battery capacity. Additionally, catalyst degradation may also be induced by mechanical shedding from the polymer binder. Alternative free-standing catalysts have been developed but their stability is still compromised.

Furthermore, in-situ characterization techniques should be employed during battery cycling and other electrochemical tests to clearly understand the reaction mechanisms and catalytic and structural transformations occurring in the catalysts here developed, tackling early-stage failures.

In summary, this PhD project describes a stepped up research from the development of a C,N-based and metal-free ORR electrocatalyst by transformation of a non-conductive C_3N_4 and a self-polymerized natural product (dopamine), whose bifunctional activity was then improved by the inclusion of Co and N-based NPs by incorporation of Co ions during DA polymerization and subsequent growing of confined ZIF-67 particles. Finally, the stability and integrity of Co,N-containing catalysts was enhanced by the successful preparation of fiber-like structures coated by a graphitic carbon layer formed from the polymerization of DA.

Publication List:

- J. Ferraz, B.; Li, B; Guo, Z.X.; Blackman, C; Liu, Z., Developing N-Rich Carbon from C_3N_4-Polydopamine Composites for Efficient Oxygen Reduction Reaction, *ChemElectroChem*, 2021, 8, 3954–3961.

- J. Ferraz, B.; Kong, J.; Li, B.; Blackman, C; Liu, Z., Co/N nanoparticles supported on a C_3N_4/Polydopamine framework as a bifunctional electrocatalyst for rechargeable zinc-air batteries, *Journal of Electroanalytical Chemistry*, 2022, 921 (7), 116702.

- J. Ferraz, B.; Kong, J.; Blackman, C; Liu, Z., Pyrolyzed ZIF-67 Particles Encapsulated into Polydopamine Coated Porous Nanofibers as an Electrocatalyst for Zinc-Air Batteries – under preparation.

- J. Ferraz, B.; Xu, Y.; Groves, A.; Ashton, T.; Sumboja, A.; Zong, Y.; Darr, J. A; Nanosized Doped Zinc Oxides as Anodes with Enhanced Cycling Stability for Metal-Aqueous Batteries Synthesized via Continuous Hydrothermal Flow Synthesis. – under preparation.